The Dissertation Committee for Jeffrey Robert Potts Certifies that this is the approved version of the following dissertation:

Preparation, Properties, and Structure-Property Relationships of Graphene-Polymer Nanocomposites

Committee:

Rodney S. Ruoff, Supervisor

Donald R. Paul

Christopher W. Bielawski

Kenneth M. Liechti

Christopher J. Ellison

Preparation, Properties, and Structure-Property Relationships of Graphene-Polymer Nanocomposites

by

Jeffrey Robert Potts, B.S.

Dissertation

Presented to the Faculty of the Graduate School of

The University of Texas at Austin

in Partial Fulfillment

of the Requirements

for the Degree of

Doctor of Philosophy

The University of Texas at Austin

December, 2012

To my parents and my wife.

Acknowledgements

First and foremost, I would like to thank my advisor, Dr. Rodney Ruoff, for his valuable guidance and support during my time at UT Austin. His willingness to let me work independently and his help in critically evaluating my results and analysis have been invaluable in shaping me into the scientist and engineer I am today. I would also like to thank my committee members Dr. Chris Bielawski, Dr. Don Paul, Dr. Ken Liechti, and Dr. Christopher Ellison. Each of them has provided me helpful advice and allowed me use of instrumentation in their laboratories, which I depended upon to complete this work.

I have been truly fortunate to meet and learn from many exceptional people during my time at UT Austin. Among them, I wish to express gratitude to Dr. Meryl Stoller and Dr. Sungjin Park for their mentorship and assistance throughout my graduate school journey. I am thankful for the friendships I have developed in graduate school, particularly with Alex Combe, Om Shankar, and Shanthi Murali. Om, I am glad our "Funday" tradition can live on in Houston! I am also grateful to Dr. Ji Ping 'J.P.' Zhou and Dr. Dwight Romanovicz who spent many hours helping me learn TEM and microtomy, both of which were crucial components of this work.

I am indebted to many people outside of UT Austin who have been of great help to me over the course of these past four years. I wish to thank my advisor at Sandia National Laboratories, Dr. Tim Boyle, for giving me the opportunity to work in his lab

for a summer as part of the NINE Program. I am greatly appreciative of Dr. Ling Du, Dr. Carl Pulford, and other folks at Goodyear Tire & Rubber Company for providing me an exciting project to work on during my last two years at UT Austin and for helping me learn the art and science of rubber materials. Special thanks go to my managers and colleagues at Baker Hughes for allowing me the opportunity to start my career while finishing my PhD, and for being supportive as I have juggled the demands of work and school these past few months.

I would never have reached this level of achievement without my friends and family. I am both fortunate and thankful to have maintained many strong friendships from college and before; their support has been a blessing. I deeply appreciate the love and support of my extended family, my grandparents, my sister and brother-in-law, and my parents. I wish to extend special thanks to my family in Austin for your support over these past few years. Mom and Dad, I could never express how grateful I am to have you as role models. Thank you for shaping me into who I am today and for always standing beside me in my endeavors. Most of all, I thank my wife and best friend, Amy, for putting up with the demands of graduate school and for pushing me to succeed. I have been able to reach this goal because you have been there for me through each and every challenge along the way. This thesis is our accomplishment.

Preparation, Properties, and Structure-Property Relationships of Graphene-Polymer Nanocomposites

Jeffrey Robert Potts, Ph.D.

The University of Texas at Austin, 2012

Supervisor: Rodney S. Ruoff

The overall objective of this work was to develop processing, structure, and property relationships in graphene/polymer nanocomposites. To this end, different types of graphene platelets were produced from graphite oxide, dispersed into various thermoplastics and elastomers, and the morphology and properties of the resulting nanocomposites were evaluated. A range of tests were carried out on the nanocomposites to assess property improvements, including stress-strain testing, dynamic mechanical analysis, and thermal and electrical conductivity testing. Extensive morphological characterization, primarily through transmission electron microscopy (TEM) analysis, was performed to gain insight into the mechanisms behind the observed property improvements.

The processing method used to disperse graphene platelets into a given polymer was found to exert significant influence over the nanocomposite morphology and properties. In both thermoplastics and elastomers, liquid-based dispersion methods were

typically found to yield a better dispersion of graphene platelets compared with melt processing; the effectiveness of melt processing appeared to depend in part upon the method used to produce the graphene platelets. Latex compounding of graphene platelets and natural rubber generated nanocomposites with a network morphology with properties that were sensitive to further processing.

The effect of graphene platelet intrinsic structure on nanocomposite properties was studied and property improvements with other nanofillers were compared to graphene platelets. The impact of platelet oxidation on nanocomposite properties was explored in two different systems and produced varying results depending on the polarity of the polymer matrix. An increased average aspect ratio of graphene platelets was not found to improve mechanical properties or a lower percolation threshold when dispersed in natural rubber. Graphene platelets produced superior reinforcement to multi-walled carbon nanotubes and exfoliated montmorillonite when dispersed in natural rubber; however, the carbon nanotubes produced the largest thermal and electrical conductivity enhancements.

Qualitative observation of platelet dispersion by TEM was found to provide excellent correlation with nanocomposite properties when comparing different processing methods or filler materials. The average platelet aspect ratio of three different nanocomposite systems was determined by quantitative TEM analysis and used as a parameter in composite models to generate modulus predictions. Good agreement was found between model predictions and the experimental data.

Table of Contents

List of Tables

List of Figures

Chapter 1:
Introduction

1.1. OVERVIEW

For many decades, particulate fillers such as carbon black and silica have been used to improve the properties of plastics and rubber materials for a wide variety of applications. In the past couple of decades, the use of nanomaterials—including exfoliated layered clays, carbon nanotubes, and most recently, graphene—as fillers in polymeric materials has become a topic of significant academic and industrial research. Polymer materials containing nanomaterials as filler (henceforth, nanofiller) are called polymer nanocomposites.[1,*]

Interest in polymer nanocomposites largely stems from the desirable combination of property changes produced by nanofillers. It has been well-established in the literature that, when properly dispersed in a compatible polymer matrix, a given quantity of nanofiller produces a larger improvement in properties (mechanical, electrical, thermal, etc.) than the same quantity of conventional filler. Potential benefits of blending nanomaterials into polymers thus include smaller property tradeoffs due to lower required loadings of filler to achieve performance targets (e.g., lower reductions in impact

[*] It has been pointed out that some conventional fillers such as carbon black are composed of nano-sized particles and use of the word "nano" in this context marks an arbitrary distinction. However, carbon black is often dispersed as micron-scale aggregates and is more rarely dispersed as individual particles or nanoscale clusters. The term "nanocomposite" will be applied throughout this work to refer to composites containing nanomaterials such as graphene and carbon nanotubes as filler which have a nanoscale dimension(s) (1-100 nm) when dispersed in a polymer matrix.

resistance or toughness[2]), reduced energy input during processing, and lower component weight.[3] This performance advantage is thought to be due to in large part to the exceptional physical properties, unique shapes, and high surface area to volume ratios of nanomaterials.[4-6]

Thus, a central issue in polymer nanocomposites research is proper dispersion of the nanofiller in the matrix so that the intrinsically high surface area of nanomaterials translates into a large amount of interfacial surface area in the nanocomposite.[7] Often, a homogeneous dispersion of nanofiller is desired to maximize interfacial surface area, but other morphologies may be more beneficial depending upon the targeted property improvements.[8] Another important consideration is chemical compatibility between the nanofiller and polymer matrix as poor compatibility reduces stress transfer at the interface and can inhibit effective dispersion.[9] Moreover, different shapes, compositions, and synthesis methods create unique considerations for each type of nanofiller.[10] To maximize property enhancements and to enable design of nanocomposites for specific applications, it is greatly desired to understand the relationships between the structure of the nanofiller, the nanocomposite processing method, the nanofiller dispersion morphology, and the nanocomposite properties.[11]

Research on polymer nanocomposites began with reports in the late 1980s that exfoliated layered silicates (often referred to as nanoclays) could greatly enhance the mechanical properties of thermoplastic polymers.[12] In the following years, carbon nanotube/polymer nanocomposites garnered significant attention.[13] Most recently, interest in graphene—a single layer of carbon atoms[14]—as a filler in polymer materials

has grown tremendously, following the first report on graphene/polymer nanocomposites by Stankovich, Ruoff and co-workers in 2006.[15] This surge in research activity is evidenced in Figure 1.1, which plots the number of hits returned in a Web of Science topical search on polymer nanocomposites containing one of these three types of nanofillers. Clearly, despite the growing popularity of graphene/polymer nanocomposites, nanoclay and carbon nanotube/polymer nanocomposites remain topics of great research interest.

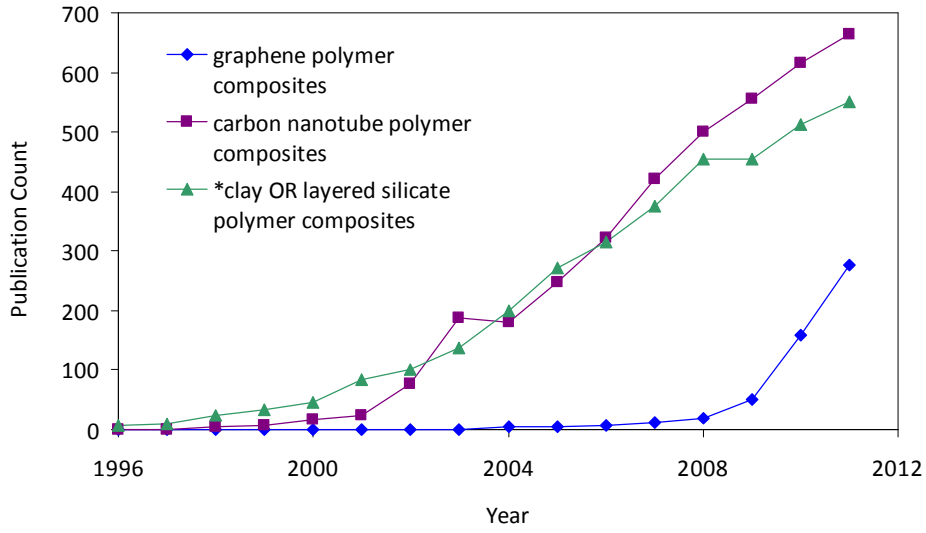

Figure 1.1. Number of publications returned by a Web of Science search on graphene, carbon nanotube, and nanoclay-filled nanocomposites (search date: 8-15-2012). Terms shown in the figure were used as topical queries.

Graphene shows great promise for use as nanocomposite filler because of its exceptional physical properties and potential for inexpensive large-scale production.[14] Although previous work on other polymer nanocomposite systems has promoted the

advancement of the graphene/polymer nanocomposite field, many challenges remain. For instance, fundamental relationships between processing method, graphene platelet structure, and nanocomposite properties have not been well-established in the literature. In addition, relatively little work has been published to date on graphene-filled elastomers. This dissertation aims to address these issues and to contribute to the growing body of knowledge in this field.

1.2. LAYOUT OF THE DISSERTATION

The dissertation begins with an introduction and background section, followed by five chapters of original research, conclusions and recommendations, and five appendices containing supplementary information. Chapter 2 presents a background on the topics of graphene-based materials and graphene/polymer nanocomposites largely based upon prior work in the literature. Chapters 3 and 4 cover graphene/thermoplastic nanocomposites, while Chapters 5 through 7 discuss graphene/elastomer (natural rubber) nanocomposites. The work in Chapters 5-7 was performed in collaboration with Goodyear Tire & Rubber Company. Chapter 3 presents a study on the effects of graphene platelet surface chemistry on the thermomechanical properties of poly(methyl methacrylate)-matrix nanocomposites produced by *in situ* polymerization. Dispersion of microwave-exfoliated graphite oxide into bisphenol-A polycarbonate via melt compounding and a morphology/property evaluation of the resulting nanocomposites is presented in Chapter 4. Chapter 5 presents a study on reduced graphene oxide/natural rubber nanocomposites made by latex co-coagulation. The unique morphology produced

by this process and the effect of milling (shear) on this morphology is explored in detail, primarily using transmission electron microscopy. Quantification of graphene platelet dispersion by transmission electron microscopy and application of micromechanical models to this nanocomposite system is also explored in Chapter 5. In the work presented in Chapter 6, thermally-exfoliated graphite oxide was blended into natural rubber by two methods: two-roll mill mixing and latex mixing. Differences in the morphology and properties of the nanocomposites made by these two approaches are compared to one another and to carbon black. Chapter 7 presents a direct comparison of the properties and morphologies of natural rubber-matrix nanocomposites blended with either graphene platelets, multi-walled carbon nanotubes, or exfoliated montmorillonite. The effect of surface oxidation and intrinsic aspect ratio of the graphene platelets is also explored in this Chapter. A summary of the work in this thesis and its significance presented in Chapter 8, along with recommendations for future work in this field.

1.3. REFERENCES

1. Paul, D. R.; Robeson, L. M. *Polymer* **2008,** 49, (15), 3187-3204.

2. Schadler, L. S.; Brinson, L. C.; Sawyer, W. G. *Journal of the Minerals, Metals and Materials Society* **2007,** 59, (3), 53-60.

3. Vaia, R. A.; Maguire, J. F. *Chemistry of Materials* **2007,** 19, (11), 2736-2751.

4. Thostenson, E. T.; Li, C. Y.; Chou, T. W. *Composites Science and Technology* **2005,** 65, (3-4), 491-516.

5. Kumar, S. K.; Krishnamoorti, R. *Annual Review of Chemical and Biomolecular Engineering* **2010,** 1, 37-58.

6. Fornes, T. D.; Paul, D. R. *Polymer* **2003,** 44, (17), 4993-5013.

7. Schadler, L. S.; Kumar, S.; Benicewicz, B. C.; Lewis, S.; Harton, S. E. *MRS Bulletin* **2007,** 32, 335-340.

8. Nan, C.-W.; Shen, Y.; Ma, J. *Annual Review of Materials Research* **2010,** 40, 131-151.

9. Han, C. D. *Advances in Polymer Science* **2010,** 231, 1-75.

10. Kim, H.; Abdala, A. A.; Macosko, C. W. *Macromolecules* **2010,** 43, 6515-6530.

11. Jancar, J.; Douglas, J. F.; Starr, F. W.; Kumar, S.; Cassagnau, P.; Lesser, A. J.; Sternstein, S. S.; Buehler, M. J. *Polymer* **2010**, 3321-3343.

12. Okada, A.; Usuki, A. *Macromolecular Materials and Engineering* **2006,** 291, 1449-1476.

13. Moniruzzaman, M.; Winey, K. I. *Macromolecules* **2006,** 39, (16), 5194-5205.

14. Park, S.; Ruoff, R. S. *Nature Nanotechnology* **2009,** 5, (4), 217-224.

15. Stankovich, S.; Dikin, D. A.; Dommett, G. H. B.; Kohlhaas, K. M.; Zimney, E. J.; Stach, E. A.; Piner, R. D.; Nguyen, S. T.; Ruoff, R. S. *Nature* **2006,** 442, (7100), 282-286.

Chapter 2:
Background

2.1. Overview of Graphene-Based Materials

Graphene has a rich history which spans over forty years of experimental work.[1] "Pristine" graphene (a single, sp^2-hybridized carbon layer free of heteroatomic defects) has been produced by several routes,[2, 3] including growth by chemical vapor deposition, micromechanical exfoliation of graphite, and growth on crystalline silicon carbide. While these approaches can yield a largely defect-free material with exceptional physical properties, current techniques of making pristine graphene do not yield large enough quantities for use in applications such as polymer nanocomposites.

An alternative and much more scalable approach to production of graphene is the use of top-down chemical methods to exfoliate graphite. Such approaches do not yield pristine graphene but rather graphene platelets—few-layer platelets or monolayer carbon sheets that may contain heteroatoms and topological defects, which resemble graphene on a local scale. While the structural defects of graphene platelets are detrimental to physical properties, these materials still exhibit exceptional characteristics.

The most common approach for the preparation of graphene platelets is the exfoliation and reduction of graphite oxide (GO). Techniques for the exfoliation of GO to graphene platelets were pioneered by Boehm and co-workers; these approaches to exfoliating graphite have since been shown to yield single carbon layers. Other

techniques to exfoliating graphite exist, but they do not achieve fully-exfoliated platelets or produce only small quantities of fully-exfoliated platelets. For example, graphite can be intercalated with atoms or molecules (such as alkali metals or mineral acids) to form graphite intercalation compounds. The intercalation weakens the interlayer interactions and facilitates the exfoliation by mechanical or thermal methods.[4] However, this approach typically yields platelets with thicknesses greater than 5 nm. Direct exfoliation of graphite into solvents[5-8] as well as chemical synthesis of graphene from polycyclic aromatic hydrocarbon precursors can produce single-layer graphene platelets, but to date these methods are limited by very low yields. Alternatively, the further development of gas phase CVD methods could potentially provide a scalable method for production of graphene.[9]

2.2. PRODUCTION, PROPERTIES, AND EXFOLIATION OF GO

In this work, GO was produced by the treatment of graphite using a modified Hummers method, in which graphite is treated with $KMnO_4$ and H_2SO_4. This reaction disrupts the delocalized electronic structure of graphite and imparts a variety of oxygen-based chemical functionalities to the surface, resulting in a typical C : O ratio of 1.4 as measured by elemental analysis by combustion. While the precise structure of GO remains a matter of debate,[10] it is thought that hydroxyl and epoxy groups are present in highest concentration on the basal plane, with carboxylic acid groups around the periphery of the sheets. GO has an expanded interlayer spacing relative to graphite which varies from 0.6 to 1.2 nm depending on humidity, due to intercalation of water

molecules.[11] A schematic of a possible chemical structure of GO is shown in Figure 2.1 (intercalated/adsorbed water molecules are omitted for clarity).

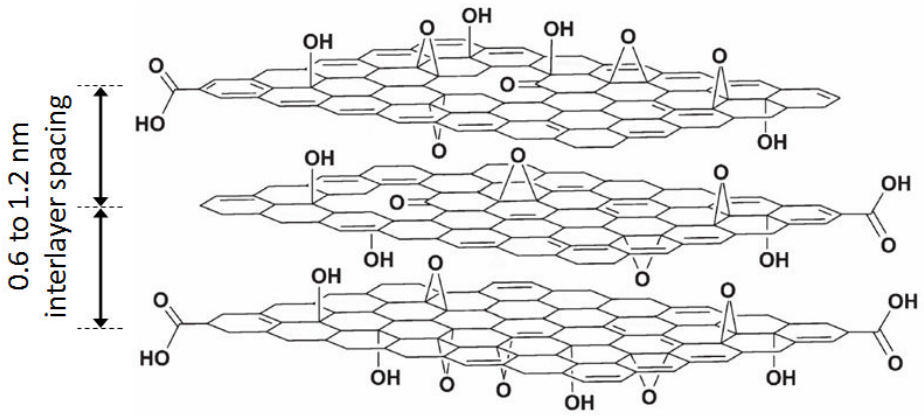

Figure 2.1. Illustration of the chemical structure of GO showing some of the functional groups thought to be present.

With few exceptions,[12] successful production of well-dispersed polymer nanocomposites with GO-derived fillers hinges largely on the exfoliation of GO prior to incorporation into a polymer matrix. Solvent-based exfoliation and thermal exfoliation techniques have emerged as two preferred routes for this step. In the former route, the hydrophilic nature and large interlayer spacing of GO (relative to graphite) facilitates direct exfoliation into water assisted by mechanical exfoliation, such as ultrasonication and/or stirring, at concentrations up to 3 mg/ml, forming colloidal suspensions of graphene oxide (henceforth, G-O).[2] Zeta potential measurements indicate that these suspensions are electrostatically stabilized by negative charges, possibly from the carboxylate groups that are believed to decorate the periphery of the lamellae.[2]

Suspensions produced by sonication of GO are found by atomic force microscopy (AFM), when deposited onto various substrates, to consist primarily of single-layer G-O platelets; however, the sonication treatment fragments the platelets, reducing their lateral dimensions by over an order of magnitude down to a few hundred nanometers.[10, 13] Mechanical stirring is one alternative route to produce single-layer G-O platelets of much larger lateral dimensions and aspect ratios when compared with G-O platelets produced by sonication; however, stirring exfoliates very slowly and in low yield.[10] Kinetically-stable G-O suspensions can be produced via sonication of GO in polar organic solvents such as DMF, PC, and NMP, at concentrations below 0.5 mg/ml.[14, 15]

GO can also be exfoliated by rapid heating, yielding thermally-expanded graphite oxide, or TEGO (also referred to commonly in the literature as functionalized graphene sheets, or FGS).[16, 17] In this exfoliation method, the dry powder is subjected to rapid heating up to temperatures such as 400 °C[18] or higher.[16] The rapid heating is believed to cause various small molecule species (e.g., CO, CO_2, water) to evolve and internal pressure to increase, forcing the sheets apart and yielding a dry, high-surface area material with a low bulk density.[17] Measurements of the surface area of TEGO by the Brunauer, Emmett, and Teller method (which measures surface area based on isothermal gas adsorption) have generally ranged from 400 to 1500 m^2/g,[16] compared with a theoretical limit of approximately 2600 m^2/g for graphene.[19] Also, GO can be exfoliated by microwave radiation, yielding a related material referred to as microwave-expanded graphite oxide, or MEGO.[20] Importantly, while G-O platelets are likely to maintain the chemical structure of GO, TEGO and MEGO are reduced by the heating process

(reported C : O ratios of 10 : 1[16] and 3 : 1,[20] respectively), and are electrically conductive (reported values of roughly 2,000 S/m for TEGO[16] and 270 S/m for MEGO[20]). Differences in the physical properties of TEGO and MEGO may be simply due to differences in temperature achieved during the exfoliation process. MEGO and TEGO materials are usually reported to exhibit "worm-like" structures of loosely-stacked platelets. Further exfoliation and in a solvent and subsequent transmission electron microscopy (TEM) or AFM observation on the platelets reveals a crumpled accordion-like morphology, with lateral dimensions of a few hundred nanometers, similar to G-O platelets exfoliated by sonication.[16, 21]

2.3. Chemical Reduction and Functionalization of G-O Platelets

The physical properties of G-O platelets are markedly different from that of graphene. Chemical reduction of G-O platelets, using reducing agents such as hydrazine monohydrate and sodium borohydride,[2] can afford graphene platelets which have physical properties similar to pristine graphene. Typical chemically-reduced G-O platelets (henceforth, RG-O) typically exhibit C : O ratios of approximately 10 : 1,[10] thus retaining some of the oxygen-based functionality originally present on the G-O platelets.[2, 22] This reduction process can cause agglomeration of the platelets[23] unless prior steps are taken to stabilize the suspension. Adjusting the pH of the suspension to increase the magnitude of the negative zeta potential of the platelets (electrostatic stabilization) or the adsorption of polymers on the platelet surface (steric stabilization) are both effective

routes to stabilizing aqueous suspensions of RG-O platelets.[24, 25] A plot of zeta potential versus pH of a 0.5 mg/ml aqueous suspension of typical G-O and RG-O platelets produced in this work is shown in Figure 2.2.

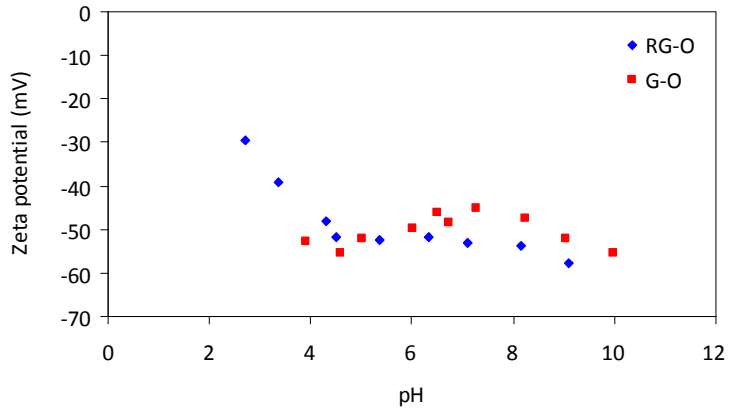

Figure 2.2. Plot of zeta potential versus pH for RG-O and G-O platelets in water at a concentration of 0.5 mg/ml.

Stable suspensions of RG-O platelets in organic solvents have also been achieved. One approach to these suspensions is progressive dilution of an aqueous suspension of G-O platelets with an organic solvent—with one possible route involving hydrazine in DMF : water (9 : 1 v/v) and further dilution in DMF to yield a stable suspension of RG-O platelets in 99% DMF. For nanocomposites processed in solution, chemical reduction of G-O platelets in a polymer solution (provided the polymer is stable to the reaction conditions) may prevent the precipitation of the RG-O platelets from the solvent, as the polymer has been reported to maintain the dispersion of RG-O platelets.[19] The oxygen-based functional groups of G-O (or residual functionality on RG-O) can also be used as

handles for chemical functionalization,[10] e.g., reactions of hydroxyl and carboxylic acid groups with isocyanates.[26]

The relationships between GO and the different graphene-based materials is summarized in Figure 2.3. In the context of polymer nanocomposites, it may be helpful to distinguish two distinct classes of graphene-based materials. TEGO and MEGO are produced by thermal exfoliation and in bulk form are dry, fluffy powders with a low bulk density. On the other hand, G-O, RG-O and other chemically modified graphene materials are exfoliated in solution and are generally handled as colloidal suspensions. These different physical characteristics have implications for the types of processing approaches that can be used to disperse these two classes of graphene platelets into polymeric materials, as will be discussed in the following section as well as in Chapter 3 and Chapter 6.

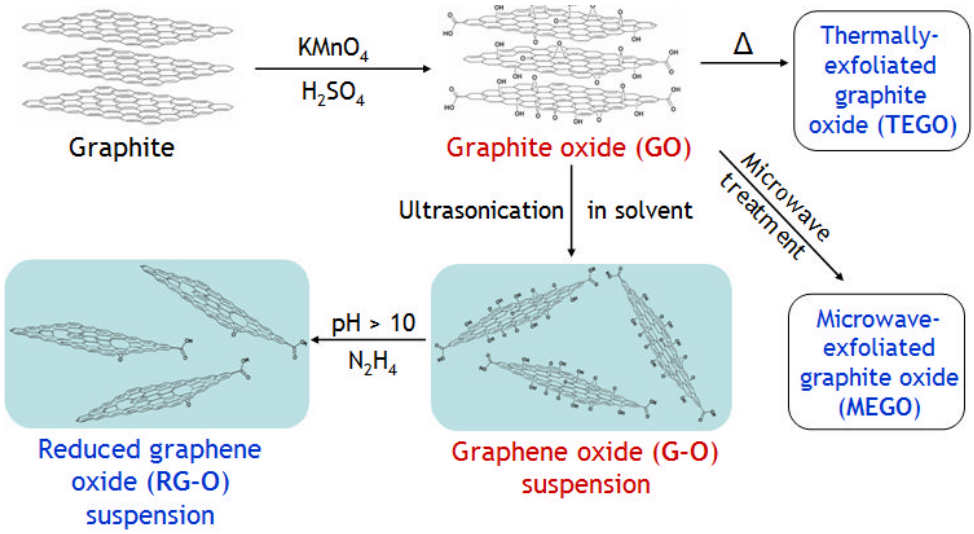

Figure 2.3. Flowchart illustrating the general routes for synthesis of graphene-based materials, derived from GO.

2.4. PREPARATION OF GRAPHENE/POLYMER NANOCOMPOSITES

Nanocomposite properties are strongly dependent on morphology, which is in turn dependent upon the graphene platelet preparation method and nanocomposite processing approach. Effective dispersion of graphite particles into high aspect ratio graphene platelets has not been achieved by any conventional processing technique. Thus, to achieve a good dispersion of high aspect ratio platelets, graphene platelets generally must be separately produced by one of the methods described in the previous section and subsequently dispersed into a polymer matrix.

As with other polymer nanocomposite systems, there are three primary dispersion methods utilized for production of graphene/polymer nanocomposites (Figure 2.4): solution/latex mixing, melt mixing, and *in situ* polymerization. Solution-based methods generally involve the mixing of colloidal suspensions of graphene platelets with the desired polymer, either itself already in solution or by dissolving in the polymer in the colloidal suspension, by simple stirring or shear mixing. The resulting suspension can then be precipitated using a non-solvent for the polymer, causing the polymer chains to encapsulate the filler upon precipitation. Alternatively, the suspension can be directly cast into a mold and the solvent removed. However, this latter technique can potentially lead to aggregation of the filler in the composite, which may be detrimental to composite properties.[27]

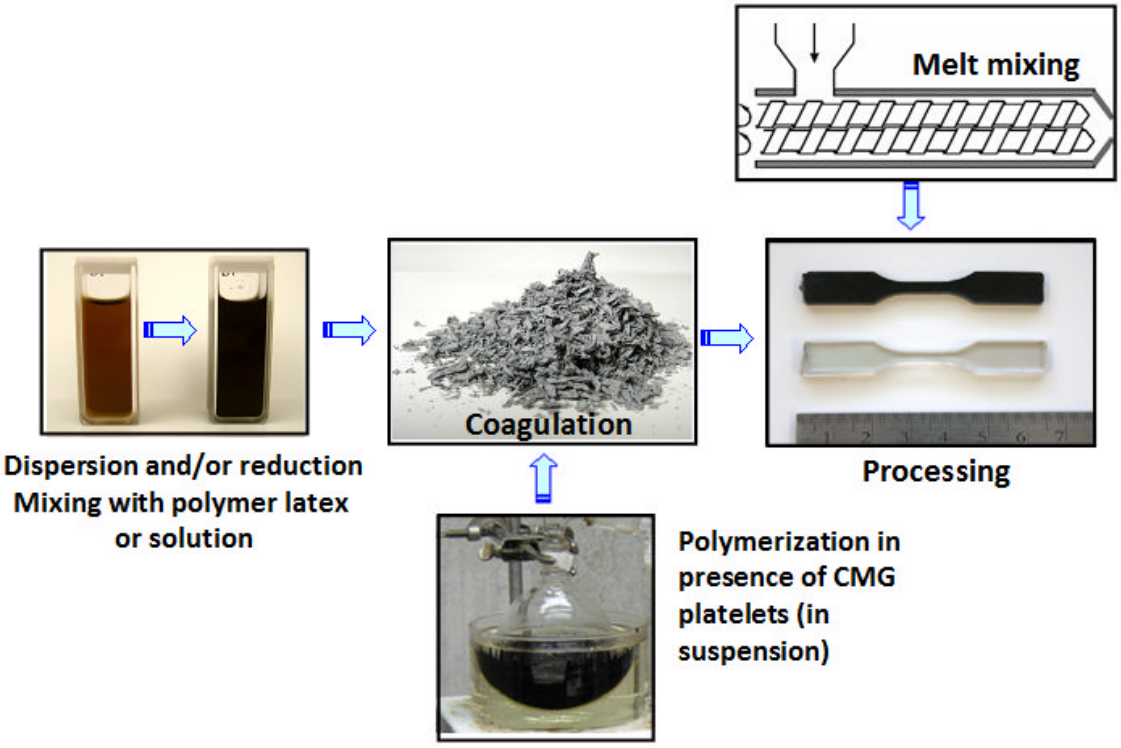

Figure 2.4. The three primary approaches for dispersing graphene into a polymer matrix.

Solution mixing has been widely reported in the literature, as graphene platelets can often be processed in either water or organic solvents. As fully-exfoliated, single-layer G-O or RG-O platelets can be dispersed in colloidal suspensions, solution mixing offers a potentially simple route to achieving an excellent dispersion of this class of graphene platelets in polymers. By comparison, TEGO or MEGO generally cannot be exfoliated into water or organic solvents without the aid of a surfactant, which may negatively effect the physical properties of the nanocomposite.[28]

In melt mixing, a polymer melt and nanofiller are mixed under high shear conditions in processing equipment such as an extruder. Relative to solution mixing, melt mixing is often considered more economical (because no solvent is used) and is most compatible with current industrial practices;[29] however, it has been suggested that melt mixing does not provide the same level of dispersion of the filler as solvent mixing or *in situ* polymerization methods.[30] Notably, no means of dispersing single- or few-layer GO-derived fillers via melt mixing without prior exfoliation have been reported akin to layered silicate nanofillers (although, with a few exceptions, direct exfoliation of layered silicates via melt mixing requires prior treatment with a surfactant to increase miscibility with the polymer host[31]). Several studies report melt mixing using TEGO as nanofiller, where TEGO could be fed directly into an extruder and dispersed into a polymer matrix without the use of any solvents or surfactants. Unfortunately, the very low bulk density (approximately 0.004 g/cm^3 based on a volumetric expansion of 500[16]) of TEGO makes handling of the dry powders difficult and poses a processing challenge, such as for feeding into processing equipment such as a melt extruder. For nanocomposites incorporating G-O platelets as filler, melt processing and molding operations may cause substantial reduction of the platelets due to their thermal instability.[32]

In situ polymerization methods for production of polymer nanocomposites generally involve mixing of filler in neat monomer (or multiple monomers), or a solution of monomer, followed by polymerization in the presence of the dispersed nanofiller. These efforts are often followed with precipitation/extraction or solution casting to generate samples for testing. Unlike what has been reported for solution mixing methods,

a high level of dispersion of graphene-based filler has been achieved via *in situ* polymerization without a prior exfoliation step.[12]

As previously mentioned, the physical form of graphene platelets (colloid or powder) appears to have strong implications for the type of effective dispersion methods that can be used to produce graphene/polymer nanocomposites. For instance, colloidal suspensions of graphene platelets can be agglomerated to yield dry powders and subsequently mixed with a polymer via melt processing,[30, 33-35] but attempts to disperse graphene platelets in this manner have yielded poor results[36, 37] despite melt processing being highly effective for dispersion of TEGO. Conversely, TEGO is reluctant to form homogeneous colloidal suspensions when dispersed into solvents, typically affording a relatively poor dispersion if mixing TEGO into polymers by solution blending processes.

2.5. MORPHOLOGY OF GRAPHENE/POLYMER NANOCOMPOSITES

As property enhancements correlate strongly with nanocomposite microstructure, effective characterization of morphology is important to establishing structure-property relationships for these materials. TEM of microtomed thin sections of the nanocomposite can allow for direct observation of dispersed graphene platelets. Thicker platelets typically show adequate contrast against the polymer matrix to be imaged without staining, whereas single-layer platelets may be difficult to directly observe by TEM.[30] Compared with TEM, wide-angle X-ray scattering (WAXS) can more rapidly provide insight into the state of dispersion over a larger volume of composite; however, since the scattering intensity varies with the concentration of the scattering feature, some

morphological information may be missed.[33] In other words, the absence of a peak corresponding to the interlayer spacing of graphite in the WAXS signal does not mean the nanocomposite is fully exfoliated; however, the presence of a peak implies a poor dispersion (i.e., intercalated or agglomerated platelets).

TEM and WAXS studies are perhaps the two most powerful means by which the state of dispersion can be assessed. Immiscibility of the phases and/or insufficient exfoliation of the graphene platelets prior to mixing with polymer can result in large agglomerates consisting of stacked platelets when observed by TEM, which may also be suggested by the presence of a diffraction peak corresponding to the interlayer spacing of GO or graphite.[30, 33, 34] Intercalated platelets retain a stacked structure but with increased interlayer spacing (on the order of a few nanometers), as evidenced by a shifted diffraction peak from that of unmodified graphite or GO.[39] As will be discussed in the following section and elsewhere in the dissertation, high aspect ratio platelets are generally found to be most beneficial to the mechanical, electrical, and thermal properties of a composite material. An exfoliated morphology is thus usually desired as it provides higher aspect ratio platelets relative to stacked or intercalated platelets.[40] This state of dispersion may be suggested by a scattering profile corresponding to that of the neat matrix polymer; however, multi-layer intercalated platelets could actually be dispersed (as observed by TEM) despite the absence of a diffraction peak. TEM micrographs can be used to effectively quantify dispersion, although there are many challenges in the technique and these are discussed at length in Chapter 5 and Appendix A.

While WAXS nor TEM can be used to assess dispersion of individual platelets, neither can detect larger-scale morphological features.[29, 41] Small-angle X-ray scattering and small-angle neutron scattering experiments have been used on a variety of nanocomposite systems to detect the presence of fractal-like aggregates of filler at length scales beyond that of individual particles, although only limited information of this nature exists on graphene/polymer nanocomposites.[33] Finally, cross-sectional analysis with scanning electron microscopy (SEM) has been used in attempt to evaluate dispersion of graphene-based filler[19] as well as to reportedly examine the surface for filler pull-out, with the goal of gaining insight into the strength of interfacial adhesion.[38, 42] However, care must be exercised when identifying the dispersed filler, as SEM generally cannot resolve the degree of exfoliation of the platelets. However, subsurface imaging with SEM has been used to image dispersion of reduced graphene oxide platelets on a larger scale, and also has been used to image nanotube networks in CNT/polymer nanocomposites.[19]

Both graphite and GO, as the precursors to many graphene-based materials, have a layered structure as do certain silicates (e.g., montmorillonite) which have been widely investigated as composite fillers.[29] Indeed, when dispersed into a polymer matrix, both nanoclays and graphene platelets exhibit similar states of dispersion depending upon factors such as the processing technique and the affinity between the phases. Moreover, nanoclay fillers often exhibit comparable aspect ratios to graphene-based fillers (up to 1000),[31] although fillers such as TEGO often appear more crumpled on a local scale relative to nanoclays (see Figure 7.2).[38]

Exfoliated graphene platelet materials are often compliant, and when dispersed in a polymer matrix are typically not observed as rigid disks, but rather as bent or crumpled platelets. Compatibility between the polymer matrix and the graphene platelets can reportedly affect the platelets' conformation.[43] If the platelets' affinity for the matrix is high, then the particles may adopt a more extended conformation. However, the platelets may gradually adopt a more crumpled conformation as the affinity between the components decreases.[43] The technique used to process the nanocomposites can also reportedly affect the microstructure: randomly-oriented, exfoliated platelets may be favored when nanocomposites are processed by solution mixing or *in situ* polymerization, compared with a more oriented and intercalated/stacked structure for nanocomposites produced by melt mixing, possibly due to restacking of the platelets.[30] The processing technique can also induce orientation of the dispersed platelets, which can be beneficial for reinforcement[44] but may raise the percolation threshold.[34] For nanocomposites processed by injection molding, platelets may be more randomly oriented near the interior of the specimen, with platelets aligned parallel to the surface.[34] By comparison, sufficiently thin, compression molded specimens[34] or solution-cast films[45] may have aligned platelets along the entire cross section.

2.6. PHYSICAL PROPERTIES OF GRAPHENE/POLYMER NANOCOMPOSITES

Exceptional multi-functional property enhancement has been reported in a variety of graphene/polymer nanocomposite systems. In general, graphene-based materials combine some of the best features of both nanoclays and carbon nanotubes—the platelet

structure of graphene allows for barrier property enhancement and effective reinforcement when randomly oriented just as with nanoclays, but are highly conductive like carbon nanotubes. This balance of properties makes graphene platelets well-suited for use as nanofiller in polymer nanocomposites.

The anisotropy (quantified by the aspect ratio) of graphene platelets creates a "jamming" effect that allows them to form a percolating network at a far lower loading than spherical particles;[46] for uniformly-dispersed particles, the percolation threshold scales with the inverse of the particle aspect ratio. The onset of connectivity percolation can be probed using melt rheology; as the particles come into contact and form an elastic network, the viscoelastic response of the polymer matrix is overwhelmed by the elastic response of the network, and the modulus shows a low-frequency plateau. This effect is illustrated in Chapter 4.

Graphene-based materials may be highly conductive (up to 35,100 S/m[47]), which can increase the conductivity of polymers by several orders of magnitude. In order for a nanocomposite with an insulating matrix to be electrically conductive, the concentration of the conducting nanofiller must be above the electrical percolation threshold, where a conductive network of nanofiller particles is formed. It has been said that a high degree of dispersion may not necessarily yield the lowest onset of electrical percolation,[41] as a sheath of polymer may coat the surfaces of well-dispersed filler and prevent direct interparticle contact. Indeed, the lowest percolation threshold achieved to date in the literature for a graphene/polymer nanocomposite (approximately 0.15 wt%) was observed when the filler was not homogeneously dispersed in the polymer matrix, but rather

segregated from the matrix to form a conductive network.[48] However, in the case of uniformly-dispersed platelets, higher intrinsic platelet aspect ratios[49] and randomly-oriented platelets[50] may be beneficial to electrical conductivity. Observations presented in Chapter 5 suggest that a segregated network of platelets is indeed beneficial for conductivity, although Chapter 7 work shows that larger-area platelets may not provide improved conductivity as they are more difficult to effectively disperse.

The in-plane elastic modulus of pristine graphene is on the order of 1 TPa.[51] G-O and RG-O platelets exhibit an appreciably lower in-plane stiffness which calculations suggest may scale inversely with an increasing level of oxidation of the platelets.[52] Results based on AFM tip-induced deformation studies suggest a modulus of RG-O platelets of 250 GPa and moduli ranging between 208 and 650 GPa for G-O platelets.[53] These relatively large modulus values (compared to most polymeric materials), coupled with the large surface areas of the platelets, allow GO-derived fillers to be the primary load-bearing component of a polymer nanocomposite.[44]

Once dispersed in a polymer matrix, these compliant sheets or thin platelets commonly adopt wavy or wrinkled structures which may effectively reduce these modulus values,[54] as crumpled platelets may tend to unfold rather than stretch in-plane under an applied tensile stress. Moreover, platelet re-stacking or incomplete exfoliation to single platelets could also lead to lower effective modulus values due to the reduction in the respective aspect ratios.[44, 55] In particular, such highly-crumpled platelet conformations are often reported in nanocomposites using TEGO as filler, which along with structural defects generated during the high-temperature exfoliation processes,[56]

may significantly reduce the effective stiffness of the platelets and thus diminish their reinforcing capability.

Aside from these issues with the intrinsic structure of GO-derived fillers, the reinforcing effectiveness observed from these materials thus far may be limited by problems with interfacial adhesion and spatial distribution of filler. Strong interfacial adhesion between the platelets and polymer matrix is crucial for effective reinforcement.[29, 57-60] Aside from making dispersion difficult, incompatibility between the phases may lower stress transfer due to low interfacial adhesion, resulting in a lower composite modulus.[61]

Micromechanical models suggest aligned fibers (i.e., CNTs) should provide larger reinforcement than aligned platelets.[62] However, in practice a perfect alignment is never achieved, and in most cases a large amount of disorientation is present (as best detected by TEM for well-dispersed platelets). For the case of randomly-oriented fillers, platelets should provide superior reinforcement to one-dimensional tubes. Indeed, work presented in Chapter 7 on natural rubber-matrix nanocomposites shows that reduced graphene oxide platelets can provide superior reinforcement to multi-walled carbon nanotubes when well-dispersed and randomly-oriented (per TEM observation).

The exceptional thermal properties of graphene-based materials have been harnessed as fillers to improve the thermal conductivity, thermal stability, and dimensional stability of polymers. Pristine graphene is highly thermally conductive; at room temperature, the thermal conductivity has been measured to be exceed 3000 W/m·K when suspended[63, 64] and approximately 600 W/m·K when supported on a SiO_2

substrate.[65] The sheet-like geometry of graphite and graphene filler can also impart significant anisotropy to the thermal conductivity of the polymer composite.[68] Significant improvements in thermal conductivity have been achieved in these systems—with composite conductivities ranging from 3 to 6 W/m·K, up from approximately 0.2 W/m·K for neat epoxy—but such large gains require relatively high carbon loadings of 20 wt% and higher. Despite the fact that CNTs show similar intrinsic thermal conductivities, some researchers have suggested that geometry of graphene-based platelets may provide lower interfacial thermal resistance and thus produce larger conductivity improvements in polymer nanocomposites.[66, 67] However, this conclusion is not supported by this work, as shown in Chapter 7.

The incorporation of GNPs and GO-derived fillers can significantly reduce gas permeation through a polymer composite relative to the neat matrix polymer. A percolating network of platelets can provide a tortuous path which inhibits molecular diffusion through the matrix, thus resulting in significantly reduced permeability.[29] Orientation of the platelets may further enhance barrier properties perpendicular to their alignment, while higher platelet aspect ratios correlate with increased barrier resistance.[29] Reductions in permeability as high as 99% (at 3.7 wt% filler) have been reported in graphene/polymer nanocomposites.[30]

2.7. REFERENCES

1. Dreyer, D. R.; Ruoff, R. S.; Bielawski, C. W. *Angewandte Chemie, International Edition in English*, DOI: 10.1002/anie.201003024.

2. Park, S.; Ruoff, R. S. *Nature Nanotechnology* **2009,** 5, (4), 217-224.

3. Zhu, Y.; Murali, S.; Cai, W.; Li, X.; Suk, J. W.; Potts, J. R.; Ruoff, R. S. *Advanced Materials* **2010,** 22, 3906-3924.

4. Jang, B. Z.; Zhamu, A. *Journal of Materials Science* **2008,** 43, (15), 5092-5101.

5. Zhang, M.; Parajuli, R. R.; Mastrogiovanni, D.; Dai, B.; Lo, P.; Cheung, W.; Brukh, R.; Chiu, P. L.; Zhou, T.; Liu, Z. F.; Garfunkel, E.; He, H. X. *Small* **2010,** 6, (10), 1100-1107.

6. Hernandez, Y.; Nicolosi, V.; Lotya, M.; Blighe, F. M.; Sun, Z.; De, S.; McGovern, I. T.; Holland, B.; Byrne, M.; Gun'Ko, Y. K. *Nature Nanotechnology* **2008,** 3, (9), 563-568.

7. Lotya, M.; Hernandez, Y.; King, P. J.; Smith, R. J.; Nicolosi, V.; Karlsson, L. S.; Blighe, F. M.; De, S.; Wang, Z.; McGovern, I. T.; Duesberg, G. S.; Coleman, J. N. *Journal of the American Chemical Society* **2009,** 131, (10), 3611-3620.

8. Lu, J.; Yang, J.-x.; Wang, J.; Lim, A.; Wang, S.; Loh, K. P. *ACS Nano* **2009,** 3, (8), 2367-2375.

9. Dato, A.; Radmilovic, V.; Lee, Z.; Phillips, J.; Frenklach, M. *Nano Letters* **2008,** 8, (7), 2012-2016.

10. Dreyer, D. R.; Park, S.; Bielawski, C. W.; Ruoff, R. S. *Chemical Society Reviews* **2010,** 39, (1), 228-240.

11. Buchsteiner, A.; Lerf, A.; Pieper, J. r. *Journal of Physical Chemistry B* **2006,** 110, (45), 22328-22338.

12. Jang, J. Y.; Kim, M. S.; Jeong, H. M.; Shin, C. M. *Composites Science and Technology* **2009,** 69, (2), 186-191.

13. Li, Z.; Zhang, W.; Luo, Y.; Yang, J.; Hou, J. G. *Journal of the American Chemical Society* **2009,** 131, (18), 6320-6321.

14. Paredes, J. I.; Villar-Rodil, S.; Martinez-Alonso, A.; Tascon, J. M. D. *Langmuir* **2008,** 24, (19), 10560-10564.

15. Zhu, Y.; Stoller, M. D.; Cai, W.; Velamakanni, A.; Piner, R. D.; Chen, D.; Ruoff, R. S. *ACS Nano* **2010,** 4, (2), 1227-1233.

16. Schniepp, H. C.; Li, J. L.; McAllister, M. J.; Sai, H.; Herrera-Alonso, M.; Adamson, D. H.; Prud'homme, R. K.; Car, R.; Saville, D. A.; Aksay, I. A. *Journal of Physical Chemistry B* **2006,** 110, (17), 8535-8539.

17. McAllister, M. J.; Li, J. L.; Adamson, D. H.; Schniepp, H. C.; Abdala, A. A.; Liu, J.; Herrera-Alonso, M.; Milius, D. L.; Car, R.; Prud'homme, R. K.; Aksay, I. A. *Chemistry of Materials* **2007,** 19, (18), 4396-4404.

18. Ruess, V. G.; Vogt, F. *Monatshefte fur Chemie* **1948,** 78, 222-242.

19. Stankovich, S.; Dikin, D. A.; Dommett, G. H. B.; Kohlhaas, K. M.; Zimney, E. J.; Stach, E. A.; Piner, R. D.; Nguyen, S. T.; Ruoff, R. S. *Nature* **2006,** 442, (7100), 282-286.

20. Zhu, Y. W.; Murali, S.; Stoller, M. D.; Velamakanni, A.; Piner, R. D.; Ruoff, R. S. *Carbon* **2010,** 48, (7), 2118-2122.

21. Bagri, A.; Mattevi, C.; Acik, M.; Chabal, Y. J.; Chhowalla, M.; Shenoy, V. B. *Nature Chemistry* **2010,** 2, (7), 581-587.

22. Boukhvalov, D. W.; Katsnelson, M. I. *Journal of the American Chemical Society* **2008,** 130, (32), 10697-10701.

23. Stankovich, S.; Dikin, D. A.; Piner, R. D.; Kohlhaas, K. A.; Kleinhammes, A.; Jia, Y.; Wu, Y.; Nguyen, S. T.; Ruoff, R. S. *Carbon* **2007,** 45, (7), 1558-1565.

24. Li, D.; Muller, M. B.; Gilje, S.; Kaner, R. B.; Wallace, G. G. *Nature Nanotechnology* **2008,** 3, (2), 101-105.

25. Stankovich, S.; Piner, R. D.; Chen, X.; Wu, N.; Nguyen, S. B. T.; Ruoff, R. S. *Journal of Materials Chemistry* **2006,** 16, 155-158.

26. Stankovich, S.; Piner, R. D.; Nguyen, S. T.; Ruoff, R. S. *Carbon* **2006,** 44, (15), 3342-3347.

27. Moniruzzaman, M.; Winey, K. I. *Macromolecules* **2006,** 39, (16), 5194-5205.

28. Bryning, M. B.; Milkie, D. E.; Islam, M. F.; Kikkawa, J. M.; Yodh, A. G. *Applied Physics Letters* **2005,** 87, 161909.

29. Paul, D. R.; Robeson, L. M. *Polymer* **2008,** 49, (15), 3187-3204.

30. Kim, H.; Miura, Y.; Macosko, C. W. *Chemistry of Materials* **2010,** 22, (11), 3441-3450.

31. Sinha Ray, S.; Okamoto, M. *Progress in Polymer Science* **2003,** 28, (11), 1539-1641.

32. Jeong, H.-K.; Lee, Y. P.; Jin, M. H.; Kim, E. S.; Bae, J. J.; Lee, Y. H. *Chemical Physics Letters* **2009,** 470, (4-6), 255-258.

33. Kim, H.; Macosko, C. W. *Macromolecules* **2008,** 41, (9), 3317-3327.

34. Kim, H.; Macosko, C. W. *Polymer* **2009,** 50, (15), 3797-3809.

35. Potts, J. R.; Murali, S.; Zhu, Y.; Zhao, X.; Ruoff, R. S. *Macromolecules* **2011,** 44, 6488-6495.

36. Potts, J. R.; Lee, S. H.; Alam, T. M.; An, J.; Stoller, M. D.; Piner, R. D.; Ruoff, R. S. *Carbon* **2011**, DOI: 10.1016/j.carbon.2011.02.023.

37. Zhan, Y. H.; Wu, J. K.; Xia, H. S.; Yan, N.; Fei, G. X. *Macromolecular Materials and Engineering* **2011,** 296, 590-602.

38. Ramanathan, T.; Abdala, A. A.; Stankovich, S.; Dikin, D. A.; Herrera-Alonso, M.; Piner, R. D.; Adamson, D. H.; Schniepp, H. C.; Chen, X.; Ruoff, R. S.; Nguyen, S. T.; Aksay, I. A.; Prud'homme, R. K.; Brinson, L. C. *Nature Nanotechnology* **2008,** 3, (6), 327-331.

39. Kai, W.; Hirota, Y.; Hua, L.; Inoue, Y. *Journal of Applied Polymer Science* **2008,** 107, 1395-1400.

40. Fu, X.; Qutubuddin, S. *Polymer* **2001,** 42, (2), 807-813.

41. Schaefer, D. W.; Justice, R. S. *Macromolecules* **2007,** 40, (24), 8501-8517.

42. Rafiee, M. A.; Rafiee, J.; Wang, Z.; Song, H. H.; Yu, Z. Z.; Koratkar, N. *Acs Nano* **2009,** 3, (12), 3884-3890.

43. Hirata, M.; Gotou, T.; Horiuchi, S.; Fujiwara, M.; Ohba, M. *Carbon* **2004,** 42, (14), 2929-2937.

44. Fornes, T. D.; Paul, D. R. *Polymer* **2003,** 44, (17), 4993-5013.

45. Chen, D.; Zhu, H.; Liu, T. *ACS Applied Materials & Interfaces*, DOI: 10.1021/am1008437.

46. Krishnamoorti, R.; Yurekli, K. *Current Opinion in Colloid & Interface Science* **2001,** 6, 464-470.

47. Chen, H.; Müller, M. B.; Gilmore, K. J.; Wallace, G. G.; Li, D. *Advanced Materials* **2008,** 20, (18), 3557-3561.

48. Pang, H.; Chen, T.; Zhang, G.; Zeng, B.; Li, Z. M. *Materials Letters* **2010,** 64, (10), 2226-2229.

49. Eda, G.; Chhowalla, M. *Nano Letters* **2009,** 9, (2), 814-818.

50. Haggenmueller, R.; Gommans, H. H.; Rinzler, A. G.; Fischer, J. E.; Winey, K. I. *Chemical Physics Letters* **2000,** 330, (3-4), 219-225.

51. Lee, C.; Wei, X.; Kysar, J. W.; Hone, J. *Science* **2008,** 321, (5887), 385-388.

52. Paci, J. T.; Belytschko, T.; Schatz, G. C. *Journal of Physical Chemistry C* **2007,** 111, 18099-18111.

53. Gómez-Navarro, C.; Burghard, M.; Kern, K. *Nano Letters* **2008,** 8, (7), 2045-2049.

54. Wakabayashi, K.; Pierre, C.; Dikin, D. A.; Ruoff, R. S.; Ramanathan, T.; Brinson, L. C.; Torkelson, J. M. *Macromolecules* **2008,** 41, (6), 1905-1908.

55. Brune, D. A.; Bicerano, J. *Polymer* **2002,** 43, 369-387.

56. Boehm, H. P.; Clauss, A.; Fischer, G.; Hofmann, U. In *Surface Properties of Extremely Thin Graphite Lamellae*, Proceedings of the Fifth Conference on Carbon, 1962; 1962.

57. Pukánszky, B.; Fekete, E., *Adhesion and surface modification*. Springer: 1999; Vol. 139, p 109-153.

58. Lv, C.; Xue, Q.; Xia, D.; Ma, M.; Xie, J.; Chen, H. *Journal of Physical Chemistry C* **2010,** 114, (14), 6588-6594.

59. Kluppel, M., *The Role of Disorder in Filler Reinforcement of Elastomers on Various Length Scales*. Springer: 2003; Vol. 164, p 86.

60. Wagner, H. D.; Vaia, R. A. *Materials Today* **2004,** 7, (11), 38-42.

61. Schadler, L. S.; Giannaris, S. C.; Ajayan, P. M. *Applied Physics Letters* **1998,** 73, (26), 3842-3844.

62. Liu, H.; Brinson, L. C. *Composites Science and Technology* **2008,** 68, (6), 1502-1512.

63. Balandin, A. A.; Ghosh, S.; Bao, W.; Calizo, I.; Teweldebrhan, D.; Miao, F.; Lau, C. N. *Nano Letters* **2008,** 8, (3), 902-907.

64. Ghosh, S.; Calizo, I.; Teweldebrhan, D.; Pokatilov, E. P.; Nika, D. L.; Balandin, A. A.; Bao, W.; Miao, F.; Lau, C. N. *Applied Physics Letters* **2008,** 92, 151911.

65. Seol, J. H.; Jo, I.; Moore, A. L.; Lindsay, L.; Aitken, Z. H.; Pettes, M. T.; Li, X.; Yao, Z.; Huang, R.; Broido, D.; Mingo, N.; Ruoff, R. S.; Shi, L. *Science* **2010,** 328, (5975), 213-216.

66. Yu, A.; Ramesh, P.; Sun, X.; Bekyarova, E.; Itkis, M. E.; Haddon, R. C. *Advanced Materials* **2008,** 20, (24), 4740-4744.

67. Lin, W.; Zhang, R.; Wong, C. P. *Journal of Electronic Materials* **2010,** 39, (3), 268-272.

68. Kalaitzidou, K.; Fukushima, H.; Drzal, L. T. *Carbon* **2007,** 45, (7), 1446-1452.

Chapter 3:

Thermomechanical Properties of Chemically Modified Graphene/Poly(methyl methacrylate) Nanocomposites

3.1. INTRODUCTION

Chemical compatibility between the polymer matrix and the nanofiller in a polymer nanocomposite is an important consideration for achieving desired property improvements. Incompatibility between the phases may make effective filler dispersion difficult and could also inhibit stress transfer from the polymer to the filler, which would be detrimental to reinforcement. An open question in the field of graphene/polymer nanocomposites is the extent to which platelet surface chemistry affects the nanocomposite properties. The result may depend on a host of different factors, such as the identity of the polymer, method of dispersion, and the chemical functionality present on the platelets. One goal of the work done in this Chapter was to provide insight to this problem by comparing the property improvements produced by hydrazine-reduced graphene oxide (RG-O) and graphene oxide (G-O) when dispersed into poly(methyl methacrylate) (PMMA), which was chosen as a model polymer matrix. Specifically, the filler morphologies and changes in the thermomechanical properties of the nanocomposites were the focus of this study.

An *in situ* polymerization method was used to produce the G-O and RG-O/PMMA nanocomposites. Originally, attempts were made to incorporate dried-down

RG-O powder, produced by hydrazine reduction of G-O platelets without steric or electronic stabilization, directly into PMMA via melt compounding. However, the resulting nanocomposites showed poor dispersion by X-ray scattering and much lower mechanical property enhancements than nanocomposites made by *in situ* polymerization. Thus, in an attempt to facilitate the dispersion of exfoliated graphene platelets, an *in situ* solution polymerization approach was pursued. Previous work has reported that GO can be intercalated with monomer or polymer, and that polymerization in the presence of GO can exfoliate the platelets. For instance, an exfoliated nanocomposite morphology was observed by intercalation of GO with a poly(ethylene oxide) macroinitiator prior to a solution-based free radical polymerization of methyl methacrylate; however, the GO was not exfoliated at all prior to polymerization.[1] Motivated by these results, it was thought that nanocomposites produced via *in situ* polymerization may have a homogeneous, isotropic dispersion of monolayer graphene platelets, as such a level of dispersion is often desired to maximize reinforcement of the polymer.[2] In addition to providing an exfoliated morphology, *in situ* polymerization would provide a convenient method for production of G-O and RG-O-filled PMMA for a comparative study of filler surface chemistry.

3.2. MATERIALS AND METHODS

SP-1 graphite (Bay Carbon), DMF (Aldrich), hydrazine monohydrate (Aldrich), and benzoyl peroxide (Aldrich) were all used as received. Methyl methacrylate (MMA; Aldrich, 99%) was vacuum filtered over alumina powder (Polysciences) to remove the polymerization inhibitor prior to use.

GO was prepared via a modified Hummers method[3] and dried for a week under vacuum. GO was then suspended in DMF (0.5 mg/ml) and exfoliated by ultrasonication (VWR B2500A-MT bath sonicator) at room temperature. The G-O platelet/DMF suspension was purged with dry nitrogen for 20 min. Filtered MMA monomer (0.2 mol) and benzoyl peroxide initiator (0.6 mmol) were added to the suspension, and then the mixture was heated to 80 °C to promote polymerization (under N_2). The reaction mixture was maintained at 80 °C until the mixture became viscous (typically 6 h). For RG-O/PMMA composites, after the polymerization was completed and while the polymer was in solution, reduction of the graphene oxide was carried out with hydrazine (1 μl per 3 mg GO) at 80 °C for 24 h. The product was then added slowly to vigorously stirred ethanol (5 : 1 with respect to the amount of DMF used) and vacuum filtered to collect the product. The filtered composite was washed with ethanol (1 : 5 ratio of DMF : ethanol) and dried under vacuum for 48 h to obtain dried flakes of composite. For use as a control sample, neat PMMA was made following the same synthetic procedure, but without G-O or RG-O platelets.

For dynamic mechanical testing, the nanocomposite flakes were ground into powder by mortar and pestle and molded into samples for testing using a hydraulic hot press (Fred S. Carver, Inc.) at 3.5 MPa and 220 °C for 10 min, using shims to control the thickness, resulting in films with a thickness of approximately 0.2 mm. The thickness of the specimen along the lateral dimension of the specimen was found to vary by approximately ±5 μm, and ~0.2 mm films could be repeatably produced across all

loadings. From the disc, samples were cut using a razor blade into small strips for dynamic mechanical testing.

Nanocomposites were also processed by injection molding for tensile testing experiments. The composite flakes (~3 g per specimen) were fed into a twin-screw DSM microcompounder (mixing chamber volume 5 ml) prior to injection molding. For all microcompounded composite samples (only those which were injection molded), the melt mixing temperature was 220 °C, with a screw speed of 100 rpm. The flakes were fed into the mixing chamber with the melt immediately flowing into a mold barrel at 230 °C and then finally injected into an ASTM D638 Specimen Type V mold at 50 MPa and 100 °C. Samples were then retrieved and set aside for conditioning at room temperature for at least 48 h prior to testing.

The viscoelastic response of the nanocomposites was measured using dynamic mechanical analysis (DMA Q800, TA Instruments). For fixed-frequency temperature scans, dynamic loading was applied at 1 Hz at 0.02% linear strain with a 0.01 N tensile force preload and a temperature ramp rate of 2 °C/min. DSC (Mettler Toledo) was performed using a ramp rate of 10 °C/min under flowing N_2 in hermetically-sealed pans. TGA (TGA4000, Perkin Elmer) was used to observe changes in thermal degradation behavior versus the neat polymer, using a ramp rate of 10 °C/min with N_2 as the sample purge gas (purge rate: 20 ml/min). For mechanical testing of the injection molded nanocomposite samples, a single pre-wired resistive strain gage (Vishay, #307441) was bonded to the thin section of the specimen. Tensile testing was performed using an Instron machine using a strain rate of 1%/min.

AFM images were recorded on a Park Scientific AutoProbe CP/MT (MultiTask) instrument with scans obtained in contact mode. Elemental analysis by combustion was performed by Atlantic Microlab, Norcross, GA, USA.

Wide-angle X-ray scattering (WAXS) studies were done using a Philips X-PERT diffractometer using Cu Kα radiation. A generating voltage of 40 kV and a current of 30 mA was used, with a 2 s dwell time. Transmission electron microscopy (TEM) and scanning electron microscopy (SEM) were used to image the morphology of the nanocomposites. For TEM, injection molded nanocomposites were microtomed to slices of 50 to 90 nm thickness using an ultra45 diamond blade (Leica Ultracut UCT, Reichert Inc.) and dropped onto standard copper TEM grids. The TEM images were acquired on a JEOL 2010F at 120 keV. SEM samples were prepared by sputter coating fractured compression molded samples using a 6 nm coating of iridium metal deposited in an Ar atmosphere. Images were acquired using a FEI Quanta-600 FEG Environmental SEM at 5 keV and 10^{-5} torr.

^{1}H and ^{13}C solution NMR was performed using a Bruker DRX400 at 399.97 and 100.54 MHz, respectively. Neat, as-made PMMA and nanocomposites were dissolved in $CDCl_3$ (~5 mg/ml) and spectra were obtained at 50 °C using a 5 mm broadband probe at 50 °C using standard pulse sequences. The ^{1}H and ^{13}C chemical shifts were all referenced to residual solvent resonances within the $CDCl_3$ solvent. Solid state ^{13}C magic angle spinning (MAS) NMR was carried out on the neat PMMA, G-O/PMMA, and RG-O/PMMA nanocomposites using a Bruker Avance400 at 100.62 MHz. Spectra were obtained using a standard cross polarization (CP) MAS sequence with variable contact

times, at room temperature with spinning at speeds between 4 and 10 kHz. The ^{13}C chemical shifts were referenced to a secondary standard glycine setting the carbonyl resonance at 176.0 ppm with respect to TMS, $\delta = 0$ ppm. FT-IR measurements were obtained using a Perkin-Elmer BX spectrometer. GPC measurements were made at ambient temperature on a home-built system equipped with a Waters Model 510 HPLC pump, two fluorinated polystyrene columns (IMBHW-3078 and I-MBLMW-3078) arranged in series, and a Waters 486 Tunable Absorbance Detector ($\lambda = 450$ nm). Molecular weight and polydispersity data are reported relative to polystyrene standards in tetrahydrofuran.

3.3. FILLER STRUCTURE

GO was produced by a modified Hummers method and was determined to have a C : O ratio of 1.24 (including contribution from water) as measured by elemental combustion analysis. GO was sonicated in DMF at 0.5 mg/ml for 1 h to create a suspension of G-O platelets. It has been previously reported that G-O can form a stable dispersion in DMF;[4] however, even at 0.5 mg/ml, some sedimentation was observed in the suspension after sitting overnight. Atomic force microscopy (AFM) was conducted on the dried-down platelets after deposition of a diluted G-O suspension onto a mica substrate, as shown in Figure 3.1. Based on the AFM images, the suspensions made by sonication in DMF consisted of mostly single-layer G-O platelets, along with some larger multi-layer platelets and also larger particles that were not exfoliated. The single-layer platelets appeared to have a large range of lateral dimensions, ranging from microns to

tens of nanometers. Thus, AFM suggests that mostly single-layer platelets were dispersed into the polymer, although restacking could potentially occur upon dispersion.

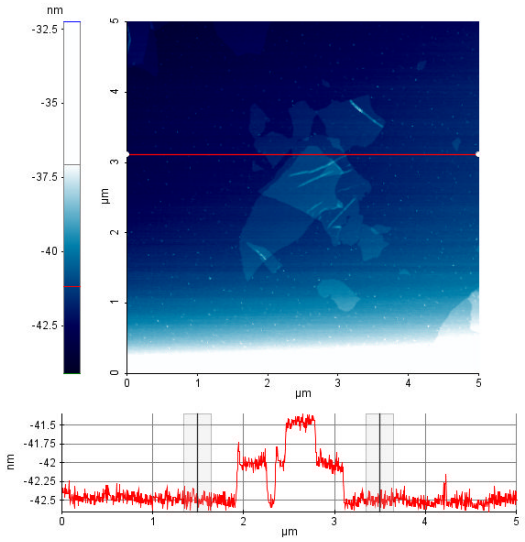

Figure 3.1. Atomic force microscopy scans of dried down platelets on freshly-cleaved mica revealed the presence of single-layer platelets in the G-O/DMF dispersion (exfoliated at 0.5 mg/ml), with a large distribution of lateral dimensions.

3.4. NANOCOMPOSITE MORPHOLOGY

In this study, the G-O platelets dispersed in the polymer solution were reduced with hydrazine monohydrate prior to precipitating the polymer out of solution. As previously mentioned, reduction of G-O platelets in the presence of a polymer has been reported to stabilize the platelets against agglomeration.[5] Indeed, this was found to be the case at lower loadings, based upon the analysis of filler dispersion presented below. As seen in Figure 3.2, visual inspection of nanocomposite powders shows a difference

between the RG-O and G-O/PMMA nanocomposites akin to the difference in appearance of isolated RG-O platelets and GO.

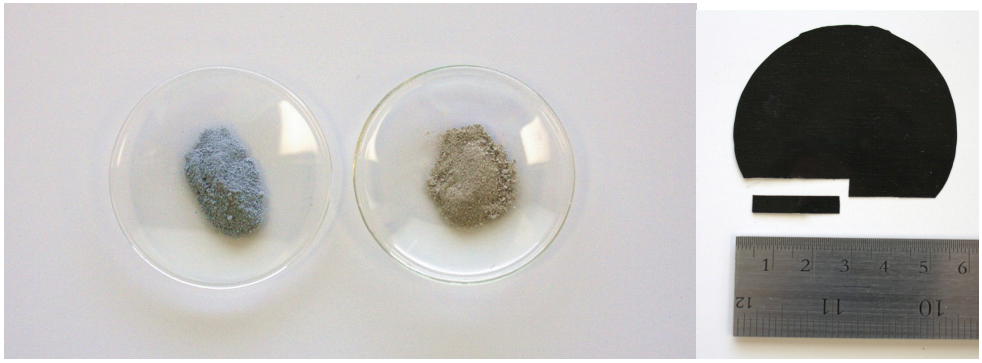

Figure 3.2. RG-O/PMMA composite powder (left watchglass) and G-O/PMMA composite powder (right watchglass) prior to processing steps, showing the difference in appearance due to chemical reduction of the G-O platelets. Compression molding of powder produced thin disks of composite material from which samples were cut for DMA testing.

It was also of interest to characterize the degree of reduction of G-O platelets as a result of processing.[6] Since G-O platelets are thermally unstable (due to evolution of small molecule species such as CO_2) and have been shown to be thermally reduced when exposed to temperatures as low as 150 °C,[7] it was of interest to investigate G-O platelet reduction as a result of processing (molding and compounding steps) which are of sufficiently high temperature to drive reduction of the platelets. For this study, an injection-molded 4 wt% G-O/PMMA specimen (~1.5 g) was immersed in DMF and stirred at room temperature until the solid was completely dissolved and the mixture appeared black. The mixture was centrifuged and the polymer solution was decanted off. The remaining solid was dispersed into DMF, and then passed through a 0.2 μm

polycarbonate membrane to isolate the platelets. The collected solids, black in color, were washed with copious amounts of ethanol followed by acetone, then dried under vacuum at room temperature at 48 h to remove residual solvent, yielding approximately 30 mg of solid. A TGA scan of this material is compared with that of neat GO and RG-O in Figure 3.3. The results suggest that the platelets are significantly reduced the microcompounding/injection molding process; the inflection near 270 °C may be due to residual PMMA. This is in agreement with recent work by Glover and co-workers, who studied time-temperature characteristics of reduction of G-O platelets in various polymer matrices and found that significant reduction occurs upon heating beyond 220 °C irrespective the composition of the polymer matrix.[6]

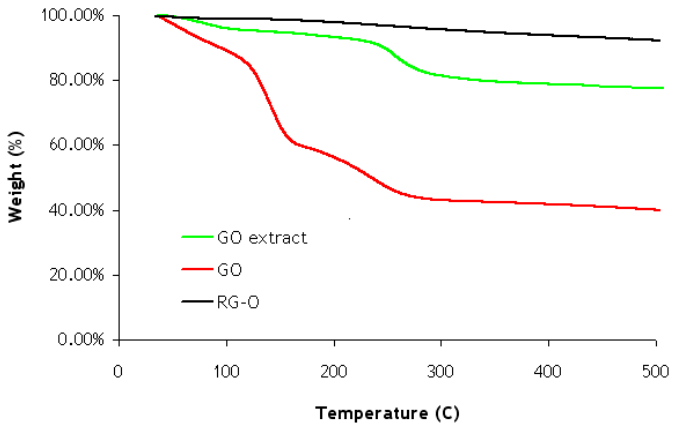

Figure 3.3. TGA curves for reduced graphene oxide (RG-O), graphite oxide (GO), and G-O platelets extracted from a PMMA/G-O composite (GO extract) after melt processing and injection molding.

The exfoliation of the platelets and the level of platelet dispersion achieved in the composites were probed by TEM and WAXS. TEM images of microtomed sections of

the nanocomposites are shown in Figure 3.5. While AFM analysis of the dried-down G-O dispersion suggests single-layer platelets may be dispersed in the matrix, they were not directly observed in the TEM analysis. Many few-layer platelets were observed and were sparsely dispersed throughout the matrix, with a wide distribution of lateral dimensions: many had lengths of hundreds of nanometers, while other platelets appeared to be several microns long. The ultrasonication process used to exfoliate GO also fragments the platelets, and is likely responsible for the small lateral dimensions of many of the platelets.[8] No difference in the level of filler dispersion or exfoliation was observed between G-O and RG-O-filled nanocomposites at 0.5 wt%, suggesting that at low loadings the reduction process does not lead to significant agglomeration of the platelets. However, at higher loadings (4 wt%), the nanocomposites appeared to show an increased number of multi-layer platelets with a larger average thickness (lower aspect ratio). Low magnification TEM images clearly showed orientation of the multi-layer tactoids in the matrix, likely due to the injection molding process.

For both G-O and RG-O filled nanocomposites, nearly all of the platelets showed a crumpled or wrinkled conformation, with some multi-layer platelets showing a corrugated structure. Although the dispersion of graphene platelets in a polymer matrix can be imaged in TEM without staining, contrast was often very low, and thus it was a challenge to ascertain the level of dispersion just from TEM observation, due to the difficulty of observing few-layer platelets at lower magnification. WAXS was performed to further analyze the state of dispersion of the nanocomposite, as shown in Figure 3.4.

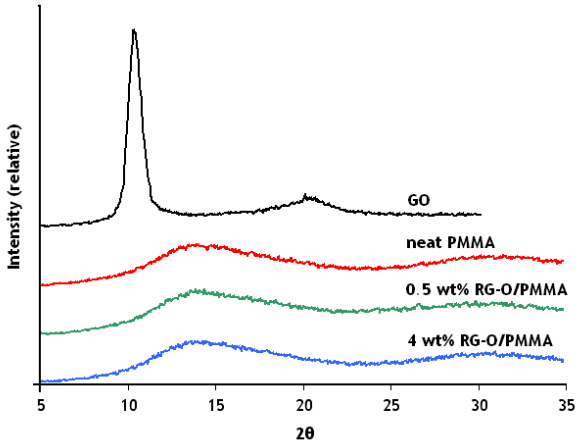

Figure 3.4. Wide angle X-ray scattering patterns of the nanocomposites. No presence of layered GO was detected at any loading, suggesting an exfoliated morphology.

The scattering intensity profile revealed no presence of diffraction peaks corresponding to the interlayer spacing of GO, suggesting an exfoliated morphology of both types of platelets in PMMA across all loadings. However, the lack of a diffraction peak in the WAXS pattern does not necessarily suggest the absence of stacked platelets,[9] as confirmed by TEM observation. This is likely because the relatively low volume percent of filler (approximately 4 vol% at the highest loading)—a fraction of which may exist as multi-layer stacks—contributes little to the scattering signal relative to the PMMA matrix. Additionally, the fracture surfaces of the nanocomposites were analyzed using SEM. The fracture surfaces were examined for the presence of filler "pull-out," as has been previously reported as evidence for matrix-filler interfacial adhesion for TEGO/PMMA nanocomposites.[10] However, PMMA is an insulating polymer and

charging on the surface of the composite prevented resolution of the cross section down to the platelet level in this study. Qualitative observations made of the fracture surface at lower magnifications suggested a cup-cone fracture mechanism for neat PMMA versus the nanocomposites, which all showed brittle fracture surfaces (Figure 3.6).

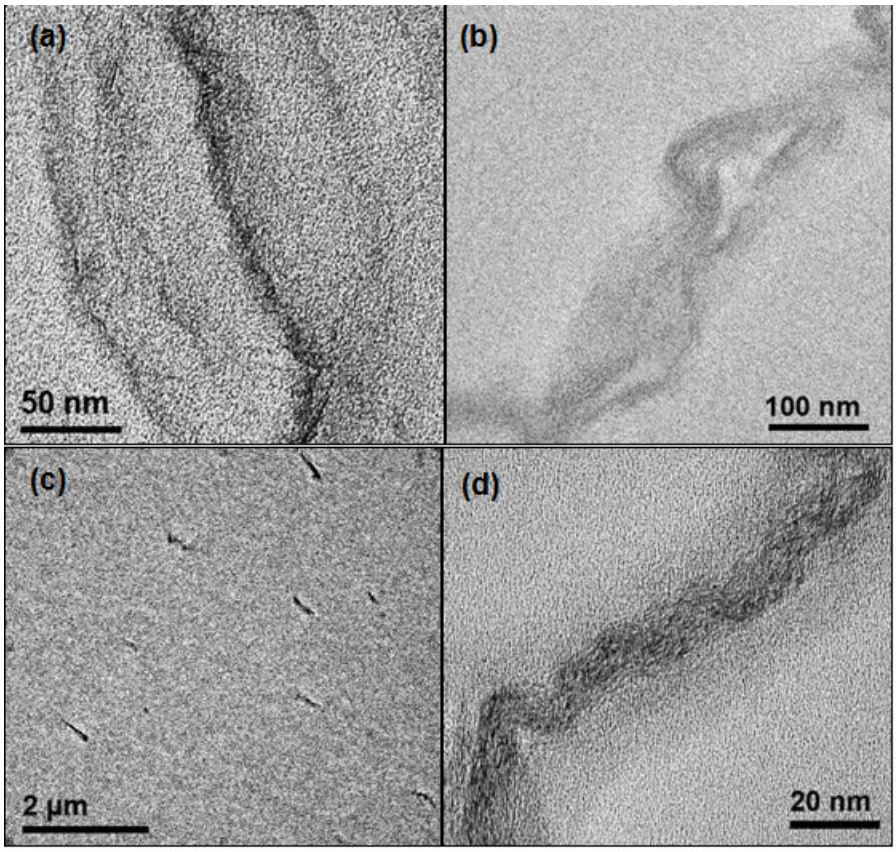

Figure 3.5. TEM images of (a) 0.5 wt% RG-O in PMMA and (b) 4 wt% RG-O in PMMA, showing the presence of multi-layer platelets with a crumpled morphology.

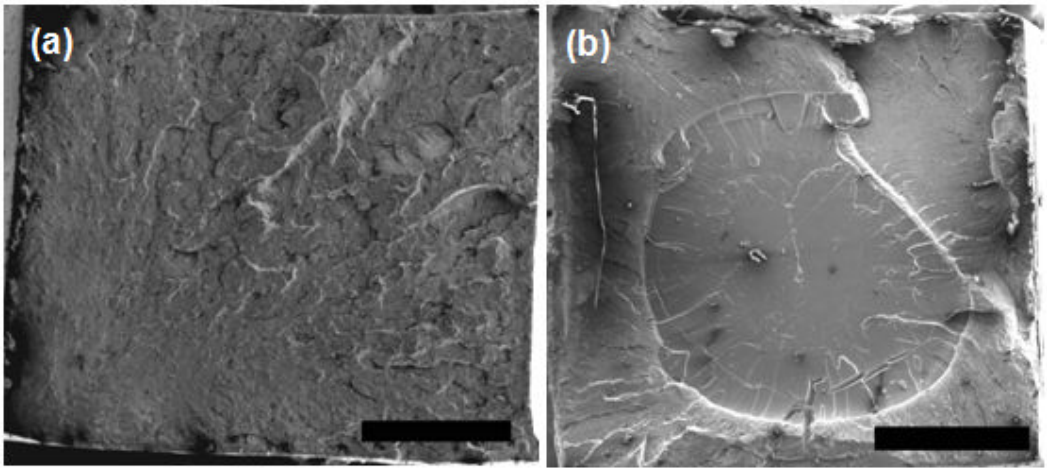

Figure 3.6. SEM images of the fracture surfaces of the nanocomposites showing (a) 2 wt% G-O/PMMA and (b) neat PMMA, showing a more brittle fracture for the composite in contrast with the cup-cone fracture of the neat polymer (scale bar = 1 mm).

3.5. Analysis of Polymer Structure

Attempts were made to characterize any change in polymer structure with nanofiller loading to investigate whether the property improvements of the nanocomposites were influenced by possible changes in polymer structure which may have been caused by the presence of G-O platelets during polymerization. To this end, FT-IR, GPC, and solution and solid-state NMR studies were performed (NMR measurements conducted by Todd Alam at Sandia National Laboratories, Albuquerque, NM). The FT-IR spectra of the nanocomposites were dominated by the polymer and no change in the spectrum was noted between neat PMMA, G-O/PMMA, or RG-O/PMMA nanocomposites.

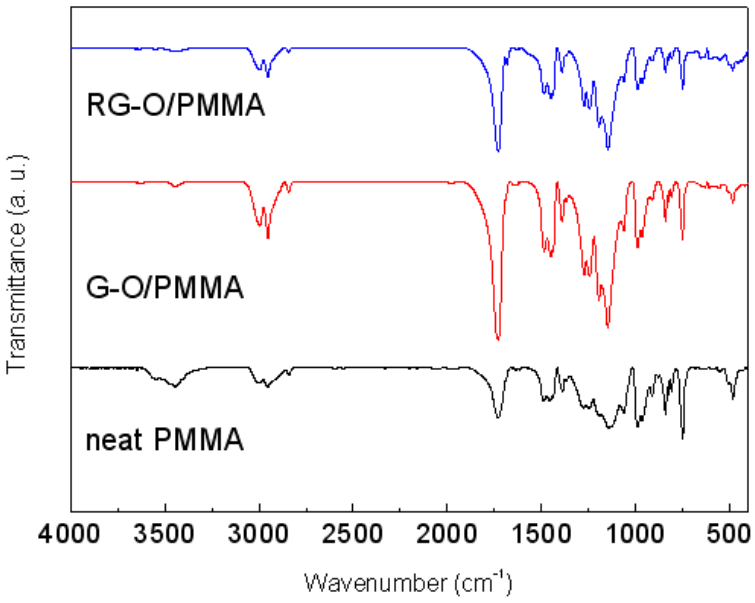

Figure 3.7. FT-IR spectra of neat PMMA compared with 2 wt% G-O/PMMA and 2 wt% RG-O/PMMA samples.

Also, no differences in the NMR spectra were observed between neat PMMA and the nanocomposites. GPC measurements indicated that the molecular weight of the nanocomposites increased slightly with higher loadings of graphene filler (Table 3.1). Figures 3.8 through 3.11 show both ^{1}H and ^{13}C solution NMR spectra of the neat PMMA and PMMA nanocomposites. NMR revealed that the dominant triad tacticity of the PMMA to be rr (syndiotactic), and tacticity of the PMMA was found to be the same for the neat, and 8 wt% RG-O/PMMA and 8 wt% G-O/PMMA samples, indicating no change in tacticity with loading of nanofiller (Table 3.2). No presence of the G-O platelets was detected in the NMR spectra.

Table 3.1. Molecular weight and polydispersity index of the neat PMMA and nanocomposites at various loadings, as measured by gel permeation chromatography.

Sample	M_w	M_w/M_n
Neat PMMA	200,900	2.06
0.05 wt% G-O/PMMA	187,500	2.09
0.25 wt% G-O/PMMA	191,600	2.17
1 wt% G-O/PMMA	179,500	1.71
2 wt% G-O/PMMA	217,400	2.38
8 wt% G-O/PMMA	280,600	1.76

Table 3.2. Tacticity ratios for neat, 8 wt% G-O/PMMA and 8 wt% RG-O/PMMA samples based on integration of the carbonyl region in the ^{13}C NMR solution spectra.

Sample	[rr] %	[mr] %	[mm] %
Neat PMMA	59.6	37.1	3.3
8 wt% G-O/PMMA	56.9	39.0	4.1
8 wt% RG-O/PMMA	60.2	35.3	4.3

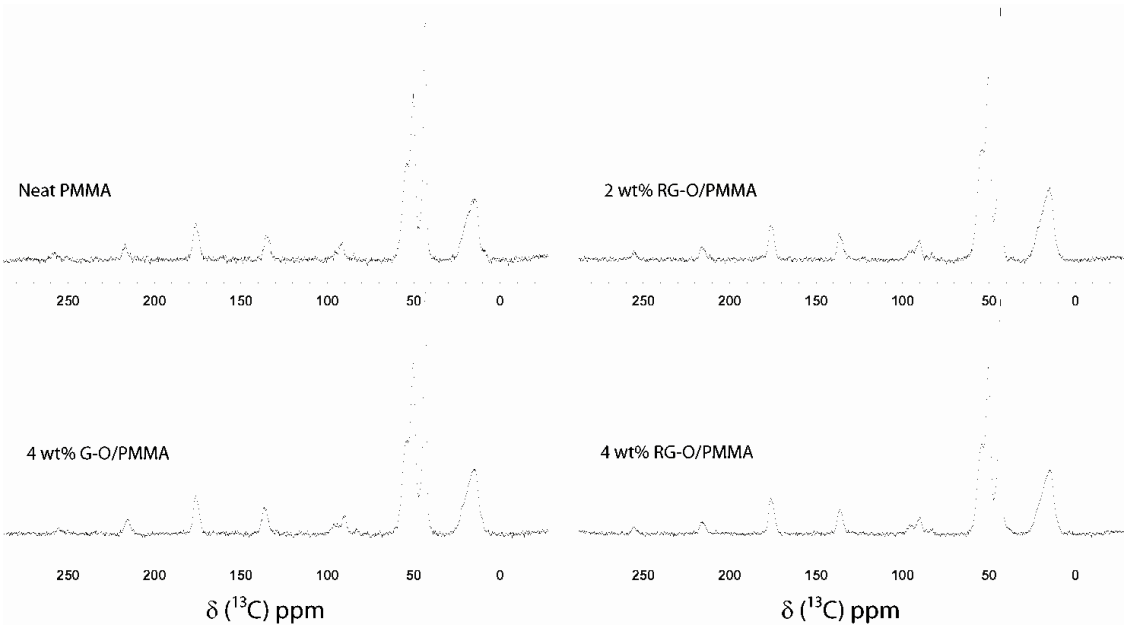

Figure 3.8. Representative solid state ^{13}C CPMAS NMR spectra of the PMMA nanocomposites (asterisks indicate spinning sidebands).

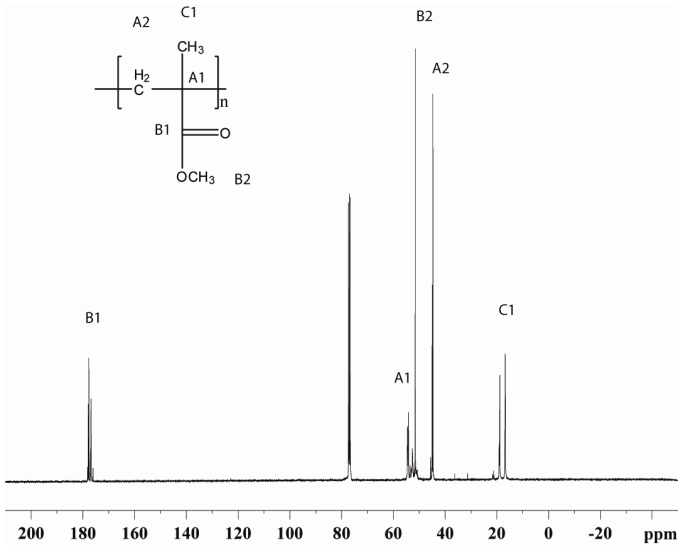

Figure 3.9. Solution ^{13}C NMR ($CDCl_3$) of neat PMMA made by free radical polymerization.

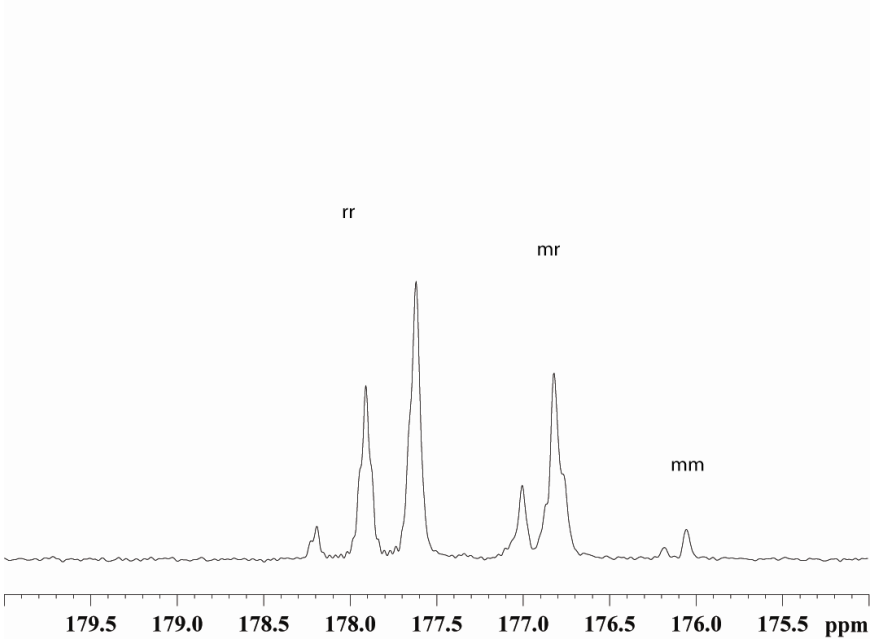

Figure 3.10. Fine structure due to the tacticity from the solution ^{13}C NMR spectrum. The dominant triad tacticity is rr (racemic) which indicates a syndiotactic polymer.

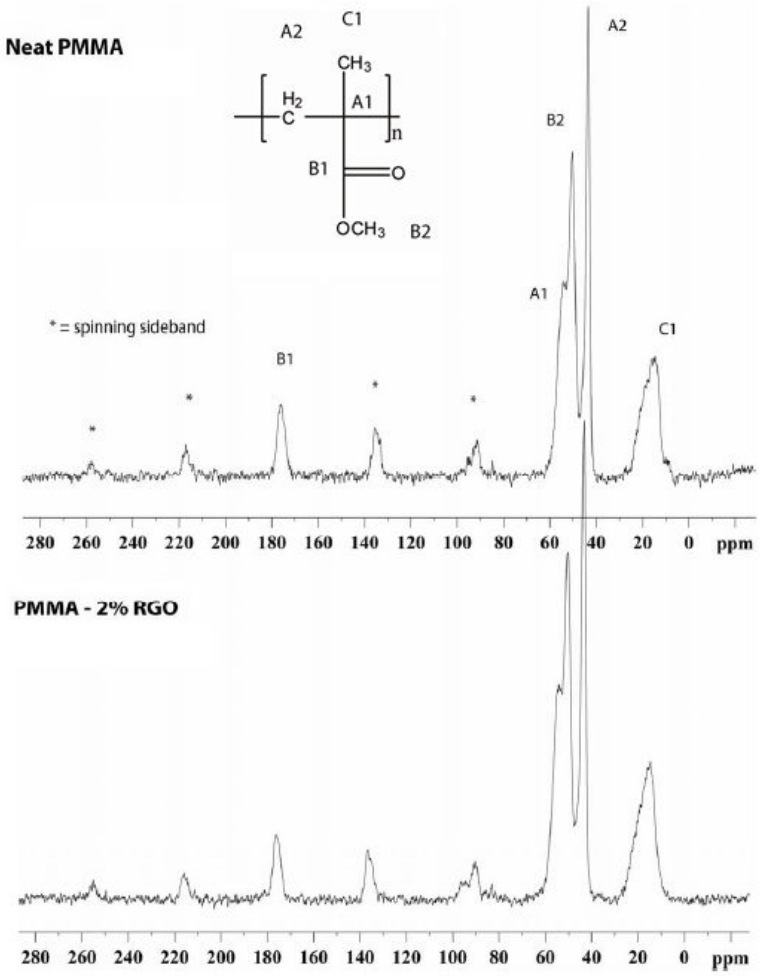

Figure 3.11. Assignment of the solid state ^{13}C CPMAS NMR spectra of neat PMMA compared with that of 2 wt% RG-O/PMMA.

3.6. NANOCOMPOSITE THERMOMECHANICAL PROPERTIES

Results from DMA experiments on the G-O/PMMA and RG-O/PMMA nanocomposites suggested that the glass transition temperatures (T_g) of the nanocomposites were shifted substantially relative to neat PMMA. The modulus values also showed increases compared with neat PMMA, indicating reinforcement (see Figure

3.12), which is consistent with results from tensile testing (presented below). The RG-O/PMMA nanocomposites show shifts in T_g of more than 15 °C at loadings down to 0.05 wt%, with only small increases in T_g beyond this loading. Notably, an increase in the area under the loss modulus peak (*E"*) was observed at higher loadings, possibly suggesting increased segmental mobility in the nanocomposites at T_g versus neat PMMA. Large shifts in the T_g of PMMA at low loadings of graphene-based filler have been reported elsewhere.[10] While this study shows a similar onset of a large T_g shift to previous work on TEGO/PMMA nanocomposites,[10] the incremental changes in T_g were much lower in this study. Moreover, even after numerous attempts, the large shifts in T_g observed by DMA were not replicated using DSC, which showed no increase in T_g even up to 4 wt% (see Figure 3.13). This could simply be an artifact of the different physics in the DSC and DMA measurements, and more recent work suggests that graphene platelets have little effect on the T_g of polymer materials and large T_g shifts may be influenced by other factors.†

† This issue is discussed further in Chapter 8 as results from follow-up DMA experiments on these G-O/PMMA and RG-O/PMMA nanocomposites are shared. Briefly, much smaller T_g shifts were observed (2-5 ºC) which could potentially be attributed to aging effects or error/bias in the original measurements.

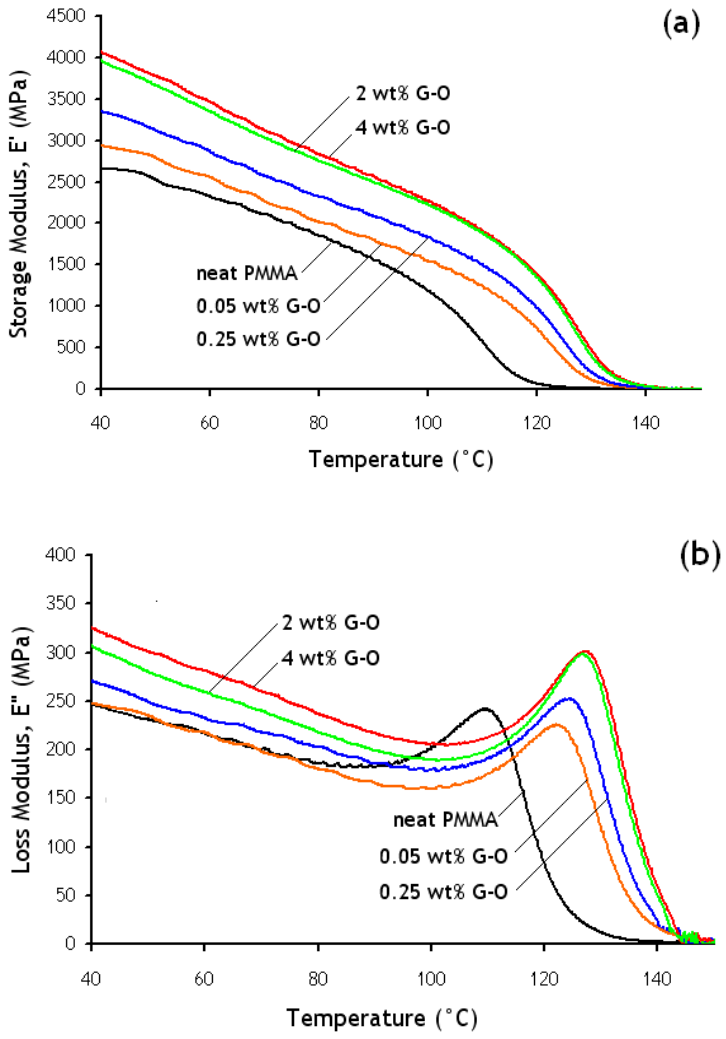

Figure 3.12. (a) Storage modulus and (b) loss modulus versus temperature for neat PMMA and G-O/PMMA nanocomposites as measured by DMA.

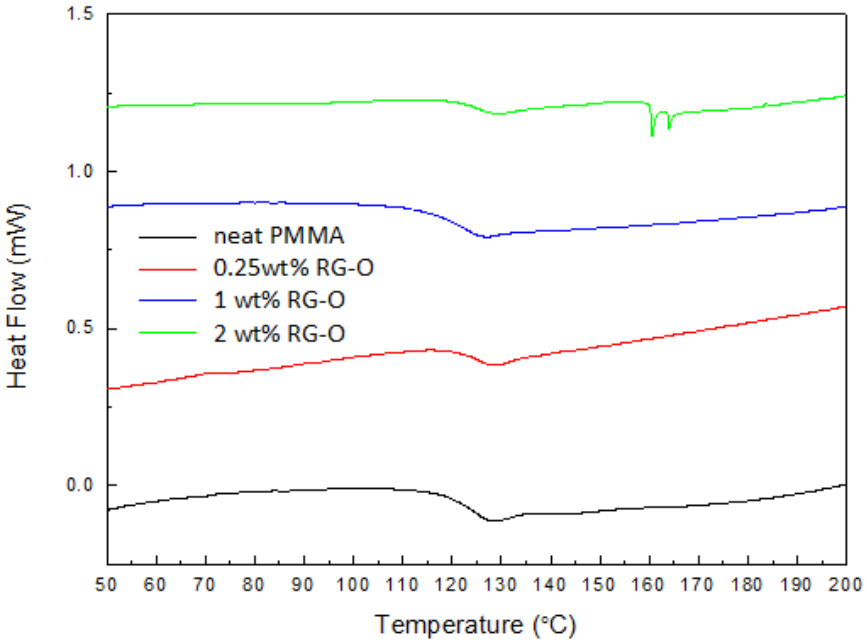

Figure 3.13. DSC scans of RG-O/PMMA nanocomposites show no shift in the T_g of the nanocomposites versus neat PMMA, contrary to DMA measurements (data from second heat shown).

G-O and RG-O platelets were found to have a significant reinforcing effect at low loadings, which tapered off at higher loadings. Table 3.3 summarizes all data obtained from tensile testing, and Figure 3.14 plots the modulus of the nanocomposites as a function of filler loading. For reference, the experimental data is compared with modulus predictions based on Mori-Tanaka theory[11, 12] which assumes unidirectional, ellipsoidal platelets and neglects possible contribution of the interphase.[13] The moduli and Poisson's ratios of the platelets and the polymer matrix, as well as the aspect ratio of the platelets, can then be used to estimate the transverse composite modulus. In this study, the

measured modulus for PMMA, made by free radical polymerization as described in the Methods section, was measured to be approximately 3.4 GPa. For calculations of the melt processed nanocomposites, the same parameters were used except for the modulus of the matrix PMMA, which was measured to be 2.4 GPa. Modulus values measured by AFM tip-induced deformation for G-O platelets range from approximately 208 GPa[14] up to 650 GPa[15] while RG-O platelets have been measured to have a modulus of 250 GPa.[15] Thus elastic modulus used for the dispersed RG-O platelets was 250 GPa.[14, 15] Other parameters used was a Poisson's ratio, ν, of PMMA equal to 0.35,[16] and equal to 0.06 for graphite.[9] These parameters can be used to calculate the transverse composite modulus following equations derived by Tandon and Weng[12] presented in Appendix B.

Table 3.3. Results of the tensile testing experiments (three samples were tested at each loading).

RG-O (wt%)	E (GPa)	% change, E	σ (MPa)	% change, σ
0	3.43 ± 0.06	-	58.1 ± 1.95	-
0.25	3.75 ± 0.57	9.5%	59.5 ± 4.25	2.4%
0.5	4.04 ± 0.22	17.8%	59.0 ± 4.75	1.5%
1	4.28 ± 0.17	25.0%	53.0 ± 5.55	-8.8%
2	4.65 ± 0.35	35.8%	57.0 ± 4.55	-1.9%
4	4.56 ± 0.18	33.0%	48.9 ± 1.15	-15.8%
G-O (wt%)	**E (GPa)**	**% change, E**	**σ (MPa)**	**% change, σ**
0.25	3.65 ± 0.06	6.4%	62.1 ± 0.60	6.9%
0.5	4.19 ± 0.03	22.2%	66.4 ± 1.75	14.3%
1	4.39 ± 0.18	28.3%	70.9 ± 0.15	22.0%
2	4.45 ± 0.00	29.9%	66.8 ± 3.05	15.0%
4	4.53 ± 0.32	32.3%	65.4 ± 5.35	12.6%

Thus assuming a value of approximately 250 GPa for both G-O and RG-O platelets, it can be seen from Figure 3.14(b) that a platelet aspect ratio (A_f) of 100 captures the trend in modulus increase quite well up to 1 wt%. However, a significant deviation is apparent at higher loadings. This deviation may be due to agglomeration of filler, which was observed in the TEM analysis (but not by WAXS, as shown in Figure 3.4). Thus, this data in conjunction with Mori-Tanaka theory is evidence for a good dispersion at lower loadings (A_f > 100 assuming a platelet modulus of 250 GPa) which progressively worsens as loading increases (A_f decreasing to approximately 30 at 4 wt% loading).

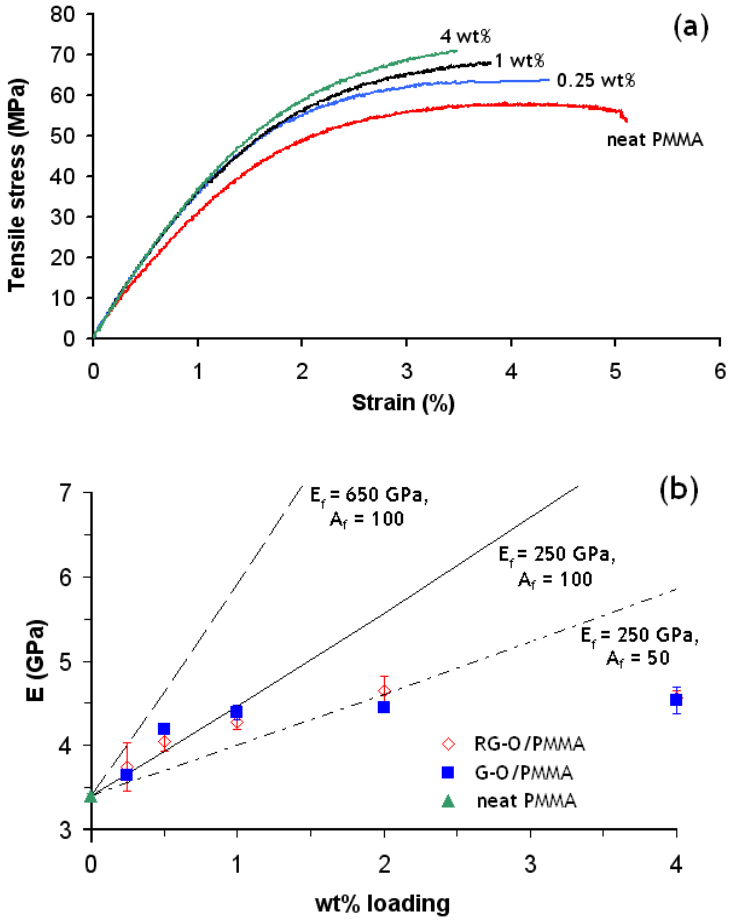

Figure 3.14. (a) Representative stress-strain curves of the nanocomposites (with G-O filler) and (b) average modulus values for G-O and RG-O-filled nanocomposites, plotted versus theoretical modulus values predicted by Mori-Tanaka theory, using various values for the platelet modulus (E_f) and aspect ratio (A_f).

While both types of nanocomposites showed similar increases in elastic modulus, the tensile strengths of the G-O/PMMA nanocomposites were markedly higher than the RG-O/PMMA nanocomposites—while G-O produced increases in tensile strength of more than 20%, RG-O, on average, caused the tensile strength of the nanocomposite to

decrease versus neat PMMA. Since both G-O and RG-O/PMMA nanocomposites showed similar dispersions of filler (at lower loadings) by TEM and WAXS analysis, this difference could perhaps be due, at least in part, to the higher presence of polar functional groups (e.g., hydroxyl, epoxide, and carboxylic acid groups) on the platelet surface, which might facilitate a more intimate contact between G-O and PMMA versus RG-O. Notably, injection molded samples were briefly subjected to microcompounding prior to molding; however, this was found to cause no discernable effect on the dynamic mechanical properties or on the dispersion based on a WAXS study. Representative stress-strain curves of G-O/PMMA nanocomposites, along with neat PMMA, are provided in Figure 3.14. Elongation at break was observed to decrease with increasing weight fraction of both types of filler, consistent with the more brittle fracture surfaces observed by SEM.

3.7. Effect of Processing Approach on Mechanical Properties

The effect of processing was also explored as part of this study. Agglomerated RG-O platelets[17] were produced by hydrazine reduction of an aqueous G-O suspension and dried down to obtain a black, powdery material. This material was directly mixed with PMMA (Polysciences; M_w = 350,000) via melt compounding in a 5 ml DSM Xplore microcompounder with an attached injection molding machine (the same instrument used for the *in situ* polymerized composites), to evaluate whether melt compounding could be used to disperse the agglomerated RG-O powder into PMMA. For this study, all zone temperatures were set to 220 °C with a screw speed of 100 rpm, and a mixer residence

time of 10 min. The extrudates were received into an ASTM mold as previously described for the *in situ* polymerized nanocomposites, and strain gages (Vishay) were attached as described previously.

The results from tensile testing experiments are shown below in comparison with that of the *in situ* polymerized nanocomposites. In addition, an effective platelet aspect ratio was estimated based on Mori-Tanaka theory as done for the *in situ* polymerized samples. As seen in Figure 3.14, the modulus increases of the melt compounded composites were much smaller for a given loading than *in situ* polymerized nanocomposites. Mori-Tanaka theory suggests a much better dispersion of RG-O filler for *in situ* polymerized samples ($A_f \sim 100$ up to 1 wt%) compared with the melt mixed samples ($A_f \sim 15$). Incremental modulus improvements were considerably higher for the *in situ* polymerized nanocomposites: at 1 wt% loading, the *in situ* polymerized RG-O/PMMA nanocomposites showed a 25% modulus increase, whereas the melt mixed RG-O/PMMA nanocomposites showed an 11% modulus increase at 1 wt%. Thus, it is concluded that melt processing is unable to effectively re-disperse agglomerated RG-O platelets into PMMA.

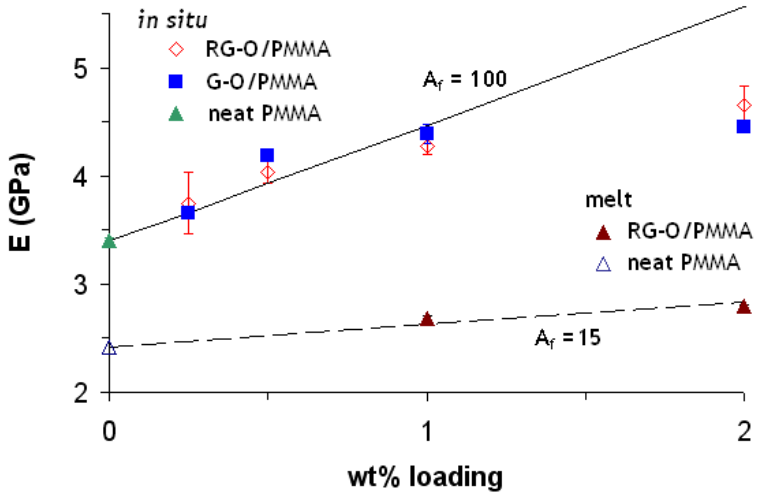

Figure 3.15. Modulus versus loading for *in situ* polymerized composites compared with melt mixed ("melt") RG-O/PMMA nanocomposites. The lines show calculations from Mori-Tanaka theory, allowing estimation of an effective platelet aspect ratio (A_f) to quantify dispersion.

3.8. Electrical Conductivity and Thermal Stability

Electrically conductive graphene/polymer nanocomposites have been widely reported, occasionally at low loadings of filler, such as 0.2 wt% as reported for a functionalized RG-O/polystyrene nanocomposite.[5] Electrically conductive PMMA matrix nanocomposites with graphene-based filler materials have also been reported.[1, 18] In this study, however, the conductivity increases were much less dramatic than have been previously reported. Indeed, at all loadings of both G-O and RG-O (for both hot pressed and injection molded specimens), the electrical conductivity remained sufficiently low such that it could not be determined with a four-probe measurement setup with a detection limit of 200 GΩ.

Graphene platelets have been widely reported to improve the thermal stability of polymer nanocomposites relative to the host polymer.[19] Non-oxidative thermal degradation studies of the composites were performed using thermogravimetric analysis (TGA). Some of these tests are provided in Figure 3.16, where the shift in the onset of the thermal degradation temperature with weight percent loading of graphene platelets is illustrated. Both G-O and RG-O-filled nanocomposites showed similarly significant improvements in the non-oxidative thermal stability compared with neat PMMA.

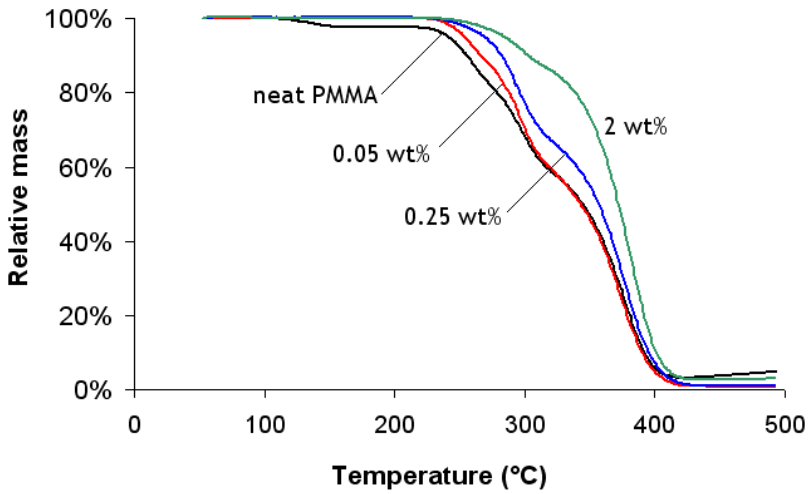

Figure 3.16. TGA curves for the RG-O composites versus neat PMMA, showing increased thermal stability with loading of RG-O. Similar trends were observed for G-O/PMMA composites.

3.9. CONCLUSIONS

Nanocomposites of PMMA were prepared with either G-O or RG-O platelets as filler. The nanocomposites were prepared using melt processing or *in situ* polymerization method and further processed using microcompounding/injection molding or hot pressing. Injection molded samples were subjected to standard tensile testing and showed increases in modulus for both types of PMMA nanocomposites, although only G-O produced an increase in tensile strength. Increases in the dynamic modulus were observed by DMA, which also demonstrated shifts of over 20°C in T_g versus neat PMMA. However, these large T_g shifts were not replicated by DSC measurements, which showed no shift in the T_g at all even at the highest loadings. Spectroscopic studies using FT-IR and NMR along with GPC revealed no evidence of variation in the structure of the polymer with increased filler loading, suggesting that the presence of graphene platelets does not have a major affect on the polymerization process. The results indicate that both RG-O and G-O fillers provide substantial property improvements relative to neat PMMA, although this study suggests that G-O platelets offer the advantage of increased tensile strength whereas RG-O platelets evidently do not. Mori-Tanaka analysis suggested a good dispersion of filler at lower loadings (up to 1 wt%), which progressively worsened at higher loadings. This may be due to agglomeration of the platelets (whether due to incomplete exfoliation and/or platelet restacking) at higher loadings.

3.10. REFERENCES

1. Jang, J. Y.; Kim, M. S.; Jeong, H. M.; Shin, C. M. *Composites Science and Technology* **2009,** 69, (2), 186-191.

2. Paul, D. R.; Robeson, L. M. *Polymer* **2008,** 49, (15), 3187-3204.

3. Hummers, W. S.; Offeman, R. E. *Journal of the American Chemical Society* **1958,** 80, (6), 1339.

4. Paredes, J. I.; Villar-Rodil, S.; Martinez-Alonso, A.; Tascon, J. M. D. *Langmuir* **2008,** 24, (19), 10560-10564.

5. Stankovich, S.; Dikin, D. A.; Dommett, G. H. B.; Kohlhaas, K. M.; Zimney, E. J.; Stach, E. A.; Piner, R. D.; Nguyen, S. T.; Ruoff, R. S. *Nature* **2006,** 442, (7100), 282-286.

6. Glover, A. J.; Cai, M.; Overdeep, K. R.; Kranbuehl, D. E.; Schniepp, H. C. *Macromolecules* **2011,** 44, 9821-9829.

7. Zhu, Y.; Stoller, M. D.; Cai, W.; Velamakanni, A.; Piner, R. D.; Chen, D.; Ruoff, R. S. *ACS Nano* **2010,** 4, (2), 1227-1233.

8. Dreyer, D. R.; Park, S.; Bielawski, C. W.; Ruoff, R. S. *Chemical Society Reviews* **2010,** 39, (1), 228-240.

9. Kim, H.; Macosko, C. W. *Macromolecules* **2008,** 41, (9), 3317-3327.

10. Ramanathan, T.; Abdala, A. A.; Stankovich, S.; Dikin, D. A.; Herrera-Alonso, M.; Piner, R. D.; Adamson, D. H.; Schniepp, H. C.; Chen, X.; Ruoff, R. S.; Nguyen, S.

T.; Aksay, I. A.; Prud'homme, R. K.; Brinson, L. C. *Nature Nanotechnology* **2008,** 3, (6), 327-331.

11. Mori, T.; Tanaka, K. *Acta Metallurgica* **1973,** 21, 571-574.

12. Tandon, G. P.; Weng, G. J. *Polymer Composites* **1984,** 5, 327-333.

13. Fornes, T. D.; Paul, D. R. *Polymer* **2003,** 44, (17), 4993-5013.

14. Suk, J. W.; Piner, R. D.; An, J.; Ruoff, R. S. *ACS Nano* **2010,** 4, 6557-6564.

15. Gómez-Navarro, C.; Burghard, M.; Kern, K. *Nano Letters* **2008,** 8, (7), 2045-2049.

16. Brandrup, J.; Immergut, E. H.; Grulke, E. A.; Abe, A.; Bloch, D. R., *Polymer Handbook*. 4 ed.; John Wiley and Sons: 1999; p 2336.

17. Stankovich, S.; Dikin, D. A.; Piner, R. D.; Kohlhaas, K. A.; Kleinhammes, A.; Jia, Y.; Wu, Y.; Nguyen, S. T.; Ruoff, R. S. *Carbon* **2007,** 45, (7), 1558-1565.

18. Chen, G.; Weng, W.; Wu, D.; Wu, C. *European Polymer Journal* **2003,** 39, (12), 2329-2335.

19. Kim, H.; Abdala, A. A.; Macosko, C. W. *Macromolecules* **2010,** 43, 6515-6530.

Chapter 4:

Preparation, Morphology, and Properties of Microwave-Exfoliated Graphite Oxide/Polycarbonate Nanocomposites

4.1. INTRODUCTION

In Chapter 2 it was proposed that two primary classes of graphene-based materials exist: graphene platelets such as RG-O which are typically handled as colloidal suspensions and TEGO or MEGO platelets that are generally handled as dry powders. It was shown in Chapter 3 that melt-state mixing of dried-down, agglomerated reduced graphene oxide particles into PMMA did not yield significant property enhancement relative to *in situ* polymerization of MMA in the presence of graphene oxide colloidal particles. However, some reports have shown that melt processing can effectively disperse dry TEGO powder into polar thermoplastic polymers.[1-5] Microwave-exfoliated graphite oxide (MEGO) has a similar structure to TEGO,[6] which suggests MEGO powders may also disperse using melt mixing and might afford property enhancements comparable to TEGO.[3] However, the procedure for making MEGO is less time- and energy-intensive than the typical TEGO synthesis;[7] in addition, there are some differences in the reported physical properties of TEGO and MEGO, such as different C : O ratios (i.e., a generally lower C : O ratio for MEGO compared to TEGO) and different values of electrical conductivity (with TEGO generally being higher than MEGO), which could possibly affect dispersion and thus the final nanocomposite properties. In light of

these differences, it was sought to investigate the property enhancements afforded by MEGO, using bisphenol-A polycarbonate (PC) as a model matrix polymer, by using melt mixing to mix dry MEGO powder with PC to create well-dispersed MEGO/PC composites without the aid of solvents.

4.2. MATERIALS AND METHODS

SP-1 graphite (Bay Carbon), bisphenol-A polycarbonate (M_w = 45,000 Da; Scientific Polymer), and all reagents used in the synthesis of GO were used as received. GO was prepared via a modified Hummers method[8] and dried for 48 h under vacuum. The GO was loaded into a glass beaker, put into a domestic microwave oven (General Electric) and heated for approximately 20 s to cause rapid exfoliation and reduction of the material (the yield of MEGO relative to the starting amount of GO was approximately 20%). The black, fluffy powder was collected and compressed by hand to facilitate weighing and loading into the processing equipment. The polymer and MEGO powder were fed into a twin-screw DSM Xplore microcompounder with a mixing chamber volume of 5 ml. The composites were mixed with MEGO at the following weight percent loadings: 0.1, 0.5, 0.8, 1.3, 2.1, and 3.0 wt%, as confirmed by thermogravimetric analysis of the extrudates. Nominal loadings were higher than the values reported here; however, since MEGO has a low bulk density and some MEGO powder was lost during handling and particularly during the mixing step, actual loadings were found to be 15-25% lower than the nominal values. For the microcompounding step, the melt mixing temperature was 250 °C, with a screw speed of 100 rpm and a residence time of 9 min. The extrudates

were retrieved directly from the mixer and placed in a desicciator at room temperature for 24 h prior to molding. The dried extrudates were then pressed using a hydraulic hot press (Wabash) at 67 kN and 250 °C for 5 min, then cooled in the mold under pressure for 5 min (the mold temperature was below 100 °C after cooling), resulting in uniform films of approximately 0.3 mm thickness.

Elemental analysis by combustion was performed by Atlantic Microlabs in Norcross, GA. XPS analysis was performed using a Kratos AXIS Ultra DLD spectrometer (monochromated Al K emission at 1486.6 eV with an operating power of 150 W). A FEI Quanta-600 environmental scanning electron microscope (SEM) was used to image the morphology of the 'worm-like' MEGO particles, which were pressed directly into carbon tape for imaging. A 30 kV accelerating voltage at approximately 10^{-6} torr was used to image the dry powders. Determination of specific surface area using the Brunauer-Emmett-Teller (BET) equation[9] was carried out on a Quantachrome Instruments Nova 2000 using nitrogen as the adsorbent at 77K.

The linear viscoelastic response of the nanocomposites was measured using dynamic mechanical analysis (DMA Q800, TA Instruments). Strips of composite of uniform width (approximately 5 mm) were cut from the hot-pressed film (thickness of roughly 0.3 mm) using a razor blade. For fixed-frequency temperature scans, dynamic loading was applied in a tensile geometry at 1 Hz at 0.02% strain with a 0.01 N tensile force preload. A temperature ramp rate of 3 °C/min was used to obtain storage and loss modulus values as a function of temperature and the tan delta peak was used to determine T_g. Thermogravimetric analysis (TGA4000, Perkin Elmer) was used to observe changes

in non-oxidative thermal degradation behavior versus the neat polymer, using a ramp rate of 10 °C/min with N_2 as the sample purge gas.

The impact strength of neat PC and the MEGO/PC nanocomposites were measured according to ASTM D256. Samples were compression molded into bars of specified dimensions (6.4 x 1.27 x 0.32 cm). Notched Izod impact tests were then performed at room temperature using a TMI Izod impact tester, with an impact velocity of 3.5 m/s.

Rheological characterization of the nanocomposites was performed using a TA Instruments AR 2000EX rheometer. All samples were tested at 230 °C under flowing nitrogen. Approximately 0.75 g of extrudates were loaded onto a 25 mm parallel plate fixture and subsequently squeezed to a disk of approximately 0.9 to 1 mm thick for testing. For each sample loading tested, a dynamic strain sweep at 1 rad/s was performed to find the limit of linear viscoelasticity. The maximum strain before the drop in storage modulus (*G'*) with increasing strain (before *G'* had decreased to ~95% of its limiting value) was recorded and used as the constant strain for the frequency sweep tests. Frequency sweeps at constant strain were then performed from 100 rad/s to 0.05 rad/s.

X-ray diffraction studies were performed using a Philips X-PERT diffractometer using Cu Kα radiation. A generating voltage of 40 kV and a current of 30 mA was used, with a 2 s dwell time. For transmission electron microscopy (TEM) imaging, the extrudates were microtomed (Leica Ultracut UCT, Reichert Inc.) at a direction perpendicular to the axis of extrusion to slices of approximately 75 nm thickness using an

ultra45 diamond blade, then placed onto copper TEM grids (Ted Pella 300 mesh). The TEM images were acquired on a JEOL 2010F at 200 keV.

Hot-pressed nanocomposite samples having approximately 0.3 mm thickness were cut into strips (roughly 3 mm wide and 5 mm long). A thin 'skin' layer deficient in the microwave-exfoliated graphite oxide platelets was removed by oxygen plasma etching (Plasma-Preen II-862, Plasmatic Systems; 2 torr O_2, 3 min, 350W) to reduce the contact resistance between the metal leads and sample tested. After etching, the small amounts of silver paste (SPI) were dropped onto the surface to lower the contact resistance of the probes, and the samples were then allowed to sit at room temperature for 24 h before measurement. Conductivity measurements were performed with a four probe conductivity apparatus (Keithley 6514 electrometers and Keithley 6221 ac/dc source); the values were checked against a dc multimeter (Keithley 2410) with a threshold detection limit of approximately 0.2 GΩ. To calculate the conductivity, the thickness t of the sample was carefully measured, and from the sheet resistance R_s measured by the four probe measurement, the resistivity was calculated as $\rho = t \times R_s$, then the conductivity calculated as $\sigma = 1/\rho$ (units of S/m).

Long-term annealing treatments were performed on the nanocomposites in attempt to randomize the orientations of the dispersed platelets with the goal of lowering the conductivity percolation threshold and raising the conductivity of the nanocomposites. For the annealing treatment, the samples were treated in a vacuum oven at 230 °C for 24 h. The conductivity measurements on the annealed samples were then performed identically to those samples which were not annealed.

A symmetric, guarded hot plate thermal conductivity apparatus was assembled and measurements were taken according to previous work.[10] Briefly, two composite specimens of equivalent size (2.54 cm x 2.54 cm x 0.3 cm) were compression molded at 250 °C and 67 kN for 3 min, then cooled inside the mold under pressure and retrieved. After conditioning for 24 h, the faces of the specimens were coated in zinc oxide thermal grease and a flexible polyimide heater (Minco, HK5951) of equivalent lateral dimensions to the specimens was sandwiched between them. Thermocouple contacts (of 0.08 mm diameter; Omega, CHAL-003) were placed on each face of the specimens. Two identical aluminum heat sinks were pressed on the outer faces of the specimens, and the whole apparatus was subsequently pressed together firmly with a spring clamp and covered with foil to provide radiation and convective shielding. A constant voltage and current was supplied (dc voltage source, Extech), and V and I were read from a display on the source (and independently measured using a multimeter) to calculate $Q = VI$ to obtain the heat flow, from which the thermal conductance and thus thermal conductivity could be calculated based on the sample geometry. Measurements at a given Q value were taken at regular intervals until the temperature readings were constant (typically 3 to 4 hours). The accuracy of the setup was verified with neat samples of Nylon 6 and polycarbonate by comparison against tabulated thermal conductivity values. For the annealing treatment, the samples were placed inside a mold (to maintain the sample geometry) and heated in a hot press (Fred S. Carver, Inc.) at 230 °C and ~1 kN for 14 h. The conductivity measurements on the annealed samples were then performed identically to those samples which were not annealed.

4.3. FILLER AND NANOCOMPOSITE MORPHOLOGY

Microwave-expanded graphite oxide consists of loosely-stacked, wrinkled platelets as shown in Figure 4.1(b). The particles appeared "worm-like" at lower magnification due to the large c-axis expansion that results from the microwave treatment. As-prepared GO was determined to have a C : O ratio of 1.4 : 1, while MEGO was found to have a C : O ratio of 3.2 : 1, suggesting that a significant concentration of oxygen-based functional groups remain after the microwave exfoliation—consistent with earlier reports on the synthesis and properties of MEGO.[7] XPS measurements also indicated the presence of oxygen-based functional groups on the platelets with a C : O ratio of 2 : 1, as shown in Figure 4.1(a). BET surface area measurements on MEGO particles yielded a specific surface area of 432 m^2/g. Upon dispersion of MEGO into PC, the nanocomposites become black in color and molded thin films (~0.3 mm) of nanocomposite become completely opaque at and above 0.5 wt% loading, as shown in Figure 4.1(c).

Wide-angle X-ray scattering and TEM were used to probe the dispersion of MEGO in the composites. X-ray scattering plots are shown for MEGO, neat PC, and MEGO/PC composites in Figure 4.2. The scattering intensity profile for MEGO is nearly featureless relative to GO, except for a slight, broad peak between 24 and 26 degrees corresponding to a d-spacing of approximately 0.35 nm. Since MEGO is largely exfoliated (relative to GO) prior to dispersion into the PC matrix, it was expected that the nanocomposites would exhibit an exfoliated morphology according to X-ray scattering analysis. Indeed, Figure 4.2 shows that no change in the scattering profile was observed

even at the highest loadings of MEGO, suggesting that the composites have an exfoliated morphology and that no significant re-stacking occurs upon dispersion.

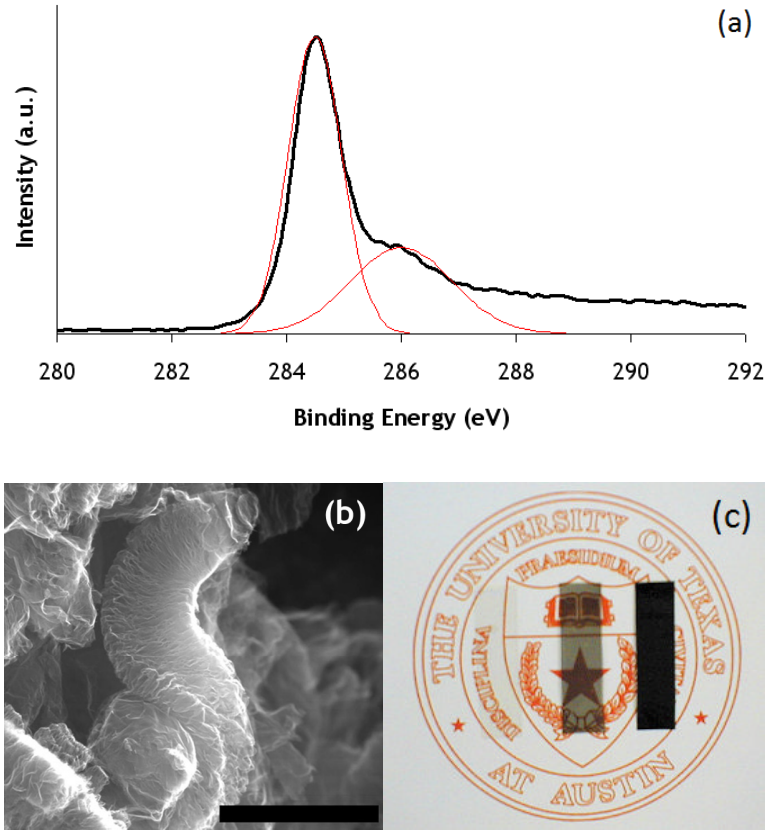

Figure 4.1. (a) C1s XPS spectrum of MEGO with peak deconvolution shown, (b) SEM image of MEGO particles (scale bar represents 5 μm). (c) Image showing the loss of optical clarity in polycarbonate as a function of MEGO loading. From left to right: neat PC, 0.1 wt% MEGO/PC, and 0.5 wt% MEGO/PC. All samples shown are ~0.30 mm thick.

Microtomed cross sections of 3.0 wt% MEGO/PC nanocomposites were analyzed by TEM. The MEGO platelets show adequate contrast against the PC matrix to allow imaging without staining, although thinner platelets (particularly at lower

magnifications) were difficult to clearly resolve. As evident from Figure 4.3, the platelets were largely multi-layered and exhibited wrinkled conformations. The platelets were evenly dispersed throughout the matrix along with a low concentration of agglomerated platelets. Many of the platelets appear to be in contact in the images, consistent with electrical and rheological measurements suggesting that the MEGO particles have formed a percolating network at this loading.

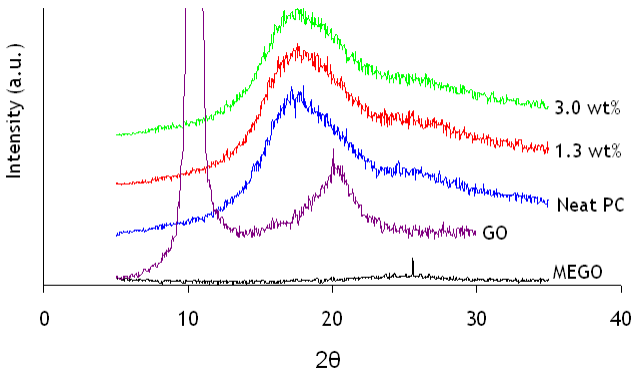

Figure 4.2. Normalized wide-angle X-ray scattering plots of GO, MEGO, neat PC, and MEGO/PC nanocomposites.

Several images of the nanocomposite cross section were analyzed in attempt to quantify the dispersion of the MEGO/PC composite. Based on analysis of over 80 platelets from several different images, an average lateral dimension and thickness of the MEGO platelets was estimated. The platelets were estimated to have an average lateral dimension of 202 nm with an average thickness of roughly 4.5 nm, translating to an average platelet aspect ratio of approximately 45. However, there is a possibility that few-layer or monolayer platelets—which may be invisible by TEM—were dispersed in

the matrix, suggesting the actual average aspect ratio of the dispersed MEGO platelets may be higher than the estimation given here. Also, complications with analyzing dispersion from these two-dimensional projections could also have affected this analysis as discussed further in Chapter 5 and Appendix A.[11]

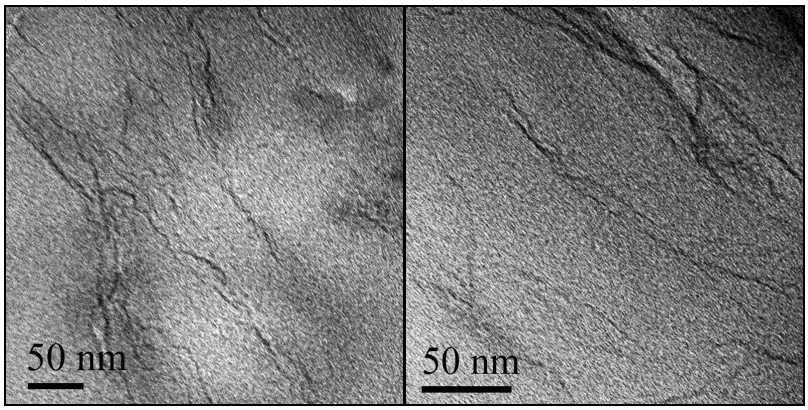

Figure 4.3. TEM images of microtomed cross sections of 3.0 wt% MEGO/PC composites, showing the presence of crumpled, multi-layered MEGO platelets dispersed throughout the PC matrix.

4.4. RHEOLOGICAL PROPERTIES

Melt rheological studies on the composites were performed to evaluate the onset of percolation as well as to attempt to quantify dispersion.[12] For each MEGO/PC nanocomposite loading tested, a strain sweep was first performed to identify the limit of linear viscoelasticity, followed by a constant-amplitude frequency sweep. The transition from liquid-like ($G' \sim \omega^2$ and $G'' \sim \omega$) to solid-like (G' and $G'' \sim \omega^0$) terminal behavior can provide a measure of the rheological percolation threshold for the composites,[13] and

can be used to calculate an effective aspect ratio (A_f) of the platelets, based on the idealized assumption of rigid, ellipsoidal tactoids.[14] Ren and co-workers[13, 14] showed with a volume-filling calculation that the nanofiller loading corresponding to the onset of percolation can be used to estimate the aspect ratio of dispersed platelets according to the equation[2]:

$$A_f = \frac{3\phi_{sphere}}{2\phi_{perc}}$$

where ϕ_{sphere} is the percolation threshold for randomly-dispersed spheres (=0.29), and ϕ_{perc} is the observed percolation threshold for this nanocomposite system. As shown in Figure 4.4, the onset of terminal behavior appeared around 2 wt% (~0.91 vol%, based on the density of graphite, 2.2 g/cm^3), suggesting A_f = 48, in good agreement with the TEM observations—particularly considering that some few- or single-layer platelets may have been invisible by TEM, which would tend to decrease the A_f estimated from that analysis.

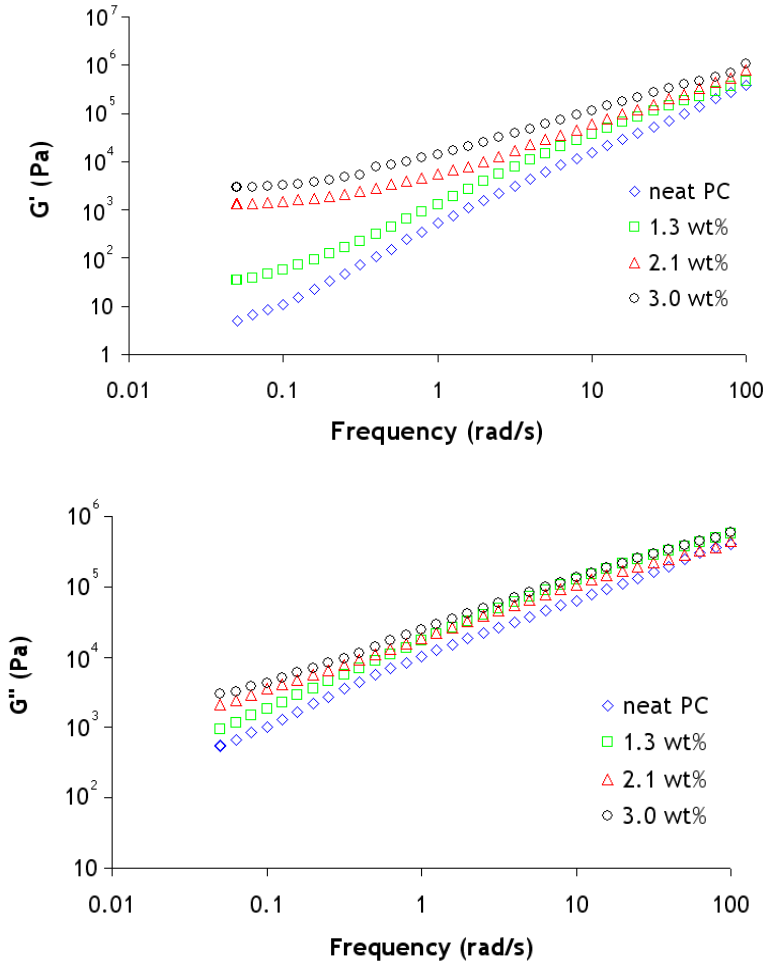

Figure 4.4. Representative frequency sweeps of MEGO/PC nanocomposite melts at 230 °C.

Table 4.1. Rheological and dynamic mechanical properties and impact strengths of neat PC and MEGO/PC nanocomposites at various loadings.

Loading	*E′* (GPa) ‡	T_g (°C)	*G′* (Pa) §	Izod strength (J/m)
Neat PC	1.74 ± 0.03	156.8 ± 0.2	5.0	700.6
0.1 wt%	1.74 ± 0.04	156.6 ± 0.2	-	-
0.5 wt%	1.82 ± 0.01	157.0 ± 0.1	15.1	88.4
0.8 wt%	1.92 ± 0.01	156.7 ± 0.2	-	-
1.3 wt%	2.07 ± 0.02	156.9 ± 0.1	44.4	41.4
2.1 wt%	2.23 ± 0.08	156.9 ± 0.1	1331	39.6
3.0 wt%	2.27 ± 0.03	157.4 ± 0.2	2921	20.0

4.5. THERMOMECHANICAL AND IMPACT PROPERTIES

The high aspect ratio and relatively high modulus of graphene platelets[15, 16] allows them to be the primary load-bearing component when dispersed into a polymer,[17] and thus significant reinforcement by graphene-based fillers has been previously reported.[18] In this study, DMA was used to probe the mechanical properties of the nanocomposites; Figure 5 provides representative plots of the storage and loss moduli (*E'* and *E"*, respectively) of the nanocomposites as a function of temperature. Generally, *E'* was found to increase with loading, with an increase in *E'* of over 30% at 3.0 wt% compared with neat PC.

‡ 1 Hz and 40 C.
§ 0.05 rad/s and 230 C.

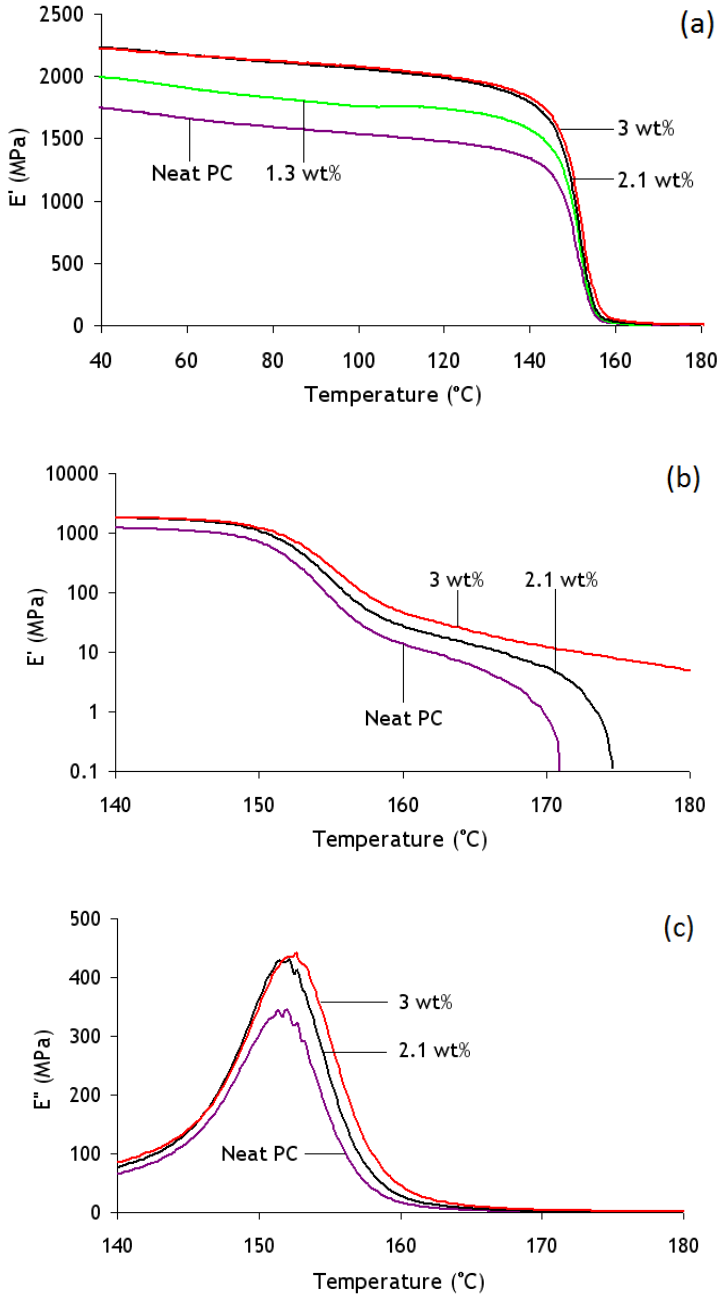

Figure 4.5. Plots of (a) storage modulus (*E'*) and (b) loss modulus (*E''*) versus temperature for various loadings of MEGO in PC.

The room-temperature storage modulus measured by DMA was used as an approximate measure of the elastic modulus for use in Mori-Tanaka analysis.[19, 20] For this study, the normalized storage moduli measured by DMA was compared to model predictions, using the A_f determined by TEM analysis and tabulated values for the Poisson's ratio, ν, of graphite and PC (equal to 0.06 and 0.37, respectively[2, 21]), to extract an "effective" modulus of the dispersed MEGO platelets with the Mori-Tanaka theory equations and procedure described in Appendix B.

Using the average platelet aspect ratio estimated from TEM analysis (A_f = 45), a value for the effective modulus of the MEGO platelets of approximately 60 MPa was calculated, based upon the measured longitudinal moduli of the nanocomposites (Figure 4.6). This value is considerably lower than the measured value for pristine graphene[22] and also lower than the measured values for graphene oxide[15] and reduced graphene oxide,[16] which may be a consequence of defects in the platelet structure and also the wrinkled configuration of the platelets, in addition to the multi-layer structure of the platelets.[23] In addition, the DMA measurements revealed very little increase in the T_g of the nanocomposites versus neat PC, consistent with other results on TEGO/PC composites.[1] In some other graphene/polymer nanocomposite systems, large increases in T_g (10 to 15 °C and, in some cases, higher) have been reported; such large increases may be due to comparatively better dispersion resulting from more complete exfoliation of the platelets prior to mixing, or resulting from the mixing step itself, or perhaps even errors in sample preparation or testing as suggested by the results in Chapter 3.

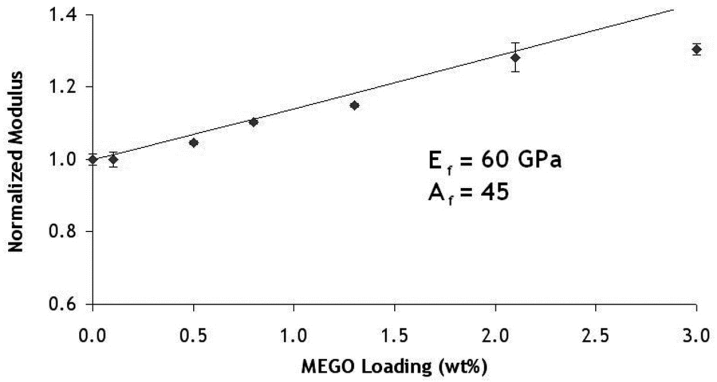

Figure 4.6. Comparison of experimental modulus data to calculations using Mori-Tanaka theory (using the aspect ratio determined by TEM) provides an estimate of platelet modulus (E_f) of approximately 60 GPa.

The exceptional impact strength of PC is one major reason for its widespread application. Previously, the inclusion of layered silicate fillers into PC has been reported to compromise ductility and caused significant decreases in the Izod impact strength.[24, 25] In this study, the MEGO/PC nanocomposites exhibited brittle fracture at room temperature with significantly lower impact strength than neat PC, as shown in Table 4.1. Thus, while MEGO can be used to significantly improve the stiffness and conductivity properties of PC, it comes at the cost of impact strength.

4.6. ELECTRICAL PROPERTIES

A variety of graphene/polymer nanocomposite systems have shown significant improvements in electrical conductivity versus the neat polymer matrix, including PC-matrix composites.[1, 3] In this study, large improvements in the electrical conductivity were observed, as tested by a four-probe conductivity apparatus. For loadings below 1.3

wt%, the resistances of the composites were sufficiently high to be out of range of the available test setup (approximately 0.2 GΩ). However, Figure 4.7(a) shows that a large increase in the conductivity of the nanocomposites began at 1.3 wt% (and increased further as the loading increased), thus suggesting an onset of conductivity percolation below that of rheological percolation. Based on the MEGO loading at the conductivity percolation threshold, A_f = 74, considerably higher than estimated from melt rheology or TEM. The onset of electrical percolation at a lower loading than rheological percolation has been established in other nanocomposite systems; however, this result stands in contrast to previous reports on TEGO-filled nanocomposites.[2, 3] It should also be noted this electrical percolation threshold is comparable to or lower than what has been previously reported for TEGO/PC nanocomposites.[3, 26]

It has been well-established in rheological studies that prolonged large-amplitude shear or other externally applied flow can suppress the terminal solid-like behavior in polymer composites by destroying a percolated network of filler particles, if one exists.[12, 13] Thus, the conductivity percolation threshold and ultimate composite conductivity can be affected by such large strain deformations. Previously, it has been reported that long-term annealing treatments under quiescent conditions can promote disorientation of dispersed, anisotropic fillers such as layered silicates[27] and, more recently, TEGO.[3] Prolonged thermal annealing of TEGO-reinforced polymer nanocomposites has been reported to improve electrical conductivity, which generally benefits from a random orientation of filler particles.[3] The mechanisms for particle disorientation are not fully understood but rheological measurements on layered silicate nanocomposites suggests

the disorientation process may be non-Brownian (i.e., not dependent upon matrix viscosity or particle size) and has a power-law dependence on time.[27]

It was thus sought to investigate whether long-term thermal annealing could further improve the conductivity of MEGO/PC nanocomposites under the presumption that the ~0.3 mm thick samples hot pressed for conductivity measurements contain a significant amount of filler alignment. For their TEGO/PC composites (M_w ~ 50 kDa), Kim and co-workers[3] calculated a rotational relaxation time of rigid Brownian platelets of 200 nm in the PC matrix to be ~60,000 s at 230 °C, and observed good experimental agreement in the modulus recovery with time, thus suggesting an appropriate time scale for annealing of MEGO/PC composites. Indeed, the electrical conductivities of the nanocomposite samples at 1.3 wt% and above were found to increase after a 24 h annealing treatment, as shown in Figure 4.7(b). However, conductivity percolation was not observed at lower loadings following the annealing treatment (i.e., the resistance of the 0.8 wt% and 0.5 wt% samples were still too high to be measured by the test setup used in this study), possibly because the concentration of platelets at these loadings is too low to form a percolated network, regardless of platelet orientation. It should also be noted that such annealing treatments can lead to dimensional instability in the sample, i.e., samples tended to flow under their own weight at high temperatures. Thus, annealing treatments must be performed in an appropriately-shaped mold to contain the sample during treatment.

Above the conductivity percolation threshold, the electrical conductivity, σ, generally scales as a power law function:

$$\sigma \propto \sigma_0(\phi - \phi_c)^t$$

where ϕ is the volume fraction loading of MEGO, ϕ_c is the conductivity percolation threshold (volume fraction), σ_0 is the conductivity of the matrix and t is a scaling exponent, which has been suggested to depend on the dimensionality of the system.[5, 28] Fitting this expression to the data, as shown in Figure 4.7(b), suggests $\phi_c \sim 0.006$ with t = 2.14 for the as-molded composite samples, and t = 1.80 for the 24 h-annealed samples. Both values of t are close to the value of 2 predicted by percolation theory for a three-dimensional conducting network.[29]

4.7. THERMAL CONDUCTIVITY AND THERMAL STABILITY

Pristine graphene has been determined to have a thermal conductivity as high as 5,000 W/m·K[30, 31] and although no measurements have been reported to date on the thermal conductivity of GO-derived materials such as MEGO or RG-O platelets, it is expected that such materials may also exhibit high thermal conductivities—albeit much lower than pristine graphene due to the presence of defects and residual functional groups. There have been several reports on the use of graphite nanoplatelets to improve the thermal conductivity of polymers, however, to date, there have been few reports on the thermal conductivity of polymer nanocomposites with graphene platelet fillers, particularly with amorphous thermoplastic matrices such as PC.

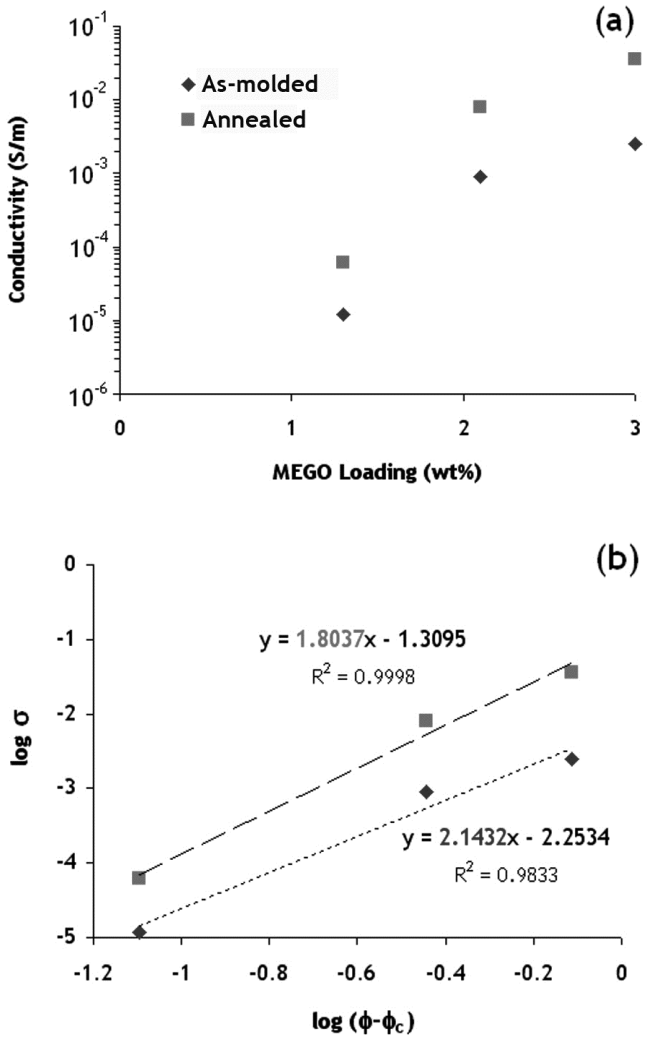

Figure 4.7. Measurements of electrical conductivity, σ, on neat PC and MEGO/PC nanocomposites; annealed samples were treated at 230 °C for 24 h. (a) Electrical conductivity data suggests electrical percolation around 1.3 wt%. At values below 1.3 wt%, the conductivity was too low to be determined, even after annealing. (b) Fitting of the conductivity power law above the percolation threshold allowed estimation of the critical exponent *t*, which was found to decrease on annealing.

In this study, thermal conductivity measurements were made at steady-state using a guarded hot plate setup as described previously. According to a previous analysis, the total uncertainty in the measurements with this setup and sample geometry is approximately 6%.[10] A sample set of results are shown in Figure 4.8 for neat PC and a 3.0 wt% MEGO/PC nanocomposite. Taking the thermal conductance, G, from the slope of a plot of Q versus T, the thermal conductivity k was then calculated according to the equation

$$k = \frac{Gt}{2A}$$

where t is the sample thickness and A is the sample area. The thermal conductivity of neat PC was measured to be 0.19 ± 0.02 W/m·K, while for the 3.0 wt% MEGO/PC composite, a value of 0.23 ± 0.03 W/m·K was obtained (see Table 4.2).

The improvement in thermal conductivity observed in this study is well below the upper bound predicted by a simple rule of mixtures;[32] despite the onset of electrical percolation around 1.3 wt% leading to large increases in electrical conductivity, only small increases in thermal conductivity were observed. Comparably small improvements in thermal conductivity have also been generally observed in carbon nanotube-filled nanocomposites,[32, 33] although it is expected that graphene-based fillers could ultimately provide superior thermal conductivity enhancement due to lower interparticle thermal resistance.[34, 35] However, relative to the large (many orders of magnitude) improvements observed in electrical conductivity, conductive fillers will generally provide much smaller improvements in thermal conductivity at equal loadings due to the considerably

smaller contrast between the thermal conductivity of the polymer matrix and the filler, compared with the contrast in the electrical conductivity.[33]

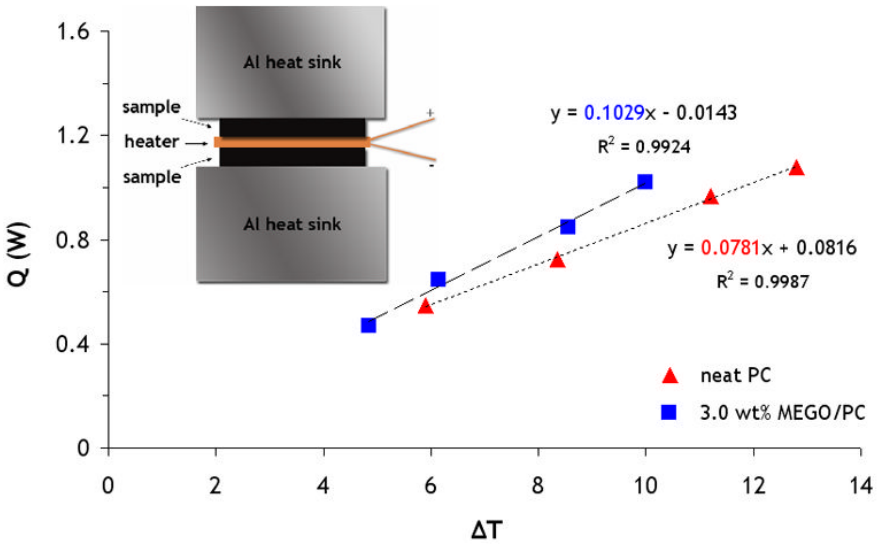

Figure 4.8. Data from thermal conductivity measurements on neat PC and MEGO/PC composites. Q represents the heat flow from the heater through the samples, while ΔT is the average temperature gradient across the two samples. The slope of the trendlines were taken as the thermal conductance, from which the thermal conductivity could be calculated for each loading tested. The inset schematic illustrates the construction of the guarded hot plate setup used to perform the measurements.

Table 4.2. Effect of long-term thermal annealing on the electrical and thermal conductivity of MEGO/PC nanocomposites.

	Electrical conductivity (S/m)		**Thermal conductivity (W/m·K)**	
	As-molded	Annealed**	As-molded	Annealed††
Neat PC	-	-	0.19 ± 0.02	-
0.5 wt%	-	-	0.18 ± 0.03	-
1.3 wt%	2.2×10^{-5}	5.1×10^{-4}	-	-
2.1 wt%	9.0×10^{-4}	5.0×10^{-3}	0.20 ± 0.03	0.22 ± 0.04
3.0 wt%	2.5×10^{-3}	0.036	0.23 ± 0.03	0.24 ± 0.02

As with the thinner films used for electrical conductivity measurements, the thicker films used for thermal conductivity measurements may have contained a significant amount of platelet orientation in the plane of the film as a result of the compression molding process. Particularly as the measurements were made transversely to the plane of platelet orientation, it was also sought to evaluate the effect of a long-term annealing treatment on the nanocomposites' thermal conductivity. However, as shown in Table 4.2, the annealing process was found to have little if any meaningful effect on the thermal conductivity of the nanocomposites, despite the significant increase observed in the electrical conductivity.

** 24 h at 230 °C.
†† 14 h at 230 °C.

Improvements in thermal conductivity can be used as a measure of dispersion; several models for predicting the thermal conductivity of polymer composites exist.[36] The equivalent inclusion method developed by Hatta and Taya allows for estimation of composite thermal conductivity both parallel and perpendicular to the plane of aligned, disk-shaped platelets in a polymer matrix[36, 37]:

$$k_c = k_m\left[1 + \frac{\phi}{S(1-\phi) + k_m/(k_f - k_m)}\right]$$

where k_c, k_m, and k_f are the thermal conductivities of the composite, matrix, and filler particles, respectively, ϕ is the volume fraction of filler, and S is a shape factor that depends on A_f and orientation according to $S = \pi/4A_f$ for measurements parallel to the plane of orientation, or $S = 1\text{-}\pi/2A_f$ for measurements perpendicular to the plane of orientation. For an A_f of 45 (as estimated from TEM analysis), the composite thermal conductivity was found to be nearly independent of the intrinsic platelet conductivity above 100 W/m·K, according to the model. Moreover, for any value of the filler conductivity greater than the matrix, the composite thermal conductivity at 3.0 wt% and $A_f = 45$ was calculated to be ~0.19 W/m·K perpendicular to the plane of orientation, thus suggesting some level of disorientation in the as-molded nanocomposites (i.e., the dispersed platelets were oriented at some range of angles to the hot pressing direction) as illustrated in Figure 4.9. While defects and residual functional groups in the structure of MEGO may limit its intrinsic thermal conductivity, this analysis suggests that the dispersion (i.e., A_f) might be the more important factor limiting the thermal conductivity of the composites,[38] particularly in light of recent work by Wang and co-workers

reporting a 400% improvement in the thermal conductivity of a (unreduced) graphene oxide/epoxy composite at 5 wt%.[39]

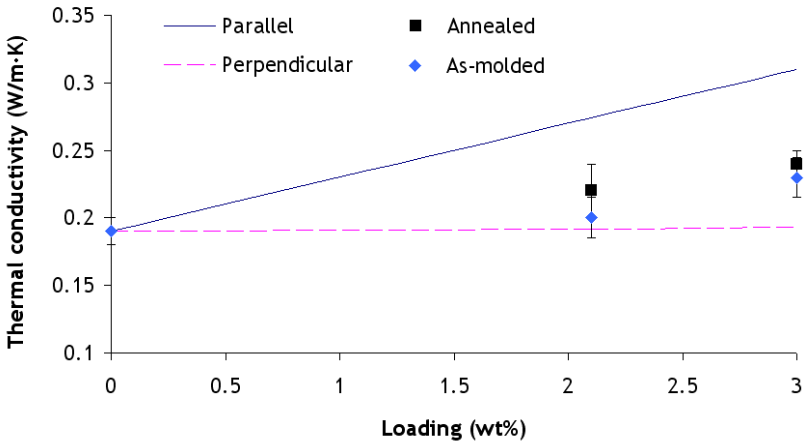

Figure 4.9. Comparison of thermal conductivity measurements to predictions of composite thermal conductivity from the Hatta and Taya model. "Parallel" denotes the model prediction of the composite conductivity parallel to the plane of the aligned platelets, while "perpendicular" represents the conductivity out-of-plane. A filler thermal conductivity of 100 W/m·K was used for the calculation, along with a matrix thermal conductivity of 0.19 W/m·K and a platelet aspect ratio of 45.

Graphene platelets have been widely reported to improve the thermal stability of polymer composites relative to the host polymer.[40] Thermal degradation studies of the nanocomposites were performed using TGA. The results are shown in Figure 4.10, where the shift in the onset of the thermal degradation temperature is plotted against loading of MEGO. Very little change in the non-oxidative thermal stability was observed with higher weight percent loadings of MEGO filler (data for other loadings not shown). Differences in the residual mass between nanocomposites of different loadings were used

to assign loading values, since some MEGO was lost during handling and particularly the mixing step.

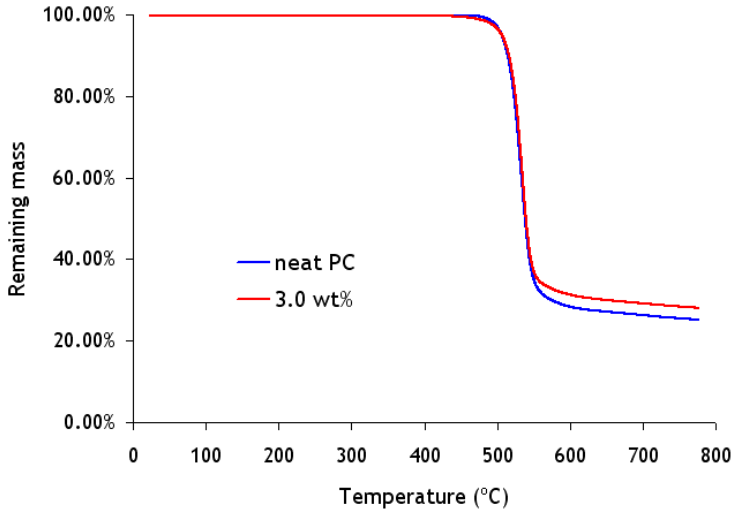

Figure 4.10. TGA plots of neat PC versus a 3.0 wt% MEGO/PC nanocomposite suggest little if any improvement in thermal stability of the nanocomposites relative to neat PC.

4.8. CONCLUSIONS

The dispersion of MEGO into PC via melt compounding resulted in multifunctional property improvements of PC. TEM images of the composites showed multi-layer platelets well-dispersed throughout the PC matrix, with an aspect ratio of ~45. Rheological measurements suggested an onset of connectivity percolation around 2.1 wt%, while electrical percolation was observed around 1.3 wt% and long-term thermal annealing of the composites well above T_g was found to improve the electrical conductivity further. However, only modest increases in thermal conductivity were observed in this study. Moreover, the improvements in stiffness and conductivity came at

the cost of diminished transparency and decreased impact strength. But despite these shortcomings, this study shows that MEGO can be easily dispersed into a suitable polymer matrix via melt compounding, while offering lower conductivity percolation thresholds and equal or better electrical conductivity than thermally-exfoliated graphite oxide and multi-walled carbon nanotubes.[28] Given the facile synthesis of MEGO, this approach described here may provide a highly attractive route to graphene/polymer nanocomposites.

4.9. REFERENCES

1. Yoonessi, M.; Gaier, J. R. *ACS Nano*, DOI: 10.1021/nn1019626.

2. Kim, H.; Macosko, C. W. *Macromolecules* **2008,** 41, (9), 3317-3327.

3. Kim, H.; Macosko, C. W. *Polymer* **2009,** 50, (15), 3797-3809.

4. Kim, H.; Miura, Y.; Macosko, C. W. *Chemistry of Materials* **2010,** 22, (11), 3441-3450.

5. Zhang, H. B.; Zheng, W. G.; Yan, Q.; Yang, Y.; Wang, J. W.; Lu, Z. H.; Ji, G. Y.; Yu, Z. Z. *Polymer* **2010,** 51, (5), 1191-1196.

6. Schniepp, H. C.; Li, J. L.; McAllister, M. J.; Sai, H.; Herrera-Alonso, M.; Adamson, D. H.; Prud'homme, R. K.; Car, R.; Saville, D. A.; Aksay, I. A. *Journal of Physical Chemistry B* **2006,** 110, (17), 8535-8539.

7. Zhu, Y. W.; Murali, S.; Stoller, M. D.; Velamakanni, A.; Piner, R. D.; Ruoff, R. S. *Carbon* **2010,** 48, (7), 2118-2122.

8. Hummers, W. S.; Offeman, R. E. *Journal of the American Chemical Society* **1958,** 80, (6), 1339.

9. Brunauer, S.; Emmett, P. H.; Teller, E. *Journal of the American Chemical Society* **1938,** 60, (2), 309-319.

10. Moore, A. L.; Cummings, A. T.; Jensen, J. M.; Shi, L.; Koo, J. H. *Journal of Heat Transfer* **2009,** 131, 091602.

11. Paul, D. R.; Robeson, L. M. *Polymer* **2008,** 49, (15), 3187-3204.

12. Vermant, J.; Ceccia, S.; Dolgovskij, M. K.; Maffettone, P. L.; Macosko, C. W. *Journal of Rheology* **2007,** 51, (3), 429-450.

13. Krishnamoorti, R.; Yurekli, K. *Current Opinion in Colloid & Interface Science* **2001,** 6, 464-470.

14. Ren, J.; Silva, A. S.; Krishnamoorti, R. *Macromolecules* **2000,** 33, 3739-3746.

15. Suk, J. W.; Piner, R. D.; An, J.; Ruoff, R. S. *ACS Nano* **2010,** 4, 6557-6564.

16. Gómez-Navarro, C.; Burghard, M.; Kern, K. *Nano Letters* **2008,** 8, (7), 2045-2049.

17. Fornes, T. D.; Paul, D. R. *Polymer* **2003,** 44, (17), 4993-5013.

18. Zhao, X.; Zhang, Q. H.; Chen, D. J.; Lu, P. *Macromolecules* **2010,** 43, (5), 2357-2363.

19. Mori, T.; Tanaka, K. *Acta Metallurgica* **1973,** 21, 571-574.

20. Tandon, G. P.; Weng, G. J. *Polymer Composites* **1984,** 5, 327-333.

21. Brandrup, J.; Immergut, E. H.; Grulke, E. A.; Abe, A.; Bloch, D. R., *Polymer Handbook*. 4 ed.; John Wiley and Sons: 1999; p 2336.

22. Lee, C.; Wei, X.; Kysar, J. W.; Hone, J. *Science* **2008,** 321, (5887), 385-388.

23. Brune, D. A.; Bicerano, J. *Polymer* **2002,** 43, 369-387.

24. Hsieh, A. J.; Moy, P.; Beyer, F. L.; Madison, P.; Napadensky, E.; Ren, J.; Krishnamoorti, R. *Polymer Engineering and Science* **2004,** 44, (5), 825-837.

25. Yoon, P. J.; Hunter, D. L.; Paul, D. R. *Polymer* **2003,** 44, 5323-5339.

26. Steurer, P.; Wissert, R.; Thomann, R.; Mulhaupt, R. *Macromolecular Rapid Communications* **2009,** 30, (4-5), 316-327.

27. Ren, J.; Casanueva, B. F.; Mitchell, C. A.; Krishnamoorti, R. *Macromolecules* **2003,** 36, 4188-4194.

28. Bauhofer, W.; Kovacs, J. Z. *Composites Science and Technology* **2009,** 69, (10), 1486-1498.

29. Kovacs, J. Z.; Velagala, B. S.; Schulte, K.; Bauhofer, W. *Composites Science and Technology* **2007,** 67, (5), 922-928.

30. Balandin, A. A.; Ghosh, S.; Bao, W.; Calizo, I.; Teweldebrhan, D.; Miao, F.; Lau, C. N. *Nano Letters* **2008,** 8, (3), 902-907.

31. Seol, J. H.; Jo, I.; Moore, A. L.; Lindsay, L.; Aitken, Z. H.; Pettes, M. T.; Li, X.; Yao, Z.; Huang, R.; Broido, D.; Mingo, N.; Ruoff, R. S.; Shi, L. *Science* **2010,** 328, (5975), 213-216.

32. Han, Z.; Fina, A. *Progress in Polymer Science* **2011,** 36, 914-944.

33. Moniruzzaman, M.; Winey, K. I. *Macromolecules* **2006,** 39, (16), 5194-5205.

34. Yu, A.; Ramesh, P.; Sun, X.; Bekyarova, E.; Itkis, M. E.; Haddon, R. C. *Advanced Materials* **2008,** 20, (24), 4740-4744.

35. Lin, W.; Zhang, R.; Wong, C. P. *Journal of Electronic Materials* **2010,** 39, (3), 268-272.

36. Hill, R. F.; Supancic, P. H. *Journal of the American Ceramic Society* **2002,** 85, (4), 851-857.

37. Hatta, H.; Taya, M. *international Journal of Engineering Science* **1986,** 24, (7), 1159-1172.

38. Sun, X.; Ramesh, P.; Itkis, M. E.; Bekyarova, E.; Haddon, R. C. *Journal of Physics: Condensed Matter* **2010,** 22, 334216.

39. Wang, S. R.; Tambraparni, M.; Qiu, J. J.; Tipton, J.; Dean, D. *Macromolecules* **2009,** 42, (14), 5251-5255.

40. Kim, H.; Abdala, A. A.; Macosko, C. W. *Macromolecules* **2010,** 43, 6515-6530.

Chapter 5:

Processing-Morphology-Property Relationships and Composite Theory Analysis of Reduced Graphene Oxide/Natural Rubber Nanocomposites

5.1. INTRODUCTION

To meet the demands of many critical applications, elastomers are blended with particulate fillers. Fillers are typically added to elastomers to improve properties such as strength and abrasion resistance, but they can also be used to enhance the electrical and thermal conductivity and permeability resistance of a rubber compound. Over the past two decades, the blending of nanomaterials—such as exfoliated layered silicates and carbon nanotubes—into elastomers has been explored in detail, with the goal of supplementing or replacing conventional fillers such as carbon black and silica.[1] The excellent physical properties, high surface area and anisotropy (aspect ratio) of many nanomaterials suggests tremendous promise for use as fillers for elastomers and polymers more generally.

Given the recent development of graphene-based materials produced by scalable chemical routes, it is of significant interest to establish effective dispersion techniques for and investigate the use of graphene-based materials for elastomer reinforcement. To date, however, a relatively small fraction of the large body of literature on graphene/polymer nanocomposites has investigated graphene-filled elastomers.[2-4] Very little work has

examined property enhancement in non-polar rubbers such as natural rubber (NR) which are of significant technological interest. Just as with thermoplastic-matrix nanocomposites, elastomeric nanocomposites can be produced by three general routes—melt compounding, *in situ* polymerization, and solution/latex mixing. Considering the ease by which kinetically stable aqueous suspensions of graphene-based materials can be made,[5-7] water-based latex mixing could provide an effective means for production of graphene/rubber nanocomposites.

Latex mixing and co-coagulation has been extensively studied with layered silicate/rubber nanocomposite systems.[1] Yu and co-workers performed the earliest studies on latex compounding of rubber latexes with pristine clay/water suspensions,[8, 9] first demonstrating the performance advantage of high aspect ratio nanoclays over carbon black. Others expanded on this work by examining the morphological characteristics of co-coagulated clay/rubber hybrids and concluded that co-coagulation excludes the possibility of an "intercalated" morphology, leading only to re-stacked or exfoliated platelets[10] while generating a "house of cards" morphology consisting of networks of nanoclay platelets confined within the interstices of the coagulated latex particles.[11] Further studies have examined the effect of processing variables on the morphology and properties of latex compounded nanoclay/rubber composites, including the use of different coagulation agents and/or drying conditions[12, 13] to improve filler dispersion and compound properties.

An analogous latex co-coagulation approach using graphene platelet suspensions could be expected to yield similar results since both exfoliated montmorillonite and

graphene platelets are high aspect ratio platelets, although graphene-based materials tend to show more crumpled conformations when dispersed in a polymer. Recently, Zhan and co-workers published a study on reduced graphene oxide/natural rubber nanocomposites fabricated by an ultrasonically-assisted latex mixing masterbatch technique.[4] Their findings illustrated the tremendous potential of graphene in natural rubber reinforcement. However, their production method involved hydrazine reduction of a graphene oxide suspension without the aid of electronic or steric stabilization, which likely caused significant flocculation and re-stacking of the reduced graphene oxide platelets prior to mixing which would be detrimental to the filler dispersion. Moreover, their work considered nanocomposites only up to 2 wt%, and it is of interest to evaluate the performance of RG-O/NR nanocomposites at higher filler loadings.

In this work, the production of RG-O/NR nanocomposites by a similar latex co-coagulation method is described, which begins with preparation of a kinetically stable dispersion of single-layer RG-O platelets. It was found that the co-coagulation process initially produces a "skeleton" or network morphology, as previously described for montmorillonite/NR nanocomposites.[11] However, it was sought to investigate what benefit to composite properties, if any, such a morphology offers relative to a more uniform, homogeneous, and well-exfoliated dispersion—the oft-cited goal in nanocomposites research. Such a consideration would also be relevant from a technological perspective. For example, latex co-coagulated nanocomposites would not likely be used directly in typical applications, but would instead be utilized as a masterbatch compound which would be diluted or otherwise mixed to some extent using,

for example, a two-roll mill or internal mixer.[1] The intense shear forces generated by these mixing operations would be expected to destroy the network morphology created by co-coagulation. Differences in the property trends between the two types of nanocomposites could also be analyzed with simple composite models to gain additional insight. Thus, the goal of this Chapter is to explore the effect of the milling process on the morphology and properties of latex co-coagulated NR/RG-O nanocomposites and also to analyze these results using simple composite models.

5.2. MATERIALS AND METHODS

RG-O filler was produced by exfoliation and reduction of graphite oxide GO. GO was synthesized by oxidation of purified natural flake graphite (SP-1, Bay Carbon) by a modified Hummers method, in batch sizes larger than in the previous Chapters. In this process, 12 g of graphite was added to 600 ml concentrated H_2SO_4, and then 50 g of $KMnO_4$ was slowly added over an ice bath. The reaction mixture was stirred at room temperature for 24 h and then put back on an ice bath, then ~1500 ml of deionized water was slowly added and H_2O_2 (30%) was added until the mixture became orange/gold in color. GO (a yellow-brown solid) was isolated by vacuum filtration and dried; the yield of GO from this procedure was approximately 22 to 25 g.

Aqueous colloidal suspensions of G-O were produced by exfoliation of GO. 500 mg of GO was added to 750 ml water and treated in an ultrasonic bath (VWR, 97043-968) for 4 h, and stirred for at least 24 h (until no turbidity was present in the mixture). Individual batches were produced in this manner and combined into larger batches for

reduction. In a typical procedure, individual G-O suspensions were combined into a 3 L round bottom flask and the pH was adjusted to ~11.5 using potassium hydroxide. Then, hydrazine monohydrate ($N_2H_4 \cdot H_2O$) in an amount equal to 1 μl per 1 mg of GO was added to the flask, which was allowed to stir for 48 h at 30 ºC to produce a kinetically-stable suspension of RG-O platelets in water.

As some mass is lost from G-O platelets upon reduction, it was desired to quantify this loss in order to determine the proper mass of GO to use to achieve a desired loading of RG-O platelets in the nanocomposites. For this step, an aqueous RG-O suspension produced from 500 mg GO was coagulated with formic acid, then filtered, dried, and weighed. This procedure was performed twice, giving an average ratio of RG-O to GO mass of 0.61. Thus, for mixing calculations, the required mass of RG-O to achieve a certain loading was calculated, and that number was then divided by 0.61 to get the amount of GO needed for that nanocomposite batch.

A latex co-coagulation procedure was used to produce the nanocomposites. NR latex supplied by Goodyear Tire & Rubber Company with a solids fraction of 61% was weighed in calculated amounts to produce nanocomposites at specific loading intervals corresponding to 2, 3, 4, and 5 wt% RG-O platelets. The RG-O suspension and NR latex were added to a beaker and stirred vigorously for 5 min until the mixture appeared homogeneous. Co-coagulation was induced by rapid addition of 10 v/v% formic acid solution. The solid(s) formed upon coagulation was isolated by vacuum filtration and dried.

Following the co-coagulation procedure, the composites were processed by two different routes to incorporate curing agent and investigate the effect of processing on morphology. One set of composites was worked on a two-roll mill (Two-roll prep mill, 4" x 8" rolls, CW Brabender Instruments). The rolls were set to a temperature of ~80 °C, a speed of 15 RPM with a friction ratio of 1.3:1, and a nip gap of 1 mm. The milling time for each batch was approximately 12 minutes. Dicumyl peroxide (DCP; 98%, Aldrich) was used as the curing agent and added at a concentration of 1 phr (part per hundred rubber), unless otherwise specified (see Section C.5). For each batch, approximately 50 g of rubber or composite was used to allow the rubber to band over the rolls, while the temperature was adjusted to create an elastic band (i.e., no crumbling/tearing of the banded compound) over the front roll in attempt to provide the best dispersion possible.[14] In addition, a neat NR control batch was prepared using the same milling conditions.

The remainder of the nanocomposites was processed in a manner as to preserve the morphology created by the co-coagulation process. In this procedure, which will henceforth be referred to as the "solution treatment" procedure, the solids (in the form of small pellets) were soaked for 24 h in a solution of DCP in toluene to swell the rubber and implant DCP into the matrix. Unless otherwise specified, 1 phr of DCP was added to the minimal amount of toluene which immersed the pellets completely. After the rubber was completely swollen by the DCP/toluene mixture, the toluene was then removed by vacuum drying for 1 week at room temperature.

Hot pressing was used to form and cure samples for testing (Wabash hydraulic press, 50-1512-2TM). Except where otherwise specified, the samples were cured at 150

°C for 60 min under a 40 kip load. The optimum curing time/temperature was determined by trial and error based upon literature precedent, as described at length in the Appendix C. For comparison, uncured nanocomposite pellets were loaded into molds and pressed for 15 min at 150 ºC and 40 kip to form parts for testing.

TEM, SEM, and WAXS were used to characterize nanocomposite morphology. For TEM imaging, thin sections (~70 nm) of composite were cut using a cryoultramicrotome (Leica Inst., DiATOME cryo 35º diamond blade) with a -120 ºC chamber temperature and a knife temperature of -95 ºC. Sections were collected onto 300 mesh Gilder grids from Ted Pella. TEM digital micrographs were acquired using a JEOL 2010F at 200 kV. SEM images were obtained using an FEI Quanta-600 FEG Environmental SEM at 20 kV and 10^{-6} torr. X-ray scattering was performed on a Philips X-PERT diffractometer using Cu Kα radiation, a generating voltage of 40 kV, a current of 30 mA, and a 2 s dwell time.

Uniaxial tensile testing was performed at room temperature with an MTS machine equipped with a 25 lb Honeywell load cell and spring-loaded clamps to prevent slippage of the specimens during testing. Data was acquired using LabVIEW. Samples were "dog-bone" shaped with approximate test section dimensions of 20 x 4 x 1 mm. Milled samples were stretched three times to an elongation of 200% prior to testing to correct for stress softening (Mullins effect[15]); green and solution treated samples were not pre-strained prior to testing due to their low elongations to break. The strain rate for all tests was 250 mm/min unless otherwise noted. DMA was performed using a TA Instruments Q800 DMA. All tests were conducted at 10 Hz from -100 ºC to 50 ºC with a ramp rate of 2

ºC/min, a strain of 0.1% to 1% (depending on loading), and a static preload of 0.01 N. Samples had dimensions of approximately 15 x 5 x 1 mm.

Electrical conductivity measurements were made using a HIOKI Ultramega ohmmeter (SM-8220) with a HIOKI SM-8000 series electrode and enclosure. Volumetric and surface resistivity measurements were made with this instrument and used to determine the volumetric and surface conductivities, respectively. The electrical conductivity of the highly conductive samples was measured with a Keithley 2410 electrometer, connected to the same HIOKI enclosure. Thermal conductivity was tested using a Hot Disk TPS 2500, with a probe type 5501, at ambient temperature. The thermal conductivity was calculated from the density, specific heat, and thermal diffusivity of the material as measured. Samples for electrical conductivity measurements were disk-shaped and ~1 mm thick with a surface area (of one face) of at least 1 cm^2. Thermal conductivity samples measured 51 mm x 51 mm x 6.4 mm.

5.3. LATEX MIXING AND CO-COAGULATION PROCESS

Latex mixing and co-coagulation is a process analogous to the solution mixing procedure commonly described in the literature, except polymer latex is used instead of a polymer solution. NR latex consists of latex particles with a broad distribution of sizes, ranging from 100 nm to 2 μm in diameter (see Appendix C for SEM images of latex particles). The pH of the as-received NR latex was 10.6, thus addition of the latex to the alkaline RG-O suspension did not lead to coagulation of the suspension. After the NR latex and RG-O suspension were mixed together to form a mixture with a homogeneous

appearance, dilute formic acid solution was added to the mixture to drive co-coagulation. Acid causes both the latex particles and the RG-O platelets to coagulate simultaneously. As a result, some of the single-layer RG-O platelets may re-stack to form multi-layer RG-O tactoids upon coagulation; these observations support the intuitive notion that it becomes more likely for platelets to re-stack as the RG-O content increases in the mixture (i.e., the loading increases). No attempt was made to optimize the coagulation process or study the effect (if any) of different coagulants and speed of addition of coagulant on morphology and properties. Rather, acid solution was added rapidly to the mixture, following the argument of Wu and co-workers.[10]

Following addition of the formic acid solution to the mixture, complete coagulation appeared to occur over a timescale of approximately 10 seconds. For nominal RG-O loadings of 6 wt% and lower, the supernatant remaining after coagulation was clear and colorless. If the loading of RG-O was increased further, then the supernatant would appear cloudier and slightly grey in color. At 10 wt% nominal loading of RG-O, it was evident that the flocculation of RG-O platelets was occurring more rapidly than coagulation of the NR latex particles, as some NR latex would coagulate separately from the composite, resulting in a "salt and pepper" appearance to the coagulated solid. The form of the coagulated solid also changed with RG-O loading. When neat NR latex was coagulated, the latex particles clumped together to form a single, large mass of rubber. As the loading of RG-O was increased, the solids became pellet-shaped and gradually decreased in size (~1 mm in diameter at 5 wt%). At 10 wt%, the coagulated solid took on

a similar appearance to flocculated RG-O platelets, the coagulated solid consisting of sub-millimeter small particles.

5.4. NANOCOMPOSITE MORPHOLOGY

WAXS was used to assess the state of dispersion by comparing scattering patterns of the nanocomposites with those of neat NR. Comparing the spectra of the solution treated nanocomposites at various loadings, a slight shoulder corresponding approximately to the d-spacing of graphite (0.8 nm) emerged at 5 wt% which became particularly pronounced by 10 wt%, suggesting the presence of a significant concentration of multi-layer tactoids (see Figure C.1). WAXS was also used to compare the state of dispersion between the solution-treated and milled nanocomposites. Close inspection of Figure 5.1 reveals that the presence of this shoulder in the spectrum is diminished following the milling process, indicating that milling improves the dispersion.

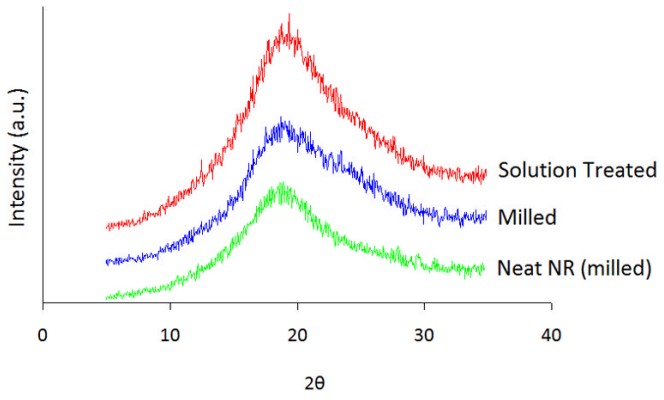

Figure 5.1. Comparison of WAXS spectra of neat NR, milled RG-O/NR, and solution treated RG-O/NR nanocomposites with 5 wt% RG-O platelets.

TEM was also used to examine the dispersion of the nanocomposites. Figure 5.2(a-b) shows the representative micrographs from uncured nanocomposite samples. The images show a nonuniform particle density over the cross-section, with submicron regions void of particles surrounded by areas of high particle density. It is speculated that the regions void of reduced graphene oxide platelets correspond to the locations of a latex particle or clumps of particles (Figure C.6 shows latex particle SEM images)—evidently, the hot pressing procedure appears to preserve the morphology created by the co-coagulation procedure. A similar morphology has been achieved by latex co-coagulation of layered silicates and natural rubber. For example, Varghese and Karger-Kocsis identified a "skeleton" structure via TEM following co-coagulation of sodium montmorillonite with NR latex (though they processed composites via solution casting, rather than hot pressing).[11] A significant concentration of multi-layer tactoids are clearly visible in some of the micrographs, which is likely due to restacking of the platelets during the coagulation process. It should be noted that thicker tactoids were more prevalent at 5 wt% than at 3 wt% (see TEM micrographs in Appendix C; Figures C.7 and C.8), suggesting that the higher the ratio of NR latex to RG-O platelets, the greater the likelihood that a latex particle would interrupt the flocculation and re-stacking of the RG-O platelets.

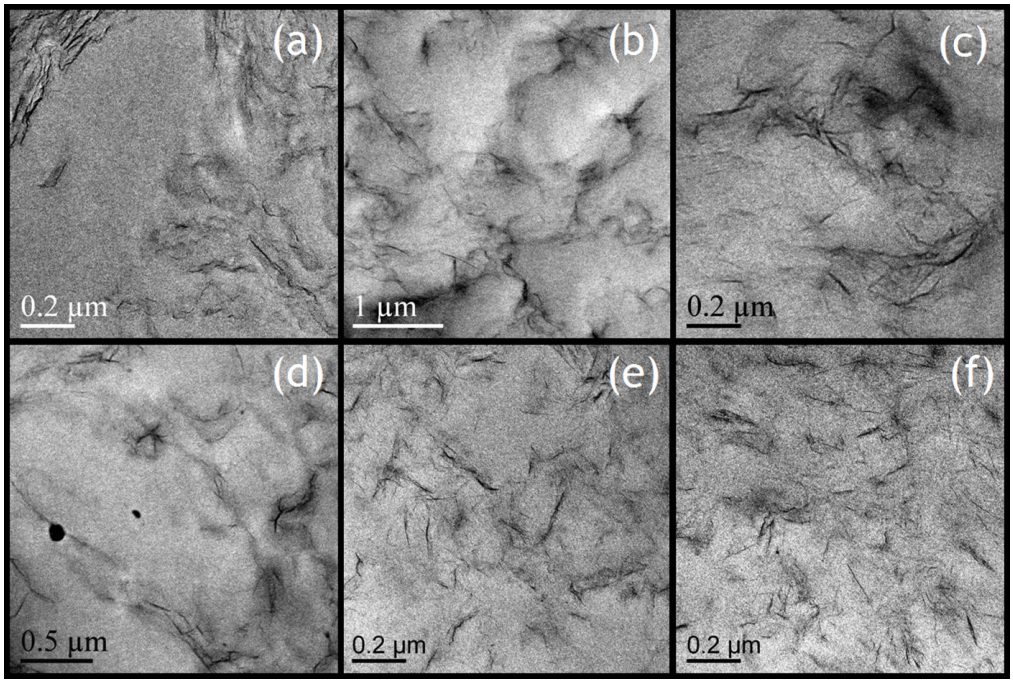

Figure 5.2. TEM micrographs of RG-O/NR nanocomposite sections. Images (a) and (b) show the "web-like" dispersion of RG-O platelets in the uncured composites, as obtained directly after latex co-coagulation. Images (c) and (d) show the dispersion in the solution treated samples, while images (e) and (f) show the morphology of the milled nanocomposites.

Images (c) and (d) in Figure 5.2 are micrographs of RG-O/NR vulcanizates processed by solution treatment. The strong resemblance of the morphology to the micrographs of Figure 5.2(a) and (b) suggests that the morphology created by latex co-coagulation is preserved if the peroxide curing agent is implanted into the rubber by solution treatment (i.e., swelling of the rubber matrix does not appreciably affect the filler morphology). Images (e) and (f) are micrographs of RG-O/NR nanocomposites which were worked on the two-roll mill. It is evident that the segregated "web-like" morphology

created by latex co-coagulation is destroyed by the milling process. The platelets are much more uniformly distributed over the cross-section and appear highly disoriented, as evidenced by the dark grey regions around the black platelet edges. Perhaps surprisingly, a significant amount of platelet disorientation was observed in the milled nanocomposites, despite the intense shear forces generated in the nip of a two-roll mill that would be expected to orient the platelets along a common axis.

Quantitative analysis of representative TEM micrographs of the solution treated and milled nanocomposites indicate a better dispersion for the milled compounds, with a slightly higher number average aspect ratio in the milled sample of roughly 44 versus 41 for the solution treated samples. Significantly fewer low aspect ratio platelets were observed in the milled samples. Thus, two-roll mil processing appears to improve the quality and uniformity of the dispersion for latex co-coagulated RG-O/NR nanocomposites.

5.5. ELECTRICAL AND THERMAL CONDUCTIVITY

Differences in nanocomposite morphology had a significant impact on the electrical and thermal conductivity properties. As evident from Figure 5.3, the solution treated samples showed a much lower electrical conductivity percolation threshold and higher electrical conductivity values than the milled samples. These results can be directly attributed to the difference in morphology between the two types of samples. Confinement of RG-O platelets between latex particles promotes a lower effective

"percolation threshold" whereby a large increase in nanocomposite conductivity is observed: since the effective volume fraction of the RG-O platelets in the interstitial areas between latex particles is much greater than the nominal volume fraction of the bulk composite, the probability of inter-particle contact is significantly greater than the case of statistical percolation of a uniform filler dispersion at an equivalent volume fraction ϕ. The segregated filler networks in the solution treated samples provide more pathways for conduction compared with the milled samples, wherein the well-dispersed platelets are coated with a sheath of polymer which inhibits electrical conduction through the filler network (requiring conduction by tunneling), resulting in lower values of electrical conductivity above the percolation threshold.[16] As shown in Appendix C, the conductivity properties of the solution treated nanocomposites are very similar to the green nanocomposites, highlighting the morphological similarities between the two types of samples observed by TEM.

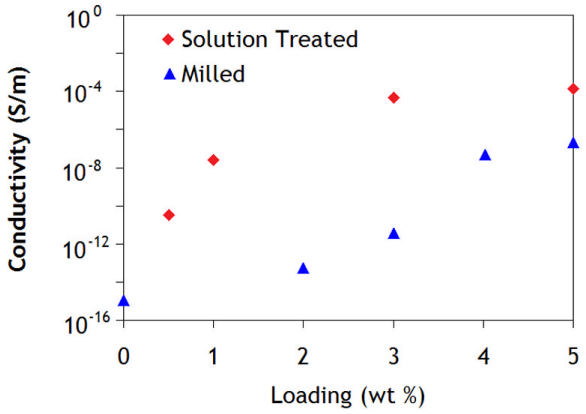

Figure 5.3. Volumetric electrical conductivity of solution treated and milled RG-O/NR nanocomposites as a function of RG-O loading.

As observed with the electrical conductivity, the network morphology of the solution treated composites is beneficial for thermal conductivity enhancement, although the difference in thermal conductivity between the two sample types is far less pronounced. Thermal conductivity results are summarized in Figure 5.4. At 5 wt%, the measured thermal conductivities of the solution treated and milled nanocomposites was 0.219 W/m·K and 0.188 W/m·K, respectively, compared with 0.157 W/m·K for neat NR. A slight improvement in thermal stability of NR was observed with incorporation of RG-O as shown in Figure C.11 in Appendix C.

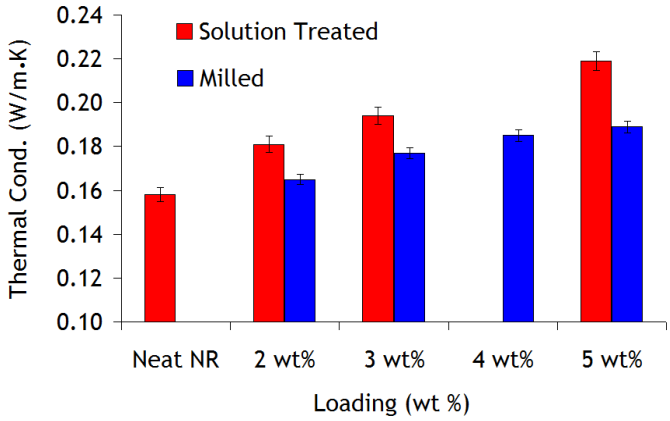

Figure 5.4. Thermal conductivities of milled and solution treated RG-O/NR nanocomposites at various loadings.

5.6. Mechanical and Viscoelastic Properties

Regardless of the processing conditions or cure state, the mechanical properties of NR were altered significantly by the RG-O platelets. Figure 5.5 illustrates trends in the

stress-strain behavior of the solution treated and milled nanocomposites. It should noted that morphological factors are not entirely responsible for the difference in properties—it is well-known that the milling process breaks down the latex particles and lowers the average molecular weight of the chains due to mechanochemical degradation, lowering the modulus of the rubber.[17, 18] However, after normalizing composite moduli to each type of control NR specimen (solution treated or milled), major differences in the property trends were evident between the two types of samples. All nanocomposites showed increased modulus and strength versus neat NR, but the dependence of modulus on RG-O loading was particularly strong for the solution treated samples. It can be seen that the stress-strain behavior of these samples trended towards the stress-strain behavior of a thermoplastic (Figure 5.5(b)), similar to the behavior observed with the uncured nanocomposites shown in Figure C.12. The difference in stiffness between the 5 wt% milled and solution treated samples is significant enough to be easily detected by hand by stretching or bending the sample.

The stress-strain behavior of the milled RG-O/NR nanocomposites contrasts sharply with that of the solution treated samples. The stress-strain curves exhibit the sigmoidal shape characteristic of neat and filled NR, showing evidence of strain-induced crystallization at high elongation. Whereas modulus increases in the solution treated samples were most pronounced at low elongations, the reinforcement effect of RG-O platelets is most pronounced at high elongations in the milled samples. For milled samples, the strain at break was still found to decrease as the loading of RG-O was increased; however, the decrease was much less pronounced than with the solution

treated samples. The milled samples showed an average strain at break of 4.26 at 5 wt%, compared with 0.61 for the 5 wt% solution treated samples—less than the amount of strain sometimes used to define a rubber (greater than 1)[19]—representing a 49% and 90% decrease in elongation versus neat NR, respectively.

Figures 5.6 and 5.7 summarize results from the tests. Initial (elastic) modulus, modulus at 100% elongation (M100), modulus at 300% elongation (M300), tensile strength, and elongation at break were determined at various loadings according to ASTM D412. Because of the low elongations to break, M100 and M300 were not determined for the solution treated samples. Figure 5.7 compares the strength and strain to break of the solution treated and milled nanocomposites, emphasizing the trends evident from the stress-strain graphs of Figure 5.5. The low elongations to break observed with the solution treated composites translated to a significantly lower fracture toughness (energy to break) compared to the milled compounds. For both sets of composites, no significant variation in fracture toughness with loading was observed, but in both cases the 3 wt% samples showed the highest energy to break of the loadings tested (see Appendix C, Figure C.14).

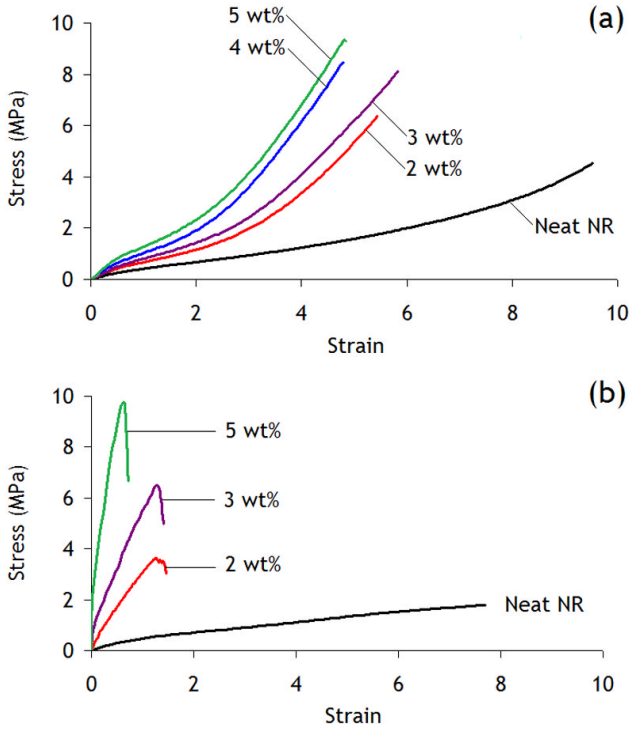

Figure 5.5. Representative stress-strain curves of the (a) milled and (b) solution treated RG-O/NR nanocomposites showing trends in the stress-strain behavior with filler loading.

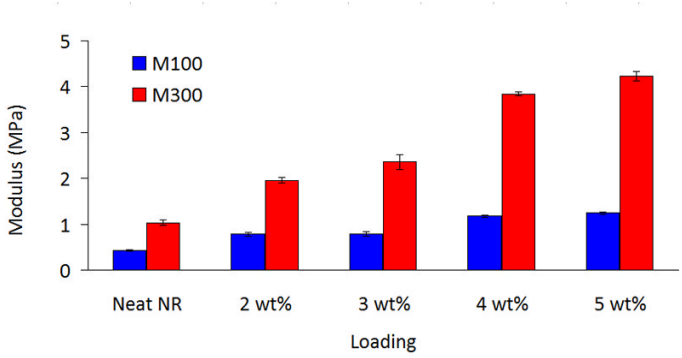

Figure 5.6. Variation in modulus at 100% elongation (M100) and 300% elongation (M300) with loading for milled RG-O/NR nanocomposites.

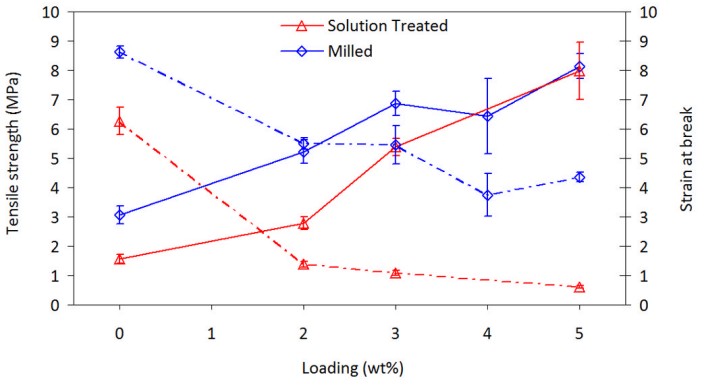

Figure 5.7. Comparison of tensile strength and strain at break between milled and solution treated RG-O/NR nanocomposites. Solid lines correspond to strength data and dashed lines indicate elongation data.

Results from DMA temperature scans are shown in Figure 5.8 and a tabular summary is provided in Appendix C, Table C.1. Larger increases in storage modulus (*E'*) were observed in the solution treated samples compared with the milled samples, although the significant difference in moduli observed between the milled and solution treated compounds in tensile testing was not reflected in the glassy moduli measured by DMA. As expected, increases in *E'* as well as disparities in *E'* between the two sample types became much more significant above T_g, as the modulus contrast between the polymer and filler (network) increases by several orders of magnitude. Comparing the storage moduli of 5 wt% nanocomposites to neat NR (Table C.1), the modulus increased by a factor of 3.4 and 2 at -100 °C, but by factors of 19.5 and 4.7 at 25 °C for the solution treated and milled nanocomposites, respectively. Strain sweeps of the nanocomposites at 25 °C showed a progressive decrease in the limiting linear strain with increasing RG-O

loading, with a sharp decrease in limiting strain at 4 wt% for the milled nanocomposites, coinciding with the onset of electrical percolation. This is the so-called "Payne effect"[20] as known in the rubber industry and more generally characteristic of filled composite melts,[21, 22] largely due to perturbation and breakdown of filler networks.[23-25] However, the solution treated samples were significantly more strain sensitive than the milled samples, supporting the existence of a more highly-connected filler network in the former type (see Figure C.15).

Analysis of tan delta and loss modulus (*E"*) peaks showed little to no change in T_g with loading; however, the shape and height of the peak changed significantly with incorporation of RG-O platelets. For both the solution treated and milled nanocomposites, a reduction in the height and breadth of the tan δ peak was observed. This suggests that RG-O has effectively immobilized NR chains near the polymer-particle interface due to favorable interfacial interactions with the NR matrix,[1] supporting the notion that favorable interfacial bonding exists in this system given the similarities in surface chemistry between RG-O and carbon black.[26, 27] The decrease in the tan δ peak amplitude was more significant for the solution treated nanocomposites—decreasing by approximately 70% and 38% for the solution treated and milled 5 wt% nanocomposites, respectively—which is the result of the large difference in *E'* between the two sample types near and above the transition zone.

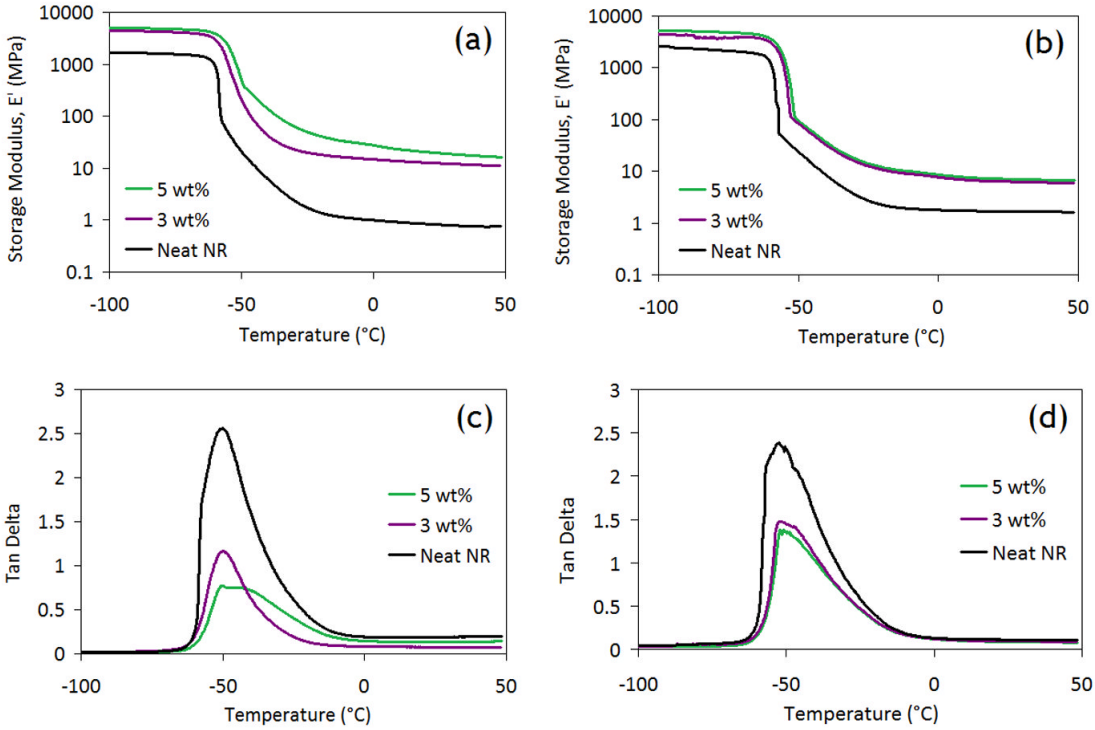

Figure 5.8. DMA plots of storage modulus versus temperature for the (a) solution treated and (b) milled RG-O/NR nanocomposites. Graphs (c) and (d) show plots of tan δ versus temperature for the solution treated and milled nanocomposites, respectively.

5.7. Discussion on Mechanical Properties

Mechanisms of reinforcement are strongly influenced by the dispersion morphology. While in both sets of nanocomposites the platelets were well-exfoliated with a high aspect ratio (see Section 5.8), in the solution treated compounds most of the platelets were arranged in a connected network structure formed within the interstitial areas between latex particles, promoting the formation of an elastic network of filler which greatly increased the stiffness of the compound. In addition, the stark difference in

elasticity of the solution treated and milled compounds may be due to the clustering of RG-O platelets in the interstitial areas between particles, preventing the interparticle diffusion of chains which provides cohesion between the latex particles. Thus, it is postulated that the web-like network morphology promotes formation of a sample-spanning elastic filler network which greatly increases stiffness, but which compromises the elongation performance by preventing welding of the interfaces between some of the latex particles.[28]

By contrast, the milled samples had a more homogeneous and uniform dispersion corresponding to the more "ideal" nanocomposite morphology. At low strains simple shear lag effects[29] result in significant initial modulus enhancement; at higher strains the uniformly-dispersed high aspect ratio RG-O platelets seemed to promote strain-induced crystallization of NR, as suggested by the Mooney-Rivlin plots in Figure 9 showing the shifting of the upturn in the curves to higher $1/\alpha$ values (thus lower strains) with increasing RG-O loading. Mooney-Rivlin analysis suggests that the crystallization process begins at progressively lower strains as the RG-O loading is increased. This conclusion is in agreement with recent work by Ozbas and co-workers, who investigated strain-induced crystallization of TEGO/NR nanocomposites[3] and, based on the ideas of Mullins and Tobin,[30] concluded that the large interfacial surface area of the platelets led to a pronounced strain amplification effect that promoted an early onset of strain-induced crystallization. Thus, modulus enhancement in the milled samples may be due to a combination of mechanical restraint by high aspect ratio platelets,[29] alignment of platelets during stretching, and promotion of strain-induced crystallization by the RG-O platelets.

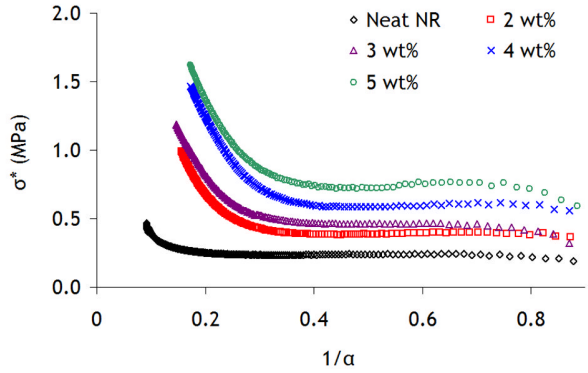

Figure 5.9. Mooney-Rivlin plots of the stress-strain curves shown in Figure 5(a), showing the progressive shifting of the onset of strain-induced crystallization to lower strains with increasing RG-O loading.

It may be noted that the modulus and strength enhancements achieved with RG-O in this study are comparable to those achieved with much higher loadings of carbon black in the literature.[30] Similar results have been reported for other nanofillers as well, such as organoclays.[31] The superior reinforcement capability of graphene-based materials likely results from a combination of the mechanisms described above—higher aspect ratio, alignment during stretching, and promotion of strain-induced crystallization. The higher aspect ratio structure of graphene is also the likely reason for the significantly lower electrical percolation threshold observed in the milled nanocomposites in this study, compared to conventional carbon black-filled compounds.[32]

5.8. QUANTIFYING DISPERSION: AN ANALYSIS OF COMPOSITE MODELS AND TEM MICROGRAPHS

A variety of micromechanical models have been developed to analyze and predict the mechanical properties of polymer composites when filled with particles of a known geometry.[33] Typical parameters in such models include the moduli of the matrix and filler, the volume fraction of filler, and a filler shape factor (e.g., aspect ratio). Some of these models provide analytical, closed form predictions of composite modulus based on these parameters allowing them to be easily utilized (see Appendix B), but many assumptions are required in their development, such as perfect interfacial adhesion and idealized filler geometries. These assumptions become more severe when these models are extended to the domain of polymer nanocomposites as particle-particle effects are ignored and the properties of the matrix polymer are assumed to be independent of the filler, despite evidence for a perturbation in polymer dynamics near a particle interface (the "interphase").[34-36] However, Fornes and Paul and others have shown that despite these simplifications, basic micromechanical models can effectively predict the properties of nanoclay/polymer nanocomposites.[29]

While the basic models considered in this work have similar predictive power, not all share the same conceptual foundation nor the same assumptions in their derivation. For example, Mori and Tanaka's model[37] was initially developed to describe the effect of inclusions in a metal based on Eshelby's solution to the equivalent inclusion problem; Tandon and Weng[38] extended Mori and Tanaka's model to describe a polymer composite and validated the model with experimental data. On the other hand, the widely-used Guth

equation to describe the elastic modulus of filled elastomers evolved from Smallwood's expression for the viscosity of filled liquids, and considers only hydrodynamic contributions to reinforcement by spherical or rod-like inhomogeneities.[39, 40] It was not the aim of this section to review or compare differences in the theoretical underpinnings of these models, as that has been covered elsewhere in detail.[33] Rather, the goal of this section was to select a few of the most-widely used models from the literature and compare their effectiveness in predicting the modulus of elastomers reinforced with graphene-based fillers or for quantifying filler dispersion in graphene-elastomer systems in terms of an average aspect ratio parameter, A_f.

An important component of most composite models is the modulus of the filler, which is challenging to determine for nanomaterials such as graphene.[41] To date, two studies have reported on the modulus of graphene platelets derived from GO.[42, 43] In one report, the modulus was found to be inversely proportional to the C : O ratio of the material; monolayer graphene oxide sheets exhibited a modulus of 650 GPa, while reduced graphene oxide had a modulus of 250 GPa.[42] In another report, graphene oxide was reported to have a modulus of 208 GPa, and no difference in modulus was reported between single and double-layer platelets at small strains. For the purposes of this analysis, 250 GPa was used as an estimate of the RG-O platelet stiffness. However, it should be noted that for this system, variations in the filler modulus have little influence on the predictions of the models. As pointed out by Kim and co-workers,[44] a plateau effect is predicted by the models as the ratio of filler to matrix modulus is increased beyond $\sim 10^4$ (assuming all other parameters held constant), a condition met by many

graphene/elastomer composite systems including the one in this study. The filler modulus is not used in the Guth equation and will thus have no effect on its predictions—see Appendix B for relevant equations.

For the calculations, values of the platelet shape factor or aspect ratio were varied in each model to achieve best fit to the data, as commonly performed in the literature in attempt to quantify filler dispersion in terms of the shape factor. Best fit curves to the data were generated, then the aspect ratio A_f (or shape factor f, in the case of the Guth model) was used as the independent parameter in the model and adjusted until the model prediction coincided with the line of best fit to the data points. The modified Halpin-Tsai model incorporates the maximum packing volume fraction ϕ_m of the filler as a parameter and was taken as 0.05 for RG-O platelets of nominal $A_f > 200$ based upon the treatise of Bicerano and co-workers[45] as described in Appendix B. The results of the curve fittings are summarized in Table 5.1. The Mori-Tanaka and Halpin-Tsai models predicted similar A_f values, showing large deviations from the data at higher loadings. The modified Halpin-Tsai model and Guth equation captured the trends in the data much more accurately, with a nonlinear increase in modulus as a function of ϕ. The shape factor in the Guth equation is also an aspect ratio but is defined for a rod-like inhomogeneity,[40] best fit to the data was achieved using a shape factor f of 44.

Table 5.1. Predictions of filler anisotropy—aspect ratio, A_f, or shape factor, f—by basic composite models.

Model	A_f or f
Mori-Tanaka	115
Halpin-Tsai	89
Modified Halpin-Tsai	53
Guth-Gold	44

To evaluate the effectiveness of the models, the predicted A_f or f was compared against the value determined from TEM analysis. In this Chapter, following a procedure described by Fornes and Paul,[29] average values of A_f were obtained from several representative TEM micrographs of 5 wt% green and milled composite samples. The procedure is illustrated in Figure A.1 and consists of converting the micrograph to a binary image to isolate the platelets from the background, then performing a shape analysis on each platelet following a spatial calibration of the micrograph. The software allows particle size to be analyzed in a variety of ways allowing for the platelet dimensions and thus average aspect ratio to be determined. It should be noted that the average value of aspect ratio determined by TEM analysis can vary significantly depending on the measurements of platelet size used in the software; these issues are discussed at some length in Appendix A. Briefly, each particle was modeled as an effective rectangle; the perimeter (measured by the software) was approximated to be half

the length of each particle while the thickness was calculated from the length and measured particle area.

A normalized histogram of particle A_f values determined from three different TEM micrographs of milled and green 5 wt% RG-O/NR nanocomposites is shown in Figure 5.10. The average A_f of the milled nanocomposites was found to be higher than for the green nanocomposites, suggesting an improvement in dispersion with milling. A considerably larger amount of low A_f tactoids (A_f < 20) was observed in the green composite micrographs. Assuming these micrographs to be truly representative of the sample dispersion, the difference may be attributed to the milling process driving further exfoliation of multi-layer tactoids. However, the higher frequency of low aspect ratio platelets in the green sample micrographs could be due to errors in identifying individual platelets. For instance, given the larger amount of platelet-platelet interaction evident from the green sample micrographs, there would be a greater probability of misidentifying two individual platelets as one thicker platelet.[29]

Comparing the values of A_f in Table 5.1 with the data shown in Figure 5.10, it appears that the Guth model provides the best results if the shape factor is interpreted directly as the aspect ratio of the platelets. In addition, the Guth equation captures the trend in reinforcement as a function of loading more effectively than the other models. Figure 5.11 compares the predictions of the four models using a shape factor or aspect ratio of 44 as determined by TEM analysis; the excellent agreement between the Guth model and the data is evident. The predictions of both the Mori-Tanaka and Halpin-Tsai

models differ from the A_f determined by microscopy by a factor of 2 or more, while the modified Halpin-Tsai model provides a much closer estimate.

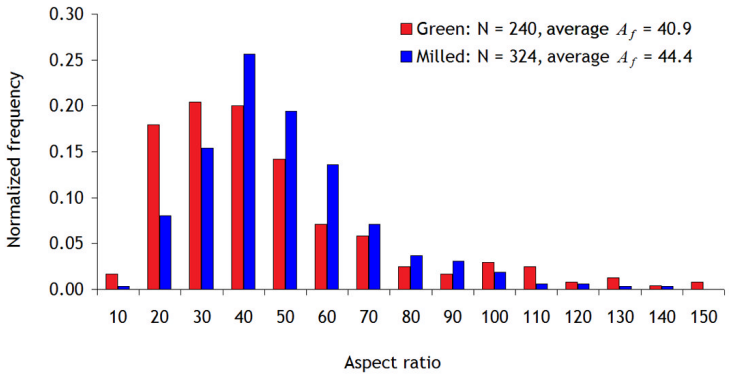

Figure 5.10. Histogram of aspect ratio (A_f) values for green and milled RG-O/NR nanocomposites as determined from TEM micrographs.

A similar analysis of composite models was conducted on nanoclay/rubber nanocomposites by Wu and co-workers,[46] who reported that the models over-predicted the modulus trends in the experimental data. To address this disparity, a filler "modulus reduction factor" was incorporated into the models in attempt to account for the effects of imperfect interfacial bonding,[47] disorientation/misalignment to the tensile axis, and multi-layer tactoids. According to their analysis, a factor of approximately 0.66 established a better agreement between the model predictions and experimental data, using the A_f values determined from TEM directly in the models. However, the results shown above suggest that no reduction factor is necessary for this system—all the models considered here either predict close to or below the experimental data when using A_f as determined

by TEM, obviating the need for any such reduction factor which would simply increase the disagreement between the models and the data.

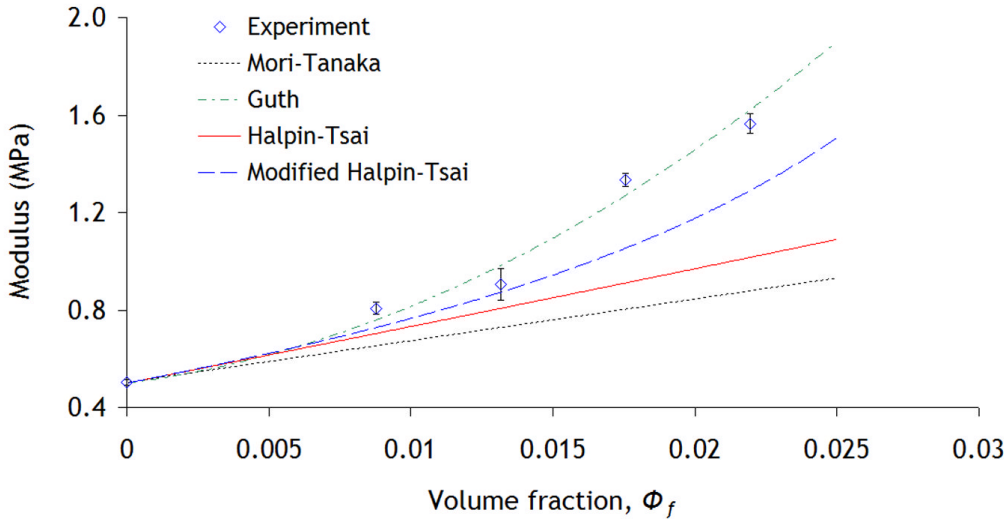

Figure 5.11. Comparison between the experimental modulus data of the milled RG-O/NR nanocomposites and predictions of the composite models, taking A_f = 44 as determined by TEM analysis.

SEM micrographs of isolated RG-O platelets (see Figure C.5) can allow estimation of platelet lateral dimensions following a similar procedure with the TEM micrographs; estimates of aspect ratio by SEM require assumption of platelet thickness which cannot be determined from SEM micrographs. Comparison of the average lateral dimension (not A_f) of the platelets as determined by TEM with the average diameter of the platelets observed in SEM micrographs reveals very different estimates of the average platelet size and distribution of sizes as discussed in Appendix A. The average platelet lateral dimension was 277 nm by SEM, while just 114 nm based on TEM analysis of the

nanocomposite sections (milled samples). The disparity could be due to several factors, most notably the irregular particle shape which makes it unlikely that the full width of the platelet would be directly visible and edge-on to the beam, and may not reflect actual changes in the dimensions of the platelets due to, e.g., particle attrition.[41] Even taking into account imperfect interfacial bonding[47] as well as other issues in quantifying dispersion from TEM micrographs,[29] the TEM quantification procedure likely underestimates A_f and thus the modified Halpin-Tsai model may indeed provide a closer estimate of the nanocomposite modulus based on the "true" particle aspect ratio.

Finally, this Chapter highlights the fact that one must be cautious in the interpretation of the A_f value determined from composite theory analysis of modulus data or other physical property measurements. All of these models assume a uniform dispersion of filler and when particle-particle interactions become significant, such as in the case of the solution treated or green compounds, the use of an A_f parameter from composite models to quantify the "quality" of the dispersion becomes questionable. Following the same procedure to analyze the experimental modulus data from the solution treated compounds, A_f predictions from the Mori-Tanaka and Halpin-Tsai models based on the fitting procedure described above were 1295 and 790, respectively. None of these models accurately modeled the trends in modulus with loading observed in the experimental data, and all predict unreasonably large aspect ratio values. The Guth equation was able to capture the trends in modulus much more effectively, but still over-estimated the filler anisotropy (f = 155). While composite theory predicts a higher aspect ratio for the solution treated samples, TEM and WAXS evidence suggests that A_f of the

solution treated samples was lower than the milled samples. Thus, these models can be used to fit to the data by adjusting A_f or f indiscriminately, but as expected they cannot be used to quantify dispersion in any meaningful way in the case of a network morphology with significant particle-particle interaction. In the case of the homogeneous dispersion, the models provide a much more accurate quantification of dispersion and indeed with the Guth equation, the predictions are very close to the experimental data. Moreover, the agreement between these models and the experimental data, along with the small change in T_g and Mooney-Rivlin analysis, suggest that reinforcement in the well-dispersed milled nanocomposites is largely due to two mechanisms: mechanical restraint—i.e., due to the high modulus and aspect ratio of the RG-O platelets rather than a perturbation in the properties of the rubber matrix[29]—as well as promotion of strain-induced crystallization by the high aspect ratio RG-O platelets.

5.9. CONCLUSIONS

Nanocomposites of RG-O platelets in a NR matrix were prepared by latex co-coagulation, then processed (to incorporate curing agent) by one of two methods: solution treatment or two-roll milling. It was demonstrated that the processing approach had a tremendous impact on the nanocomposite morphology and thus properties. Solution treatment (implantation of peroxide curing agent by swelling the NR in toluene) preserved the segregated filler network morphology produced by the co-coagulation procedure, whereas the milling process destroyed this network and generated a

homogeneous dispersion of RG-O platelets in the NR matrix. The continuous network morphology was shown to be advantageous for conductivity properties and greatly increased the stiffness of the composite versus neat NR, but also significantly reduced the elongation to break the samples. The milled nanocomposites also exhibited enhanced stiffness and strength while maintaining a high elongation to break. It was proposed that reinforcement in the solution treated or green nanocomposites was due to formation of a sample-spanning network of strongly-interacting RG-O platelets located in the interstitial regions between latex particles, whereas in the milled nanocomposites, reinforcement is due to simple mechanical restraint (i.e., modulus contrast between the polymer and well-dispersed filler) along with promotion of strain-induced crystallization by the high aspect ratio RG-O platelets.

The property changes with filler loading were analyzed using basic composite models established in the literature. The dispersion of filler for both sets of composite samples was quantified using models describing elastic modulus. In general, since property improvements changed more dramatically with filler loading in the case of the solution treated composites, a better dispersion (higher A_f) was predicted for these samples. However, quantifying dispersion by these models is not particularly meaningful in this instance, since the dispersion is highly non-ideal. It was indeed shown that there were significant discrepancies between the dispersion as quantified by TEM and the dispersion quantified by composite theory in the case of the solution treated samples. On the other hand, the composite models—in particular the Guth model—appeared to offer much more reasonable estimates of A_f (or f) for the milled nanocomposites, which had a

uniform and homogeneous filler dispersion. For samples processed on the mill, application of the Guth model or modified Halpin-Tsai model may provide meaningful and useful predictions for engineering purposes of modulus and/or quantifications of filler dispersion although a discrepancy appears to exist between the particle size determined by TEM and other methods.

The core focus of this work was on the significant impact that processing can have on morphology and properties. The property measurements on the milled RG-O/NR nanocomposites should be of significant interest from a technological perspective, as latex co-coagulation of nanocomposites followed by milling parallels the masterbatch processing approach that could be used industrially. The properties of the solution treated nanocomposites—with their low percolation threshold and low modulus, semicrystalline thermoplastic-like mechanical properties—could be of interest in their own right for certain applications.

5.10. REFERENCES

1. Galimberti, M., *Rubber-Clay Nanocomposites*. John Wiley & Sons: Hoboken, New Jersey, 2011.

2. Ozbas, B.; O'Neill, C. D.; Register, R. A.; Aksay, I. A.; Prud'homme, R. K.; Adamson, D. H. *Journal of Polymer Science Part B: Polymer Physics* **2012,** 50, 910-916.

3. Ozbas, B.; Toki, S.; Hsiao, B. S.; Chu, B.; Register, R. A.; Aksay, I. A.; Prud'homme, R. K.; Adamson, D. H. *Journal of Polymer Science Part B: Polymer Physics* **2012,** 50, 718-723.

4. Zhan, Y. H.; Wu, J. K.; Xia, H. S.; Yan, N.; Fei, G. X. *Macromolecular Materials and Engineering* **2011,** 296, 590-602.

5. Li, D.; Muller, M. B.; Gilje, S.; Kaner, R. B.; Wallace, G. G. *Nature Nanotechnology* **2008,** 3, (2), 101-105.

6. Park, S.; An, J. H.; Jung, I. W.; Piner, R. D.; An, S. J.; Li, X. S.; Velamakanni, A.; Ruoff, R. S. *Nano Letters* **2009,** 9, (4), 1593-1597.

7. Park, S.; Ruoff, R. S. *Nature Nanotechnology* **2009,** 5, (4), 217-224.

8. Zhang, L.; Wang, Y.; Wang, Y.; Sui, Y.; Yu, D.-S. *Journal of Applied Polymer Science* **2000,** 78, (11), 1873-1878.

9. Wang, Y.; Zhang, L.; Tang, C.; Yu, D.-S. *Journal of Applied Polymer Science* **2000,** 78, (11), 1879-1883.

10. Wu, Y.-P.; Wang, Y.-Q.; Zhang, H.-F.; Wang, Y.-Z.; Yu, D.-S.; Zhang, L.-Q.; Yang, J. *Composites Science and Technology* **2005,** 65, 1195-1202.

11. Varghese, S.; Karger-Kocsis, J. *Polymer* **2003,** 44, 4921-4927.

12. Valadares, L. F.; Leite, C. A. P.; Galembeck, F. *Polymer* **2006,** 47, (2), 672-678.

13. Pojanavaraphan, T.; Magaraphan, R. *European Polymer Journal* **2008,** 44, (7), 1968-1977.

14. White, J. L., *Rubber Processing: Technology - Materials - Principles*. Hanser/Gardner: Cincinnati, Ohio, 1995.

15. Mullins, L. *Rubber Chemistry and Technology* **1969,** 42, 339-362.

16. Bauhofer, W.; Kovacs, J. Z. *Composites Science and Technology* **2009,** 69, (10), 1486-1498.

17. Busse, W. F. *Industrial & Engineering Chemistry Research* **1931,** 24, (2), 140-146.

18. Mark, J. E.; Erman, B.; Eirich, F. R., *The Science and Technology of Rubber*. 3rd ed.; Elsevier 2010.

19. Wood, L. A.; Bullman, G., W. *Journal of Polymer Science* **1972,** 10, 43-50.

20. Payne, A. R. *Journal of Applied Polymer Science* **1962,** 6, (19), 57-63.

21. Kim, H.; Macosko, C. W. *Macromolecules* **2008,** 41, (9), 3317-3327.

22. Krishnamoorti, R.; Yurekli, K. *Current Opinion in Colloid & Interface Science* **2001,** 6, 464-470.

23. Bokobza, L. *Macromolecular Materials and Engineering* **2004,** 289, 607-621.

24. Wang, X.; Roberston, C. G. *Physical Review E: Statistical, Nonlinear, and Soft Matter Physics* **2005,** 72, 031406.

25. Voet, A. *Journal of Polymer Science: Macromolecular Reviews* **1980,** 15, 327-373.

26. Donnet, J.-B.; Voet, A., *Carbon Black: Physics, Chemistry, and Elastomer Reinforcement*. Marcel Dekker: New York, 1976; p 351.

27. Dreyer, D. R.; Park, S.; Bielawski, C. W.; Ruoff, R. S. *Chemical Society Reviews* **2010,** 39, (1), 228-240.

28. Steward, P. A.; Hearn, J.; Wilkinson, M. C. *Advances in Colloid and Interface Science* **2000,** 86, 195-267.

29. Fornes, T. D.; Paul, D. R. *Polymer* **2003,** 44, (17), 4993-5013.

30. Mullins, L.; Tobin, N. R. *Journal of Applied Polymer Science* **1965,** 9, 2993-3009.

31. Arroyo, M.; Lopez-Manchado, M. A.; Herrero, B. *Polymer* **2003,** 44, (8), 2447-2453.

32. Nan, C.-W.; Shen, Y.; Ma, J. *Annual Review of Materials Research* **2010,** 40, 131-151.

33. Tucker, C. L.; Liang, E. *Composites Science and Technology* **1999,** 59, 655-671.

34. Ellison, C. J.; Torkelson, J. M. *Nature Materials* **2003,** 2, (10), 695-700.

35. Bansal, A.; Yang, H.; Li, C.; Cho, K.; Benicewicz, B. C.; Kumar, S. K.; Schadler, L. S. *Nature Materials* **2005,** 4, (9), 693-698.

36. Rittigstein, P.; Priestley, R. D.; Broadbelt, L. J.; Torkelson, J. M. *Nature Materials* **2007,** 6, (4), 278-282.

37. Mori, T.; Tanaka, K. *Acta Metallurgica* **1973,** 21, 571-574.

38. Tandon, G. P.; Weng, G. J. *Polymer Composites* **1984,** 5, 327-333.

39. Bergström, J. S.; Boyce, M. C. *Rubber Chemistry and Technology* **1999,** 72, (4), 633-656.

40. Guth, E. *Journal of Applied Physics* **1945,** 16, (20), 20-25.

41. Paul, D. R.; Robeson, L. M. *Polymer* **2008,** 49, (15), 3187-3204.

42. Gómez-Navarro, C.; Burghard, M.; Kern, K. *Nano Letters* **2008,** 8, (7), 2045-2049.

43. Suk, J. W.; Piner, R. D.; An, J.; Ruoff, R. S. *ACS Nano* **2010,** 4, 6557-6564.

44. Kim, H.; Abdala, A. A.; Macosko, C. W. *Macromolecules* **2010,** 43, 6515-6530.

45. Bicerano, J.; Douglas, J. F.; Brune, D. A. *Journal of Macromolecular Science, Part C: Polymer Reviews* **1999,** 39, (4), 561-642.

46. Wu, Y.; Jia, Q.; Yu, D.-S.; Zhang, L. *Polymer Testing* **2004,** 23, 903-909.

47. Shia, D.; Hui, C. Y.; Burnside, S. D.; Giannelis, E. P. *Polymer Composites* **1998,** 19, (5), 608-617.

Chapter 6:

Two-Roll Mill Processing of Thermally-Exfoliated Graphite Oxide/Natural Rubber Nanocomposites

6.1. INTRODUCTION

In this Chapter, the effectiveness of a "melt" compounding approach to disperse TEGO into NR was evaluated. Recent work has examined the preparation and properties of TEGO/NR nanocomposites produced by solution mixing.[1, 2] However, dispersion of TEGO into NR by direct compounding is of greater industrial significance as fillers such as carbon black are generally dispersed into elastomers without the use of solvents, using mixing equipment such as an internal (Banbury) mixer or, for smaller compounding operations, a two-roll mill.[3]

Preliminary measurements on nanocomposites produced by direct milling of TEGO into NR showed small property enhancements, particularly relative to the RG-O/NR nanocomposites which were the focus of the previous Chapter. In an attempt to improve properties further, ultrasound-assisted latex compounding was used to mix master batches of TEGO and NR prior to two-roll milling to break down the TEGO particles prior to milling. The effectiveness of these two processing approaches are

evaluated by comparing the morphology and properties of the two sets of TEGO/NR nanocomposites to each other and to NR filled with carbon black.

6.2. MATERIALS AND METHODS

GO was produced using a modified Hummers method as described in previous Chapters. To produce TEGO, GO was added into a 1 L beaker covered with aluminum foil on a hot plate set at 400 °C; this caused rapid expansion of the GO to yield a fluffy, black powder. The powder was collected from the beaker and dried for at least 24 h in a vacuum oven at 40 ºC prior to use. Carbon black (CB) from Alfa Aesar was used in this study, with a specific surface area of 50 m^2/g according to the manufacturer. NR latex was provided by Goodyear Tire & Rubber Company and DCP was used as-received from Aldrich. NR latex was coagulated with 5 vol% formic acid (Aldrich) and dried in vacuum prior to milling. Latex "pre-mixing" was achieved by adding TEGO powder to water (approximately 1 g in 1 L), treating on an ultrasonic bath for ~20 min with stirring, addition of NR latex and stirring/sonicating for 20 min, followed by co-coagulation with formic acid.

A two-roll prep mill (4" x 8" rolls, CW Brabender Instruments) was used for the mixing of filler and curing agent. The rolls were set to a temperature of approximately 60 °C, a speed of 15 RPM with a friction ratio of 1.3:1, and a nip gap of 1 mm. For each 5 part per hundred rubber (phr) masterbatch, a sufficient quantity of NR or composite was used to allow complete banding on the roll (>50 g). A total milling time of 10 min was

used for dispersion of filler into NR (10 min also used for the pre-mixed nanocomposites). It should be noted that the low bulk density of TEGO makes it susceptible to becoming airborne and flying away from the mill rather than mixing into the rubber. To address this issue, the TEGO was compressed by hand into pellets that were charged into the mill. After addition of filler, the rubber was cut from the mill and weighed to ensure that the mass had increased by the required amount. Portions of the 5 phr masterbatches were diluted with neat NR to achieve lower loading levels; at this stage DCP was added at a concentration of 1 phr. Milling time for dilution and DCP incorporation was approximately 10 min, for a total milling time of 20 min. 5 phr nanocomposites and neat NR batches were also milled for a total of 20 min. The neat NR and TEGO/NR nanocomposites were molded and cured in a Wabash hot press at 150 °C for 50 min under a 40 kip load.

TEM, SEM, and WAXS were used to characterize filler or nanocomposite morphology as described in Chapter 5. Uniaxial tensile testing was performed at room temperature with an MTS machine equipped with a 25 lb Honeywell load cell and spring-loaded clamps to prevent slippage of the specimens during testing. Five samples were tested at each loading for each type of filler. Data were acquired using LabVIEW. Dog-bone type samples had approximate test section dimensions of 20 × 4 × 1 mm. Samples were stretched five times to an elongation of ~200% prior to testing to correct for the Mullins softening. The strain rate for all tests was 500 mm/min. Dynamic mechanical analysis (DMA) tests were performed using a TA Instruments Q800 DMA. All tests were conducted at 10 Hz from -100 to 50 °C with a ramp rate of 3 °C/min, a strain of 0.1% to

1% (depending on loading), and a static preload of 0.01 N. Samples for DMA testing had dimensions of approximately 15 x 5 x 1 mm. Electrical conductivity and thermal conductivity tests were performed as described in Chapter 5.

XPS analysis was performed using a Kratos AXIS Ultra DLD spectrometer (monochromated Al K emission at 1486.6 eV with an operating power of 150 W). Determination of specific surface area using the Brunauer-Emmett-Teller (BET) equation was carried out on a Quantachrome Instruments Nova 2000 using nitrogen as the adsorbent at 77 K.

6.3. PROPERTIES OF TEGO

Figure 6.1 shows SEM micrographs of TEGO particles, revealing the "accordion-like" structure of the material consisting of highly wrinkled and exfoliated graphene-like platelets loosely stacked together. The TEGO material used in this study had a BET surface area of 454 m^2/g and a C : O ratio of 4 : 1, as determined by X-ray photoelectron spectroscopy (see Figure D1). This C : O ratio is lower than reported elsewhere for TEGO and may be due to the exfoliation temperature of 400 °C used in this study, as many other reports use temperatures of 1000 °C or more to produce TEGO.[3, 4] The lower processing temperature was chosen for more rapid production of larger quantities (~10 g) of TEGO in a glass beaker compared with tube furnace exfoliation and annealing at higher temperature.

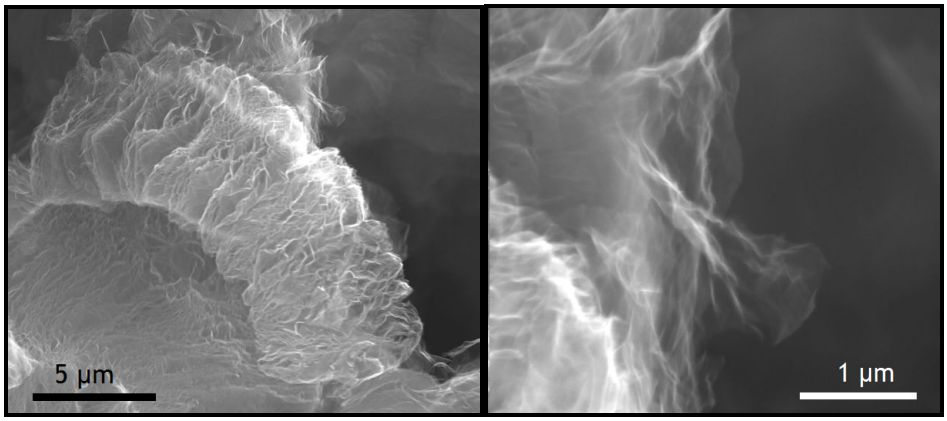

Figure 6.1. TEGO particles produced by thermal expansion of GO. SEM micrographs showing their accordion-like structure and highly wrinkled platelets.

6.4. NANOCOMPOSITE PROPERTIES

The high modulus and high aspect ratio of graphene-based materials confers significant modulus and strength improvements to polymers if properly dispersed. Several previous studies have demonstrated the effective dispersion of TEGO[5] and related materials[6] into various polymer matrices by melt compounding. Moreover, recent work has reported on the effective dispersion of layered silicates into NR by two roll mill processing.[7] In light of these results and the presumed thermodynamic compatibility between graphene-based materials and NR,[8] it was hoped that two-roll mill processing would lead to excellent dispersion of TEGO. However, the expected property improvements were not realized by this dispersion method alone. On the other hand, significant increases in modulus and strength were observed in TEGO/NR nanocomposites subjected to a latex "pre-mixing" step (henceforth, L-TEGO/NR). Figure

6.2 shows stress-strain curves from the two types of TEGO-reinforced NR nanocomposites.

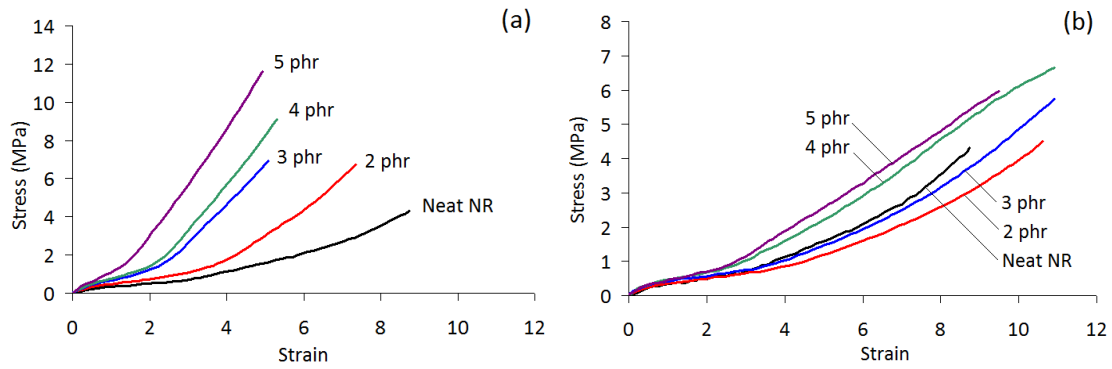

Figure 6.2. Representative stress-strain curves of (a) L-TEGO/NR nanocomposites and (b) TEGO/NR nanocomposites, each at various loadings.

Figure 6.3 summarizes mechanical property data over the range of loadings tested. The modulus at 100% elongation (M100) and at 300% elongation (M300) of the TEGO/NR nanocomposites decreased relative to neat NR at 2 phr and 3 phr loading, with small increases over neat NR with 4 and 5 phr TEGO. Conversely, at just 2 phr, M100 of the L-TEGO/NR nanocomposites was 38% higher than the M100 of the 5 phr TEGO/NR nanocomposites. Differences in M300 enhancement were particularly pronounced between the two types of nanocomposites. Mirroring the trends observed in RG-O/NR nanocomposites, the L-TEGO/NR nanocomposites showed increasing tensile strength but decreasing strain at break with increasing TEGO loading.

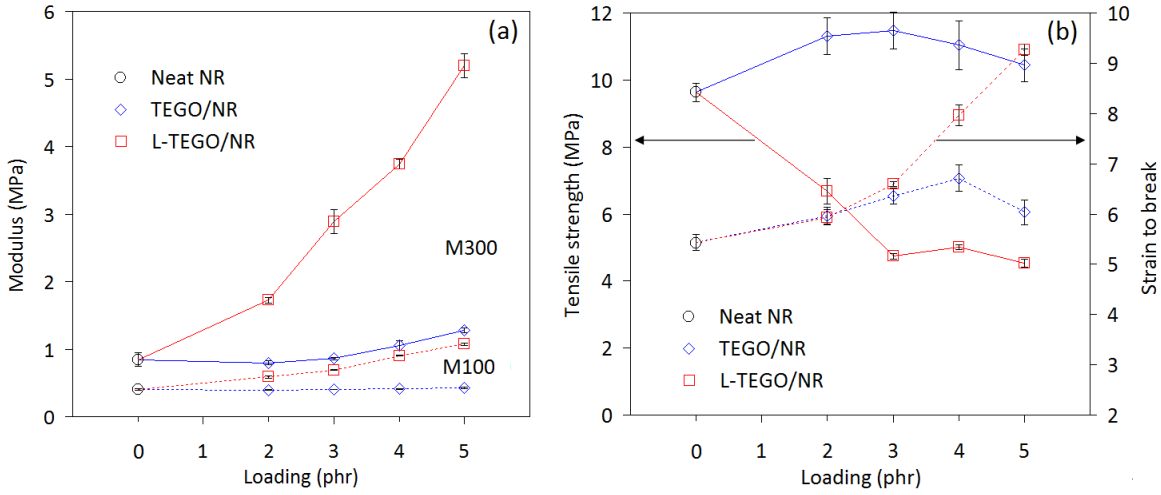

Figure 6.3. Summary of (a) modulus data, and (b) strength and elongation data of the nanocomposites. M100 and M300 represent modulus at 100% elongation and 300% elongation, respectively, as determined by ASTM D412.

The enhancement of electrical conductivity in polymer nanocomposites is strongly dependent upon the filler morphology; the formation of percolating pathways between filler particles is necessary to render an insulating polymer such as NR electrically conductive.[9] Work on RG-O/NR nanocomposites in the previous Chapter showed maximum enhancement in conductivity not when the filler was homogeneously dispersed, but rather arranged into a connected "web-like" structure of platelets. In this study, both processing approaches led to homogeneous filler dispersions, and consequently the electrical conductivity of these TEGO nanocomposites was lower than observed with the RG-O/NR nanocomposites. For homogeneous dispersions as produced by mill processing, more well-exfoliated platelets should result in maximum conductivity enhancement.[10] The L-TEGO/NR nanocomposites exhibited higher conductivity both in

and out of the sample plane, suggesting a better dispersion or higher average aspect ratio of the dispersed platelets compared with the TEGO/NR nanocomposites (Figure 6.4).

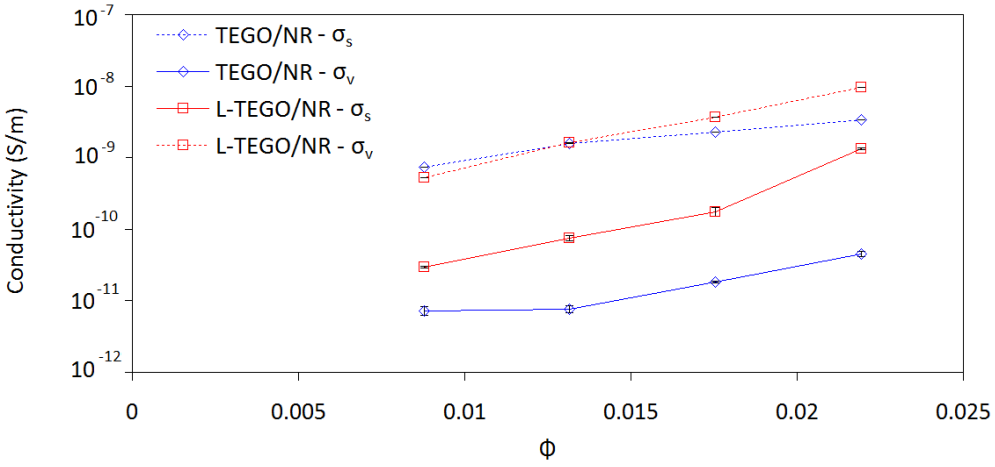

Figure 6.4. Electrical conductivity of TEGO/NR and L-TEGO/NR nanocomposites as a function of volume fraction of TEGO, ϕ. Solid lines indicate volumetric conductivity data (σ_v; through-plane) and dashed lines indicate sheet conductivity data (σ_s; in-plane).

Figure 6.5 shows Mooney-Rivlin plots of reduced stress σ^* versus reciprocal extension ratio α based on the selected stress-strain curves presented in Figure 6.2. The upturn in σ^* shifts to lower $1/\alpha$ values with higher loading as a result of promotion of strain-induced crystallization by the presence of the filler;[8, 11] this trend is particularly evident in the L-TEGO/NR Mooney-Rivlin curves. This comparison is further evidence for a better dispersion of filler in the L-TEGO/NR samples as described in the following section.

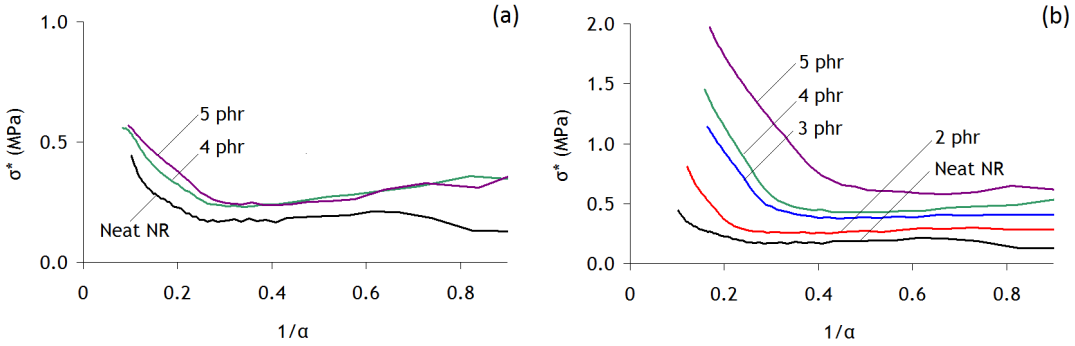

Figure 6.5. Mooney-Rivlin plots of (a) TEGO/NR and (b) L-TEGO/NR nanocomposites (curves for 2 and 3 phr TEGO/NR nanocomposites not included for clarity).

6.5. NANOCOMPOSITE MORPHOLOGICAL EVALUATION AND COMPOSITE THEORY ANALYSIS

Based on the property measurements presented in Section 6.4, it was expected that morphological characterization via WAXS and TEM would reveal an improved dispersion in the L-TEGO/NR nanocomposites compared with the TEGO/NR nanocomposites. As shown in Appendix D (Figure D.2), no evidence of a graphite or GO peak was observed in the WAXS spectra, suggesting an exfoliated morphology in both types of nanocomposites.

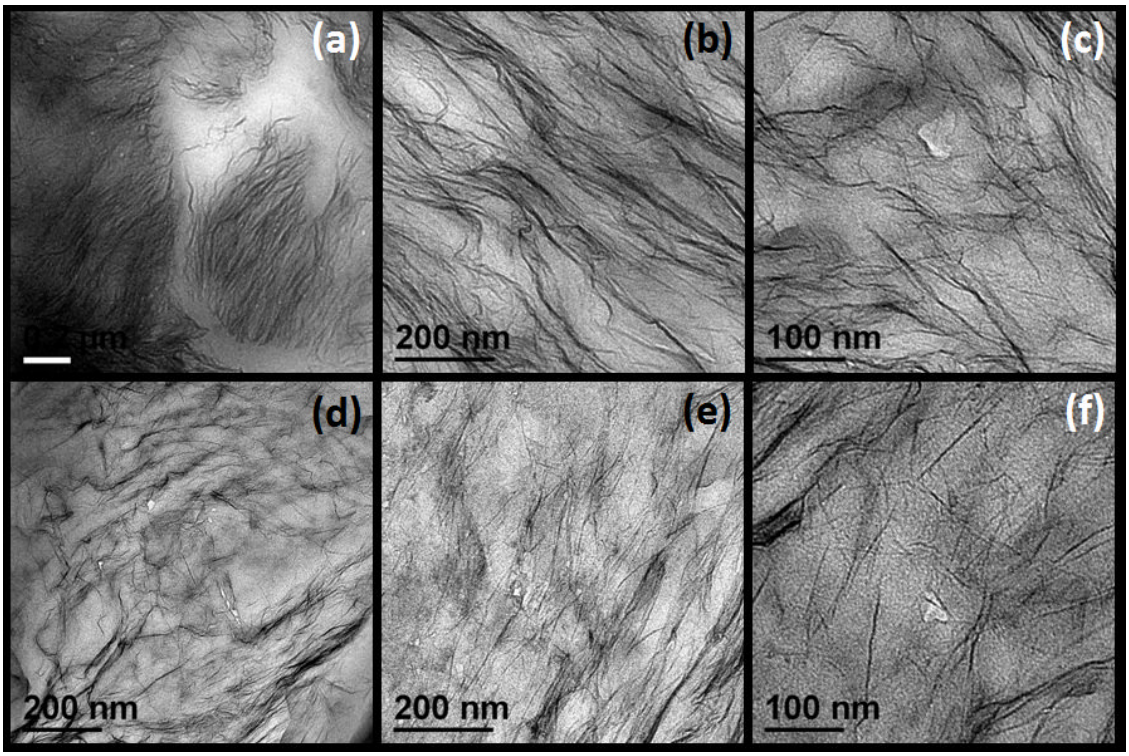

Figure 6.6. TEM micrographs of (a-c) TEGO/NR and (d-f) L-TEGO/NR nanocomposites. Scale bar in image (a) is 200 nm.

TEM micrographs of thin sections of the nanocomposites are presented in Figure 6.6 and show some clear differences in the dispersions. TEGO/NR micrographs revealed significant variation in the dispersion over the cross section—some regions showed highly-exfoliated, randomly-oriented platelets while others showed large particles consisting of bundles of platelets (see Figure 6.6(a) and Figure D.5). Many platelets exhibited wrinkled conformations, consistent with the disordered structure observed by SEM (Figure 6.1) and other observations on TEGO and TEGO-filled polymers.[4, 6] By comparison, the L-TEGO/NR nanocomposites exhibited a more uniform state of

dispersion, with far fewer unexfoliated TEGO particles. In addition, the platelets appeared less wrinkled in the L-TEGO/NR nanocomposites, perhaps because the dispersion of TEGO into pH 11 water by sonication could flatten out the corrugated platelets due to ionization of residual functional groups.[12] Evidently the ultrasonic treatment, despite not achieving a stable suspension of individual TEGO platelets, promotes breakup of large particles and facilitates the dispersion of few-layer TEGO platelets into the NR matrix.

It was sought to quantify the apparent improvement in dispersion in terms of an average aspect ratio of platelets, A_f. The methods utilized in the dispersion quantification procedure of Chapter 5 were extended to this work, to determine A_f of the two types of nanocomposites. Figure 6.7 presents a histogram of A_f values determined from several TEM images at various magnifications for both types of nanocomposites at 5 phr loading (see Figure D.6 for an illustration of the procedure). The amount of disorientation and platelet overlap made identification of individual platelets challenging, and thus the average A_f values may only represent a rough estimate.[13] Still, despite the tremendous dispersion enhancement suggested by the property measurements, similar average A_f values were determined from TEM analysis for the two types of nanocomposites—34 for TEGO/NR, compared with 38 for L-TEGO/NR. Even in light of the challenges in the procedure for quantifying dispersion,[13] the small disparity in A_f between the two types of nanocomposites suggests that the stark difference in mechanical properties cannot simply be attributed to more effective load bearing by higher aspect ratio particles.

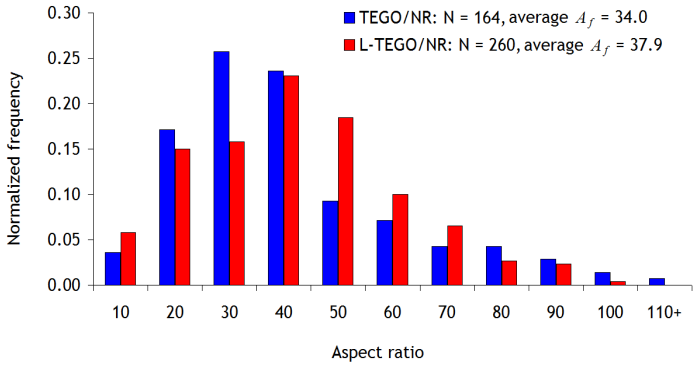

Figure 6.7. Histogram showing A_f values of TEGO platelets determined by image analysis of representative TEM images of TEGO/NR and L-TEGO/NR nanocomposites.

Indeed, closer inspection of the micrographs suggests that while the particle/tactoid aspect ratios may be similar, the average lateral and thickness dimensions of the individual platelets are not. The average platelet thicknesses and lateral dimensions were 2.0 nm and 77.6 nm for L-TEGO/NR, and 5.7 nm and 194 nm for TEGO/NR, respectively. Calculations of surface area to volume ratio at a fixed volume show that, assuming a perfect dispersion, the amount of interfacial surface area per unit volume is higher in the L-TEGO/NR nanocomposites by a roughly a factor of 3. This difference is likely greater as the presence of closely-spaced and overlapping platelets required some platelets to be excluded from the analysis. Tactoids consisting of many parallel, closely-spaced platelets would lower the average A_f if considered as a single particle, and such a morphology would be less effective for reinforcement compared with well-exfoliated and homogeneously-dispersed platelets as it would restrict the ability of the chains to adsorb

onto the platelet surface.[13] The impact of a higher amount of accessible interfacial surface area on mechanical properties can be qualitatively understood using the concept of "bound rubber" in which chains adsorbed onto the surface of TEGO platelets are immobilized and therefore increase the effective volume fraction of filler,[8] enhancing the strain amplification effect[14] of the filler and promoting strain-induced crystallization at lower applied strains. Thus while the average platelet A_f of the two dispersions were similar, the larger amount of accessible interfacial surface area and more uniform dispersion in the L-TEGO/NR nanocomposites could have resulted in the much larger reinforcement effect observed relative to TEGO/NR. Additionally, as enhancement in conductivity is largely governed by percolation of conductive platelets,[9, 10] the large gaps between tactoids evident in, e.g., Figure 6.6(a), could be responsible for the differences in thermal and electrical conductivity between the two types of nanocomposites.

The average A_f determined by w analysis was compared with composite models that exhibited close agreement with the experimental data on RG-O/NR nanocomposites from Chapter 5; further details on the calculations are provided in the Appendices B and D. As shown in Table 6.1, in this study good agreement between the Guth equation prediction and experimental modulus data was obtained when taking the shape factor f equal to A_f as determined from TEM analysis. The A_f of TEGO/NR nanocomposites determined by TEM analysis was larger than the predictions of any of the models investigated here, however. This could be due to the nature of the dispersion, consisting of high aspect ratio platelets arranged in a morphology roughly corresponding to an intercalated structure.

Table 6.1. Aspect ratio predictions of composite models based upon experimental initial modulus data.

Model	TEGO/NR	L-TEGO/NR
Guth equation	22	39
Modified Halpin-Tsai	18	47
Mori-Tanaka	33	90

6.6. COMPARISON OF TEGO AND CARBON BLACK-FILLED NR

What advantage, if any, do graphene-based fillers provide over carbon black, the most widely-used reinforcing filler material? Table 6.2 summarizes the properties of TEGO and CB-filled NR nanocomposites at 5 phr loading. Properties of RG-O/NR nanocomposites produced by latex co-coagulation,[15] subjected to a similar milling procedure and cured with 1 phr DCP, are also presented for reference. Clearly, despite the dramatic property enhancement conferred by the latex pre-mixing procedure, the mechanical property improvements of the L-TEGO/NR nanocomposites were considerably smaller than achieved with the RG-O/NR nanocomposites. Mechanical property enhancements with CB were comparable to TEGO when dispersed into NR directly on a two-roll mill. CB also provided larger enhancement in thermal conductivity than any of the graphene-based fillers, although it provided the lowest enhancement in electrical conductivity. This latter result may be explained in part by observations that the thermal conductivity decreases with increasing modulus contrast between the matrix and filler, due to increasing Kapitza resistance.[16-18] The greater modulus and aspect ratio of

TEGO platelets compared with CB could thus provide greater reinforcement and electrical conductivity enhancement (as higher aspect ratio promotes filler percolation), with the disadvantage of relatively smaller thermal conductivity enhancement.

Table 6.2. Property comparison of NR-matrix nanocomposites with different fillers at 5 phr loading. (Standard error of measurements omitted for clarity. Thermal conductivity represented by k, σ_v represents volumetric conductivity, and σ_s represents sheet conductivity. RG-O platelets were dispersed into NR by a latex co-coagulation method).

Filler	M100 (MPa)	M300 (MPa)	σ_t (MPa)	Strain at break	k (W/m·K)	σ_v (S/m)	σ_s (S/m)
TEGO	0.426	1.28	6.05	8.96	0.166	4.50×10^{-11}	3.41×10^{-9}
L-TEGO	1.074	5.2	10.9	5.03	0.180	1.32×10^{-9}	9.69×10^{-9}
CB	0.508	1.19	6.28	8.34	0.228	6.73×10^{-12}	5.36×10^{-10}
RG-O	1.588	9.01	10.2	3.19	0.190	5.10×10^{-6}	7.91×10^{-7}
Neat NR	0.405	0.842	5.15	8.44	0.157	6.72×10^{-16}	1.97×10^{-13}

Figure 6.8 shows results from DMA temperature scans on the nanocomposites. TEGO, L-TEGO, and CB-filled NR all showed similar average values of glassy modulus (approximately 3.8 GPa) and similar average T_g values (-44 to -46 °C), with the L-TEGO/NR samples showing the largest modulus in the rubbery region above T_g. All nanocomposites showed a decreased tan delta peak height and breadth versus neat NR, suggesting strong interfacial bonding between the matrix and filler.[15] L-TEGO/NR nanocomposites exhibited the smallest tan delta peak, reflecting the better dispersion of filler and higher accessible interfacial surface area in those samples.

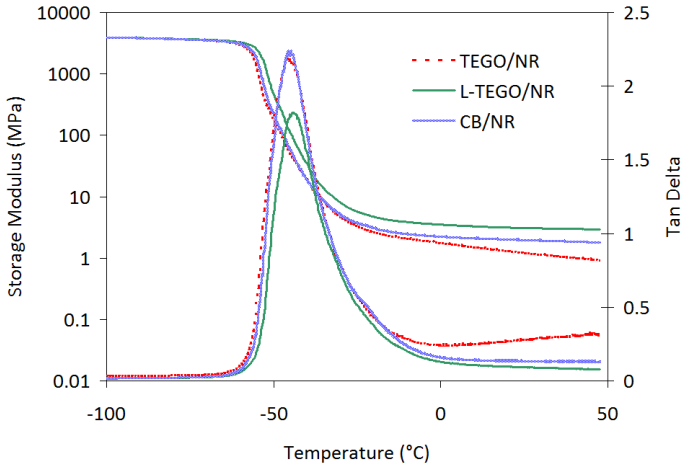

Figure 6.8. Dynamic mechanical analysis plots from temperature scans on the nanocomposites.

6.7. CONCLUSIONS

Two-roll mill processing was used to disperse TEGO into NR. Property improvements achieved by direct milling of TEGO into NR were small and comparable to those provided by carbon black; however, by pre-mixing TEGO with NR latex followed by milling, substantial property enhancements were achieved. As quantitative TEM analysis suggested a small difference in dispersion (in terms of an average platelet aspect ratio), the large property improvements in the L-TEGO/NR nanocomposites were attributed to a more uniform dispersion of TEGO platelets, coupled with a larger accessible interfacial surface area.

While ultrasonic treatment of TEGO in water does not produce a stable suspension of exfoliated TEGO platelets, it does serve to break down the particles and

facilitates the dispersion of high aspect ratio platelets into the NR matrix during milling. These results suggest that effective dispersion of TEGO into NR using conventional rubber processing equipment, without the use of solvents or pre-mixing with latex, could pose a significant challenge.

6.8. REFERENCES

1. Ozbas, B.; O'Neill, C. D.; Register, R. A.; Aksay, I. A.; Prud'homme, R. K.; Adamson, D. H. *Journal of Polymer Science Part B: Polymer Physics* **2012,** 50, 910-916.

2. Ozbas, B.; Toki, S.; Hsiao, B. S.; Chu, B.; Register, R. A.; Aksay, I. A.; Prud'homme, R. K.; Adamson, D. H. *Journal of Polymer Science Part B: Polymer Physics* **2012,** 50, 718-723.

3. Mark, J. E.; Erman, B.; Eirich, F. R., *The Science and Technology of Rubber*. 3rd ed.; Elsevier 2010.

4. McAllister, M. J.; Li, J. L.; Adamson, D. H.; Schniepp, H. C.; Abdala, A. A.; Liu, J.; Herrera-Alonso, M.; Milius, D. L.; Car, R.; Prud'homme, R. K.; Aksay, I. A. *Chemistry of Materials* **2007,** 19, (18), 4396-4404.

5. Schniepp, H. C.; Li, J. L.; McAllister, M. J.; Sai, H.; Herrera-Alonso, M.; Adamson, D. H.; Prud'homme, R. K.; Car, R.; Saville, D. A.; Aksay, I. A. *Journal of Physical Chemistry B* **2006,** 110, (17), 8535-8539.

6. Kim, H.; Abdala, A. A.; Macosko, C. W. *Macromolecules* **2010,** 43, 6515-6530.

7. Zhu, Y. W.; Murali, S.; Stoller, M. D.; Velamakanni, A.; Piner, R. D.; Ruoff, R. S. *Carbon* **2010,** 48, (7), 2118-2122.

8. Qureshi, M. N.; Qammar, H. *Materials Science and Engineering C* **2010,** 30, 590-596.

9. Bauhofer, W.; Kovacs, J. Z. *Composites Science and Technology* **2009,** 69, (10), 1486-1498.

10. Nan, C.-W.; Shen, Y.; Ma, J. *Annual Review of Materials Research* **2010,** 40, 131-151.

11. Zhan, Y. H.; Wu, J. K.; Xia, H. S.; Yan, N.; Fei, G. X. *Macromolecular Materials and Engineering* **2011,** 296, 590-602.

12. Ma, X.; Zachariah, M. R.; Zangmeister, C. D. *Nano Letters* **2012,** 12, 486-489.

13. Fornes, T. D.; Paul, D. R. *Polymer* **2003,** 44, (17), 4993-5013.

14. Mullins, L.; Tobin, N. R. *Journal of Applied Polymer Science* **1965,** 9, 2993-3009.

15. Potts, J. R.; Shankar, O.; Du, L.; Ruoff, R. S. *Macromolecules* **2012**, DOI: 10.1021/ma300706k.

16. Cui, W.; Du, F.; Zhao, J.; Zhang, W.; Yang, Y.; Xie, X.; Mai, Y.-W. *Carbon* **2011,** 49, 495-500.

17. Clancy, T. C.; Gates, T. S. *Polymer* **2006,** 47, 5990-5996.

18. Peters, J. E.; Papavassiliou, D. V.; Grady, B. P. *Macromolecules* **2008,** 41, 7274-7277.

19. Galimberti, M., *Rubber-Clay Nanocomposites*. John Wiley & Sons: Hoboken, New Jersey, 2011.

Chapter 7:

Natural Rubber Nanocomposites by Latex Compounding: Effect of Filler Structure and Aspect Ratio

7.1. INTRODUCTION

In Chapter 1 it was mentioned that much of the recent research on polymer nanocomposites has focused on the use of three classes of anisotropic nanomaterials as filler: nanoclays, carbon nanotubes, and graphene platelets. All of these nanofillers have been heralded for their potential to produce multifunctional property enhancement in polymers at much lower loadings than conventional filler materials such as carbon black.[1, 2] Many comparisons between these three types of nanofillers have been drawn in the literature, but relatively few reports have directly compared the properties of nanocomposites mixed with these different fillers, using the same processing technique and testing procedures.[3-5] Thus, it is of interest to investigate the relative strengths and weaknesses of nanoclays, carbon nanotubes, and graphene platelets in improving the properties of polymers.

Chapter 5 presented work using latex compounding to produce RG-O/NR nanocomposites. The goal of the study presented in this Chapter was to compare the effectiveness of nanoclays and carbon nanotubes to RG-O in improving the mechanical, electrical, and thermal properties of NR using this same latex mixing approach.

Unmodified sodium montmorillonite (henceforth, MMT) and nitric acid-treated multi-walled carbon nanotubes (MWNTs) can both form kinetically-stable suspensions in water and were thus chosen for comparison to RG-O. Although single-walled carbon nanotubes may provide superior property enhancement to MWNTs, they are significantly more expensive than MWNTs and are thus less likely to be utilized in large-scale elastomer applications such as tires, seals, and membranes. In addition, a technique to rapidly produce large-area RG-O platelets was discovered (see Appendix E for details) and in light of the theoretical benefits of increased platelet aspect ratio on nanocomposite properties,[6] it was sought to investigate what practical advantages (if any) these large aspect ratio platelets might provide. Thus, two primary goals were established for this study: (1) to compare property improvements in NR produced by incorporation of MWNTs, MMT platelets, and RG-O platelets by latex mixing, and (2) to evaluate the effect of oxidation and the average intrinsic platelet aspect ratio of graphene platelets on nanocomposite properties.

7.2. MATERIALS AND METHODS

NR water-based latex was provided by Goodyear Tire & Rubber Company. Sodium montmorillonite (Na+ Cloisite) was sourced from Southern Clay Products, Inc. MWNTs were carboxylic acid-functionalized and provided as an aqueous suspension (Nano-Lab, Inc., Waltham, MA) at a concentration of 10 mg/ml. SP-1 flake graphite from Bay Carbon was used as the graphite precursor to GO and thus G-O and RG-O platelets.

All chemicals were used as received. GO was produced using a modified Hummers method as described previously.

Suspensions containing large-area graphene oxide platelets were produced by exfoliating GO particles in water using a Resodyn LabRAM mixer. The LabRAM mixer uses acoustic energy at resonance to mix wet or dry mixtures, and was found to produce kinetically-stable suspensions of G-O platelets. An effective dispersion protocol was developed by trial-and-error on standard GO/water mixtures (0.5 mg/ml). Atomic force microscopy scans and SEM analysis on dried-down G-O suspensions suggested that GO was exfoliated into single-layer G-O platelets with average lateral dimensions more than five times larger than G-O platelets produced by ultrasonication; dynamic light scattering (DLS) results also agreed with these findings. More details on the exfoliation process, characterization and analysis of the large-area G-O platelets are provided in Appendix E.

All nanocomposites were produced using a latex co-coagulation approach as utilized in the work on RG-O/NR nanocomposites presented in Chapter 5. In this approach, the nanofiller was first dispersed into water by ultrasonication or was otherwise provided as a dispersion in water by the manufacturer (as in the case of the MWNTs). The functionalized MWNTs, which were provided as a 10 mg/ml dispersion in water, were diluted to a 1 mg/ml dispersion (while maintaining a pH of ~10) prior to mixing with NR latex. G-O and MMT platelets were dispersed in water at 1 mg/ml by vigorous stirring for 24 h followed by sonication in an ultrasonic cleaning bath (VWR) for 4 h. Suspensions of RG-O and large-area reduced graphene oxide (henceforth, LA-RG-O) were produced by reduction of graphene oxide and large-area graphene oxide (exfoliated

in the LabRAM mixer), respectively, using hydrazine monohydrate as the reductant (3 µl of hydrazine per 1 ml of graphene oxide suspension). Prior to reduction, the pH of the graphene oxide suspensions were raised to 11 using KOH to prevent agglomeration of the platelets upon addition of hydrazine.[7]

NR latex was mixed with the aqueous nanofiller suspension in a beaker with vigorous stirring for ~5 min; then, the mixture was coagulated with a dilute formic acid solution. This latex mixing approach was carried out to produce 5 phr master batches of each type of nanocomposite. After separation and drying of the coagulated solids, DCP curing agent and neat NR solids (produced by latex coagulation) were added to the 5 phr master batch on a two-roll mill (CW Brabender 2-roll prep mill, 50 ºC, 15 rpm, 1 mm gap) to produce nanocomposites with 2, 3, 4, and 5 phr filler with 1 phr DCP. For the 5 phr nanocomposites tested in this work, only DCP was added on the mill. Total milling time for each nanocomposite was ~15 min. After milling, the rubber was cured into sheets and/or molded into specimens directly for testing using a Wabash hot press at 160º C for 40 min.

TEM and WAXS were performed as described in Chapter 5. SEM, DLS, and AFM were used to analyze G-O platelet size (more details in Appendix E). SEM images were obtained using an FEI Quanta-600 FEG Environmental SEM at 30 kV and 10^{-6} Torr. DLS and zeta potential measurements were performed using a Zetasizer Nano ZS instrument (Malvern Instruments). AFM scans were performed on a Park Scientific AutoProbe CP/MT instrument in contact mode.

Uniaxial tensile testing was performed at room temperature with an MTS machine equipped with a 50 lb Honeywell load cell and spring-loaded clamps to prevent slippage of the specimens during testing. Five samples were tested at each loading for each type of filler. Test data was acquired using LabVIEW. Dog-bone type samples had approximate test section dimensions of 20 × 4 × 1 mm. Samples were stretched three times to an elongation of ~200% prior to testing to correct for the Mullins effect.[8] The strain rate for all tests was 500 mm/min. DMA tests were performed using a TA Instruments Q800 DMA. All tests were conducted at 10 Hz from -100 to 50 °C with a ramp rate of 3 °C/min, a strain of 0.1% to 1% (depending on loading), and a static preload of 0.01 N. Samples for DMA testing had dimensions of approximately 15 x 5 x 1 mm.

Electrical and thermal conductivity measurements were performed as described in Chapter 5. TGA scans were performed on ~20 mg samples cut into small pieces from cured specimens, using a Perkin Elmer TGA4000 instrument under flowing N_2 (20 ml/min) and a ramp rate of 10 ºC/min.

7.3. FILLER AND NANOCOMPOSITE MORPHOLOGY

Each type of nanofiller in this study was homogeneously dispersed in kinetically-stable suspensions (>2 weeks for RG-O suspensions, several months for as-received MWNT suspensions) prior to mixing with the NR latex. The nanoplatelet suspensions were deposited onto freshly-cleaved mica for imaging by AFM in non-contact mode, to determine whether the platelets were exfoliated into single layers in suspension. AFM scans were performed on the same suspensions used to produce nanocomposites, without

special preparation or purification steps (i.e., without centrifugation, washing, or dialysis to purify the suspensions). These AFM scans showed evidence of predominately single-layer platelets dispersed in RG-O, LA-RG-O, and MMT suspensions. While the number of images collected does not allow for a statistically significant comparison of platelet lateral dimensions by AFM, it is evident from Figure 7.1 that both MMT and RG-O platelets were of irregular shapes, while MMT platelets had generally larger lateral dimensions than RG-O platelets. MMT platelets were found to be approximately 1 nm thick, while RG-O platelets were roughly 0.6 nm thick. Many impurities were found in the AFM images of each type of filler studied, perhaps due to residual salts.[27] More details on the LA-RG-O suspensions and precursor large-area G-O platelets are provided in Appendix E.

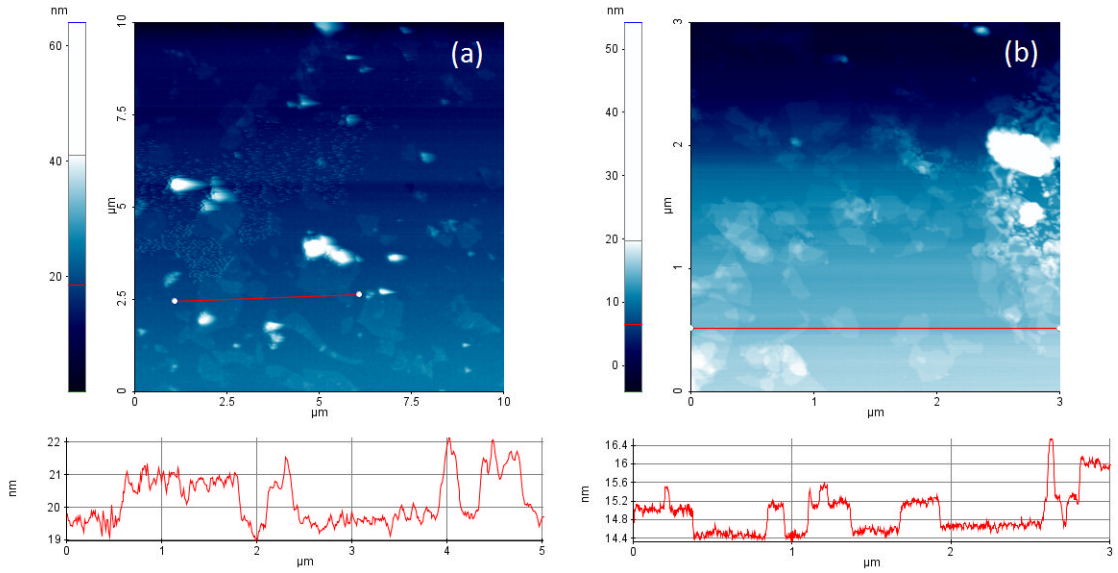

Figure 7.1. Non-contact mode AFM images and height profiles of dried-down suspensions of (a) MMT platelets and (b) RG-O platelets on freshly-cleaved mica. Note the difference in scale between the two images.

The morphology of the nanocomposites was evaluated by TEM and WAXS. WAXS patterns from each type of nanocomposite at 5 phr loading are shown in Figure 7.2. With the exception of the MWNT/NR sample, it is evident that no emergence of a diffraction peak was observed in any of the samples. In the case of MWNT/NR nanocomposites, the broad, low-intensity peak centered around 25º can be attributed to the spacing between the concentric graphitic layers of the MWNTs (d_{002} ~ 0.34 nm)[9] and is not necessarily indicative of poor dispersion.

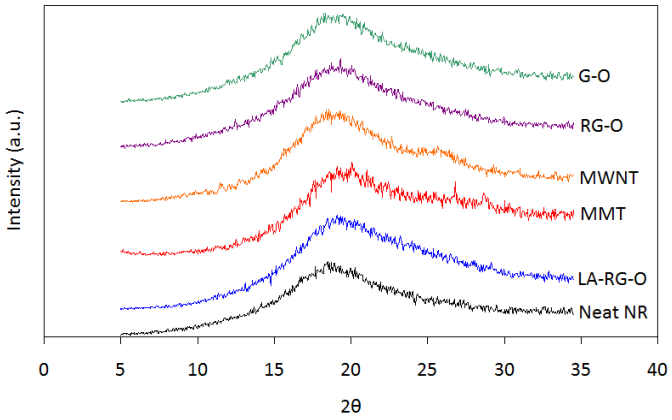

Figure 7.2. Wide-angle X-ray scattering patterns from the nanocomposites at 5 phr loading.

A montage of TEM micrographs is provided in Figure 7.3, with one representative image from each type of nanocomposite. TEM observation showed the filler to be uniformly dispersed over the cross section in all samples. However, there were differences in the level of filler exfoliation achieved. For instance, comparing Figure 7.3(b) to Figure 7.3(c), it is evident that more multi-layer tactoids were present in the G-

O/NR nanocomposites than in the RG-O/NR nanocomposites. While it is difficult to draw a direct comparison between the quality of the dispersions of the MWNTs and the platelet-shaped fillers due to the difference in shape, the MWNTs generally appeared to be well-dispersed with few bundles. In summary, while a homogeneous dispersion was obtained for each type of nanocomposite, the G-O, MMT, and LA-RG-O-filled nanocomposites appeared to show a greater concentration of multi-layer platelets than the RG-O/NR nanocomposites.

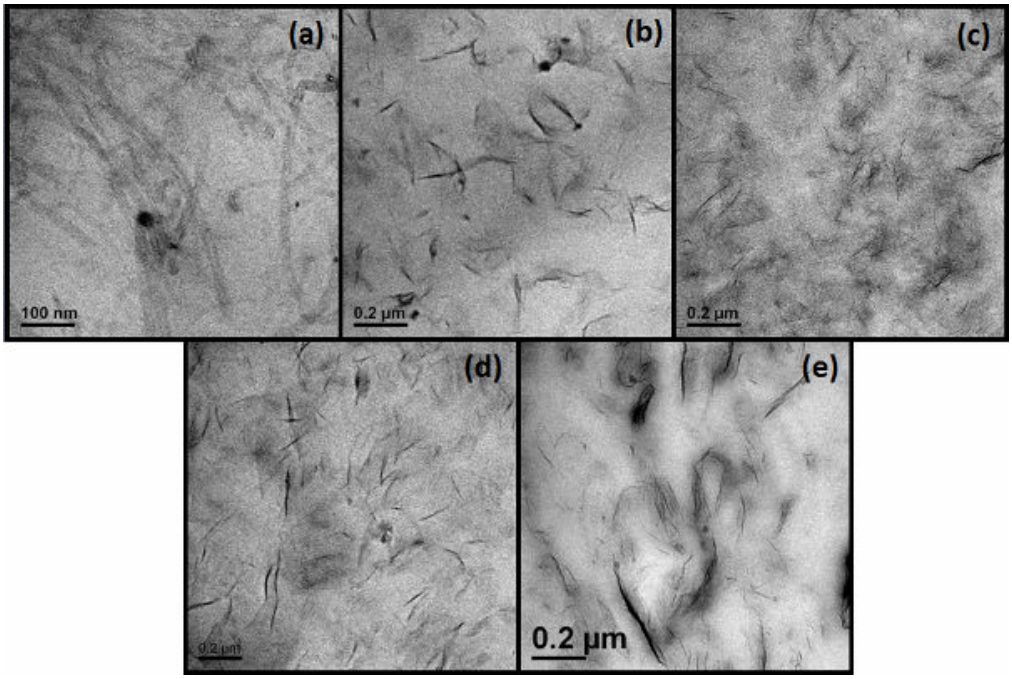

Figure 7.3. TEM micrographs from each type of nanocomposite in this study. (a) NR filled with 5 phr MWNTs, (b) G-O, (c) RG-O, (d) MMT, (e) LA-RG-O.

7.4. ELECTRICAL AND THERMAL PROPERTIES

MMT platelets, which are electrically insulating, had little effect on the electrical conductivity of NR as expected. Although G-O platelets are also insulating, during the curing process the platelets received prolonged exposure to elevated temperature (160 ºC) and were likely reduced to some extent,[10, 11] which may account for the minor conductivity increase observed. Of the conductive fillers examined in this study, MWNTs produced the largest conductivity enhancement, while LA-RG-O platelets showed by far the smallest conductivity increases (Figure 7.4).

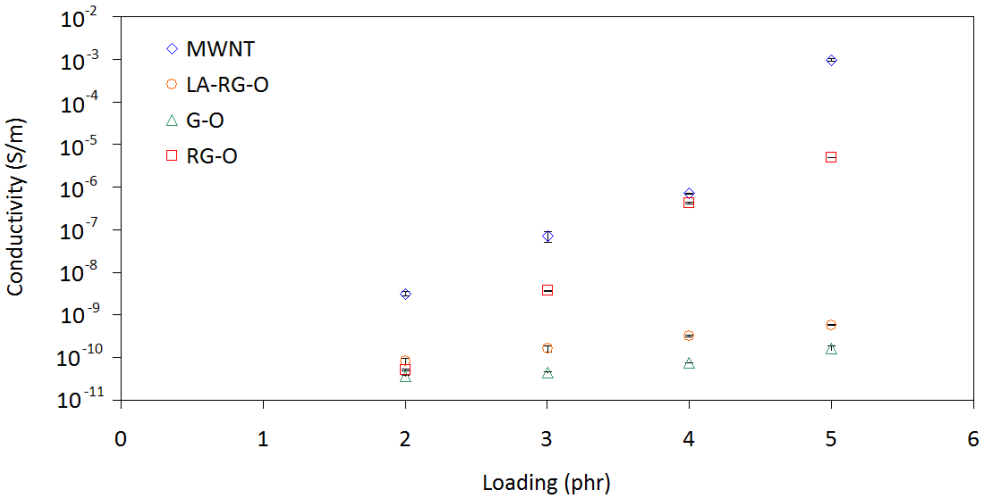

Figure 7.4. Volumetric electrical conductivities of the nanocomposites from 2 to 5 phr loading. Data from MMT-filled nanocomposites are excluded as there was no practical change in conductivity over the loading range tested.

It is postulated that the superior conductivity of the MWNTs stems from their intrinsically higher aspect ratio and web-like dispersion morphology,[12] allowing for more conductive pathways to span through the matrix compared with the platelet fillers. The

conductivity enhancement provided by LA-RG-O platelets was inferior to the RG-O platelets, despite the larger intrinsic aspect ratio of the LA-RG-O platelets which would be expected to lead to improved conductivity if well-dispersed.[6] This result is possibly understood by examination of the TEM micrographs such as shown in Figure 7.3, as the dispersion of LA-RG-O appeared to be worse than RG-O. An explanation for this difference in dispersion quality is proposed in Section 7.6.

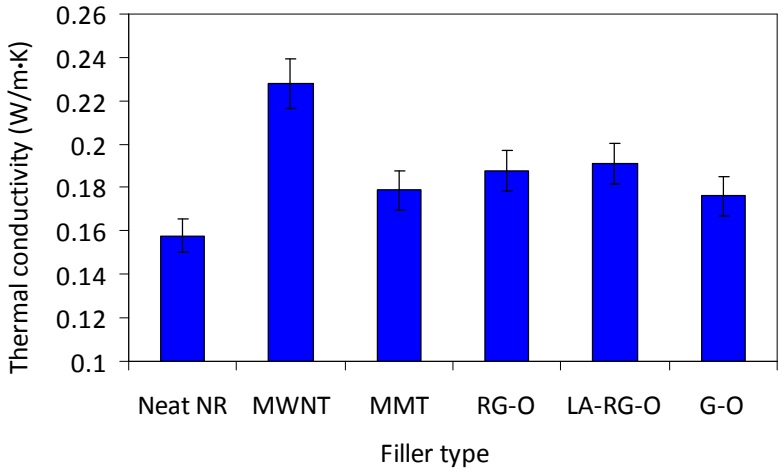

Figure 7.5. Thermal conductivities of the nanocomposites at 5 phr loading compared with neat NR.

Results from thermal conductivity tests on the nanocomposites are provided in Figure 7.5. All fillers improved the thermal conductivity of NR, but MWNTs provided the largest enhancement, raising the thermal conductivity by over 44% to ~0.23 W/m·K. This result is contrary to statements suggesting that the platelet geometry of graphene-based materials should provide lower interfacial thermal resistance and thus allow them

to endow larger thermal conductivity enhancement to polymers than nanotubes. In addition, each nanofiller used in this study improved in the thermal stability of NR—the onset of thermal degradation, measured by TGA temperature scans, was shifted to some extent by the presence of fillers as illustrated by the representative curves in Figure 7.6.

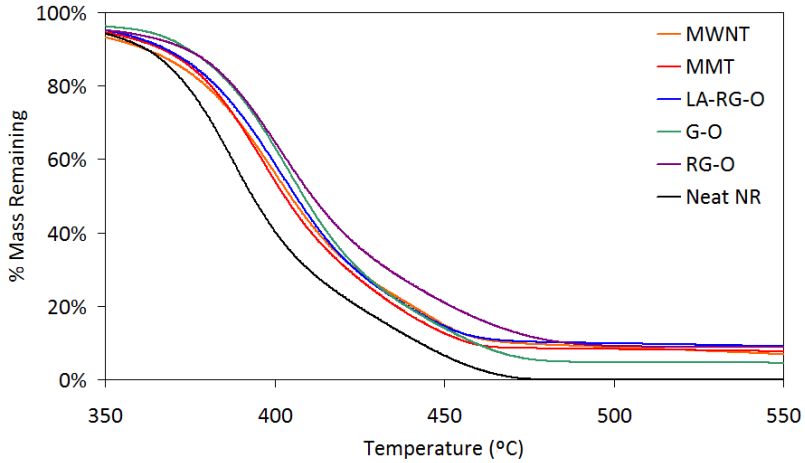

Figure 7.6. TGA scans of the nanocomposites versus neat NR.

7.5. MECHANICAL AND VISCOELASTIC PROPERTIES

Uniaxial tension tests and dynamic mechanical analysis were used to evaluate differences in the mechanical and viscoelastic properties of the nanocomposites. Figure 7.7 shows representative stress-elongation curves from tension tests on neat NR and the nanocomposites at 5 phr loading. It is evident that RG-O platelets provided the most dramatic reinforcing effect of the fillers considered in this study, while MMT and G-O resulted in the smallest improvements. Data on the modulus (stress) at 100% elongation,

tensile strength, and elongation to break for each type of nanocomposite with filler loadings from 2 to 5 phr is provided in Figure 7.8. It is worth noting that that the RG-O/NR nanocomposites tested in this Chapter showed higher strength and moduli but lower elongation to break than the RG-O/NR nanocomposites discussed in Chapter 5, despite using the same NR and RG-O synthesis procedure. However, there are three factors that may account for this difference: a higher strain rate during stress-strain testing in this work (500 mm/min compared with 250 mm/min), different milling conditions (15 min at 50 ºC instead of 12 min at 80 ºC), and production of nanocomposites at lower loadings by masterbatch dilution as opposed to direct co-coagulation of 2, 3, and 4 phr nanocomposites.

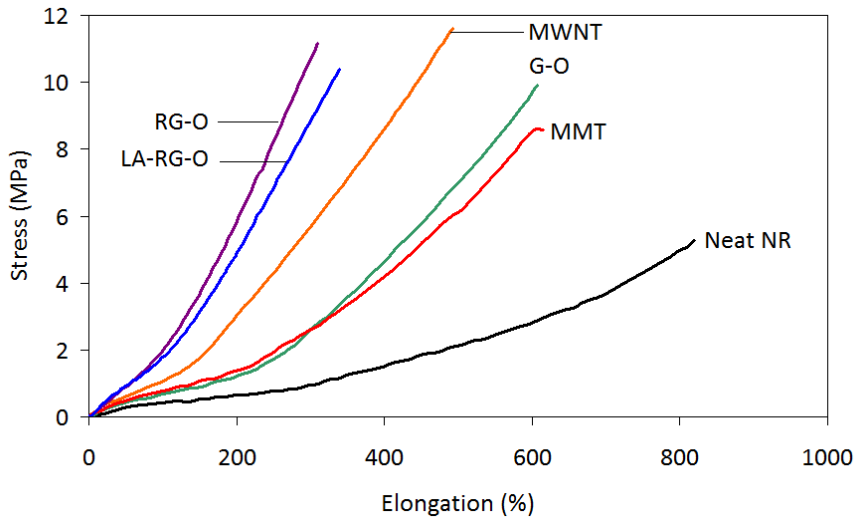

Figure 7.7. Representative stress-strain curves of the nanocomposites.

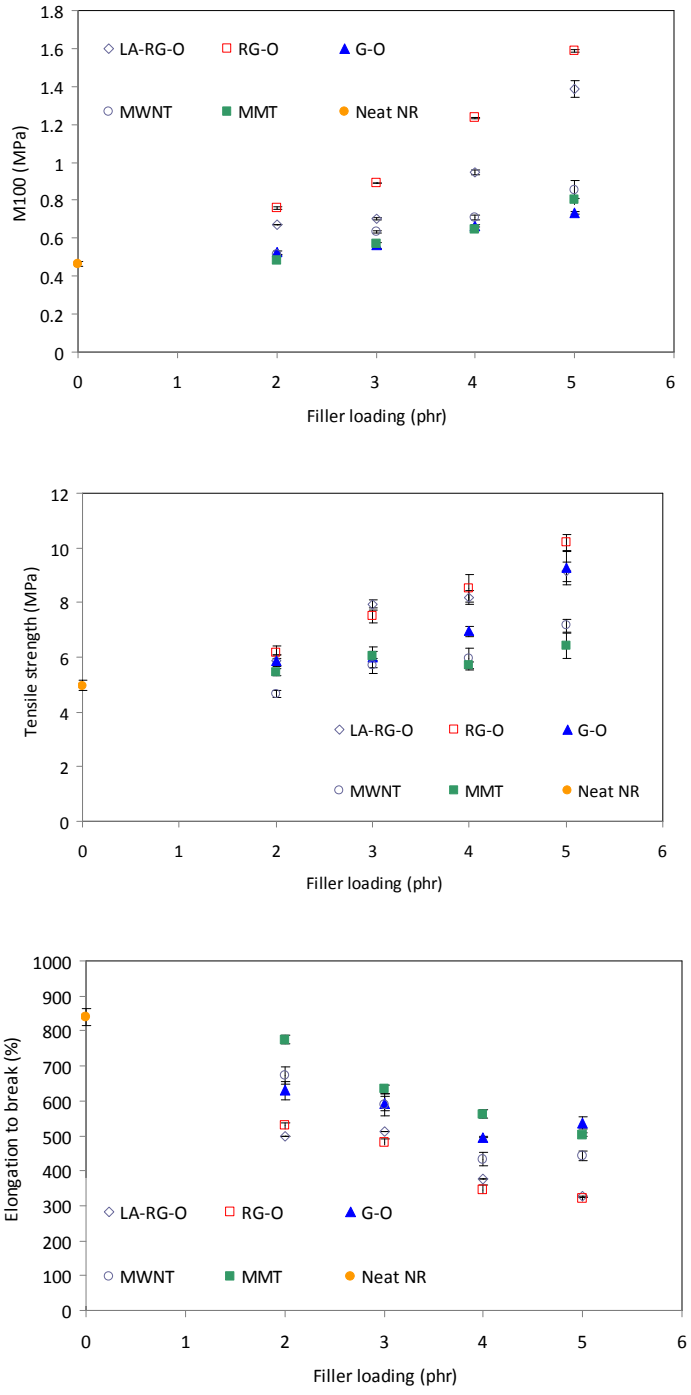

Figure 7.8. Modulus at 100% elongation (M100), tensile strength, and elongation to break of the nanocomposites over the range of loadings tested.

Representative data from DMA temperature scans of the 5 phr nanocomposites are shown in Figure 7.9. Increments in storage modulus at a given temperature were comparable to modulus increases measured from tension tests; in addition, the relative ordering of modulus increases between the nanocomposites was the same both above and below T_g. Changes in the intensity and breadth of the tan delta peaks shown in Figure 7.9(b) appeared to correlate strongly with qualitative differences in thermodynamic compatibility between the nanofiller and NR matrix—the hydrophobic RG-O, L-RG-O, and MWNT fillers showed substantial reductions in the tan delta peak size versus neat NR, while the hydrophilic G-O and MMT fillers showed much smaller decreases or even an increase in peak height in some tests. As such changes in the tan delta peak height and breadth are often used as an indicator of chain mobility at the nanofiller interfaces;[13] these results thus suggest good interfacial bonding between RG-O, LA-RG-O, or MWNTs and the NR matrix.

7.6. DISCUSSION

These results illustrate how differences in compatibility between the filler and matrix can affect properties. The starting point for production of each type of nanocomposite was a kinetically-stable aqueous suspension of the nanofiller, which was mixed with NR latex and subsequently co-coagulated. However, the surface chemistry mismatch between MMT or G-O platelets and NR may have driven some agglomeration of filler during further processing (two-roll milling and/or hot pressing). Much more significant mechanical property improvements were observed for the MWNT- and RG-

O-filled systems, likely because these nanofillers have better thermodynamic compatibility with NR and thus stronger interfacial bonding than G-O or MMT platelets. Modulus and strength were found to increase with filler loading while elongation to break decreased; these trends are not universally observed in elastomer nanocomposite systems and seem to be heavily dependent upon the processing method, elastomer matrix, and cure system.[14-19]

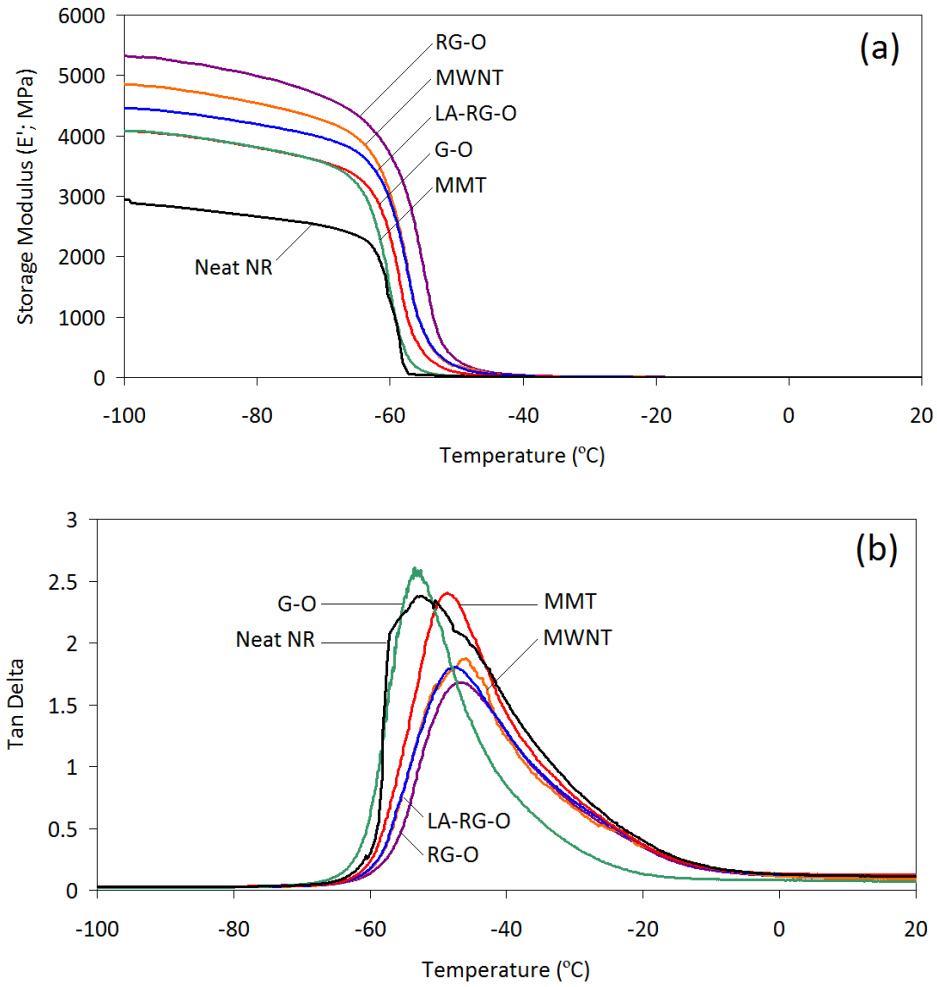

Figure 7.9. Representative DMA plots of (a) storage modulus and (b) tan delta versus temperature for the nanocomposites.

What is the reason for the lower property improvements achieved using RG-O platelets of larger average aspect ratio? Incomplete exfoliation of platelets may have been a factor, although the characterization presented in Appendix E suggests that the initial exfoliation of GO using the LabRAM mixer was effective, with the resulting suspension consisting primarily of single-layer large-area G-O platelets. It is thus postulated that two other factors primarily account for this result: (1) a wide platelet size distribution in LA-RG-O suspensions and (2) an increased tendency of large-area platelets to aggregate in suspension. Approximately 50% of the platelets in LA-RG-O suspensions had lateral dimensions (as measured by SEM analysis) of less than 1 μm, compared with 93% of platelets in the "conventional" RG-O suspensions—hence, LA-RG-O suspensions did not consist entirely of high aspect ratio platelets. In addition, it is well known that colloidal suspensions containing larger particles are less stable and coagulate more rapidly than suspensions with smaller particles,[20] and this greater tendency of larger platelets to agglomerate and re-stack before and during coagulation could make effective dispersion more difficult than smaller RG-O platelets.

Another variable that may have affected the results in this work is the degree of cure of each type of nanocomposite. Fillers can have an impact on cure kinetics with varying effects reported for nanoclay and carbon nanotube-filled nanocomposites depending upon the cure system, interfacial chemistry, and type of rubber matrix.[21-24] The cure system has even been reported to affect the degree of exfoliation of nanoclays.[25] A long curing time was uniformly applied to all the nanocomposites in this study to try and eliminate the effect of different cure kinetics, although different ultimate degrees of cure

and bonding between filler and matrix may have been achieved. Such differences in cross-link density would likely not have an appreciable effect on conductivity properties, however.

7.7. CONCLUSIONS

In this work, NR-matrix nanocomposites were mixed with various nanofillers using latex co-coagulation in an effort to compare the property enhancements provided by each type of nanofiller. Three classes of nanofiller were evaluated in this study: nanoclay (exfoliated sodium montmorillonite), multi-walled carbon nanotubes, and graphene platelets. The graphene platelets used in this study consisted of graphene oxide, reduced graphene oxide, and large-area reduced graphene oxide platelets. These three types of graphene-based materials were tested to investigate the effect of platelet structure on nanocomposite properties.

Standard morphological characterization techniques (WAXS, TEM) indicated that a homogeneous dispersion of nanofiller was achieved in each nanocomposite system, although the degree of nanofiller exfoliation varied. RG-O/NR nanocomposites appeared to show the best overall dispersion and consequently showed the largest mechanical property enhancements of the group. Use of suspensions containing large-area RG-O platelets, however, were not found confer greater improvements in properties as the dispersion evidently worsened with increasing platelet lateral dimensions. MMT and G-O/NR nanocomposites showed the smallest changes in mechanical properties, perhaps due to a combination of interfacial chemistry mismatch and significant concentrations of

multi-layer tactoids in both dispersions (per TEM observation). MWNTs produced the largest improvements in the thermal and electrical conductivity of NR.

The primary contribution of this study is that (1) it helps establish the relative benefits and disadvantages of these nanofillers in improving the properties of NR and (2) it illustrates the effects that graphene platelet structure has on nanocomposite properties. This work suggests that MWNTs are most effective (of the nanofillers considered here) in enhancing nanocomposite conductivity properties, while RG-O platelets provide superior reinforcement. When dispersed into a chemically compatible polymer matrix, combinations of graphene platelets and carbon nanotubes could perhaps lead to an optimum balance of properties or have synergistic effects.[26] This work also highlights the importance of choosing nanofillers that are chemically compatible with the matrix; in this study, hydrophilic filler materials were much less effective at increasing modulus and strength of NR despite a uniform dispersion. Finally, increased average lateral dimensions of the graphene platelets was found to be detrimental to nanocomposite properties in this case, possibly because larger platelets are more prone to aggregate/re-stack while suspended in water. Increasing the average aspect ratio of the platelets may prove beneficial if aggregation of the platelets can be prevented.

7.8. REFERENCES

1. Alexandre, M.; Dubois, P. *Materials Science and Engineering R Reports* **2000,** 28, (1-2), 1-63.

2. Moniruzzaman, M.; Winey, K. I. *Macromolecules* **2006,** 39, (16), 5194-5205.

3. Du, J.; Zhao, L.; Zeng, Y.; Zhang, L.; Li, F.; Liu, P.; Liu, C. *Carbon* **2011,** 49, 1094-1100.

4. Potschke, P.; Abdel-Goad, M.; Pegel, S.; Jehnichen, D.; Mark, J. E.; Zhou, D. H.; Heinrich, G. *Journal of Macromolecular Science, Part A: Pure and Applied Chemistry* **2010,** 47, (1), 12-19.

5. Steurer, P.; Wissert, R.; Thomann, R.; Mulhaupt, R. *Macromolecular Rapid Communications* **2009,** 30, (4-5), 316-327.

6. Nan, C.-W.; Shen, Y.; Ma, J. *Annual Review of Materials Research* **2010,** 40, 131-151.

7. Li, D.; Muller, M. B.; Gilje, S.; Kaner, R. B.; Wallace, G. G. *Nature Nanotechnology* **2008,** 3, (2), 101-105.

8. Mullins, L. *Rubber Chemistry and Technology* **1969,** 42, 339-362.

9. Fornes, T. D.; Baur, J. W.; Sabba, Y.; Thomas, E. L. *Polymer* **2006,** 47, (5), 1704-1714.

10. Traina, M.; Pegoretti, A. *Journal of Nanoparticle Research* **2012,** 14, 801.

11. Glover, A. J.; Cai, M.; Overdeep, K. R.; Kranbuehl, D. E.; Schniepp, H. C. *Macromolecules* **2011,** 44, 9821-9829.

12. Endo, M.; Noguchi, T.; Ito, M.; Takeuchi, K.; Hayashi, T.; Kim, Y. A.; Wanibuchi, T.; Jinnai, H.; Terrones, M.; Dresselhaus, M. S. *Advanced Functional Materials* **2008,** 18, (21), 3403-3409.

13. Galimberti, M., *Rubber-Clay Nanocomposites*. John Wiley & Sons: Hoboken, New Jersey, 2011.

14. Bokobza, L. *Polymer* **2007,** 48, 4907-4920.

15. Sengupta, R.; Chakraborty, S.; Bandyopadhyay, S.; Dasgupta, S.; Mukhopadhyay, R.; Auddy, K.; Deuri, A. S. *Polymer Engineering and Science* **2007,** 47, 1956-1974.

16. Ramorino, G.; Bignotti, F.; Pandini, S.; Ricco, T. *Composites Science and Technology* **2009,** 69, 1206-1211.

17. Fakhru'l-Razi, A.; Atieh, M. A.; Girun, N.; Chuah, T. G.; El-Sadig, M.; Biak, D. R. A. *Composite Structures* **2006,** 75, 496-500.

18. Hrachova, J.; Komadel, P.; Chodak, I. *Journal of Materials Science* **2008,** 43, 2012-2017.

19. Varghese, S.; Karger-Kocsis, J. *Polymer* **2003,** 44, 4921-4927.

20. Birdi, K. S., *Surface and Colloid Chemistry: Principles and Applications*. CRC Press: 2012.

21. Sui, G.; Zhong, W.; Yang, X.; Zhao, S. *Macromolecular Materials and Engineering* **2007,** 292, 1020-1026.

22. Yue, D.; Liu, Y.; Shen, Z.; Zhang, L. *Journal of Materials Science* **2006,** 41, 2541-2544.

23. Likozar, B. *Polymer Engineering and Science* **2011,** 51, 542-549.

24. Lopez-Manchado, M. A.; Arroyo, M.; Herrero, B.; Biagiotti, J. *Journal of Applied Polymer Science* **2003,** 89, 1-15.

25. Das, A.; Stockelhuber, K. W.; Jurk, R.; Heinrich, G. *Macromolecular Symposia* **2010,** 291-292, 95-105.

26. Yu, A.; Ramesh, P.; Sun, X.; Bekyarova, E.; Itkis, M. E.; Haddon, R. C. *Advanced Materials* **2008,** 20, (24), 4740-4744.

27. Piner, R. D., Xu, T. T., Fisher, F. T., Qiao, Y., Ruoff, R. S. *Langmuir* **2003**, 19, 7995-8001.

Chapter 8:
Summary and Conclusions

8.1. Summary and Discussion of Work

The primary contribution of this dissertation centered around five chapters of original research on graphene/polymer nanocomposites. The goal of this work was to try and advance both knowledge and understanding of these promising materials by focusing upon structure-property relationships. The purpose of this Chapter is to summarize the findings of this work and to provide commentary on their importance and limitations. The Chapter ends with recommendations for future work in this field.

In Chapter 3, work was presented on G-O and RG-O/PMMA nanocomposites. This was the first project undertaken for this dissertation. PMMA was chosen as a "model" matrix for its ease of synthesis by free radical polymerization and amenability to melt processing. It was hypothesized that G-O platelets would provide superior reinforcement to RG-O as PMMA is a polar polymer and the greater oxygen content of G-O compared with RG-O might confer better stress transfer at the matrix-filler interface. However, this hypothesis was not supported by the data. A consistently greater tensile strength was observed with the G-O/NR nanocomposites, but this could be attributed to other factors besides reinforcement, e.g., greater porosity in the RG-O/NR samples. Chemical analysis of the polymer in each sample suggests that the presence of G-O or

RG-O platelets during the polymerization had little effect on the chemical structure (tacticity or molecular weight) of PMMA.

While the study of platelet chemistry yielded indefinite results, the comparison of tensile test data of injection molded samples produced by melt compounding versus *in situ* polymerization strongly supported the conclusion that the latter method is considerably more effective in dispersing G-O or RG-O platelets and improving mechanical properties. It is particularly notable just how ineffective RG-O platelets were in improving the mechanical properties of PMMA when dispersed by melt compounding. Others have reported similarly poor reinforcement with RG-O when dispersed by melt compounding.[2] These results suggest that when RG-O platelets are agglomerated, a significant degree of irreversible restacking of the platelets occurs, which compromises their ability to be re-dispersed into a polymer matrix.

It is worthwhile to briefly revisit the results presented in Chapter 3 on T_g shifts measured by DMA at very low loadings of G-O and RG-O platelets. It was initially reported in an associated paper based upon Chapter 3 work that T_g shifts as large as 20 ºC were measured by DMA. The validity of such unexpectedly large property enhancements, which have been reported in other papers on graphene/polymer nanocomposites, has recently become a point of contention in the literature, particularly with regards to reported T_g shifts and modulus enhancements.[3, 4] Thus, in attempt to validate the results reported in this Chapter, previously un-tested RG-O/PMMA nanocomposite samples (produced during the original work) were cut from films and tested by DMA according to the procedure described in Section 3.2. These DMA

measurements revealed T_g shifts of 2-5 ºC relative to neat PMMA for 0.5, 1, and 2 wt% RG-O/PMMA samples, despite prior measurements of T_g shifts of 15 ºC or higher at these loadings. The reason for this discrepancy is unclear. As the values of the T_g of the RG-O/PMMA nanocomposites were considerably lower than originally measured (approximately 130 ºC, where original measurements showed T_gs of up to 145 ºC), it could be that aging effects are at least partially responsible for the difference. It is also noted that DSC results did not agree with the DMA data initially, providing a helpful check against what now appears to be questionable data obtained by DMA. Based on this follow-up study, it is thus concluded that RG-O does not produce significant T_g shifts in PMMA. Notably, no major shifts in T_g were reported in any other nanocomposite system in this dissertation.

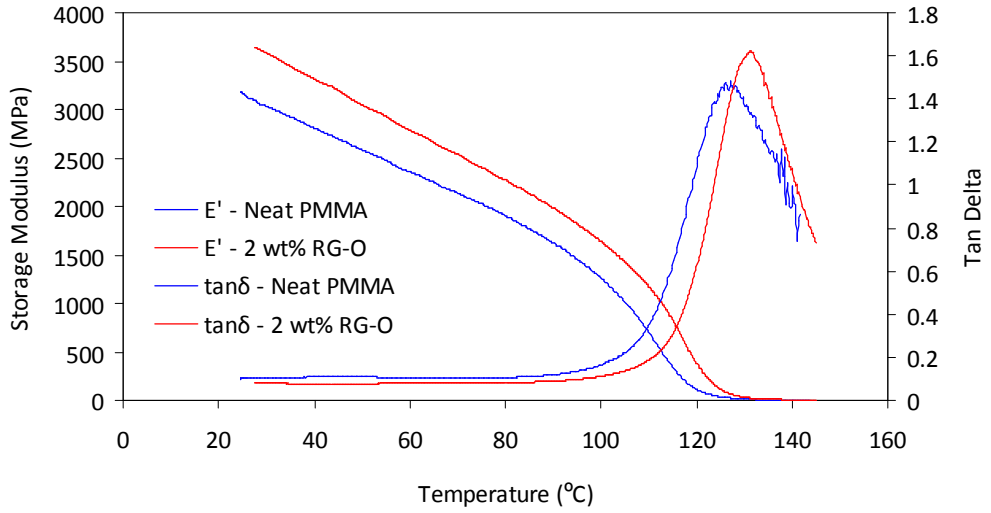

Figure 8.1. DMA temperature scans of the neat PMMA and 2 wt% RG-O/PMMA nanocomposites from Chapter 3. T_g shifts of no more than 5 ºC were observed in a follow-up study of remaining samples more than two years after the original measurements.

The work of Chapter 4 showed that MEGO can be effectively dispersed into a suitable thermoplastic polymer via melt processing. One important contribution of this Chapter is that milder GO exfoliation conditions (i.e., use of microwave processing or lower thermal treatment temperatures) can produce a graphene-based material with greater oxygen content and thus greater polarity, which may have facilitated dispersion into a polar thermoplastic such as PC. It was also found that prolonged thermal annealing of the nanocomposite could reproducibly result in electrical conductivity enhancement. The mechanism the conductivity improvement from annealing was attributed to disorientation of the dispersed MEGO platelets, based upon prior work and analysis by Kim and co-workers and Ren et al.[5, 6] as well as theoretical models. However, the practicality of such annealing treatments to improve conductivity is questionable given the energy input required and the difficulty in maintaining the shape of the molded part during annealing.

The next three Chapters were focused on graphene platelet/elastomer nanocomposites that were studied in collaboration with Goodyear Tire & Rubber Company. Chapter 5 presented work on RG-O/NR nanocomposites produced by latex compounding. The contributions of the study were two-fold: one, it demonstrated multi-functional property enhancement of NR by RG-O; two, it investigated the effect of processing on morphology. These results highlight the importance of consideration of the filler morphology in the "design" of nanocomposites. Moreover, the as-made or solution cured RG-O/NR nanocomposites have a suite of properties that could possibly find use in

applications where the compliance of a rubber but the stiffness of a thermoplastic at higher elongations and high conductivity would be desired. Molding of specimens preserved the unique morphology created by latex co-coagulation, suggesting that this procedure could be used to produce useful articles on a small but potentially practical scale.

Chapter 5 also presented an in-depth analysis of TEM micrographs to quantify dispersion as well as the use of simple micromechanical composite models to describe modulus enhancement in RG-O/NR nanocomposites. Given that dispersion quantification by TEM is very time-consuming and riddled with complications,[7] and in light of the numerous assumptions present in simple composite models, one may question the value of such an analysis. However, such modeling studies offer at least two benefits. One, agreement between composite models and experimental data lends insight into the reinforcement mechanisms present in nanocomposites. Fornes and Paul discussed this issue at length in their work on nanoclay/polymer nanocomposites,[4, 7] but essentially, the agreement between simple composite model predictions and experimental data suggests that "nano-effects"—such as percolation of interphase polymer domains surrounding the nanofiller particles[8]—do not play a major role in nanocomposite reinforcement. This conclusion is also supported by the results of this work, for both thermoplastic and elastomer/graphene nanocomposites. The second benefit is that this work provides guidance for the utilization of simple composite models in nanocomposites engineering and development. Dispersion by TEM was quantified in three Chapters of this work (3, 5, and 6) for both RG-O and TEGO/MEGO materials, with A_f values falling between 38 and

45 in all three systems considered as shown in Table 8.1, despite use of different processing methods and different types of graphene platelets. (In another report, a value of 88 was obtained for a melt-mixed TEGO/polyester nanocomposite, although far fewer total particles were analyzed.[9]) Thus, one could use this information to estimate a range of possible modulus values for elastomer or thermoplastic-matrix nanocomposites at a given loading. This is important as it can be seen that use of A_f values estimated from measurements made by scattering or imaging methods (e.g., via SEM or DLS) would give much higher predictions of nanocomposite modulus than observed experimentally. Also, use of the proper composite model would be necessary to achieve reasonable estimates. This work shows that the Guth equation provides good estimates of modulus for elastomer nanocomposites, while this and other work suggests that Mori-Tanaka or Halpin-Tsai models appear to provide better predictions for thermoplastic-matrix nanocomposites.

Table 8.1. Average A_f values determined from quantitative TEM analysis on three of the nanocomposite systems in this work.

Nanocomposite	Processing method	Loading	A_f by TEM
MEGO/PC	Melt processing	3 wt%	45
RG-O/NR	Latex mixing	5 wt%	44
TEGO/NR	Melt processing	5 wt%	34
TEGO/NR	Latex mixing	5 wt%	38

The work in Chapter 6 investigated the problem of dispersion of graphene platelets directly into an NR matrix using a two-roll mill and compared the effectiveness of a latex mixing approach. This work was motivated by the results of Chapter 4 and related literature reports wherein effective dispersion of TEGO or MEGO was obtained by melt processing. Prior to this study, no report existed in the literature on dispersion of TEGO into an elastomer by a "melt" processing approach.

Despite the positive results of Chapter 4, the mill-processed TEGO/NR nanocomposites showed minimal property improvements relative to neat NR, providing similar multi-functional property enhancement to CB at the same loadings. However, it was found that by pre-mixing the TEGO and NR via an ultrasonically-assisted latex mixing procedure, followed by two-roll mill mixing to incorporate the DCP curing agent, that the properties of TEGO/NR nanocomposites could be dramatically improved. The reason for this improvement was essentially attributed to better dispersion based upon extensive TEM analysis.

Chapter 7 was dedicated to a comparison of different nanofillers in improving the mechanical, electrical, and thermal properties of NR. Three classes of nanofillers were chosen for this study: graphene platelets, multi-walled carbon nanotubes, and exfoliated montmorillonite ("nanoclay"). The motivation for this work was to directly evaluate the relative strengths and weaknesses between these fillers. These results could help researchers in this field to make a more informed selection of nanofillers to meet a particular performance target(s).

The nanofillers examined in this Chapter were mixed into NR by latex compounding. Each nanofiller was dispersed into a stable aqueous suspension prior to mixing with NR latex. After co-coagulation with the NR latex and two-roll mill processing, each of the nanofillers were found to be homogeneously dispersed in the NR matrix when examined by TEM. However, TEM revealed some differences in the level of exfoliation of the nanofillers, and significant differences in reinforcement and conductivity properties were measured. RG-O platelets were found to produce the largest increases in stiffness and strength, whereas MWNTs produced the greatest thermal and electrical conductivity improvements. Na-MMT platelets did not improve conductivity and provided the smallest mechanical property changes of the three types of fillers. Because MMT platelets were found to be dispersed as single-layer platelets in water prior to mixing/coagulation with the NR latex, it was speculated that a mismatch in chemistry between the hydrophilic MMT platelets and the hydrophobic NR matrix worsened the dispersion and thus the properties of the MMT/NR nanocomposites relative to RG-O and MWNT-filled NR. Effective dispersion of organically-modified clays in NR would likely result in larger mechanical property enhancement than observed with unmodified sodium montmorillonite.

Another component of this work was an investigation on the influence of graphene platelet structure on properties. As in Chapter 3, the property improvements conferred by G-O platelets and RG-O platelets were directly compared. It was found that G-O platelets provided inferior reinforcement to their reduced counterparts, despite being well-dispersed and exfoliated into single-layer platelets prior to mixing with NR. The

difference in reinforcement provided by G-O and RG-O platelets thus illustrates the importance of chemical compatibility between the matrix and nanofiller. In addition, RG-O platelets of relatively large average lateral dimensions (approximately five times greater than "conventional" RG-O platelets) were dispersed into NR to evaluate the effect of the platelet aspect ratio on properties. The use of large-area RG-O platelets was unexpectedly found to be detrimental to properties relative to conventional RG-O platelets, despite the well-established theoretical benefits of increased platelet aspect ratio.[10] The negative effect of using large-area RG-O platelets was attributed to agglomeration/restacking of the platelets in suspension, prior to or during the co-coagulation procedure, as larger platelets are more prone to agglomeration (and their suspensions are less kinetically-stable) than smaller platelets. These results do not necessarily point to high aspect ratio (>1000) platelets producing inferior property enhancements when dispersed in a polymer matrix, but rather highlight some difficulties in getting large-area platelets effectively dispersed into a polymer matrix in the first place.

In summary, this body of work has helped develop further understanding of relationships between graphene platelet structure, processing method, and nanocomposite properties, through the study of both thermoplastic and elastomer/graphene nanocomposite systems. This work reinforces that the processing approach and chemical compatibility of the matrix and filler are two key considerations in the development of graphene-filled polymers and nanocomposites more generally. This work also showed TEM to be a powerful method for analysis of filler dispersion, which helps provide

insight into nanocomposite properties. This work also leaves important questions for future consideration and raises some new ones, as discussed in the following section.

8.2. Recommendations and Future Work

Based on the work in Chapters 5 and 7, it appears that RG-O platelets are particularly well-suited for reinforcement of nonpolar elastomers such as NR when dispersed by latex mixing. As this processing approach is common practice in industry to produce carbon black-filled elastomer masterbatches,[11] RG-O/NR masterbatches (or masterbatches with other elastomers, e.g., styrene-butadiene rubber or butadiene rubber) could thus potentially provide significant technological benefit in tires and other applications utilizing similar masterbatches in compound formulation. Much more detailed studies could be performed on these nanocomposites to better evaluate their suitability for use in such applications.

Indeed, one major limitation of this work is the limited scope of property measurements considered. The nanocomposites studied in this work were evaluated primarily on the basis of their mechanical, electrical, and thermal properties which could be tested by simple laboratory measurements. It would be of great interest to qualify some of these nanocomposite systems using tests aimed at specific applications. For example, how does the morphology of graphene platelets dispersed in an elastomer affect the extrusion resistance or rapid gas decompression resistance of the nanocomposite, for use in sealing applications? A good example of such practically-oriented nanocomposites testing in the scientific literature is seen in the work by Endo and co-workers.[12] This

dissertation clearly demonstrates the great potential for graphene in producing multi-functional property enhancement based upon simple laboratory tests, but further analysis is needed to determine whether these property enhancements would translate into improved performance of elastomeric components in application.

Another open question is how graphene platelets influence properties when mixed with conventional fillers in existing compounds. This could provide a new paradigm for nanocomposites research—instead of displacing all filler materials with a low loading of a single nano-filler as is typically done in academic research, the nano-filler could be considered as another additive to a compound, specifically formulated (functionalized) for compatibility with a given elastomer, cure system, or other additives. Nanotechnology companies such as Nanocyl have begun marketing nanocomposite masterbatches specifically for this purpose. Incorporation of graphene-based materials into elastomer compounds containing high loadings of carbon black and other fillers could produce unique morphologies and properties that could be of great scientific and industrial interest.

Further consideration of interfacial chemistry and bonding in nanocomposite systems is warranted in light of this work.[13] Poor stress transfer may limit the reinforcing capability of graphene platelets[14, 15] as a result of weak interfacial bonding, particularly in elastomeric nanocomposites.[16] The work of Chapter 7 clearly illustrates the influence that matrix-filler chemical compatibility has on nanocomposite properties. While RG-O and MWNT show excellent mechanical property enhancement in NR which is thus indicative of strong interfacial bonding, modification of the surface chemistry to promote covalent

bonding could dramatically improve upon these results. To date, there have been very few literature reports of elastomer nanocomposites with covalent bonding at the matrix-filler interface.

Another open question of a more fundamental nature relates to the discrepancy mentioned in Chapter 5 over SEM/AFM measurements of isolated graphene platelet lateral dimensions and TEM analysis of platelets dispersed in a polymer matrix. This discrepancy is implicit throughout much of the literature as graphene platelets are often cited as having intrinsic aspect ratios of 1000 or more, yet average aspect ratios measured by quantitative TEM analysis of dispersed graphene platelets are more than an order of magnitude lower. It would be of interest to examine this problem in detail to elucidate the reasons for this discrepancy. Is misalignment of platelets to the beam axis making the platelets appear thicker and thus lowering the average A_f? If TEM limitations were found to be the underlying reason and a much greater A_f was measured through more careful sample preparation or analysis, then it would provide contrary result to the good agreement between TEM analysis, composite model predictions, and experimental modulus data reported herein, and would consequently suggest poor interfacial bonding in these systems. Alternatively, evidence may be found to suggest that particle attrition occurs during shear mixing processes and that few-layer graphene platelets indeed predominately exist in most graphene/polymer nanocomposite systems, which would reinforce the need to develop reliable functionalization protocols that could allow for homogeneous dispersions of single-layer chemically-modified graphene platelets.

There are many other potential research directions to pursue following this work. For instance, does dispersion of TEGO in a Banbury-style mixer provide a better dispersion and larger property enhancement than TEGO dispersed on a two-roll mill? How does use of TEGO with a higher C : O ratio affect dispersion and properties? One could also investigate the effect of coagulation speed or coagulant on properties of latex-mixed RG-O/elastomer nanocomposites. Fundamental questions remain from the work of Chapters 3 and 4. For example, is the improved conductivity in annealed nanocomposites truly due to disorientation of platelets and formation of conductive pathways, or is another factor at play, such as further thermal reduction of the MEGO platelets? How does solution mixing compare as a dispersion method for G-O and RG-O versus *in situ* polymerization and melt processing? Finally, a more detailed nanofiller comparison study as in Chapter 7 could be performed with more careful consideration of the curing system as well as use of other dispersion methods to compare property enhancement. For example, how does organically-modified clay disperse into an elastomer by mill compounding or internal mixing, compared with TEGO and/or multi-walled carbon nanotubes? Extending such a study to include evaluation of properties such as permeability and dielectric strength could also be of great value to the field.

8.3. REFERENCES

1. Mullins, L. Softening of rubber by deformation. *Rubber Chemistry and Technology* **1969,** 42, 339-362.

2. Zhan, Y. H.; Wu, J. K.; Xia, H. S.; Yan, N.; Fei, G. X. Dispersion and Exfoliation of Graphene in Rubber by an Ultrasonically-Assisted Latex Mixing and In Situ Reduciton Process. *Macromolecular Materials and Engineering* **2011,** 296, 590-602.

3. Kim, H.; Abdala, A. A.; Macosko, C. W. Graphene/Polymer Nanocomposites. *Macromolecules* **2010,** 43, 6515-6530.

4. Paul, D. R.; Robeson, L. M. Polymer nanotechnology: Nanocomposites. *Polymer* **2008,** 49, (15), 3187-3204.

5. Kim, H.; Macosko, C. W. Processing-property relationships of polycarbonate/graphene composites. *Polymer* **2009,** 50, (15), 3797-3809.

6. Ren, J.; Casanueva, B. F.; Mitchell, C. A.; Krishnamoorti, R. Disorientation Kinetics of Aligned Polymer Layered Silicate Nanocomposites. *Macromolecules* **2003,** 36, 4188-4194.

7. Fornes, T. D.; Paul, D. R. Modeling properties of nylon 6/clay nanocomposites using composite theories. *Polymer* **2003,** 44, (17), 4993-5013.

8. Qiao, R.; Catherine Brinson, L. Simulation of interphase percolation and gradients in polymer nanocomposites. *Composites Science and Technology* **2009,** 69, (3-4), 491-499.

9. Kim, H.; Macosko, C. W. Morphology and properties of polyester/exfoliated graphite nanocomposites. *Macromolecules* **2008,** 41, (9), 3317-3327.

10. Nan, C.-W.; Shen, Y.; Ma, J. Physical Properties of Composites Near Percolation. *Annual Review of Materials Research* **2010,** 40, 131-151.

11. Mark, J. E.; Erman, B.; Eirich, F. R., *The Science and Technology of Rubber*. 3rd ed.; Elsevier 2010.

12. Endo, M.; Noguchi, T.; Ito, M.; Takeuchi, K.; Hayashi, T.; Kim, Y. A.; Wanibuchi, T.; Jinnai, H.; Terrones, M.; Dresselhaus, M. S. Extreme-Performance Rubber Nanocomposites for Probing and Excavating Deep Oil Resources Using Multi-Walled Carbon Nanotubes. *Advanced Functional Materials* **2008,** 18, (21), 3403-3409.

13. Kim, H.; Kobayashi, S.; AbdurRahim, M. A.; Zhang, M. J.; Khusainova, A.; Hillmyer, M. A.; Abdala, A. A.; Macosko, C. W. Graphene/polyethylene nanocomposites: Effect of polyethylene functionalization and blending methods. *Polymer* **2011,** 52, (8), 1837-1846.

14. Cai, M.; Glover, A. J.; Wallin, T. J.; Kranbuehl, D. E.; Schniepp, H. C. Direct Measurement of the Interfacial Attractions between Functionalized Graphene and Polymers in Nanocomposites. *AIP Conference Proceedings* **2010,** 1255, 95-97.

15. Gong, L.; Kinloch, I. A.; Young, R. J.; Riaz, I.; Jalil, R.; Novoselov, K. S. Interfacial Stress Transfer in a Graphene Monolayer Nanocomposite. *Advanced Materials* **2010,** 22, 2694-2697.

16. Shia, D.; Hui, C. Y.; Burnside, S. D.; Giannelis, E. P. An Interface Model for the Prediction of Young's Modulus of Layered Silicate-Elastomer Nanocomposites. *Polymer Composites* **1998,** 19, (5), 608-617.

Appendix A:

Quantifying Dispersion by Transmission Electron Microscopy

Of the methods often used in the literature to assess nanocomposite dispersion, transmission electron microscopy (TEM) is perhaps the most powerful and informative method as it allows the level of exfoliation of the particles and their spatial distribution to be directly observed. Qualitatively, dispersion is assessed by TEM according to the dimensions of the platelets (thickness and aspect ratio), and whether or not the platelets are distributed evenly over the cross section. States of dispersion can be also be assigned to the micrographs depending on whether or not the platelets are stacked together. However, with the use of image analysis software, it is possible to quantify the dispersion of graphene platelets in terms of an aspect ratio,[1, 2] A_f, which in turn can be used to compare dispersion—particularly between two or more types of related systems, such as in this study—in a more concrete way.

As mentioned in Chapter 5, there are many issues complicating accurate determination of particle aspect ratio using the ImageJ software. First, the method requires accurate identification of particles. Thin particles may require tracing, which provides a possible source of error as proper identification of platelets can be difficult. Additional complications arise with the software used to analyze the binary images, ImageJ.[3] Each particle is separately identified by the software and shape characteristics

such as the particle area and perimeter can be provided according to the user's specifications. However, no explicit values of the particle length or thickness are provided by the ImageJ software. Depending on which quantities are used as the thickness and length, the estimates of the particle aspect ratios can vary widely. For example, by taking the particle length to be equal to half the perimeter and dividing by the minimum caliper distance of the particle ("MinFeret"), the number average aspect ratio of the platelets in Figure A.1 was calculated to be approximately 16. On the other hand, taking the perimeter as half the particle length and dividing it into the area to get a thickness, followed by an aspect ratio, gives a number average aspect ratio of 110. Given the degree of variability in determination of an average A_f value, a detailed analysis of the different measures of particle dimensions was compared against independent measurements was performed as described below.

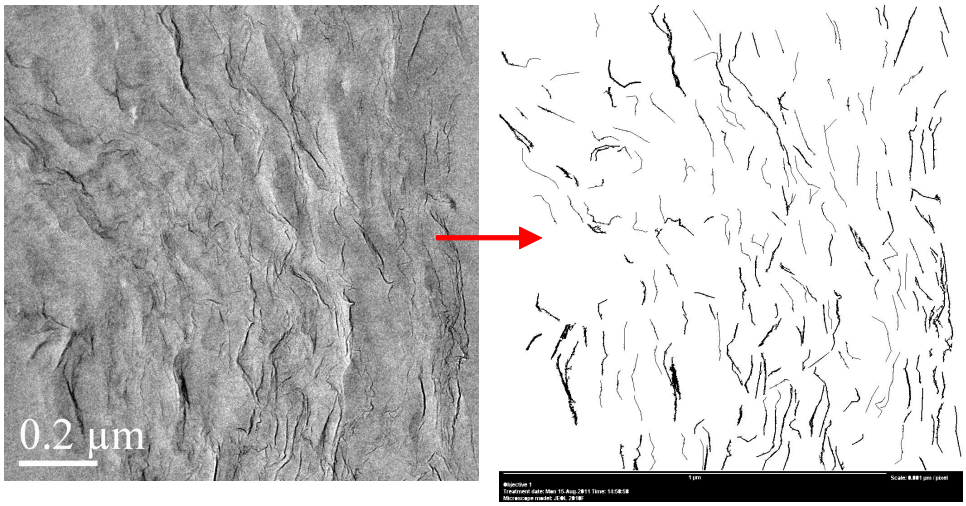

Figure A.1. Identification and isolation of platelets in TEM micrographs for dispersion quantification.

As shown in Figure A.2, small section of a TEM micrograph was isolated and analyzed to illustrate the disparity amongst the different measures of particle size and shape. This particular area was chosen as it contains three particles of different aspect ratio and importantly of different shape—one elongated particle, one slightly bent particle, and one highly curved particle.

Method A: Let "Feret" = ℓ. Assume a rectangular shape such that thickness $t = A / \ell$. The quotient ℓ / t gives the aspect ratio, A_f.

Method B: Let Perimeter/2 = ℓ. Assume a rectangular shape such that $t = A / \ell$; then $\ell / t = A_f$.

Method C: Divide the major and minor axes of the ellipse.

Method D: Let Perimeter/2 = ℓ. Take the minimum caliper distance "MinFeret" to be equal to t. Then $\ell / t = A_f$.

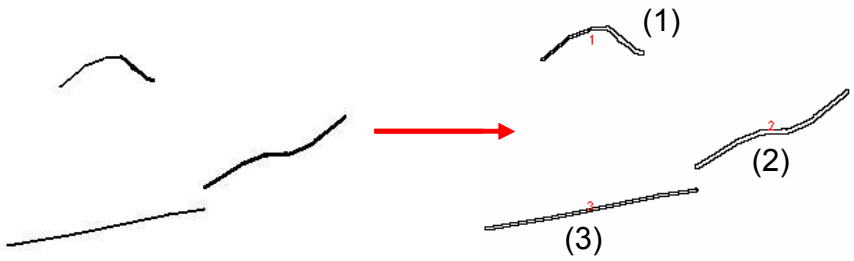

Figure A.2. Outline of particles (left) and ImageJ traces (right) from a TEM micrograph of a 5 wt% RG-O/NR nanocomposite for use in illustrating variability in particle size quantification.

Table A.1. Comparison of different particle size definitions and their predictions of aspect ratio with the independently measured value of aspect ratio.

Particle #	Method A	Method B	Method C	Method D	Direct Measure
1	28.3	43.2	3.2	4.1	**36.5**
2	38.9	46.0	12.1	10.6	**42.0**
3	78.2	88.0	61.5	37.0	**77.0**

Clearly, the use of an ellipse to fit the particles causes the aspect ratio of the curved particles to be significantly underestimated, while the disparity is less pronounced for the elongated particle. Given that the low amount of contrast in the micrographs could preclude identification of single layer platelets and the irregular shape of the platelets, the *Af* is likely to be underestimated slightly by the quantification procedure. Comparing the results of Table A.1, then, it is recommended that Method B be used to provide the most accurate estimate of the average aspect ratio of the platelets; that is, by assuming each platelet can be modeled by an effective rectangle of area $A = \ell \times t$, taking the perimeter (determined by the software) as 2ℓ, and dividing A / ℓ to get t and thus A_f for each platelet.

As pointed out in Chapter 5, there appears to be a discrepancy between the size of the platelets observed by SEM and TEM. Given that SEM cannot resolve the thickness of the platelets, comparisons of lateral dimensions between the two microscopy methods is more appropriate. Several SEM micrographs at varying magnification levels were

analyzed following a similar procedure as with the TEM micrographs. Platelets were approximated as circular shapes and an effective diameter was calculated from the platelet area directly measured by the software. Figure A.3 shows a histogram comparing the two microscopy methods. This analysis shows a major difference in lateral dimensions of the platelets which could be due to a variety of factors such as the irregular shape of the platelets preventing accurate determination of lateral dimensions. From this analysis, it is believed the aspect ratio quantified by TEM is lower than the "true" average aspect ratio of the platelets, especially when taking into account focusing errors and disorientation of platelets which can increase their apparent thickness, low contrast preventing identification of some platelets, etc.

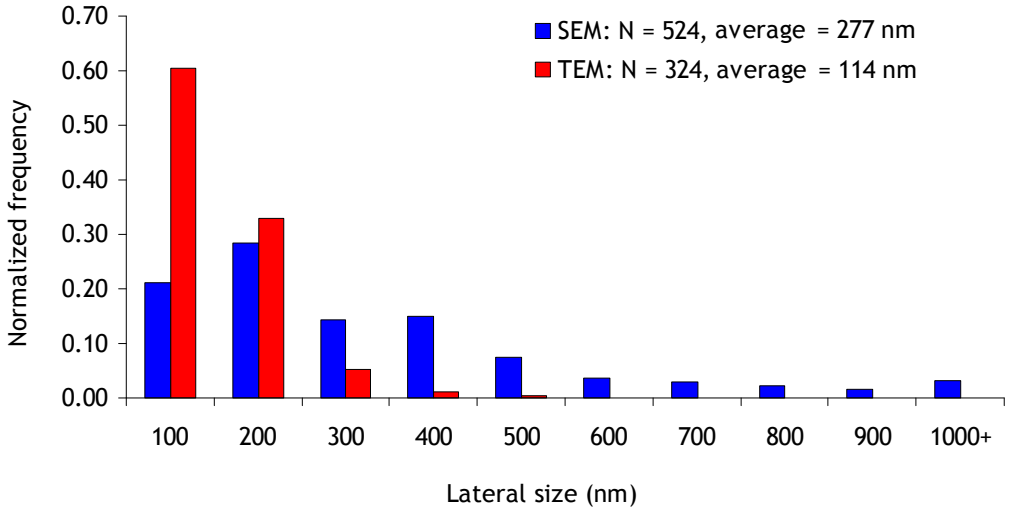

Figure A.3. Histogram comparing the lateral dimensions of RG-O platelets as determined from SEM and TEM analyses.

REFERENCES

1. Fornes, T. D.; Paul, D. R. Modeling properties of nylon 6/clay nanocomposites using composite theories. *Polymer* **2003,** 44, (17), 4993-5013.

2. Kim, H.; Abdala, A. A.; Macosko, C. W. Graphene/Polymer Nanocomposites. *Macromolecules* **2010,** 43, 6515-6530.

3. Rasband, W. S. ImageJ. http://imagej.nih.gov/ij/ (April 12, 2012)

Appendix B:

Micromechanical Models: Equations and Calculation Details

B.1. MORI-TANAKA MODEL

For polymer composites which are transverse isotropic, the composite modulus can be approximated by analytical expressions based on Mori-Tanaka theory.[1, 2] The measured values of the nano-filler aspect ratio, along with tabulated values for the Poisson's ratio, ν, of graphite (equal to 0.37[3, 4]) and the polymer matrix (as determined from the literature for the specific polymer), and a graphene platelet modulus (E_f; generally taken as 250 GPa), can be used to predict the modulus of the nanocomposite at various volume fractions of filler:

$$E = \frac{E_m}{1 + \phi(-2\nu_m A_3 + (1-\nu_m)A_4 + (1+\nu_m)A_5 A)/2A}$$

where E is the (transverse) composite modulus, E_m is the matrix elastic modulus, ϕ is the volume fraction of filler (converted from weight percent based on the density of graphite, ~2.28 g/cm^3), and the A_n are parameters that can be calculated from ϕ, E_m, E_f, and ν following equations derived by Tandon and Weng.[2]

B.2. HALPIN-TSAI MODEL (UNMODIFIED AND MODIFIED)

The Halpin-Tsai model assumes a uniform dispersion of disk-shaped inhomogeneities of defined aspect ratio in a polymer matrix.[5, 6] As with the Mori-Tanaka model, the measured matrix elastic modulus (E_m) was determined from experiment, while E_f was taken as 250 GPa. The equations used to perform the calculations are:

$$E = \frac{E_m(1+\zeta\eta\phi_f)}{1-\eta\phi_f}, \text{ where } \eta = \frac{E_f/E_m - 1}{E_f/E_m + \zeta}$$

where E_f and E_m is the filler and matrix modulus, ϕ_f is the volume fraction of filler, and ζ is a shape factor given by $\zeta = 2A_f$, where A_f is the aspect ratio of the disk-shaped platelet.

Nielsen modified the Halpin-Tsai model[7] to account for deviations between experiment and model predictions at high volume fractions of filler. In his modification, the maximum volume packing fraction ϕ_m is incorporated into the model through a factor φ as:

$$E = \frac{E_m(1+\zeta\eta\phi_f)}{1-\varphi\eta\phi_f}, \text{ where } \varphi = 1 + \phi\ [(1-\phi_m)/\phi_m^2]$$

ϕ_m can be interpreted as the ratio of the actual volume fraction of filler to the apparent volume fraction of filler, and could thus be related to the dispersion in the composite. Incorporation of the maximum volume packing fraction serves to increase the modulus predictions by the model at higher volume fractions, particularly for lower values of ϕ_m as illustrated by, e.g., by Wu and co-workers.[8] For randomly packed anisotropic particles,

ϕ_m is associated with the rigidity percolation threshold and was estimated as 0.05 for RG-O platelets of nominal $A_f > 200$ based upon the treatise of Bicerano and co-workers,[9] who provide an equation to estimate the ϕ_m of high A_f ellipsoids, as well as previous experimental results[10, 11] obtained from exfoliated mica particles.

B.3. GUTH EQUATION

The Guth equation considers only hydrodynamic reinforcement by rigid filler particles and is based on the work of Einstein and Smallwood and later of Guth and Gold,[8, 12, 13] who introduced a quadratic term into the Einstein equation to account for interactions between particles. Guth later posited that the reinforcing effect of spherical fillers was enhanced by the formation of anisotropic filler aggregates, for which he derived a relationship between the elastic modulus of the filled rubber and the volume fraction of filler[14]:

$$E = E_m(1 + 0.67f\phi + 1.62(f\phi)^2)$$

where E_m is the matrix modulus, f is a shape factor describing the ratio of the length to width of the particle, and ϕ is the volume fraction of filler. Note that the predictions of the Guth equation depend only upon the loading and geometry of the filler, and the matrix modulus—there is no dependence on the filler modulus as with the other models used in this study.

B.4. REFERENCES

1. Mori, T.; Tanaka, K. Average stress in matrix and average elastic energy of materials with misfitting inclusions. *Acta Metallurgica* 1973, 21, 571-574.

2. Tandon, G. P.; Weng, G. J. The effect of aspect ratio of inclusions on the elastic properties of unidirectionally aligned composites. *Polymer Composites* 1984, 5, 327-333.

3. Brandrup, J.; Immergut, E. H.; Grulke, E. A.; Abe, A.; Bloch, D. R., *Polymer Handbook*. 4 ed.; John Wiley and Sons: 1999; p 2336.

4. Kim, H.; Macosko, C. W. Morphology and properties of polyester/exfoliated graphite nanocomposites. *Macromolecules* 2008, 41, (9), 3317-3327.

5. Halpin, J. C.; Kardos, J. L. The Halpin-Tsai Equations: A Review. *Polymer Engineering and Science* 1976, 16, (5), 344-352.

6. Tucker, C. L.; Liang, E. Stiffness predictions for unidirectional short-fiber composites: Review and evaluation. *Composites Science and Technology* 1999, 59, 655-671.

7. Nielsen, L. E. Generalized Equation for the Elastic Moduli of Composite Materials. *Journal of Applied Physics* 1970, 41, (11), 4626-4627.

8. Wu, Y.; Jia, Q.; Yu, D.-S.; Zhang, L. Modeling Young's modulus of rubber-clay nanocomposites using composite theories. *Polymer Testing* 2004, 23, 903-909.

9. Bicerano, J.; Douglas, J. F.; Brune, D. A. Model for the Viscosity of Particle Dispersions. *Journal of Macromolecular Science, Part C: Polymer Reviews* 1999, 39, (4), 561-642.

10. King, J. A.; Via, M. D.; Morrison, F. A.; Wiese, K. R.; Beach, E. A.; Cieslinski, M. J.; Bogucki, G. R. Characterization of exfoliated graphite nanoplatelets/polycarbonate composites: electrical and thermal conductivity, and tensile, flexural, and rheological properties. *Journal of Composite Materials* 2011, DOI: 10.1177/0021998311414073.

11. Fisa, B.; Vu-Khanh, T.; Remillard, B. Extrusion of mica filled polypropylene. *Journal of Thermoplastic Composites* 1988, 1, 361-370.

12. Guth, E.; Gold, O. *Physical Review* 1938, 53, 322.

13. Bokobza, L. The Reinforcement of Elastomeric Networks by Fillers. *Macromolecular Materials and Engineering* 2004, 289, 607-621.

14. Guth, E. Theory of Filler Reinforcement. *Journal of Applied Physics* 1945, 16, (20), 20-25.

Appendix C:

Supporting Data on Reduced Graphene Oxide/Natural Rubber Nanocomposites

C.1. Scanning Electron Microscopy Images and X-ray Scattering Data

WAXS was performed at different loadings to evaluate dispersion as function of loading. From 1 to 4 wt%, no evidence of a GO/graphite diffraction peak was observed. However, a slight shoulder corresponding approximately to the interlayer spacing of graphite (0.8 nm) was observed at 5 wt% which became particularly pronounced by 10 wt%, suggesting the presence of a significant concentration of multi-layer tactoids.

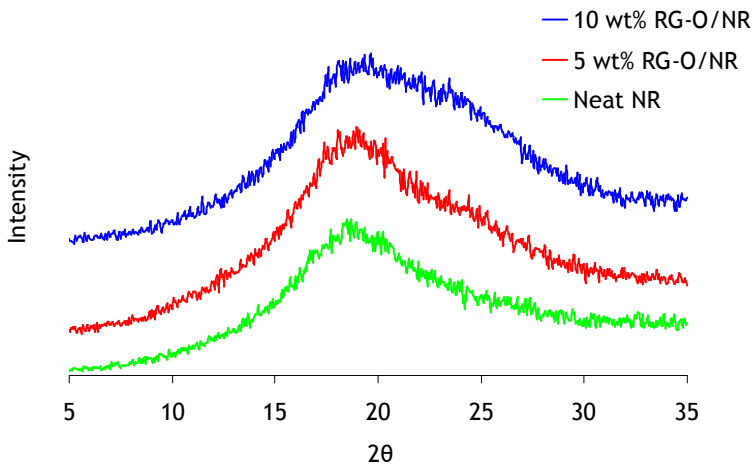

Figure C.1. WAXS spectrum of green RG-O/NR nanocomposites at different loadings.

SEM micrographs of 5 wt% RG-O/NR fracture sections (fractured from stress-strain testing) are shown in Figure C.2 through C.4. Samples that provided "representative" data (i.e., samples that did not fracture at low elongation) were set aside for SEM analysis; no surface preparation was done prior to imaging. The texture of the fracture surface of all three samples, regardless of processing/cure state, appeared to have a clumpy texture. However, the surfaces of the cured samples appeared to have a smoother texture. Fracture surfaces of solution treated and milled samples appeared similar.

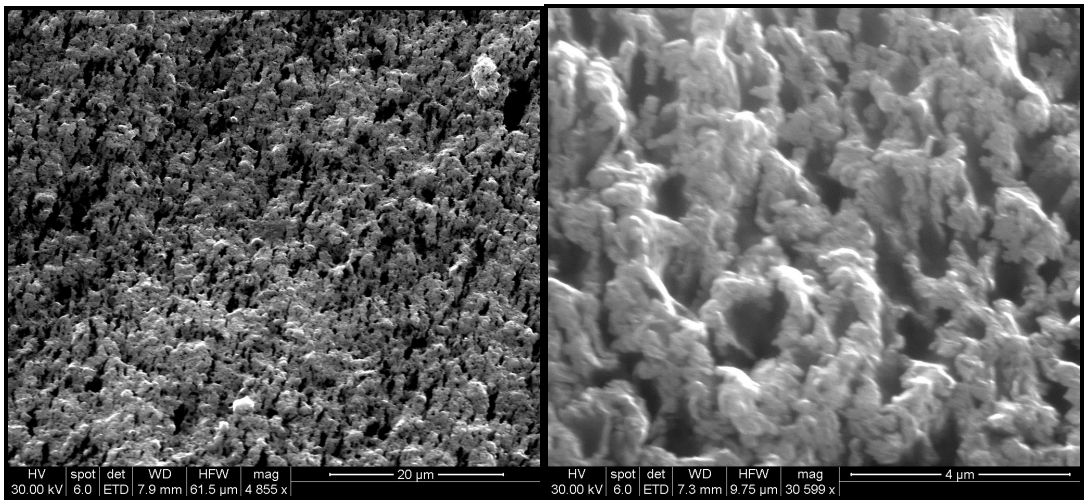

Figure C.2. SEM micrographs of the fracture surface of a green (uncured) 5 wt% RG-O/NR nanocomposite.

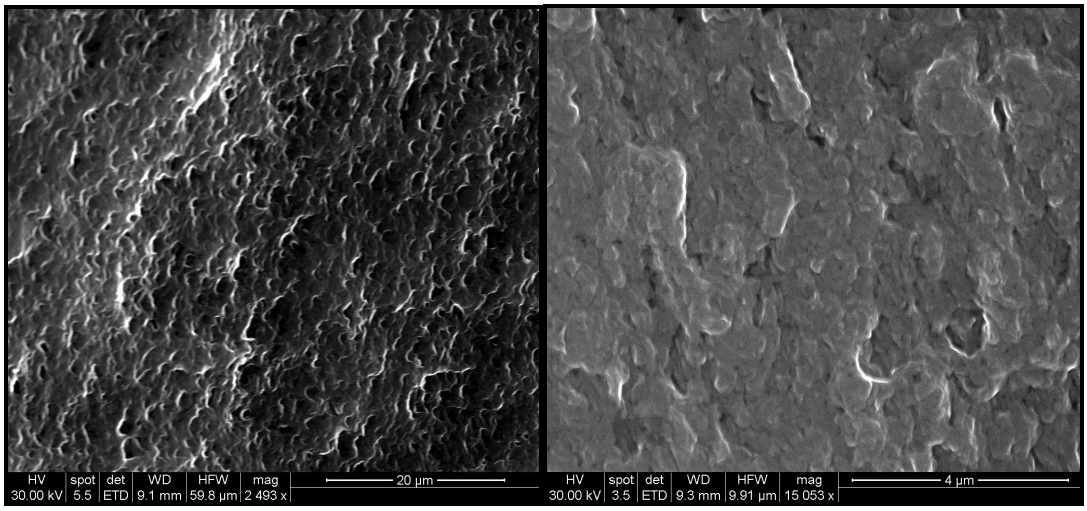

Figure C.3. SEM micrographs of the fracture surface of a solution treated 5 wt% RG-O/NR nanocomposite.

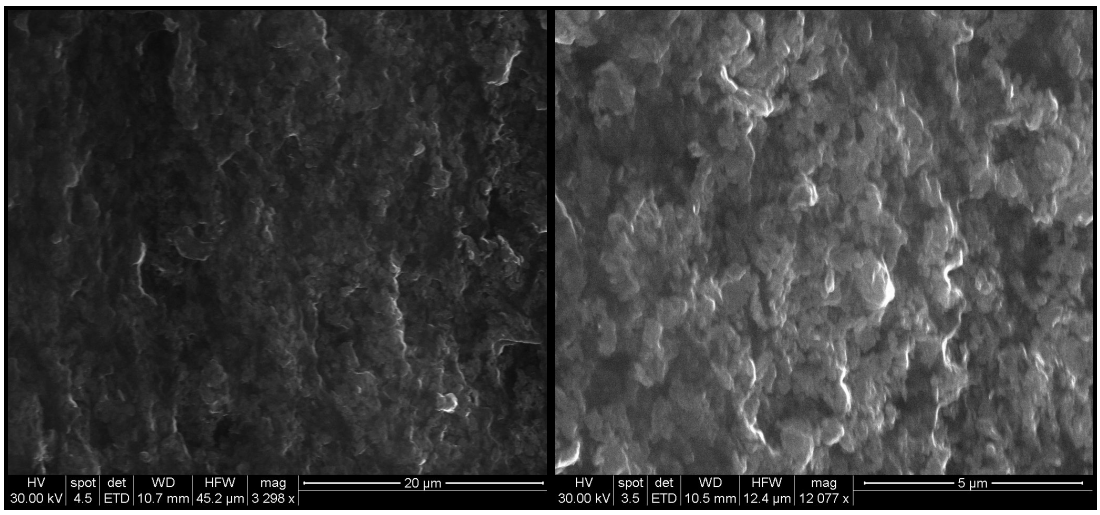

Figure C.4. SEM micrographs of the fracture surface of a milled 5 wt% RG-O/NR nanocomposite.

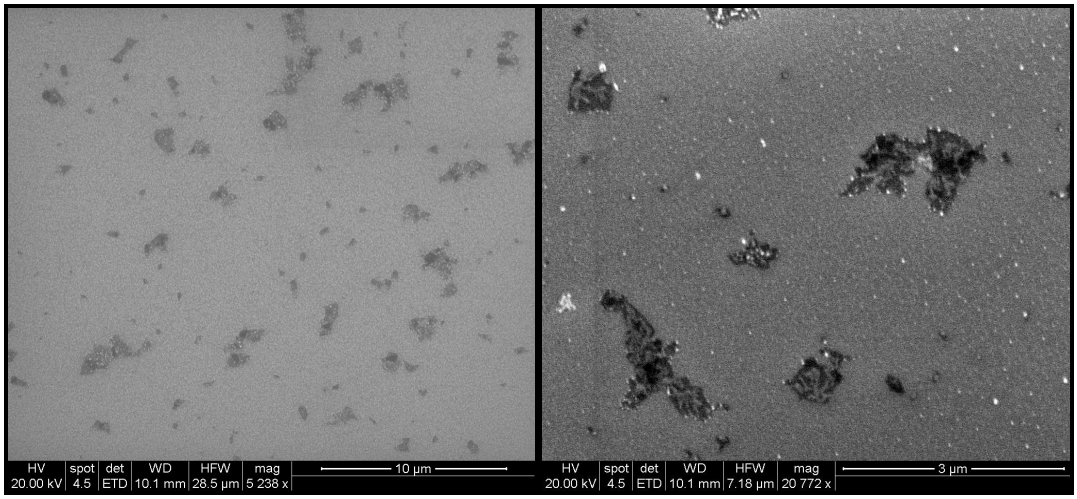

Figure C.5. SEM micrographs of RG-O platelets on a Si wafer, dried down from a highly dilute aqueous RG-O suspension (white particles may be KOH used to adjust pH).

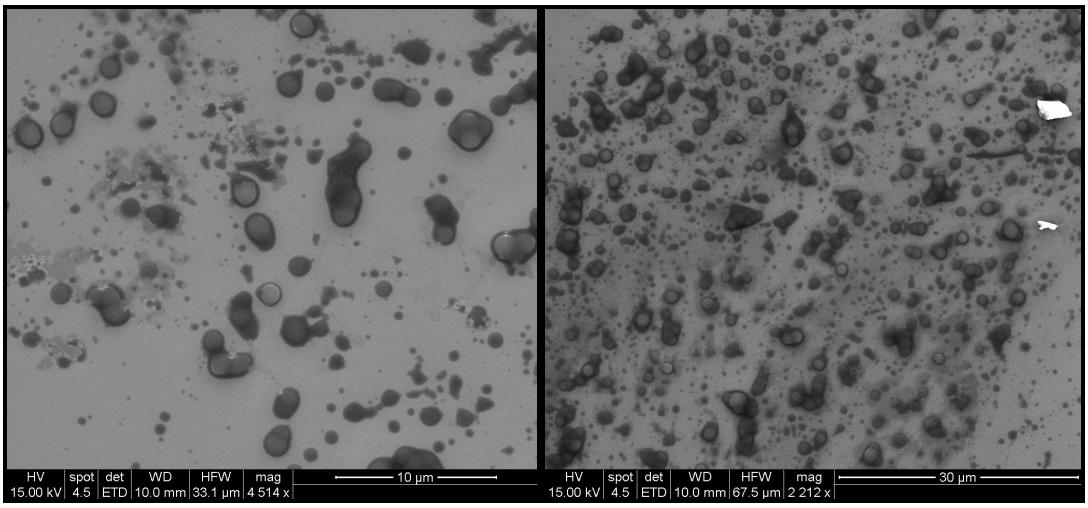

Figure C.6. SEM micrographs of NR latex particles on a Si wafer, dried down from a highly dilute NR latex suspension.

Objects appearing to be RG-O platelets were barely visible at high magnifications (>100,000x), but identification of these objects, if indeed RG-O platelets and not features

of the fracture surface, provides no useful information on the nature of the dispersion as achieved by TEM. It may be possible to analyze high magnification images for evidence of platelet "pull-out" for evidence of good (or bad) interfacial adhesion, although extensive analysis of these samples provided no insight in this regard.

C.2. SUPPLEMENTARY TEM IMAGES

TEM images of ~70 nm thin cryomicrotomed nanocomposite sections were acquired using a JEOL-2010F at 200 kV. Comparing the dispersions of the 3 wt% and 5 wt% RG-O/NR samples as represented by Figure C.7 and Figure C.8, respectively, there appeared to be a higher concentration of multi-layer tactoids in the 5 wt% sample. This observation is consistent with the WAXS results, which show the emergence of a slight peak corresponding to the interlamellar spacing of graphite around 5 wt% which gets stronger by 10 wt%. In addition, the platelets in the 3 wt% appeared to be more randomly oriented than the 5 wt% sample, as evidenced by the dark grey areas around the platelet edges in Figure C.7 and the predominately edge-on orientation apparent in the micrographs of Figure C.8. The higher degree of orientation in the 5 wt% sample could be the effect of packing constraints (between latex particles or clumps of latex particles) on the higher volume fraction of platelets. In both samples and in particular the 5 wt% sample, isolated regions of the sections appeared to have an excellent dispersion (Figure C.8). However, such regions were not representative of the sections overall, as there were large areas devoid of any platelets. By contrast, all regions of the milled RG-O/NR sections appeared very similar to the micrographs of Figure 5.5, with the platelets very

evenly dispersed over the cross section. Higher-magnification images such as Figure C.9 more clearly show the high level of exfoliation of the platelets.

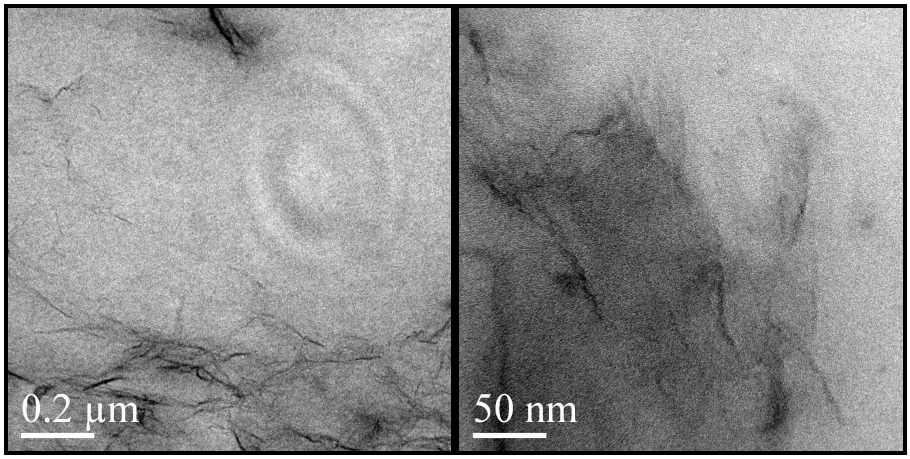

Figure C.7. TEM micrographs of green 3 wt% RG-O/NR nanocomposites.

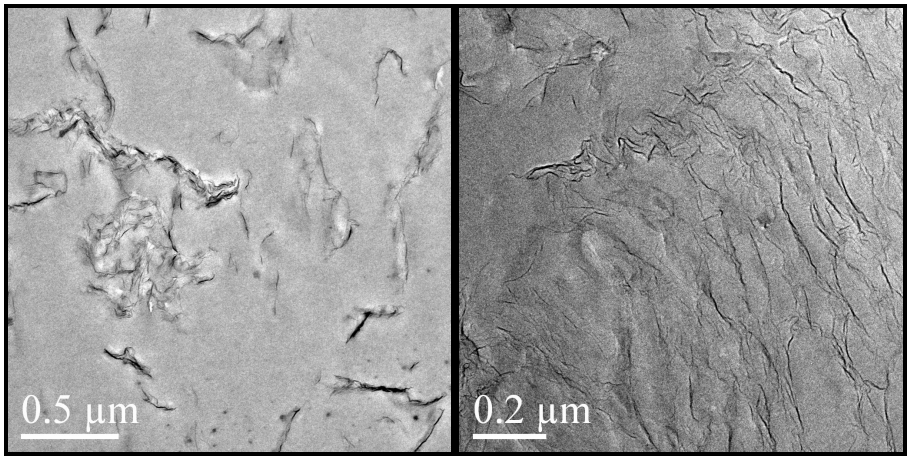

Figure C.8. TEM micrographs of green 5 wt% RG-O/NR nanocomposites.

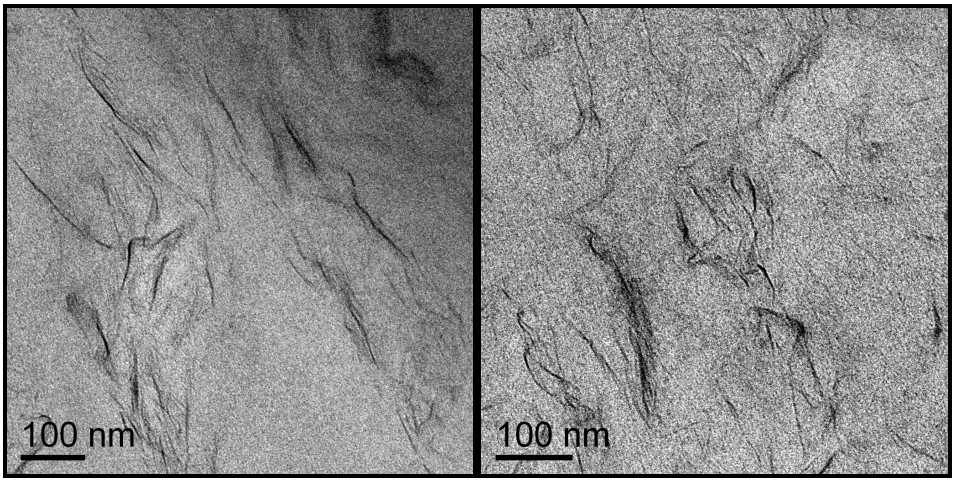

Figure C.9. TEM micrographs of milled, DCP-cured 5 wt% RG-O/NR nanocomposites showing high aspect ratio structure of dispersed RG-O platelets.

C.3. PROPERTIES OF UNCURED NR/RG-O NANOCOMPOSITES

As a baseline for the comparison to the properties of the solution treated (cured) nanocomposites, the electrical conductivity and thermal stability properties of the green (uncured) nanocomposites were measured. Electrical conductivity measurements showed similar trends in conductivity versus filler loading as shown in Figure C.10 (compare with Figure 5.3) as well as similar values of conductivity at higher loadings. As shown in Figure C.11, there was little change in the thermal stability of the nanocomposites versus neat NR, and no clear trend in thermal stability with increasing loading.

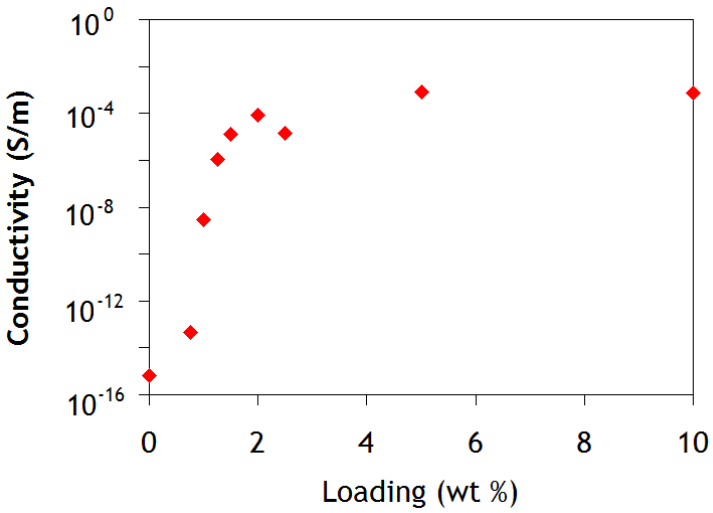

Figure C.10. Electrical conductivity as a function of loading of green RG-O/NR nanocomposites.

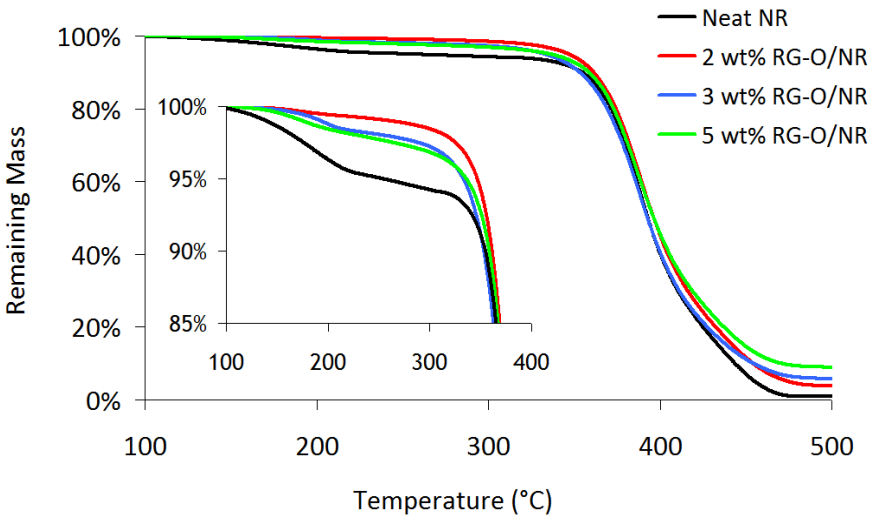

Figure C.11. Thermal stability of green RG-O/NR nanocomposites.

Representative stress-strain curves of the green RG-O/NR nanocomposites at selected loadings are shown in Figure C.12. The shape of the curves change in a similar fashion to the solution treated nanocomposites, approaching the stress-strain behavior of a low-modulus thermoplastic at higher loadings. The strain at break decreases with increasing loadings of RG-O filler. As with the solution treated nanocomposites, it is believed that the RG-O platelets, which are confined to interstitial regions between latex particles, prevent interparticle diffusion of NR chains following coagulation of the particles. Thus, interfaces between RG-O platelets and NR latex particles could serve as "flaws" which lead to fracture of the samples at low elongations.

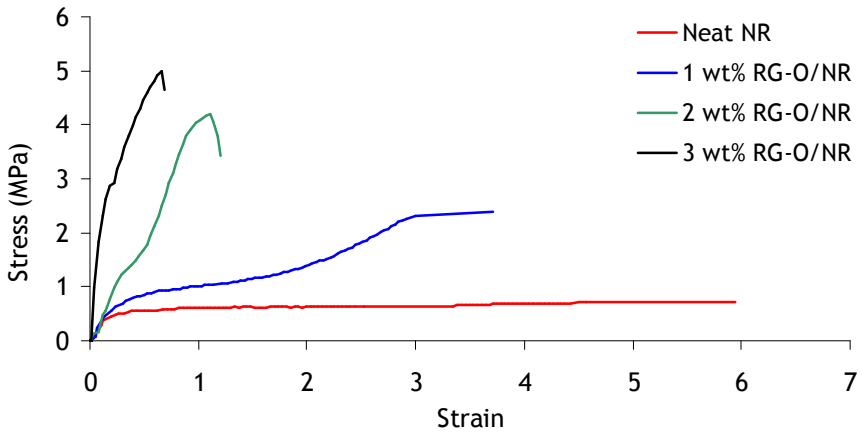

Figure C.12. Stress-strain curves of latex co-coagulated RG-O/NR nanocomposites.

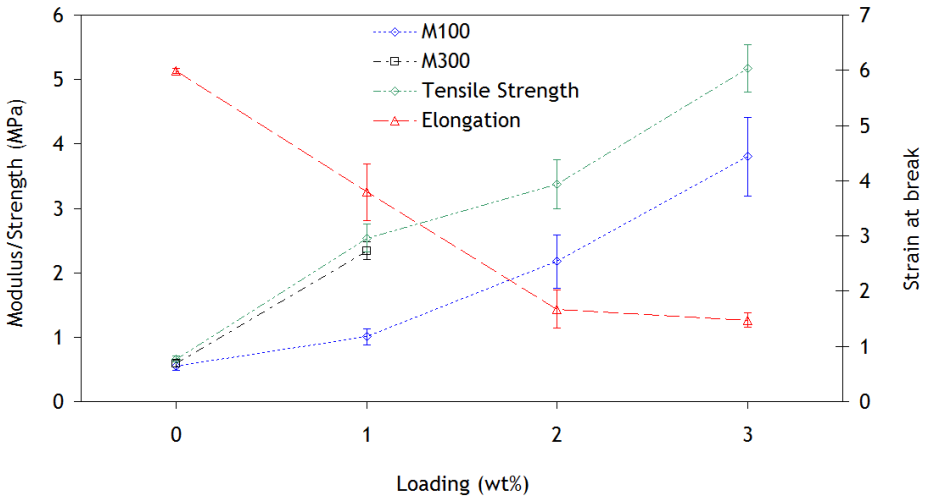

Figure C.13. Trends in the modulus at 100% and 300% elongation (M100 and M300, respectively), tensile strength, and strain at break for the RG-O/NR nanocomposites.

C.4. ADDITIONAL DATA ON MECHANICAL AND VISCOELASTIC PROPERTIES OF CURED NANOCOMPOSITES

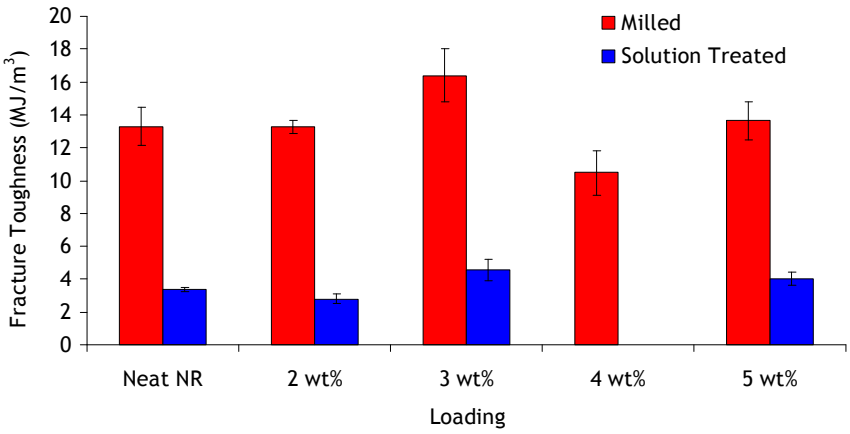

Figure C.14. Variation in facture toughness of the nanocomposites with RG-O loading.

Table C.1. Dynamic mechanical properties of solution treated RG-O/NR nanocomposites.

Loading	T_g	Tanδ at T_g	E' at -100 ºC	E' at 25 ºC
Neat NR	-50.1 ± 0.1	2.39 ± 0.10	1523 ± 90	0.99 ± 0.11
2.0 wt%	-49.1 ± 0.2	1.20 ± 0.09	3755 ± 220	7.00 ± 0.41
3.0 wt%	-49.7 ± 0.2	1.08 ± 0.10	4649 ± 150	12.2 ± 0.20
5.0 wt%	-50.4 ± 0.5	0.81 ± 0.05	5137 ± 93	19.3 ± 0.28

Table C.2. Dynamic mechanical properties of milled RG-O/NR nanocomposites.

Loading	T_g	Tanδ at T_g	E' at -100 ºC	E' at 25 ºC
Neat NR	-52.5 ± 0.1	2.42 ± 0.04	2659 ± 120	1.51 ± 0.04
2.0 wt%	-51.8 ± 0.2	1.95 ± 0.09	3564 ± 159	2.81 ± 0.03
3.0 wt%	-51.6 ± 0.1	1.67 ± 0.07	3801 ± 95	3.40 ± 0.06
4.0 wt%	-51.5 ± 0.4	1.48 ± 0.12	4399 ± 320	6.25 ± 0.04
5.0 wt%	-51.1 ± 0.3	1.38 ± 0.05	5279 ± 150	7.08 ± 0.05

Strain sweeps of neat NR and RG-O/NR nanocomposites were performed at 25 °C and 1 Hz in an elongational geometry. Defining a critical limiting strain as 90% of the plateau modulus value, the average limiting strains (from three strain sweeps per sample)

for the milled nanocomposites were 6.25, 2.3, 2.05, 1.45, and 0.81 for the neat, 2 wt%, 3 wt%, 4 wt%, and 5 wt% samples, respectively.

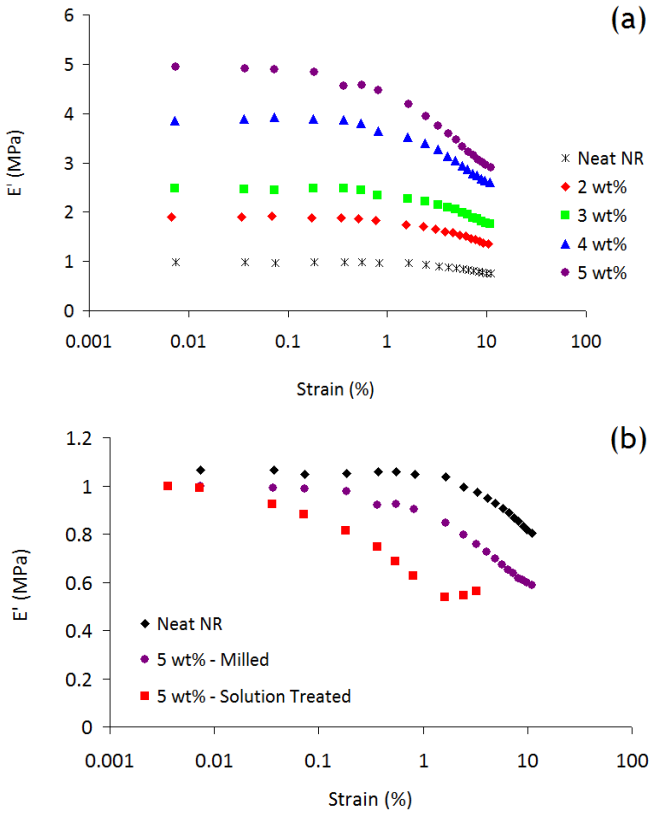

Figure C.15. (a) Representative strain sweeps of milled RG-O/NR nanocomposites at various loadings. (b) Normalized strain sweep comparison of 5 wt% milled and solution treated samples.

S.5. Effect of Cure Conditions on Properties

A variety of cure systems can be used to crosslink NR; peroxide curing was employed in this work for the sake of simplicity as traditional sulfur cure systems typically require the use of accelerators and anti-oxidants to achieve full cure.[1] Peroxide

cure systems create C–C bonds between the chains which are stronger than the monosulfidic and polysulfidic bonds formed in sulfur curing systems and peroxide-cured compounds are generally more thermally stable than sulfur-cured compounds. However, sulfur-cured compounds have generally been reported to show higher elongations at break, higher T_gs,[2] and higher tear strength for a given content of curing agent.

In the results presented in Chapter 5, all property data on the nanocomposites utilized the same cure system: 1 phr DCP cured at 150 °C for 60 min. At 150 °C, DCP has a half life of 15 minutes and thus 60 min of curing should be sufficient to decompose 94% of the DCP. As a quantitative cross-linking agent, one C–C bond is produced for each molecule of DCP that decomposes.[3] However, it is widely known that the presence of filler particles can affect the curing process dramatically via, e.g., radical abstraction, which can consequently affect the final cure state. It was thus sought to evaluate the effect of DCP concentration and curing conditions on the mechanical properties of NR and 5 wt% RG-O/NR nanocomposites. DCP concentrations between 0.5 and 3 phr were considered in light of prior research by Wood and co-workers[4, 5] showing that concentrations of 5 phr DCP and higher resulted in NR vulcanizates with low tensile strength and low elongation to break (below 100%). No attempt was made to directly monitor cure kinetics of the elastomer nanocomposites in this study, which could be the basis for future work in this area.

Figure C.16 illustrates the effect of DCP concentration on the mechanical properties of the nanocomposites. The modulus at 100% elongation, M100, was seen to increase in a linear fashion with increasing DCP concentration. However, the tensile

strength and elongation at break were maximized at intermediate DCP concentrations. For the neat NR vulcanizates, the combination of strength and elongation reached a plateau between 1 and 2 phr, with a sharp drop in both properties occurring at 3 phr DCP. For the nanocomposites, a pronounced peak in strength and elongation to break was observed at 1 phr. It should be noted that the testing speed of the nanocomposites for this study of curing concentration was 500 mm/min, compared with 250 mm/min for the results presented in Chapter 5, which may account for the minor differences in average strength and elongation to break for the samples between those results and those in Figure 5.7.

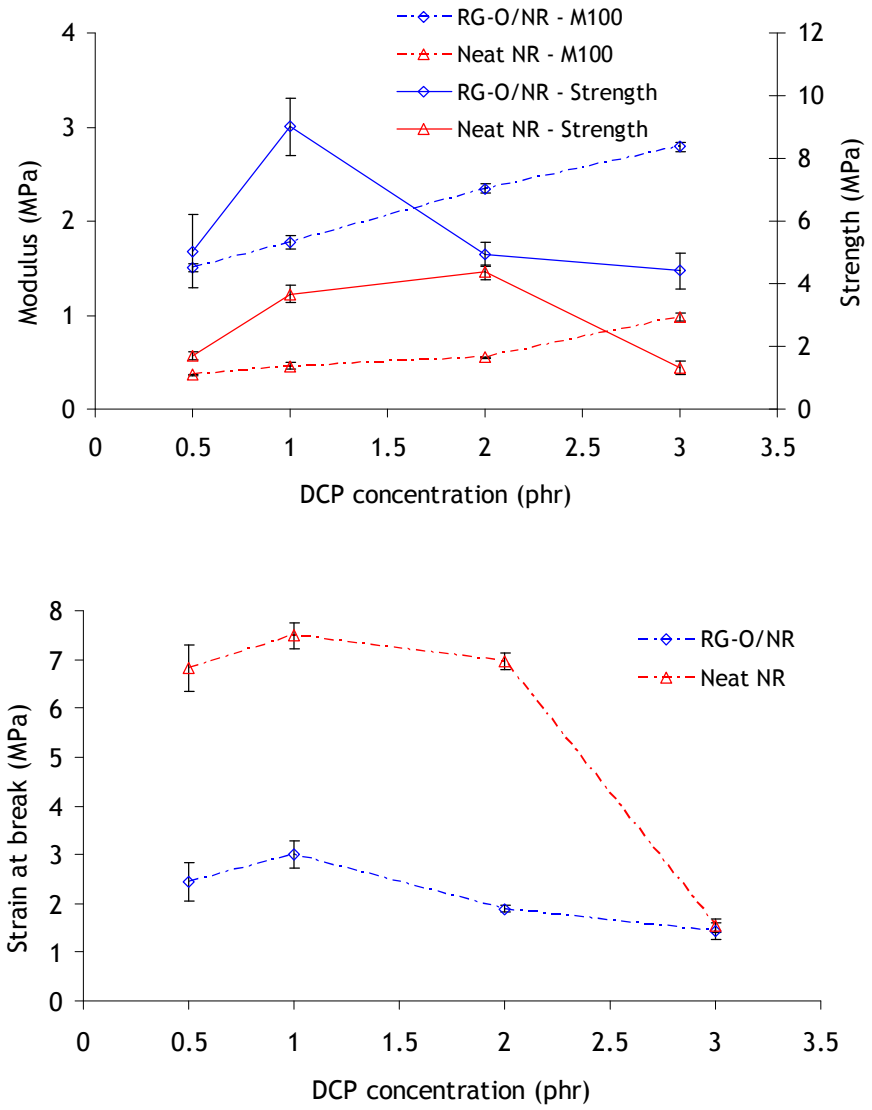

Figure C.16. Effect of DCP concentration on (a) modulus at 100% elongation and tensile strength and (b) strain at break of neat NR and 5 wt% RG-O/NR nanocomposites.

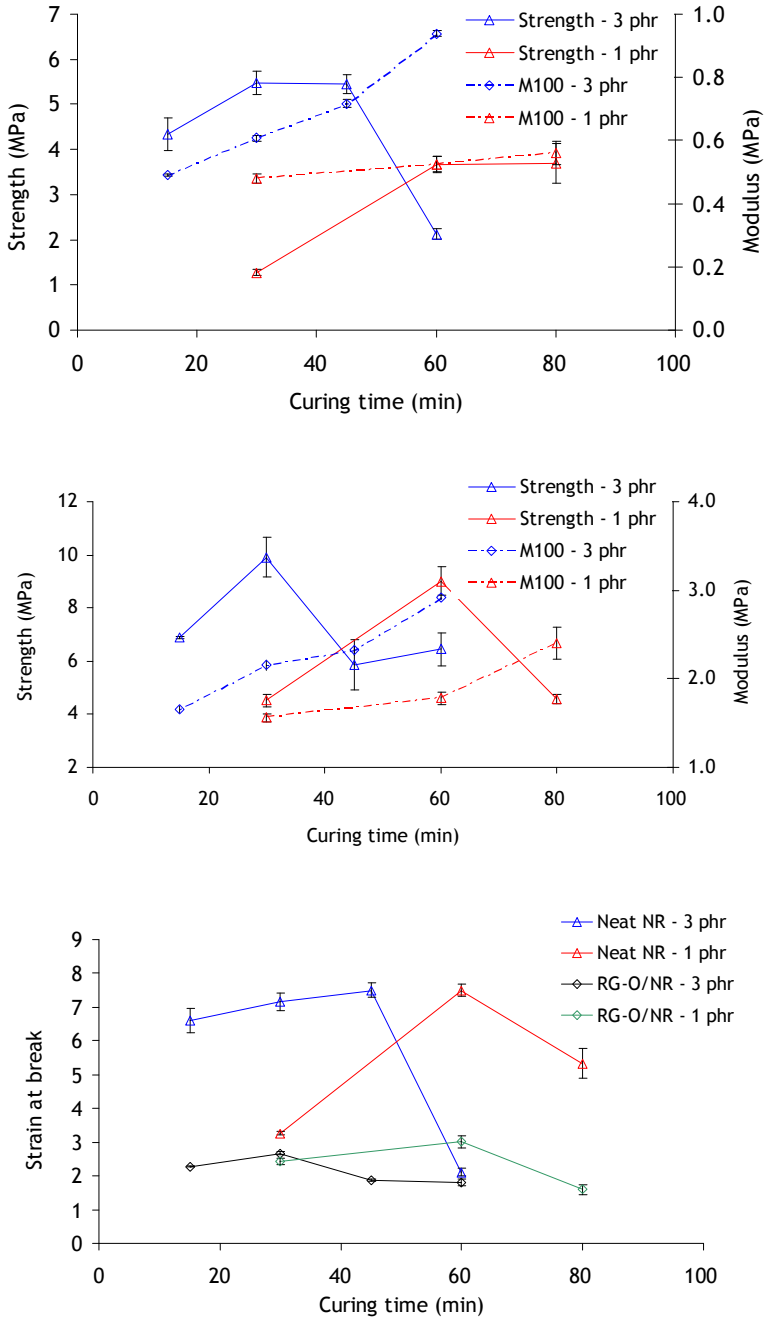

Figure C.17. Effect of cure time on (a) the strength and M100 of neat NR, (b) the strength and M100 of 5 wt% RG-O/NR nanocomposites, and (c) the strain at break of neat NR and RG-O/NR. Samples were cured at 150 °C.

C.6. COMPOSITE MODEL EQUATIONS AND MODULUS DETERMINATION

The quality of the experimental modulus data is highly important as the models were compared to experimental data. To establish confidence in the modulus values, the elastic moduli of neat NR and the nanocomposites were determined in two ways: 1) by fitting lines to the experimental data at strains less than 0.05, and 2) calculations based on material constants obtained from the Mooney-Rivlin plot according to the equation $E = 6 \cdot (C_1 + C_2)$. The elastic modulus values determined by both approaches are presented in Table C.3. While the absolute values of the moduli determined by the two methods differ by over a factor of 2, the trends in the moduli are quite similar, and when normalized to the value of neat NR, both sets of data roughly superimpose on one another. Given the excellent agreement in the modulus increment as function of filler loading between the two sets of data, the values obtained by curve-fitting were taken as representative values of the elastic moduli of the compounds. For the Mori-Tanaka and Halpin-Tsai models, a linear fit was used (R^2 = 0.967); for the Guth and modified Mori-Tanaka models a power law fit was used (R^2 = 0.999).

Table C.3. Experimental elastic moduli of neat NR and RG-O/NR nanocomposites as determined by fitting a line to the stress-strain data below 10% strain, and from analysis of Mooney-Rivlin plots of the data.

Loading		**Initial Modulus**		**Mooney-Rivlin**	
Sample	**Volume fraction**	**Modulus (MPa)**	**Normalized Modulus**	**Modulus (MPa)**	**Normalized modulus**
Neat NR	0.000	0.503	1.000	0.237	1.000
2 wt%	0.009	0.807	1.604	0.380	1.603
3 wt%	0.013	0.904	1.797	0.462	1.949
4 wt%	0.018	1.333	2.650	0.589	2.485
5 wt%	0.022	1.564	3.109	0.722	3.046

C.7. REFERENCES

1. Dick, J. S., *Rubber Technology: Compounding and Testing for Performance*. Carl Hanser Verlag: Munich, 2001.

2. Hagen, R.; Salmen, L.; Stenberg, B. Effect of the Type of Crosslink on Viscoelastic Properties of Natural Rubber. *Journal of Polymer Science Part B: Polymer Physics* **1996,** 34, 1997-2006.

3. Lorenz, O.; Parks, C. R. The Crosslinking Efficiency of Some Vulcanizing Agents in Natural Rubber. *Journal of Polymer Science* **1961,** 12, 299-312.

4. Wood, L. A.; Bullman, G., W. Creep and Other Tensile Properties of Rubber Cross-linked by Dicumyl Peroxide. *Journal of Polymer Science* **1972,** 10, 43-50.

5. Wood, L. A.; Bullman, G., W.; Decker, G. E. Modulus of Natural Rubber Crosslinked by Dicumyl Peroxide. I. Experimental Observations. *Rubber Chemistry and Technology* **1972,** 45, 1388-1402.

Appendix D:

Supporting Data on Thermally-Exfoliated Graphite Oxide/Natural Rubber Nanocomposites

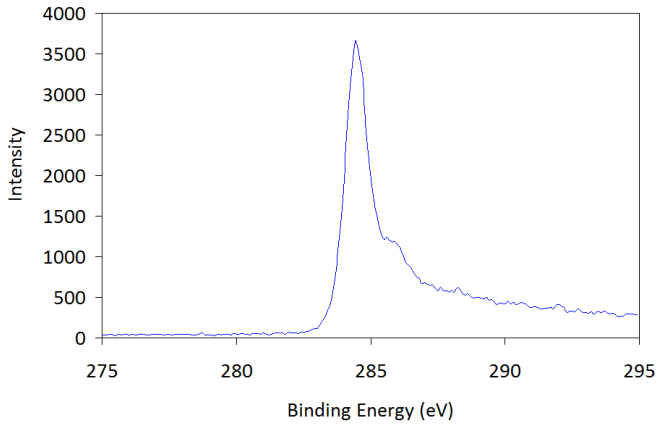

Figure D.1. X-ray photoelectron C 1s spectra of TEGO.

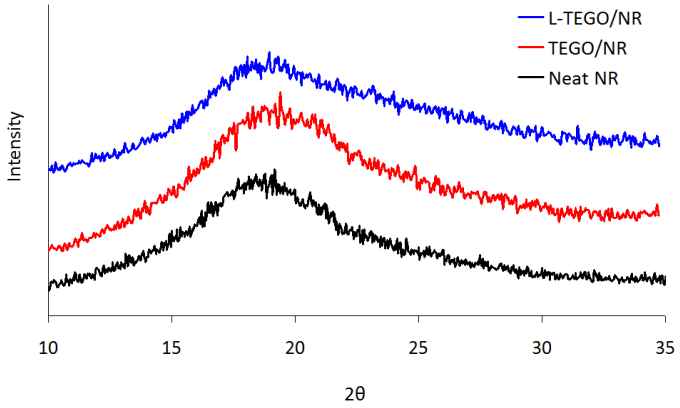

Figure D.2. Wide-angle X-ray scattering plots of TEGO/NR nanocomposites.

Figure D.2 compares the WAXS patterns of neat NR with the two types of nanocomposites at 5 phr TEGO loading. No major differences in the spectra were observed, although the broad scattering peak centered around $2\theta = 18°$ was suppressed somewhat in the L-TEGO/NR samples. However, no evidence of an emergence of a graphitic/GO peak was observed in the spectra.

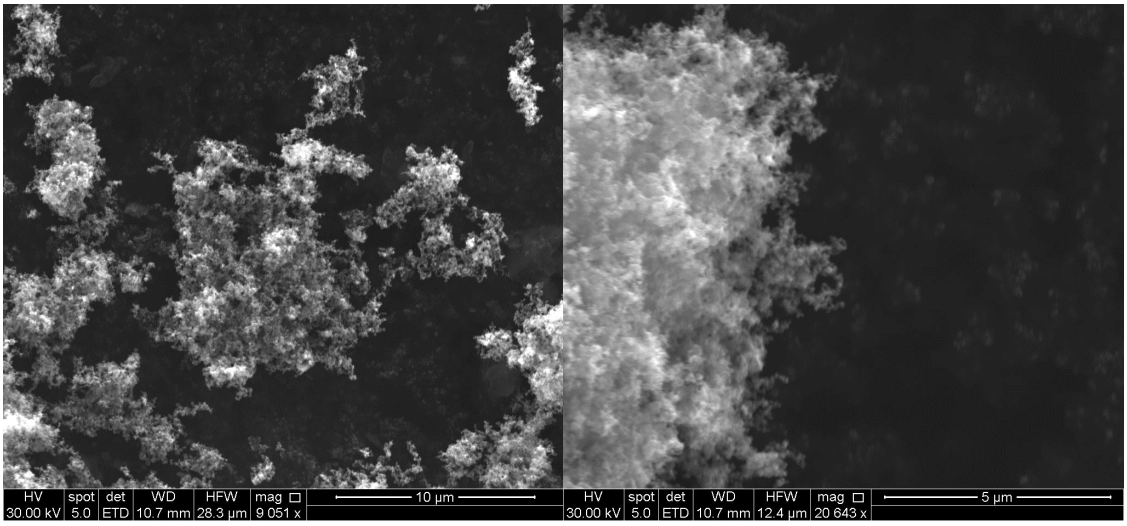

Figure D.3. SEM images of carbon black.

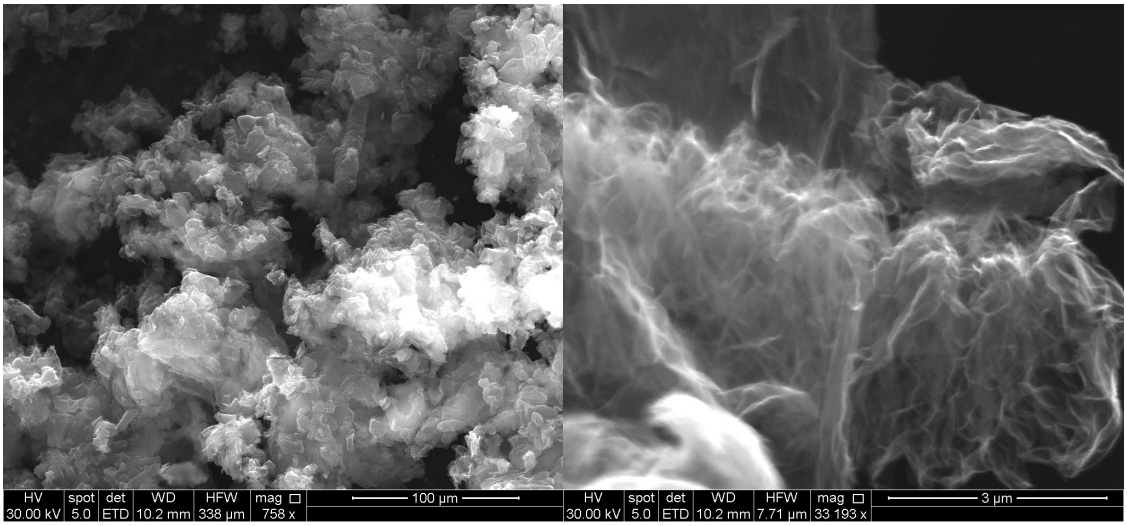

Figure D.4. SEM images of TEGO.

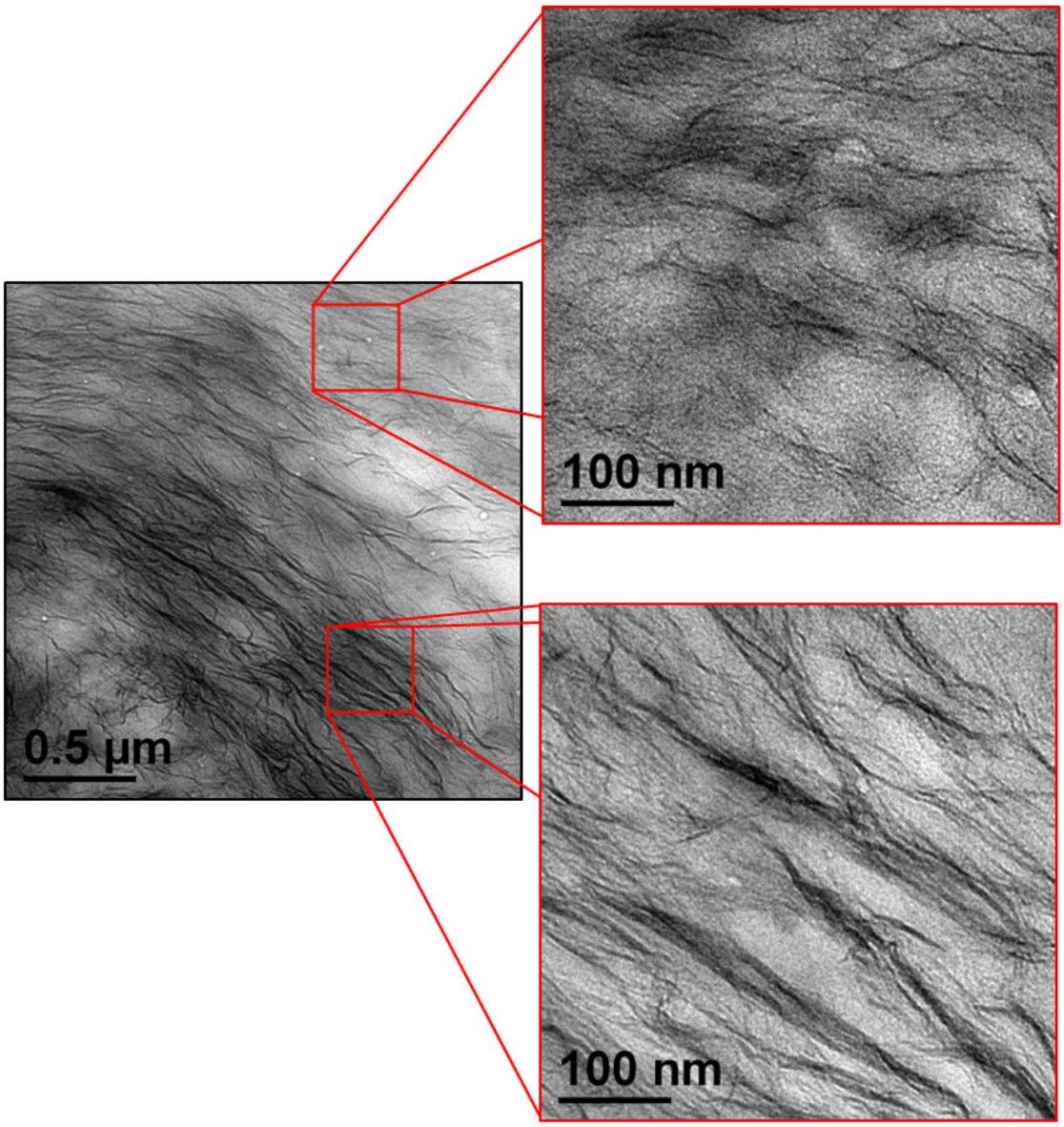

Figure D.5. TEM micrographs of TEGO/NR nanocomposites showing the variation in dispersion over the cross section. Certain regions contained predominately highly-exfoliated platelets, while others regions had thicker and more crumpled platelets showing more orientation. In still other regions (e.g., near the scale bar of the leftmost image), the platelets were more randomly-oriented. By contrast, the dispersion in the L-TEGO/NR nanocomposites was generally much more uniform over the cross section with a sparse distribution of larger tactoids.

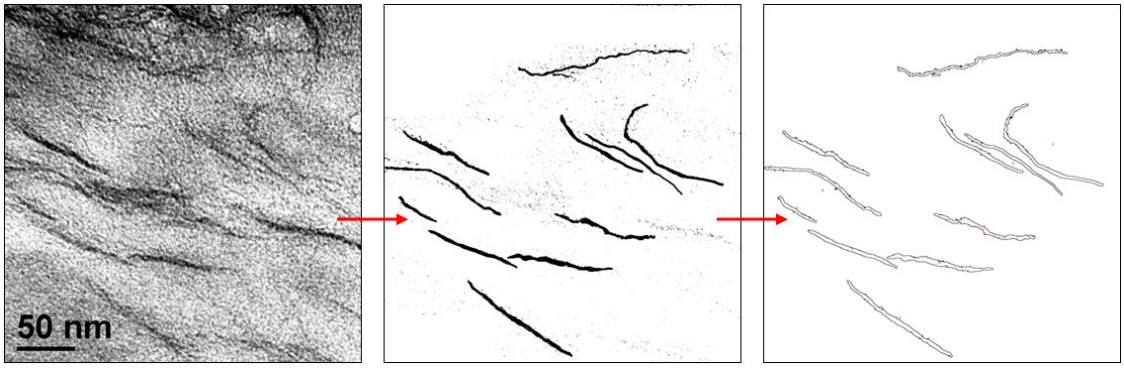

Figure D.6. Illustration of the procedure of quantifying dispersion, starting with contrast enhancement and, if necessary, careful outlining of edge-on particles in the micrograph. Particles obscured by the image edges or heavily overlapped with other platelets were excluded. A threshold filter was applied and the scaled particle sizes were determined using ImageJ[1] software. Further details on the procedure can be found elsewhere.[2] For this image, the average platelet thickness (11 particles) was determined to be 2.2 nm, the average lateral dimension (width) was 120.1 nm, and the average A_f was 55.7. Micrographs at higher magnifications generally tended to show higher values of A_f compared with images at lower magnifications, which also tended to include more particles.

Composite theory modeling was performed as described in Appendix B. The predictions of three composite models—Mori-Tanaka, modified Halpin-Tsai, and Guth—were compared with experimental data in this study. Analytical expressions based on Mori-Tanaka theory were derived by Tandon and Weng.[3, 4] The measured values of the composite moduli and aspect ratio, along with tabulated values for the Poisson's ratio, ν, of natural rubber and graphite (equal to ~0.5 and 0.37, respectively[5, 6]), and a graphene platelet modulus (E_f) of 250 GPa[7, 8] were used in the calculation.

REFERENCES

1. Rasband, W. S. ImageJ. http://imagej.nih.gov/ij/ (April 12),

2. Fornes, T. D.; Paul, D. R. Modeling properties of nylon 6/clay nanocomposites using composite theories. *Polymer* **2003,** 44, (17), 4993-5013.

3. Mori, T.; Tanaka, K. Average stress in matrix and average elastic energy of materials with misfitting inclusions. *Acta Metallurgica* **1973,** 21, 571-574.

4. Tandon, G. P.; Weng, G. J. The effect of aspect ratio of inclusions on the elastic properties of unidirectionally aligned composites. *Polymer Composites* **1984,** 5, 327-333.

5. Brandrup, J.; Immergut, E. H.; Grulke, E. A.; Abe, A.; Bloch, D. R., *Polymer Handbook*. 4 ed.; John Wiley and Sons: 1999; p 2336.

6. Kim, H.; Macosko, C. W. Morphology and properties of polyester/exfoliated graphite nanocomposites. *Macromolecules* **2008,** 41, (9), 3317-3327.

7. Gómez-Navarro, C.; Burghard, M.; Kern, K. Elastic properties of chemically derived single graphene sheets. *Nano Letters* **2008,** 8, (7), 2045-2049.

8. Suk, J. W.; Piner, R. D.; An, J.; Ruoff, R. S. Mechanical Properties of Monolayer Graphene Oxide. *ACS Nano* **2010,** 4, 6557-6564.

Appendix E:

Produciton and Analysis of Aqeuous Suspensions of Large-Area Graphene Oxide Platelets

GO was found to exfoliate to single graphene oxide sheets in water using a Resodyn LabRAM mixer, a mixing device that uses acoustic energy at resonance to mix materials. G-O platelets exfoliated using this device were found to be largely single layer with average lateral dimensions of up to nine microns, as confirmed by AFM, SEM, and DLS. Average platelet aspect ratios of these large-area G-O platelets are as high as 1000, as compared with ~150 for G-O platelets exfoliated by sonication. By use of acoustic energy of sufficient amplitude, full exfoliation can be achieved in just ten minutes with minimal sedimentation of the platelets. Exfoliation was minimal in organic solvents such as DMF and *N*-methylpyrrilidone. This instrument thus offers an attractive route to rapid production of large-area graphene oxide sheets that are unachievable by sonication or that exfoliate very slowly and in low yield by mechanical stirring.

The mixer works by finding the resonant frequency of the water/GO suspension (typical value, ~61 Hz). The intensity of the mixing (at that frequency) can then be varied as desired, using up to 100 Gs of acceleration to shake the contents in the mixer to produce micro-eddy currents thought to be responsible for providing the mixing action. Initial evaluation of mixing conditions was performed by trial-and-error: a set of

GO/water mixtures (5 mg of GO in 10 ml water) were prepared, mixed on the LabRAM mixer, and left to sit to observe the degree of sedimentation over a period of time. Generally it was found that intensities of more than 40 Gs were necessary to successfully exfoliate GO into a kinetically-stable G-O platelet suspension (stable for more than 1 day). Beyond that threshold, longer mixing times or higher-intensity mixing seemed to produce more stable suspensions, though mixing time appeared to be the more important parameter. However, prolonged mixing (>12 h) at intensities above 80 G resulted in excessive heating of the suspension and damaged the acrylic mixing container.‡‡ For this study, a mixing intensity of 60 G for 12 h was thus used to produce the large-area G-O suspensions.

Because G-O platelets can be more easily analyzed by techniques such as AFM and SEM, G-O platelets exfoliated by sonication and Resodyn mixing were compared in this section, rather than RG-O platelets. However, similar relative size distributions would be expected in the RG-O platelets produced from these two types of G-O platelets, per DLS analysis of G-O platelets before and after reduction.

The suspensions created by the LabRAM mixer exhibited the Tyndall effect, confirming the presence of colloidal G-O platelets. Samples for SEM analysis were prepared by deposition of dilute G-O suspensions onto p-doped (conductive) Si wafers and evaporation of water in an oven at 50 ºC. Several SEM images were taken at different

‡‡ It is recommended that plastic containers be used for mixing, particularly at higher intensities/longer times, as glass vials broke during mixing on multiple occasions during these trials.

magnifications of the two dispersions and the two sets of images were analyzed using ImageJ software to determine the average platelet size. Briefly, this analysis technique consists of binary conversion of the SEM images (such that platelets are black and the background white; see Figure E.1), followed by application of the particle size analysis feature built into the program. This method was also employed in the particle size analysis in Appendix C. The primary disadvantages of this method are that (1) SEM cannot distinguish between single- and multi-layer platelets, and (2) overlapping platelets can be difficult to distinguish, creating the appearance of one larger platelet. The results of the platelet size analysis by ImageJ are shown in Figure E.2.

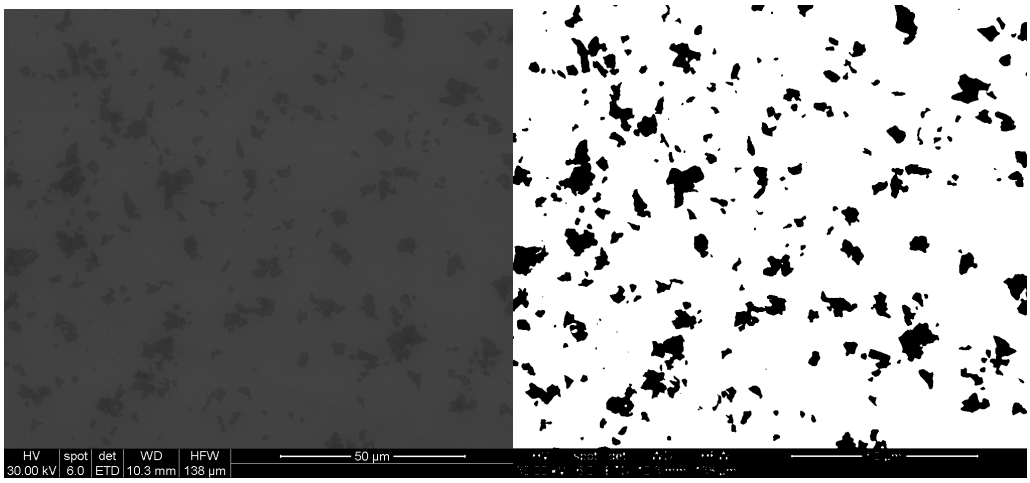

Figure E.1. Example of an SEM image of large-area G-O platelets on a Si wafer converted to a binary image for particle size analysis using ImageJ software.

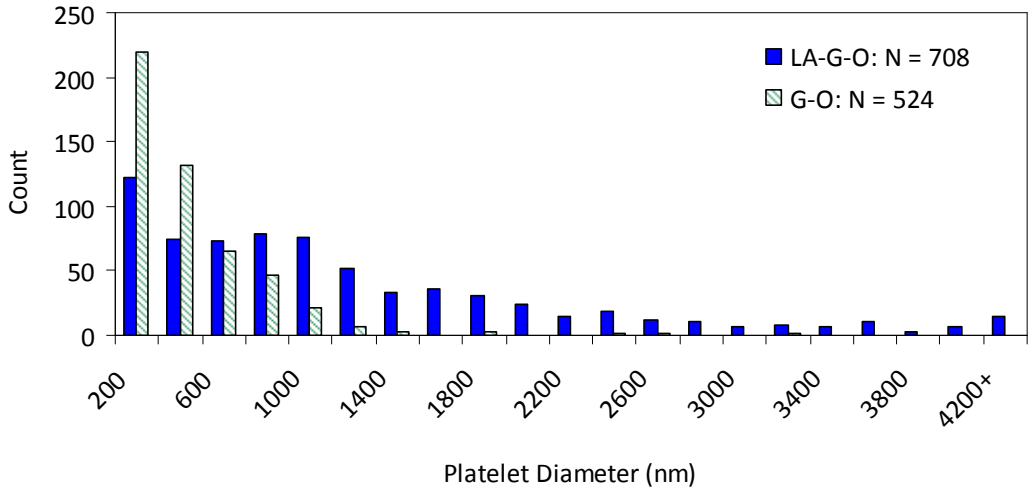

Figure E.2. Platelet diameter distribution comparison between G-O and large-area G-O platelets as determined by SEM analysis. Platelet diameter distribution of large-area G-O platelets is for platelets exfoliated at 70 G for 12 h in the LabRAM mixer. Platelet diameter distribution of G-O platelets corresponds to a suspension produced by 1 h of sonication.

As shown in Figure E.2 and Figure E.3, the G-O platelets produced by exfoliation in the LabRAM mixer are of irregular shape, largely single-layer, and are of a wide range of lateral dimensions. Although the largest cohort of platelets in both suspensions were less than 200 nm in diameter, there was a far greater number of platelets in the LabRAM-exfoliated suspension with dimensions of >1 μm. Thus, the LabRAM mixer is a relatively effective method for rapid production of large-area G-O platelets.

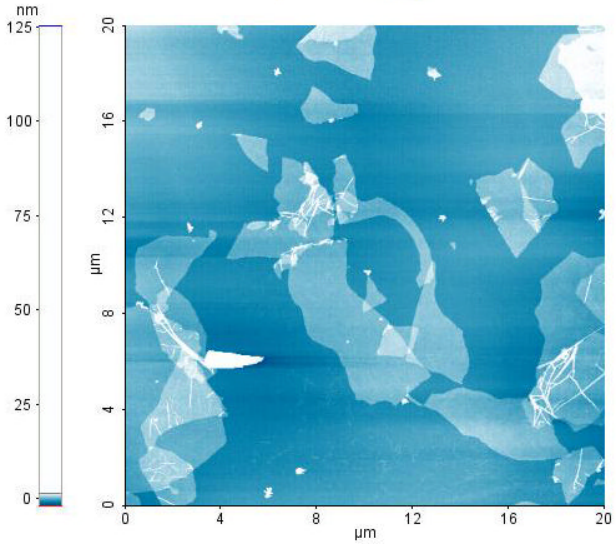

Figure E.3. AFM image of large-area G-O platelets showing the irregular shape and single-layer thickness of most platelets (mixer conditions: 70 G, 12 h).

DLS measurements agree with these conclusions. Average particle sizes produced using the LabRAM mixer were as much as six times larger than platelets produced by sonication, not taking into account the inaccuracy of DLS measurements for particles larger than 1 µm. Generally, the more intense the exfoliation protocol (in terms of mixing time and intensity), the smaller the average platelet size, but the greater the stability of the suspension. Indeed, the differences in suspension stability were readily observable: suspensions produced by exfoliation at 70 G for 3 h (see Table E.1 below) would exhibit significant sedimentation after only 1-2 days, whereas longer exfoliation times resulted in suspensions stable for 1-2 weeks or more. Thus, in any prospective application, the limited shelf life of such large-area G-O suspensions would need to be taken into account

and ideally, the platelets mixed into a polymer host or suitably functionalized soon after production.

Table E.1. Sizes of G-O platelets as measured by DLS along with zeta potential of each suspension. Note correlation between larger platelet size and lower absolute value of zeta potential (lower stability).

Conditions	size by DLS (nm)	ζ potential (mV)
Ultrasonication, 1 h	159	-50.4
70G, 3 h	989	-35.0
70G, 12 h	564	-39.2
100G, 20 min	684	-40.5

Bibliography

1. Paul, D. R.; Robeson, L. M. Polymer nanotechnology: Nanocomposites. *Polymer* **2008,** 49, (15), 3187-3204.

2. Schadler, L. S.; Brinson, L. C.; Sawyer, W. G. Polymer nanocomposites: a small part of the story. *Journal of the Minerals, Metals and Materials Society* **2007,** 59, (3), 53-60.

3. Vaia, R. A.; Maguire, J. F. Polymer nanocomposites with prescribed morphology: going beyond nanoparticle-filled polymers. *Chemistry of Materials* **2007,** 19, (11), 2736-2751.

4. Thostenson, E. T.; Li, C. Y.; Chou, T. W. Nanocomposites in context. *Composites Science and Technology* **2005,** 65, (3-4), 491-516.

5. Kumar, S. K.; Krishnamoorti, R. Nanocomposites: Structure, Phase Behavior, and Properties. *Annual Review of Chemical and Biomolecular Engineering* **2010,** 1, 37-58.

6. Fornes, T. D.; Paul, D. R. Modeling properties of nylon 6/clay nanocomposites using composite theories. *Polymer* **2003,** 44, (17), 4993-5013.

7. Schadler, L. S.; Kumar, S.; Benicewicz, B. C.; Lewis, S.; Harton, S. E. Designed Interfaces in Polymer Nanocomposites: A Fundamental Viewpoint. *MRS Bulletin* **2007,** 32, 335-340.

8. Nan, C.-W.; Shen, Y.; Ma, J. Physical Properties of Composites Near Percolation. *Annual Review of Materials Research* **2010,** 40, 131-151.

9. Han, C. D. On the Mechanisms Leading to Exfoliated Nanocomposites Prepared by Mixing. *Advances in Polymer Science* **2010,** 231, 1-75.

10. Kim, H.; Abdala, A. A.; Macosko, C. W. Graphene/Polymer Nanocomposites. *Macromolecules* **2010,** 43, 6515-6530.

11. Jancar, J.; Douglas, J. F.; Starr, F. W.; Kumar, S.; Cassagnau, P.; Lesser, A. J.; Sternstein, S. S.; Buehler, M. J. Current issues in research on structure-property relationships in polymer nanocomposites. *Polymer* **2010**, 3321-3343.

12. Okada, A.; Usuki, A. Twenty Years of Polymer-Clay Nanocomposites. *Macromolecular Materials and Engineering* **2006,** 291, 1449-1476.

13. Moniruzzaman, M.; Winey, K. I. Polymer nanocomposites containing carbon nanotubes. *Macromolecules* **2006,** 39, (16), 5194-5205.

14. Park, S.; Ruoff, R. S. Chemical methods for the production of graphenes. *Nature Nanotechnology* **2009,** 5, (4), 217-224.

15. Stankovich, S.; Dikin, D. A.; Dommett, G. H. B.; Kohlhaas, K. M.; Zimney, E. J.; Stach, E. A.; Piner, R. D.; Nguyen, S. T.; Ruoff, R. S. Graphene-based composite materials. *Nature* **2006,** 442, (7100), 282-286.

16. Dreyer, D. R.; Ruoff, R. S.; Bielawski, C. W. *Angewandte Chemie, International Edition in English*, DOI: 10.1002/anie.201003024.

17. Zhu, Y.; Murali, S.; Cai, W.; Li, X.; Suk, J. W.; Potts, J. R.; Ruoff, R. S. Graphene and Graphene Oxide: Synthesis, Properties, and Applications. *Advanced Materials* **2010,** 22, 3906-3924.

18. Jang, B. Z.; Zhamu, A. Processing of nanographene platelets (NGPs) and NGP nanocomposites: a review. *Journal of Materials Science* **2008,** 43, (15), 5092-5101.

19. Zhang, M.; Parajuli, R. R.; Mastrogiovanni, D.; Dai, B.; Lo, P.; Cheung, W.; Brukh, R.; Chiu, P. L.; Zhou, T.; Liu, Z. F.; Garfunkel, E.; He, H. X. Production of Graphene Sheets by Direct Dispersion with Aromatic Healing Agents. *Small* **2010,** 6, (10), 1100-1107.

20. Hernandez, Y.; Nicolosi, V.; Lotya, M.; Blighe, F. M.; Sun, Z.; De, S.; McGovern, I. T.; Holland, B.; Byrne, M.; Gun'Ko, Y. K. High-yield production of graphene by liquid-phase exfoliation of graphite. *Nature Nanotechnology* **2008,** 3, (9), 563-568.

21. Lotya, M.; Hernandez, Y.; King, P. J.; Smith, R. J.; Nicolosi, V.; Karlsson, L. S.; Blighe, F. M.; De, S.; Wang, Z.; McGovern, I. T.; Duesberg, G. S.; Coleman, J. N. Liquid Phase Production of Graphene by Exfoliation of Graphite in Surfactant/Water Solutions. *Journal of the American Chemical Society* **2009,** 131, (10), 3611-3620.

22. Lu, J.; Yang, J.-x.; Wang, J.; Lim, A.; Wang, S.; Loh, K. P. One-Pot Synthesis of Fluorescent Carbon Nanoribbons, Nanoparticles, and Graphene by the Exfoliation of Graphite in Ionic Liquids. *ACS Nano* **2009,** 3, (8), 2367-2375.

23. Dato, A.; Radmilovic, V.; Lee, Z.; Phillips, J.; Frenklach, M. Substrate-Free Gas-Phase Synthesis of Graphene Sheets. *Nano Letters* **2008,** 8, (7), 2012-2016.

24. Dreyer, D. R.; Park, S.; Bielawski, C. W.; Ruoff, R. S. The chemistry of graphene oxide. *Chemical Society Reviews* **2010,** 39, (1), 228-240.

25. Buchsteiner, A.; Lerf, A.; Pieper, J. r. Water Dynamics in Graphite Oxide Investigated with Neutron Scattering. *Journal of Physical Chemistry B* **2006,** 110, (45), 22328-22338.

26. Jang, J. Y.; Kim, M. S.; Jeong, H. M.; Shin, C. M. Graphite oxide/poly(methyl methacrylate) nanocomposites prepared by a novel method utilizing macroazoinitiator. *Composites Science and Technology* **2009,** 69, (2), 186-191.

27. Li, Z.; Zhang, W.; Luo, Y.; Yang, J.; Hou, J. G. How Graphene Is Cut upon Oxidation? *Journal of the American Chemical Society* **2009,** 131, (18), 6320-6321.

28. Paredes, J. I.; Villar-Rodil, S.; Martinez-Alonso, A.; Tascon, J. M. D. Graphene oxide dispersions in organic solvents. *Langmuir* **2008,** 24, (19), 10560-10564.

29. Zhu, Y.; Stoller, M. D.; Cai, W.; Velamakanni, A.; Piner, R. D.; Chen, D.; Ruoff, R. S. Exfoliation of Graphite Oxide in Propylene Carbonate and Thermal Reduction of the Resulting Graphene Oxide Platelets. *ACS Nano* **2010,** 4, (2), 1227-1233.

30. Schniepp, H. C.; Li, J. L.; McAllister, M. J.; Sai, H.; Herrera-Alonso, M.; Adamson, D. H.; Prud'homme, R. K.; Car, R.; Saville, D. A.; Aksay, I. A. Functionalized single graphene sheets derived from splitting graphite oxide. *Journal of Physical Chemistry B* **2006,** 110, (17), 8535-8539.

31. McAllister, M. J.; Li, J. L.; Adamson, D. H.; Schniepp, H. C.; Abdala, A. A.; Liu, J.; Herrera-Alonso, M.; Milius, D. L.; Car, R.; Prud'homme, R. K.; Aksay, I. A. Single sheet functionalized graphene by oxidation and thermal expansion of graphite. *Chemistry of Materials* **2007,** 19, (18), 4396-4404.

32. Ruess, V. G.; Vogt, F. *Monatshefte fur Chemie* **1948,** 78, 222-242.

33. Zhu, Y. W.; Murali, S.; Stoller, M. D.; Velamakanni, A.; Piner, R. D.; Ruoff, R. S. Microwave assisted exfoliation and reduction of graphite oxide for ultracapacitors. *Carbon* **2010,** 48, (7), 2118-2122.

34. Bagri, A.; Mattevi, C.; Acik, M.; Chabal, Y. J.; Chhowalla, M.; Shenoy, V. B. Structural evolution during the reduction of chemically derived graphene oxide. *Nature Chemistry* **2010,** 2, (7), 581-587.

35. Boukhvalov, D. W.; Katsnelson, M. I. Modeling of Graphite Oxide. *Journal of the American Chemical Society* **2008,** 130, (32), 10697-10701.

36. Stankovich, S.; Dikin, D. A.; Piner, R. D.; Kohlhaas, K. A.; Kleinhammes, A.; Jia, Y.; Wu, Y.; Nguyen, S. T.; Ruoff, R. S. Synthesis of graphene-based nanosheets via chemical reduction of exfoliated graphite oxide. *Carbon* **2007,** 45, (7), 1558-1565.

37. Li, D.; Muller, M. B.; Gilje, S.; Kaner, R. B.; Wallace, G. G. Processable aqueous dispersions of graphene nanosheets. *Nature Nanotechnology* **2008,** 3, (2), 101-105.

38. Stankovich, S.; Piner, R. D.; Chen, X.; Wu, N.; Nguyen, S. B. T.; Ruoff, R. S. Stable aqueous dispersions of graphitic nanoplatelets via the reduction of exfoliated graphite oxide in the presence of poly(sodium 4-styrenesulfonate). *Journal of Materials Chemistry* **2006,** 16, 155-158.

39. Stankovich, S.; Piner, R. D.; Nguyen, S. T.; Ruoff, R. S. Synthesis and exfoliation of isocyanate-treated graphene oxide nanoplatelets. *Carbon* **2006,** 44, (15), 3342-3347.

40. Bryning, M. B.; Milkie, D. E.; Islam, M. F.; Kikkawa, J. M.; Yodh, A. G. Thermal conductivity and interfacial resistance in single-wall carbon nanotube epoxy composites. *Applied Physics Letters* **2005,** 87, 161909.

41. Kim, H.; Miura, Y.; Macosko, C. W. Graphene/Polyurethane Nanocomposites for Improved Gas Barrier and Electrical Conductivity. *Chemistry of Materials* **2010,** 22, (11), 3441-3450.

42. Sinha Ray, S.; Okamoto, M. Polymer/layered silicate nanocomposites: a review from preparation to processing. *Progress in Polymer Science* **2003,** 28, (11), 1539-1641.

43. Jeong, H.-K.; Lee, Y. P.; Jin, M. H.; Kim, E. S.; Bae, J. J.; Lee, Y. H. Thermal stability of graphite oxide. *Chemical Physics Letters* **2009,** 470, (4-6), 255-258.

44. Kim, H.; Macosko, C. W. Morphology and properties of polyester/exfoliated graphite nanocomposites. *Macromolecules* **2008,** 41, (9), 3317-3327.

45. Kim, H.; Macosko, C. W. Processing-property relationships of polycarbonate/graphene composites. *Polymer* **2009,** 50, (15), 3797-3809.

46. Potts, J. R.; Murali, S.; Zhu, Y.; Zhao, X.; Ruoff, R. S. Microwave-exfoliated graphite oxide/polymer composites. *Macromolecules* **2011,** 44, 6488-6495.

47. Potts, J. R.; Lee, S. H.; Alam, T. M.; An, J.; Stoller, M. D.; Piner, R. D.; Ruoff, R. S. Thermomechanical properties of chemically modified graphene/poly(methyl methacrylate) composites made by in situ polymerization. *Carbon* **2011**, DOI: 10.1016/j.carbon.2011.02.023.

48. Zhan, Y. H.; Wu, J. K.; Xia, H. S.; Yan, N.; Fei, G. X. Dispersion and Exfoliation of Graphene in Rubber by an Ultrasonically-Assisted Latex Mixing and In Situ Reduciton Process. *Macromolecular Materials and Engineering* **2011,** 296, 590-602.

49. Ramanathan, T.; Abdala, A. A.; Stankovich, S.; Dikin, D. A.; Herrera-Alonso, M.; Piner, R. D.; Adamson, D. H.; Schniepp, H. C.; Chen, X.; Ruoff, R. S.; Nguyen, S.

T.; Aksay, I. A.; Prud'homme, R. K.; Brinson, L. C. Functionalized graphene sheets for polymer nanocomposites. *Nature Nanotechnology* **2008,** 3, (6), 327-331.

50. Kai, W.; Hirota, Y.; Hua, L.; Inoue, Y. Thermal and Mechanical Properties of a Poly(e-caprolactone)/Graphite Oxide Composite. *Journal of Applied Polymer Science* **2008,** 107, 1395-1400.

51. Fu, X.; Qutubuddin, S. Polymer-clay nanocomposites: exfoliation of organophilic montmorillonite nanolayers in polystyrene. *Polymer* **2001,** 42, (2), 807-813.

52. Schaefer, D. W.; Justice, R. S. How nano are nanocomposites? *Macromolecules* **2007,** 40, (24), 8501-8517.

53. Rafiee, M. A.; Rafiee, J.; Wang, Z.; Song, H. H.; Yu, Z. Z.; Koratkar, N. Enhanced Mechanical Properties of Nanocomposites at Low Graphene Content. *Acs Nano* **2009,** 3, (12), 3884-3890.

54. Hirata, M.; Gotou, T.; Horiuchi, S.; Fujiwara, M.; Ohba, M. Thin-film particles of graphite oxide 1: High-yield synthesis and flexibility of the particles. *Carbon* **2004,** 42, (14), 2929-2937.

55. Chen, D.; Zhu, H.; Liu, T. In Situ Thermal Preparation of Polyimide Nanocomposite Films Containing Functionalized Graphene Sheets. *ACS Applied Materials & Interfaces*, DOI: 10.1021/am1008437.

56. Krishnamoorti, R.; Yurekli, K. Rheology of polymer layered silicate nanocomposites. *Current Opinion in Colloid & Interface Science* **2001,** 6, 464-470.

57. Chen, H.; Müller, M. B.; Gilmore, K. J.; Wallace, G. G.; Li, D. Mechanically Strong, Electrically Conductive, and Biocompatible Graphene Paper. *Advanced Materials* **2008,** 20, (18), 3557-3561.

58. Pang, H.; Chen, T.; Zhang, G.; Zeng, B.; Li, Z. M. An electrically conducting polymer/graphene composite with a very low percolation threshold. *Materials Letters* **2010,** 64, (10), 2226-2229.

59. Eda, G.; Chhowalla, M. Graphene-based composite thin films for electronics. *Nano Letters* **2009,** 9, (2), 814-818.

60. Haggenmueller, R.; Gommans, H. H.; Rinzler, A. G.; Fischer, J. E.; Winey, K. I. Aligned single-wall carbon nanotubes in composites by melt processing methods. *Chemical Physics Letters* **2000,** 330, (3-4), 219-225.

61. Lee, C.; Wei, X.; Kysar, J. W.; Hone, J. Measurement of the elastic properties and intrinsic strength of monolayer graphene. *Science* **2008,** 321, (5887), 385-388.

62. Paci, J. T.; Belytschko, T.; Schatz, G. C. Computational Studies of the Structure, Behavior upon Heating, and Mechanical Properties of Graphite Oxide. *Journal of Physical Chemistry C* **2007,** 111, 18099-18111.

63. Gómez-Navarro, C.; Burghard, M.; Kern, K. Elastic properties of chemically derived single graphene sheets. *Nano Letters* **2008,** 8, (7), 2045-2049.

64. Wakabayashi, K.; Pierre, C.; Dikin, D. A.; Ruoff, R. S.; Ramanathan, T.; Brinson, L. C.; Torkelson, J. M. Polymer-graphite nanocomposites: Effective dispersion and major property enhancement via solid-state shear pulverization. *Macromolecules* **2008,** 41, (6), 1905-1908.

65. Brune, D. A.; Bicerano, J. Micromechanics of nanocomposites: comparison of tensile and compressive elastic moduli, and prediction of effects of incomplete exfoliation and imperfect alignment on modulus. *Polymer* **2002,** 43, 369-387.

66. Boehm, H. P.; Clauss, A.; Fischer, G.; Hofmann, U. In *Surface Properties of Extremely Thin Graphite Lamellae*, Proceedings of the Fifth Conference on Carbon, 1962; 1962.

67. Pukánszky, B.; Fekete, E., *Adhesion and surface modification*. Springer: 1999; Vol. 139, p 109-153.

68. Lv, C.; Xue, Q.; Xia, D.; Ma, M.; Xie, J.; Chen, H. Effect of Chemisorption on the Interfacial Bonding Characteristics of Graphene- Polymer Composites. *Journal of Physical Chemistry C* **2010,** 114, (14), 6588-6594.

69. Kluppel, M., *The Role of Disorder in Filler Reinforcement of Elastomers on Various Length Scales*. Springer: 2003; Vol. 164, p 86.

70. Wagner, H. D.; Vaia, R. A. Nanocomposites: issues at the interface. *Materials Today* **2004,** 7, (11), 38-42.

71. Schadler, L. S.; Giannaris, S. C.; Ajayan, P. M. Load transfer in carbon nanotube epoxy composites. *Applied Physics Letters* **1998,** 73, (26), 3842-3844.

72. Liu, H.; Brinson, L. C. Reinforcing efficiency of nanoparticles: A simple comparison for polymer nanocomposites. *Composites Science and Technology* **2008,** 68, (6), 1502-1512.

73. Balandin, A. A.; Ghosh, S.; Bao, W.; Calizo, I.; Teweldebrhan, D.; Miao, F.; Lau, C. N. Superior thermal conductivity of single-layer graphene. *Nano Letters* **2008,** 8, (3), 902-907.

74. Ghosh, S.; Calizo, I.; Teweldebrhan, D.; Pokatilov, E. P.; Nika, D. L.; Balandin, A. A.; Bao, W.; Miao, F.; Lau, C. N. Extremely high thermal conductivity of graphene: Prospects for thermal management applications in nanoelectronic circuits. *Applied Physics Letters* **2008,** 92, 151911.

75. Seol, J. H.; Jo, I.; Moore, A. L.; Lindsay, L.; Aitken, Z. H.; Pettes, M. T.; Li, X.; Yao, Z.; Huang, R.; Broido, D.; Mingo, N.; Ruoff, R. S.; Shi, L. Two-dimensional phonon transport in supported graphene. *Science* **2010,** 328, (5975), 213-216.

76. Yu, A.; Ramesh, P.; Sun, X.; Bekyarova, E.; Itkis, M. E.; Haddon, R. C. Enhanced Thermal Conductivity in a Hybrid Graphite Nanoplatelet-Carbon Nanotube Filler for Epoxy Composites. *Advanced Materials* **2008,** 20, (24), 4740-4744.

77. Lin, W.; Zhang, R.; Wong, C. P. Modeling of Thermal Conductivity of Graphite Nanosheet Composites. *Journal of Electronic Materials* **2010,** 39, (3), 268-272.

78. Kalaitzidou, K.; Fukushima, H.; Drzal, L. T. Multifunctional polypropylene composites produced by incorporation of exfoliated graphite nanoplatelets. *Carbon* **2007,** 45, (7), 1446-1452.

79. Hummers, W. S.; Offeman, R. E. Preparation of graphitic oxide. *Journal of the American Chemical Society* **1958,** 80, (6), 1339.

80. Glover, A. J.; Cai, M.; Overdeep, K. R.; Kranbuehl, D. E.; Schniepp, H. C. In Situ Reduction of Graphene Oxide in Polymers. *Macromolecules* **2011,** 44, 9821-9829.

81. Mori, T.; Tanaka, K. Average stress in matrix and average elastic energy of materials with misfitting inclusions. *Acta Metallurgica* **1973,** 21, 571-574.

82. Tandon, G. P.; Weng, G. J. The effect of aspect ratio of inclusions on the elastic properties of unidirectionally aligned composites. *Polymer Composites* **1984,** 5, 327-333.

83. Suk, J. W.; Piner, R. D.; An, J.; Ruoff, R. S. Mechanical Properties of Monolayer Graphene Oxide. *ACS Nano* **2010,** 4, 6557-6564.

84. Brandrup, J.; Immergut, E. H.; Grulke, E. A.; Abe, A.; Bloch, D. R., *Polymer Handbook*. 4 ed.; John Wiley and Sons: 1999; p 2336.

85. Chen, G.; Weng, W.; Wu, D.; Wu, C. PMMA/graphite nanosheets composite and its conducting properties. *European Polymer Journal* **2003,** 39, (12), 2329-2335.

86. Yoonessi, M.; Gaier, J. R. Highly Conductive Multifunctional Graphene Polycarbonate Nanocomposites. *ACS Nano*, DOI: 10.1021/nn1019626.

87. Zhang, H. B.; Zheng, W. G.; Yan, Q.; Yang, Y.; Wang, J. W.; Lu, Z. H.; Ji, G. Y.; Yu, Z. Z. Electrically conductive polyethylene terephthalate/graphene nanocomposites prepared by melt compounding. *Polymer* **2010,** 51, (5), 1191-1196.

88. Brunauer, S.; Emmett, P. H.; Teller, E. Adsorption of gases in multimolecular layers. *Journal of the American Chemical Society* **1938,** 60, (2), 309-319.

89. Moore, A. L.; Cummings, A. T.; Jensen, J. M.; Shi, L.; Koo, J. H. Thermal Conductivity Measurements of Nylon 11-Carbon Nanofiber Nanocomposites. *Journal of Heat Transfer* **2009,** 131, 091602.

90. Vermant, J.; Ceccia, S.; Dolgovskij, M. K.; Maffettone, P. L.; Macosko, C. W. Quantifying dispersion of layered nanocomposites via melt rheology. *Journal of Rheology* **2007,** 51, (3), 429-450.

91. Ren, J.; Silva, A. S.; Krishnamoorti, R. Linear Viscoelasticity of Disordered Polystyrene-Polyisoprene Block Copolymer Based Layered-Silicate Nanocomposites. *Macromolecules* **2000,** 33, 3739-3746.

92. Zhao, X.; Zhang, Q. H.; Chen, D. J.; Lu, P. Enhanced Mechanical Properties of Graphene-Based Poly(vinyl alcohol) Composites. *Macromolecules* **2010,** 43, (5), 2357-2363.

93. Hsieh, A. J.; Moy, P.; Beyer, F. L.; Madison, P.; Napadensky, E.; Ren, J.; Krishnamoorti, R. Mechanical Response and Rheological Properties of Polycarbonate Layered-Silicate Nanocomposites. *Polymer Engineering and Science* **2004,** 44, (5), 825-837.

94. Yoon, P. J.; Hunter, D. L.; Paul, D. R. Polycarbonate nanocomposites. Part 1. Effect of organoclay structure on morphology and properties. *Polymer* **2003,** 44, 5323-5339.

95. Steurer, P.; Wissert, R.; Thomann, R.; Mulhaupt, R. Functionalized Graphenes and Thermoplastic Nanocomposites Based upon Expanded Graphite Oxide. *Macromolecular Rapid Communications* **2009,** 30, (4-5), 316-327.

96. Ren, J.; Casanueva, B. F.; Mitchell, C. A.; Krishnamoorti, R. Disorientation Kinetics of Aligned Polymer Layered Silicate Nanocomposites. *Macromolecules* **2003,** 36, 4188-4194.

97. Bauhofer, W.; Kovacs, J. Z. A review and analysis of electrical percolation in carbon nanotube polymer composites. *Composites Science and Technology* **2009,** 69, (10), 1486-1498.

98. Kovacs, J. Z.; Velagala, B. S.; Schulte, K.; Bauhofer, W. Two percolation thresholds in carbon nanotube epoxy composites. *Composites Science and Technology* **2007,** 67, (5), 922-928.

99. Han, Z.; Fina, A. Thermal conductivity of carbon nanotubes and their polymer nanocomposites: A review. *Progress in Polymer Science* **2011,** 36, 914-944.

100. Hill, R. F.; Supancic, P. H. Thermal Conductivity of Platelet-Filled Polymer Composites. *Journal of the American Ceramic Society* **2002,** 85, (4), 851-857.

101. Hatta, H.; Taya, M. Equivalent Inclusion Method for Steady State Heat Conduction in Composites. *international Journal of Engineering Science* **1986,** 24, (7), 1159-1172.

102. Sun, X.; Ramesh, P.; Itkis, M. E.; Bekyarova, E.; Haddon, R. C. Dependence of the thermal conductivity of two-dimensional graphite nanoplatelet-based composites on the nanoparticle size distribution. *Journal of Physics: Condensed Matter* **2010,** 22, 334216.

103. Wang, S. R.; Tambraparni, M.; Qiu, J. J.; Tipton, J.; Dean, D. Thermal Expansion of Graphene Composites. *Macromolecules* **2009,** 42, (14), 5251-5255.

104. Choongho, Y.; Kim, Y. S.; Kim, D.; Grunlan, J. C. Thermoelectric Behavior of Segregated-Network Polymer Nanocomposites. *Nano Letters* **2008,** 8, (12), 4428-4432.

105. Galimberti, M., *Rubber-Clay Nanocomposites*. John Wiley & Sons: Hoboken, New Jersey, 2011.

106. Ozbas, B.; O'Neill, C. D.; Register, R. A.; Aksay, I. A.; Prud'homme, R. K.; Adamson, D. H. Multifunctional Elastomer Nanocomposites with Functionalized Graphene Single Sheets. *Journal of Polymer Science Part B: Polymer Physics* **2012,** 50, 910-916.

107. Ozbas, B.; Toki, S.; Hsiao, B. S.; Chu, B.; Register, R. A.; Aksay, I. A.; Prud'homme, R. K.; Adamson, D. H. Strain-Induced Crystallization and Mechanical Properties of Functionalized Graphene Sheet-Filled Natural Rubber. *Journal of Polymer Science Part B: Polymer Physics* **2012,** 50, 718-723.

108. Park, S.; An, J. H.; Jung, I. W.; Piner, R. D.; An, S. J.; Li, X. S.; Velamakanni, A.; Ruoff, R. S. Colloidal Suspensions of Highly Reduced Graphene Oxide in a Wide Variety of Organic Solvents. *Nano Letters* **2009,** 9, (4), 1593-1597.

109. Zhang, L.; Wang, Y.; Wang, Y.; Sui, Y.; Yu, D.-S. Morphology and Mechanical Properties of Clay/Styrene-Butadiene Rubber Nanocomposites. *Journal of Applied Polymer Science* **2000,** 78, (11), 1873-1878.

110. Wang, Y.; Zhang, L.; Tang, C.; Yu, D.-S. Preparation and Characterization of Rubber-Clay Nanocomposites. *Journal of Applied Polymer Science* **2000,** 78, (11), 1879-1883.

111. Wu, Y.-P.; Wang, Y.-Q.; Zhang, H.-F.; Wang, Y.-Z.; Yu, D.-S.; Zhang, L.-Q.; Yang, J. Rubber-pristine clay nanocomposites prepared by co-coagulating rubber latex and clay aqueous suspension. *Composites Science and Technology* **2005,** 65, 1195-1202.

112. Varghese, S.; Karger-Kocsis, J. Natural rubber-based nanocomposites by latex compounding with layered silicates. *Polymer* **2003,** 44, 4921-4927.

113. Valadares, L. F.; Leite, C. A. P.; Galembeck, F. Preparation of natural rubber-montmorillonite nanocomposite in aqueous medium: evidence for polymer-platelet adhesion. *Polymer* **2006,** 47, (2), 672-678.

114. Pojanavaraphan, T.; Magaraphan, R. Prevulcanized natural rubber latex/clay aerogel nanocomposites. *European Polymer Journal* **2008,** 44, (7), 1968-1977.

115. White, J. L., *Rubber Processing: Technology - Materials - Principles*. Hanser/Gardner: Cincinnati, Ohio, 1995.

116. Mullins, L. Softening of rubber by deformation. *Rubber Chemistry and Technology* **1969,** 42, 339-362.

117. Busse, W. F. Mastication of Rubber: An Oxidation Process. *Industrial & Engineering Chemistry Research* **1931,** 24, (2), 140-146.

118. Mark, J. E.; Erman, B.; Eirich, F. R., *The Science and Technology of Rubber*. 3rd ed.; Elsevier 2010.

119. Wood, L. A.; Bullman, G., W. Creep and Other Tensile Properties of Rubber Cross-linked by Dicumyl Peroxide. *Journal of Polymer Science* **1972,** 10, 43-50.

120. Payne, A. R. The Dynamic Properties of Carbon Black-Loaded Natural Rubber Vulcanizates. *Journal of Applied Polymer Science* **1962,** 6, (19), 57-63.

121. Bokobza, L. The Reinforcement of Elastomeric Networks by Fillers. *Macromolecular Materials and Engineering* **2004,** 289, 607-621.

122. Wang, X.; Roberston, C. G. Strain-induced nonlinearity of filled rubbers. *Physical Review E: Statistical, Nonlinear, and Soft Matter Physics* **2005,** 72, 031406.

123. Voet, A. Reinforcement of Elastomers by Fillers: Review of Period 1967-1976. *Journal of Polymer Science: Macromolecular Reviews* **1980,** 15, 327-373.

124. Donnet, J.-B.; Voet, A., *Carbon Black: Physics, Chemistry, and Elastomer Reinforcement*. Marcel Dekker: New York, 1976; p 351.

125. Steward, P. A.; Hearn, J.; Wilkinson, M. C. An overview of polymer latex film formation and properties. *Advances in Colloid and Interface Science* **2000,** 86, 195-267.

126. Mullins, L.; Tobin, N. R. Stress Softening in Rubber Vulcanizates. Part I. Use of a Strain Amplification Factor to Describe the Elastic Behavior of Filler-Reinforced Vulcanized Rubber. *Journal of Applied Polymer Science* **1965,** 9, 2993-3009.

127. Arroyo, M.; Lopez-Manchado, M. A.; Herrero, B. Organo-montmorillonite as substitute of carbon black in natural rubber compounds. *Polymer* **2003,** 44, (8), 2447-2453.

128. Tucker, C. L.; Liang, E. Stiffness predictions for unidirectional short-fiber composites: Review and evaluation. *Composites Science and Technology* **1999,** 59, 655-671.

129. Ellison, C. J.; Torkelson, J. M. The distribution of glass-transition temperatures in nanoscopically confined glass formers. *Nature Materials* **2003,** 2, (10), 695-700.

130. Bansal, A.; Yang, H.; Li, C.; Cho, K.; Benicewicz, B. C.; Kumar, S. K.; Schadler, L. S. Quantitative equivalence between polymer nanocomposites and thin polymer films. *Nature Materials* **2005,** 4, (9), 693-698.

131. Rittigstein, P.; Priestley, R. D.; Broadbelt, L. J.; Torkelson, J. M. Model polymer nanocomposites provide an understanding of confinement effects in real nanocomposites. *Nature Materials* **2007,** 6, (4), 278-282.

132. Bergström, J. S.; Boyce, M. C. Mechanical Behavior of Particle Filled Elastomers. *Rubber Chemistry and Technology* **1999,** 72, (4), 633-656.

133. Guth, E. Theory of Filler Reinforcement. *Journal of Applied Physics* **1945,** 16, (20), 20-25.

134. Bicerano, J.; Douglas, J. F.; Brune, D. A. Model for the Viscosity of Particle Dispersions. *Journal of Macromolecular Science, Part C: Polymer Reviews* **1999,** 39, (4), 561-642.

135. Wu, Y.; Jia, Q.; Yu, D.-S.; Zhang, L. Modeling Young's modulus of rubber-clay nanocomposites using composite theories. *Polymer Testing* **2004,** 23, 903-909.

136. Shia, D.; Hui, C. Y.; Burnside, S. D.; Giannelis, E. P. An Interface Model for the Prediction of Young's Modulus of Layered Silicate-Elastomer Nanocomposites. *Polymer Composites* **1998,** 19, (5), 608-617.

137. Harwood, J. A. C.; Payne, A. R. Stress Softening in Natural Rubber Vulcanizates. Part IV. Unfilled Vulcanizates. *Journal of Applied Polymer Science* **1966,** 10, 1203-1211.

138. Qureshi, M. N.; Qammar, H. Mill processing and properties of rubber-clay nanocomposites. *Materials Science and Engineering C* **2010,** 30, 590-596.

139. Ma, X.; Zachariah, M. R.; Zangmeister, C. D. Crumpled Nanopaper from Graphene Oxide. *Nano Letters* **2012,** 12, 486-489.

140. Alexandre, M.; Dubois, P. Polymer-layered silicate nanocomposites: preparation, properties and uses of a new class of materials. *Materials Science and Engineering R Reports* **2000,** 28, (1-2), 1-63.

141. Du, J.; Zhao, L.; Zeng, Y.; Zhang, L.; Li, F.; Liu, P.; Liu, C. Comparison of electrical properties between multi-walled carbon nanotube and graphene nanosheet/high density polyethylene composites with a segregated network structure. *Carbon* **2011,** 49, 1094-1100.

142. Potschke, P.; Abdel-Goad, M.; Pegel, S.; Jehnichen, D.; Mark, J. E.; Zhou, D. H.; Heinrich, G. Comparisons Among Electrical and Rheological Properties of Melt-Mixed Composites Containing Various Carbon Nanostructures. *Journal of Macromolecular Science, Part A: Pure and Applied Chemistry* **2010,** 47, (1), 12-19.

143. Fornes, T. D.; Baur, J. W.; Sabba, Y.; Thomas, E. L. Morphology and properties of melt-spun polycarbonate fibers containing single- and multi-wall carbon nanotubes. *Polymer* **2006,** 47, (5), 1704-1714.

144. Traina, M.; Pegoretti, A. In situ reduction of graphene oxide dispersed in a polymer matrix. *Journal of Nanoparticle Research* **2012,** 14, 801.

145. Endo, M.; Noguchi, T.; Ito, M.; Takeuchi, K.; Hayashi, T.; Kim, Y. A.; Wanibuchi, T.; Jinnai, H.; Terrones, M.; Dresselhaus, M. S. Extreme-Performance Rubber Nanocomposites for Probing and Excavating Deep Oil Resources Using Multi-Walled Carbon Nanotubes. *Advanced Functional Materials* **2008,** 18, (21), 3403-3409.

146. Bokobza, L. Multiwall carbon nanotube elastomeric composites: A review. *Polymer* **2007,** 48, 4907-4920.

147. Sengupta, R.; Chakraborty, S.; Bandyopadhyay, S.; Dasgupta, S.; Mukhopadhyay, R.; Auddy, K.; Deuri, A. S. A Short Review on Rubber/Clay Nanocomposites With Emphasis on Mechanical Properties. *Polymer Engineering and Science* **2007,** 47, 1956-1974.

148. Ramorino, G.; Bignotti, F.; Pandini, S.; Ricco, T. Mechanical reinforcement in natural rubber/organoclay nanocomposites. *Composites Science and Technology* **2009,** 69, 1206-1211.

149. Fakhru'l-Razi, A.; Atieh, M. A.; Girun, N.; Chuah, T. G.; El-Sadig, M.; Biak, D. R. A. Effect of multi-wall carbon nanotubes on the mechanical properties of natural rubber. *Composite Structures* **2006,** 75, 496-500.

150. Hrachova, J.; Komadel, P.; Chodak, I. Effect of montmorillonite modification on mechanical properties of vulcanized natural rubber composites. *Journal of Materials Science* **2008,** 43, 2012-2017.

151. Birdi, K. S., *Surface and Colloid Chemistry: Principles and Applications*. CRC Press: 2012.

152. Sui, G.; Zhong, W.; Yang, X.; Zhao, S. Processing and Material Characteristics of a Carbon-Nanotube-Reinforced Natural Rubber. *Macromolecular Materials and Engineering* **2007,** 292, 1020-1026.

153. Yue, D.; Liu, Y.; Shen, Z.; Zhang, L. Study on preparation and properties of carbon nanotubes/rubber composites. *Journal of Materials Science* **2006,** 41, 2541-2544.

154. Likozar, B. Modeling of Chemical Kinetics of Elastomer/Hydroxyl- and Carboxyl-Functionalized Multiwalled Carbon Nanotubes Nanocomposites' Cross-Linking. *Polymer Engineering and Science* **2011,** 51, 542-549.

155. Lopez-Manchado, M. A.; Arroyo, M.; Herrero, B.; Biagiotti, J. Vulcanization Kinetics of Natural Rubber-Organoclay Nanocomposites. *Journal of Applied Polymer Science* **2003,** 89, 1-15.

156. Das, A.; Stockelhuber, K. W.; Jurk, R.; Heinrich, G. Routes to Rubber Nanocomposites. *Macromolecular Symposia* **2010,** 291-292, 95-105.